CRANFIELD UNIVERSITY

GILBERTO MATERANO BLANCO

NUMERICAL MODELLING OF PRESSURE RISE COMBUSTION FOR REDUCING EMISSIONS OF FUTURE CIVIL AIRCRAFT

SCHOOL OF ENGINEERING

PhD
Academic Year: 2013-2014

Supervisor: Professor Mark Savill
April, 2014

CRANFIELD UNIVERSITY

SCHOOL OF ENGINEERING
Department of Power and Propulsion

PhD

Academic Year 2013-2014

Gilberto Ignacio Materano Blanco

NUMERICAL MODELLING OF PRESSURE RISE COMBUSTION FOR REDUCING EMISSIONS OF FUTURE CIVIL AIRCRAFT

Supervisor: Professor Mark Savill
April, 2014

This thesis is submitted in partial fulfilment of the requirements for the degree of Doctor of Philosophy

Me gustaría dedicarle este trabajo a mi familia, y en particular a mi querida madre "Sra. María Elizabeth Blanco de Materano", quien en vida me enseñó con su dedicación y entrega a ser fuerte y a luchar para alcanzar las metas deseadas, sin importar lo difícil que parezcan.

Gilberto Materano

16/Abril/2014

ABSTRACT

This work assesses the feasibility of designing and implementing the wave rotor (WR), the pulse detonation engine (PDE) and the internal combustion wave rotor (ICWR) as part of novel Brayton cycles able to reduce emissions of future aircraft. The design and evaluation processes are performed using the simplified analytical solution of the devices as well as 1D-CFD models. A code based on the finite volume method is built to predict the position and dimensions of the slots for the WR and ICWR. The mass and momentum equations are coupled through a modified SIMPLE algorithm to model compressible flow. The code includes a novel tracking technique to ensure the global mass balance. A code based on the method of characteristics is built to predict the profiles of temperature, pressure and velocity at the discharge of the PDE and the effect of the PDEs array when it operates as combustion chamber of gas turbines. The detonation is modelled by using the NASA-CEA code as a subroutine whilst the method of characteristics incorporates a model to capture the throttling and non-throttling conditions obtained at the PDE's open end during the transient process. A medium-sized engine for business jets is selected to perform the evaluation that includes parameters such as specific thrust, specific fuel consumption and efficiency of energy conversion. The ICWR offers the best performance followed by the PDE; both options operate with a low specific fuel consumption and higher specific thrust. The detonation in an ICWR does not require an external source of energy, but the PDE array designed is simple. The WR produced an increase in the turbine performance, but not as high as the other two devices. These results enable the statement that a pressure rise combustion process behaves better than pressure exchangers for this size of gas turbine. Further attention must be given to the NOx emission, since the detonation process is able to cause temperatures above 2000 K while dilution air could be an important source of oxygen.

Keywords:

Wave Rotor, Pulse Detonation Engine, Internal Combustion Wave Rotor, Gas turbine, Performance

ACKNOWLEDGEMENTS

I would like to use this opportunity to express my gratitude and thanks to Professor A. M. Savill, who gave me the chance to turn a dream into reality. Thanks for his support, guidance and dedication, and now as well as a PhD, I believe I have the necessary skills and tools to continue to develop new knowledge.

I would like to thank the CleanSky project which opened its doors to me to contribute to this worthy cause that intends to transform the future of aviation through the development of new environment-friendly technologies to ensure a sustainable world.

I would also thank Dr Timos Kipouros, Dr David Macmanus and Dr Bobby Sethi for the useful information and discussions during the execution of this research over topics such as efficient programming, combustion and compressible flow. Also, I would like to thank the administrative staff, Isobel, Gill and Nicola for their selfless desire to help me with administration matters.

I wish to thank all my friends and colleagues in the Power and Propulsion Science Group who shared with me difficult moments as well as moments of great happiness. I really enjoyed working with them.

I wish to thank all my friends outside the University, since they made me and my family feel at home during our stay in UK.

Finally, I am grateful to Louise Woodland for her involvement in editing the text of this work.

TABLE OF CONTENTS

LIST OF FIGURES

LIST OF TABLES

LIST OF ABBREVIATIONS

$\#_{PDE}$	Number of PDE
$\left\|Y_{(f)}\right\|$	Amplitude of the harmonics
$\bar{u}_{SW}$	Average velocity of the SW relative to the channels
$\dot{\omega}_{NO}$	Source or destruction term of NOx
$\dot{\omega}_{NO}$	Source term of NO in a combustion process
$\dot{\omega}_i$	Source or destruction term of component i
$\dot{\omega}_i$	Source term of component i in a combustion process
$\emptyset_{high}$	Higher value of the rank in the decision making matrix
$\emptyset_{PDE}$	PDE's diameter
$\emptyset_{in}$	Internal diameter of the PDE's array
$\emptyset_{low}$	Lowest value of the rank in the decision making matrix
Δt_{cycle}	Interval of time of a cycle, variable implemented during the study of PDE and ICWR
$\Delta t_{sim.}$	Interval of time per cycle predicted by the simulation
Δt_{LPA}	Interval of time in which the LPA port is open, in (s)
Δt_{step}	Time step in (s)
A_t	Transversal area of the channels in (m^2)
C_A, C_b	Molar concentration of species a and b
C_p	Specific heat at constant pressure
C_u	Partial derivative of u in respect to p, in the domain's boundaries
C_v	Specific heat at constant volume
F_S	Samples Frequency
F_e	Mass flux through the face (e) shown in Figure 3-14
F_s	Specific thrust in (N.s/kg)
M_x	Mach number of the shock wave relative to the upstream fluid
P_0	Total or stagnation pressure in (Pa) or (atm)
PR_{total}	Total pressure ratio
$Q_{net,p}$	Heat value of fuel, in (J/kg) equal to 43.1e6 J/kg for Jet-A (Saravanamuttoo 2008)
S_c	Source term
T_0	Total or stagnation temperature in (K)

T_{ref}	Temperature at the reference condition
$a_{P,m}$	Cells' coefficient "a"obtained in the node P from the momentum equation
$f_{(t)}$	Square wave defined by the Fourier series
f_0	Fundamental frequency
f_{FFT}	FFT resolution
f_w	Waveform frequency
k_f	Forward rate constant
k_r	Reverse rate constant
l_x, l_y	New coordinate system
$\dot{m}$	Mass flow in (kg/sec)
m_{CH}	Mass entering through a channel of the WR
p'	Pressure correction
q_n	Injected heat in (J/kg))
t_{max}	Time implemented to stop the simulation in SIMPLE
u'	Velocity correction in (m/s)
u_A	Flow injection velocity into the channels (m/s)
u_a	Velocity of the airplane (m/s)
$u_{channel}$	Velocity relative to the channel
u_j	Average velocity of the jet plume at the turbine's nozzle
u_{stator}	Velocity relative to the stator
u_t	Tangential velocity in (m/s)
w_{HPT}	Output work of the high pressure turbine in (J/kg)
w_{WR}	Input work of the wave rotor in (J/kg)
$w_{compressor}$	Input work of the compressor in (J/kg)
$\eta_{Compressor}$	Polytropic efficiency of the compressor
$\eta_{Diffuser}$	Isentropic efficiency of the diffuser
η'_a, η'_b	Rate exponents of reactant's species a and b
η_e	Efficiency of energy conversion
η_{pc}	Polytropic efficiency of the compression process inside the WR
η_{pe}	Polytropic efficiency of the expansion process inside the WR
η_{shick}	Isentropic efficiency of the SW compression
ω_0	Angular frequency

∅	Equivalence ratio, score given to each criterion in the decision making matrix, diameter
1D	One dimensional
2D	Two dimensional
3D	Three dimensional
A	Transversal area at the nozzle exhaust, cell face area, in (m^2), state inside the wave rotor (see Figure 3-1), pre-exponential factor
b	Boundary node
BC	Brayton cycle
BL	Baseline gas turbine
C-	Characteristic line projected in the negative direction
C+	Characteristic line projected in the positive direction
CFD	Computational fluid dynamics
CH	Channel
CJ	Chapman-Jouguet condition
D	Diameter
DDT	Deflagration detonation transition
d_e	Diffusion coefficient in the pressure correction equation
e	Cell's face at the east of P
E	Activation energy in $(J/kmol)$, Experiment
f	Fuel air ratio
Ff	Fundamental frequency in Hz
FFT	Fast Fourier transform
FJ	Fickett-Jacobs cycles
h	Specific enthalpy in (J/kg), channels' height
H	Enthalpy in (J)
HC	Humphrey cycle
HPA	High pressure air port
HPG	High pressure gas port
ICWR	Internal Combustion Wave Rotor
J-	Riemann invariants that follows C-
J+	Riemann invariants that follows C+
k	Heat capacity ratio

Kp	Convection coefficient in the pressure correction equation
L	Channels' length, Longitudinal distance
LP	Left port
LPA	Low pressure air port
LPG	Low pressure gas port
LPG1	Low pressure gas port used to feed the high pressure gas turbine, see Figure 3-1
LPG2	Low pressure gas port used to feed the low pressure gas turbine, see Figure 3-1
M	Mach Number, Model
m	Mass in (kg), Momentum equation
Mm	Molar mass of the mixture
n	Number of time steps
N	Number of chemical species
P	Node in the central cell
p	Pressure in (Pa.) or (atm)
PDE	Pulse Detonation Engine
ppm	Particles per million
PR	Pressure ratio
q	Heat of reaction in (j/kg)
R	Particular gas constant in (J/KgK)
RP	Right port
RR	Reaction rate
R_u	Universal constant of gases in (J/KmolK)
s	Specific entropy in (J/kgK), channel width, in (m)
SFC	Specific fuel consumption in (kg/kN.h)
SW	Shock wave
T	Temperature in (K)
t	Time in (min.)
T	Period
TVD	Total variation diminishing
TY	Function to overlap the temperature and fuel mass fraction, see Eq.(5-26)
u	Velocity in (m/s)

UMIST	Upstream Monotonic Interpolation for Scalar Transport
WR	Wave Rotor
x	Distance in (m)
Y	Pitch line distance in (m)
ZND	Zel'dovich, Neuman, Doing model
$\Delta h_{f,i}^{o}$	Enthalpy of formation of component i in (j/kg.K)
ΔS	Change of entropy (J/kgK)
Ψ	Factor implemented to evaluate the performance of the detonation process inside an ICWR
NDt	Minimum number of time steps between the device's ports
Y	Mass fraction
a	Speed of sound in (m/s), Cells' coefficient obtained after the domain discretization
f	Harmonics' frequency
β	Channels' angle in (^{o}), temperature exponent
θ	Angle between planes (Prandth- Meyer expansion); ports' angle in (^{o})
λ	Detonation cells size
μ	Angle of the forward and rearward Mach lines (Prandth- Meyer expansion) in (^{o})
ν	Specific volume in (m^3/kg)
ρ	Density in (kg/m^3)
τ	Fluid compressibility
ω	Angular velocity
ϕ	Scalar, equivalence ratio

Subscripts

$T_{ref,j}$	Temperature of reference of the component j
A	Fluid state inside the WR, see Figure 3-1
att	Attenuated value
b	boundary
BL	Baseline gas turbine
c	Compression process

CH	Channel
comp	compressor
core	Core flow of the gas turbine
E	East node in respect to P, see Figure 3-14
e	East face in respect to node P, see Figure 3-14
f	fuel
H	Rankine-Hugoniot curve
HPA	High pressure air port
HPG	High pressure gas port
HPT	High pressure turbine
i	Component i of a gases mixture, node index
ICWR	Internal combustion wave rotor
in	Inlet, internal diameter of the PDE array
j	A component of the reactants or products in a reaction process
LPA	Low pressure air port
LPG	Low pressure gas port
LPG1	Low pressure gas port used to feed the high pressure gas turbine, see Figure 3-1
LPG2	Low pressure gas port used to feed the low pressure gas turbine, see Figure 3-1
m	Momentum equation
max	Maximum scalar value obtained during the simulation
min	Minimum scalar value obtained during the simulation
nb	Neighbouring node of P
out	Outlet
P	Node P, see Figure 3-14
PDE	Pulse detonation engine
s	Isentropic trajectory
w	Wave
WR	Wave Rotor
inj	Injection condition
p	Isobaric trajectory
v	Isochoric trajectory

Superscripts

-	Mean value
$*$	Attenuated signal
o	Value computed in the nearest past time

1 INTRODUCTION

1.1 Background

During the 20th century, one of the greatest technological advances in aeronautics was the development of the gas turbine for aircraft propulsion. This development started with the design patented by Mr Frank Whittle in 1930 for the propulsion system of the Gloster Meteor, the first turbojet aircraft built in UK, in 1941(Online 2013).

Simultaneously, from 1936 to 1939 Mr Hans von Ohain developed and built the first aircraft gas turbine for the propulsion of the Heinkel He 178 Turbojet, in Germany (Online 2013), and later in 1940 Mr Anselm Franz designed and built the Jumo 004 with the support of Prof. Dr. Herbert Wagner (father of the turboprop in 1935). The Jumo 004 was the first gas turbine with an axial compressor designed for the propulsion of the Me262 (Friends 2007).

Since those days the use of gas turbines for aircraft propulsion has grown because of the advances in technology, which has led to the design of more efficient gas turbines, able to increase flight velocity with less noise than the previous propeller engines. Therefore, this period can be considered as the era when modern aviation emerged.

The gas turbine is a thermal machine that receives high quality energy from the exothermal reaction of fuel and air. Part of this energy provides the power generation or impulse for aircraft propulsion and the remaining part is released into the environment which acts as a low-quality energy reservoir.

As in any internal combustion engine, the chemical composition of the working fluid in the aircraft gas turbine changes when it crosses the cycle, from air and fuel to the combustion products. Thus, the operation of this cycle can only be possible through the expulsion of gases to the environment and their subsequent replacement with fresh air.

The effects of emissions when they are released into the atmosphere, such as global warming and climate change and the expected growth in demand for air

transport, has led the European Economic Community in collaboration with private organizations to establish the Clean Sky project.

The Clean Sky project was born in 2008 with the aim of developing new environmentally friendly technologies leading to the next generation of aircraft producing less emissions and noise.

In this regard, Cranfield University has been actively working as part of this initiative by bringing an important source of novel research that has helped to meet the objectives proposed for 2020 (80 % CO^2 reduction and 65 % noise reduction). However, new and more demanding targets are required for 2050.

A significant reduction of CO_2 emissions and noise in modern aircraft can be achieved by integrating different disciplines which involves the following topics (Clean Sky Project 2011):

- Selection of new materials
- Drag reduction
- Flight paths optimization
- Gas turbine performance

The Department of Power and Propulsion in Cranfield University has assumed the commitment of evaluating novel gas turbine concepts. This research aims to study novel alternatives such as the pressure exchanger and the pressure rise combustion process by using numerical methods with regards to possibly controlling and reducing environmental emissions from civil aircraft gas turbine engines.

1.2 Problem Statement

A significant reduction of CO_2 produced by a gas turbine can be feasible if the fuel consumption of the machine is reduced during its operation. New options able to achieve a remarkable effect on the turbine efficiency must be considered.

The ideal Brayton cycle gives the maximum efficiency that a gas turbine is able to reach, since all the processes involved are internally reversible. Hence, it is implemented as a benchmark cycle to evaluate the performance of conventional gas turbines (Cengel & Boles 2007).

As for any thermal machine, the Brayton cycle increases its thermal efficiency if the heat injection occurs at a higher average temperature and the heat rejection occurs at a lower average temperature. So, the efficiency increases with the compressor pressure ratio for fixed values of the cycle's maximum and minimum temperature (Cengel & Boles 2007).

The behaviour described above is also observed in conventional gas turbines. However, an efficient increment of the compression pressure ratio is difficult to achieve by implementing a mechanical compressor, because a higher number of compression stages is required and therefore the losses are expected to increase. There is an increase in the ratio between the surface area and the flow area (especially in small compressors) whilst large leakage passages are observed at high pressure stages (Weber 1995).

The substitution of the combustion process of a conventional gas turbine by an option that follows a semi-isochoric trajectory would result in an imminent increase of the gas turbine efficiency; an isochoric trajectory produces an increase of the fluid pressure that maximizes the work delivered by the turbine whilst the heat injected into the cycle is reduced as consequence of the differences in magnitude between the Cv and Cp of gases.

Based on the above, future gas turbines can achieve a better thermal efficiency if they include one of the following options:

- Increasing the efficiency of the compression process over that obtained through mechanical compressors for higher compressor pressure ratios
- Changing the combustion chamber by a device able to implement a combustion processes that follows a semi-isochoric trajectory

The first option is possible by using multiple shock waves in a serial arrangement during the fluid compression through pressure exchangers, whilst

the second option is possible by substituting the isobaric combustion process by a pressure rise combustion process; both alternatives are described next.

1.2.1 Efficient increase of the compression pressure ratio through pressure exchangers

A single shock wave with a finite but small jump of pressure can achieve a compression process with efficiencies higher than 95 %. Therefore, a device able to produce serial shock waves of this type only requires a small compressor located upstream of the device to achieve an efficient compression processes with pressure ratios of 30 or higher (Weber 1995; Akbari, Nalim & Mueller 2006; Weber 1992).

Figure 1-1 presents the isentropic compression efficiency achieved by shock waves, mechanical compressors and diffusers at different pressure ratios. The best performance of shock waves is obtained when their strength gives pressure ratios up to 2.2.

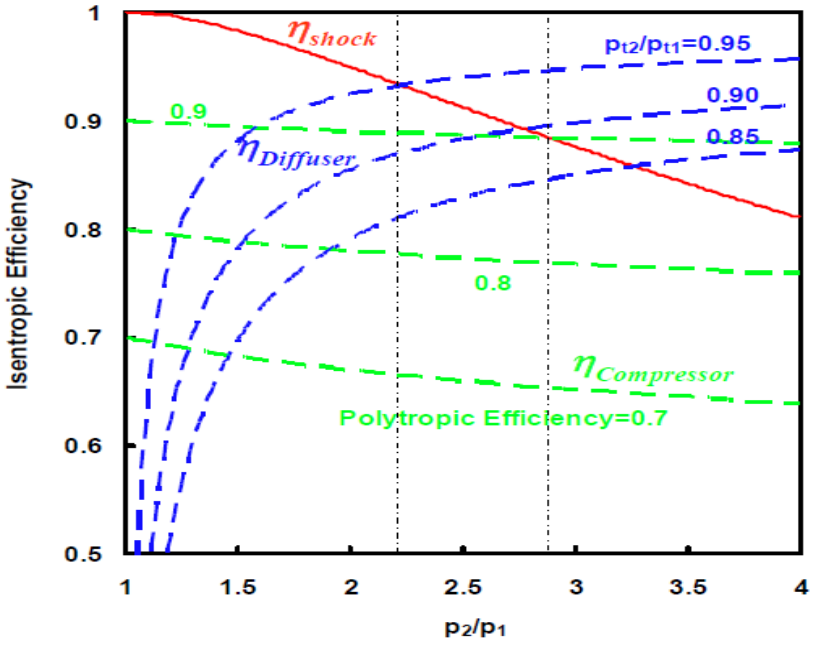

Figure 1-1 Effect of the pressure gain in the isentropic efficiency of shock waves (η_{Shock}), diffusers $(\eta_{Diffuser})$,, and polytropic efficiency of compressors $(\eta_{Compressor})$, (Akbari, Nalim & Mueller 2006)

Pressure exchangers are devices in which two fluids are suddenly brought into contact at different pressure levels to produce shock waves; the energy transfer is a consequence of the compressible flow phenomena.

Early experiments of pressure exchangers started at the beginning of the 20th century and the first pressure exchanger implemented as a component of a thermal cycle was a wave rotor. The device was designed by Claude Seippel in 1940 as a component of a locomotive engine (Hirceaga et al. 2005; Selppel 1946). However, the commercial use of this design was not possible due to its poor efficiency as well as its crude integration (weaknesses in technology).

Later Brown Boveri & Cie (BBC) began the study of wave rotors as turbochargers of diesel engines, which resulted in the ABB's Comprex® turbo charger; initially implemented in 1987 in the Mazda 626 Capella and later tested in Mercedes Benz, Peugeot and Ferrari (Piechna et al. 2004).

1.2.2 New benchmark cycle for gas turbines, the pressure-rise combustion process

Once the fluid goes out of the combustion chamber during the cycle it is able to produce work through an adiabatic expansion process in which the system tries to reach the equilibrium with the heat reservoir (dead state). The work potential available during this process is called thermochemical availability or exergy (Wark 1995).

The exergy of a fluid rises with an increase of pressure and temperature above the dead state (usually set at ambient condition). As a consequence, the maximum exergy value at the outlet of the heat injection in a Brayton Cycle is fixed by the compressor's delivered pressure and the maximum temperature allowed by the cycle.

The exergy value after the combustion process can be higher if the process of heat injection follows a different trajectory than the isobaric path; such as the injection of heat in a pressure rise process (pressure rise combustion process).

The ideal Humphrey cycle is a good example of these novel alternatives, which is composed of four internally reversible processes, as follows:

- Isentropic compression
- Injection of heat at constant volume
- Isentropic expansion
- Rejection of heat at constant pressure

Figure 1-2 presents the trajectories followed by the Humphrey cycle (red lines) and the Brayton cycle (blue lines) in a T-s diagram. In both cases the state at the exhaust of the compressor is obtained after compressing air through an isentropic process using a compressor pressure ratio of 20, the maximum cycle temperature is 1200 K and the ambient is set at 1 atm and 298 K.

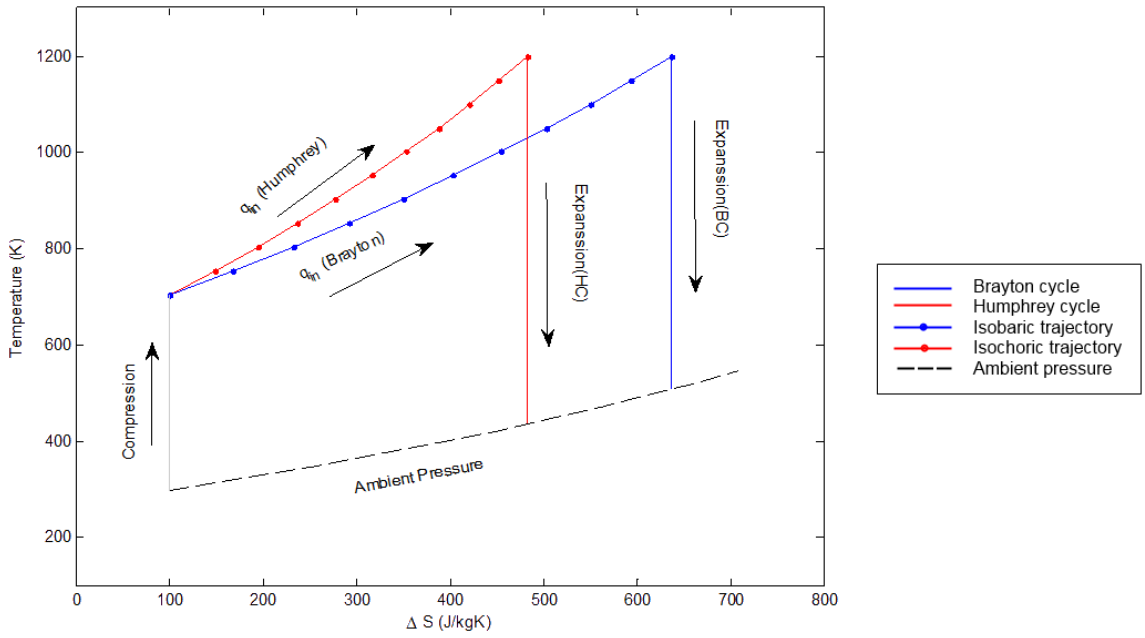

Figure 1-2 T-s diagram representing the path followed by the Humphrey cycle during the heat injection and expansion process (red lines), as well as the path followed by the Brayton cycle (blue lines)

As the T-s diagram shows, the compression work is the same in both cycles as well as the temperature reached by the fluid at the end of the heat injection, but when the process is at constant volume, the fluid reaches a higher pressure and therefore a higher exergy (increase of the fluid potential work).

Although both alternatives have the same increase of temperature, the heat injected during an isochoric process is also lower than in a constant pressure process, because the specific heat at constant volume in gases is lower than the one at constant pressure (Cv < Cp) (Cengel & Boles 2007).

The increase of the exergy at the outlet of the chamber as well as the reduction of the heat injection confirm that the Humphrey cycle reaches a higher thermal efficiency than the Brayton cycle, if both of them have the same compression pressure ratio and maximum temperature.

Figure 1-3 shows the thermal efficiency of the Humphrey cycle and its improvement in respect to the Brayton cycle at different values of compression pressure ratio and maximum temperature of the cycle. The best performance of the Humphrey cycle is achieved when the compression pressure ratio is the lowest and the maximum temperature of the cycle is the highest, all of this is in agreement with the observations by (Heiser & Pratt 2002).

Although the Humphrey cycle has been incorporated into a gas turbine in some patents (Hagen 1975; Zdvorak 1999) the cycle was only presented in this work to show the potential of the pressure rise combustion processes.

The Fickett-Jacobs cycle is also classified as a pressure rise combustion process but this offers a better performance than the Humphrey cycle because it involves a detonation mechanism that gives a small reduction of the fluid specific volume; a topic that will be addressed in the following chapter.

1.3 The aim and objectives of the present work

The aim of this project is to develop a novel research to assess the feasibility and merit of technology such as “Pressure Exchangers” and “Pressure Rise Combustion Processes” as an alternative combustor in gas turbines of civil aircraft by implementing numerical methods.

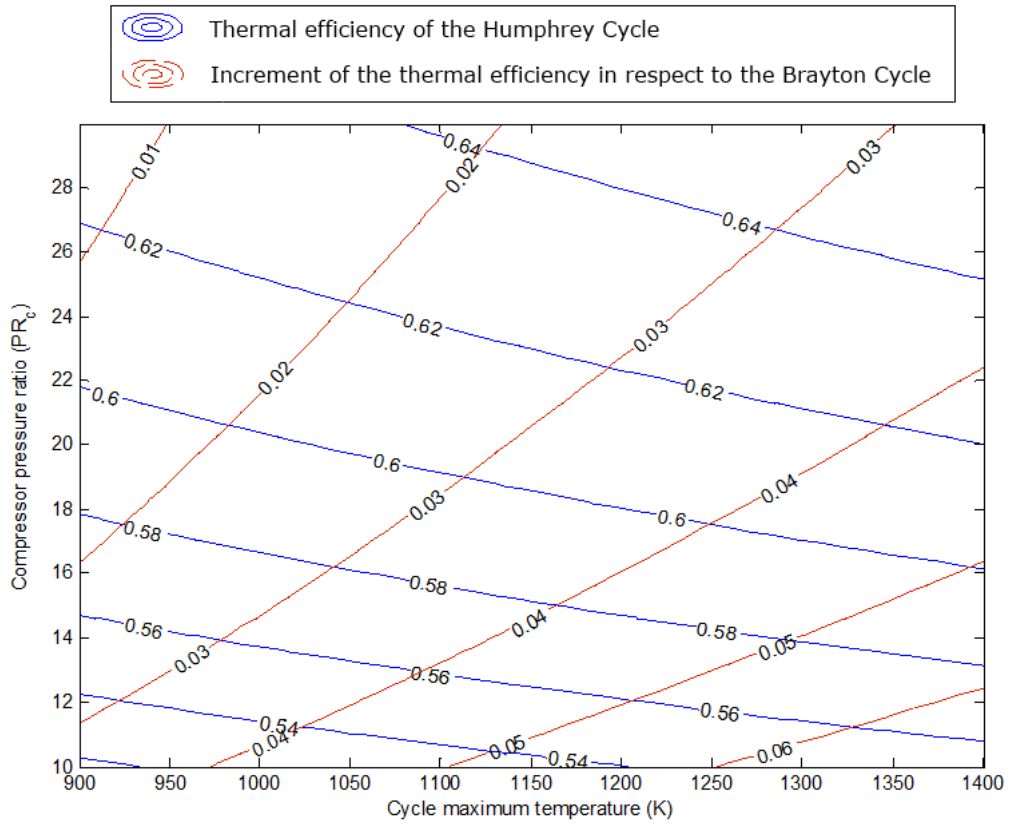

Figure 1-3 Estimation of the thermal efficiency achieved by the Humphrey cycle and its increment in respect to the Brayton cycle at different values of cycle maximum temperature and compressor pressures ratio, assuming constant Cp and Cv.

In order to achieve this aim, the following objectives are considered:

- Recognize the main characteristic of the different alternatives that form “Pressure Rise Combustion” and “Pressure Exchangers”.
- Develop numerical models able to predict the performance of selected concepts for future prediction of their performance and emissions.
- Develop a sensitivity analysis to predict the parameters that significantly affect the production of emissions and efficiency of selected concepts.
- Propose a novel alternative able to achieve the CLEANSKY goal of reducing emissions by 2050.

1.4 Thesis Organization

This chapter defines the motivation behind the study of "pressure exchangers" and "pressure rise combustors" as alternative components of gas turbines in future civil aircraft. The characteristics of the novel cycles as well as their effect in the cycle thermal efficiency of future gas turbines are also addressed. Finally, the aim and objectives of this project are outlined.

Chapter two presents the literature review of this work, with an overview of the theoretical background that describes the operation of wave rotors, pulse detonation engines and internal combustion wave rotors. This chapter also includes a brief description of the theories that support the compression process through shock waves as well as the detonation process.

Chapter three describes the methodology followed during the performance evaluation of wave rotors as components of civil aircraft gas turbines. In this chapter the stages implemented to obtain a reliable assessment of the device performance are presented, which includes the simplified analytical solution to estimate the device boundary conditions, followed by the development of a 1D-CFD in-house code to estimate the wave rotor dimensioning and the results validation using 2D-CFD models. This chapter also includes the performance evaluation of a wave rotor as a component of a commercial gas turbine.

Chapter four defines the methodology followed during the performance evaluation of pulse detonation engines as components of civil aircraft gas turbines through numerical techniques such as the method of characteristics and the finite volume method. The performance evaluation includes the efficiency achieved by the novel cycle as well as the NOx emissions estimation in a PDE from an array fed by the core flow of a turbofan (the combustion chamber is substituted by multiple PDEs).

Chapter five presents the methodology followed during the performance evaluation of an ICWR including the modification done to the 1D CFD in-house code to simulate the reaction mechanism and the NOx production. This chapter

also includes the code validation as well as its implementation on the performance evaluation of ICWR in commercial gas turbines.

Chapter six presents a general analysis of the results obtained during each chapter, as well as the advantages and disadvantages observed with the implementation of the novel alternatives. Finally, the conclusions of this work and future recommendations are stated.

2 LITERATURE REVIEW

2.1 Compressible flow

A fluid is a substance formed by molecules that move randomly and independently from each other; whose level of vibration and number of collisions gets higher when the internal energy increases.

In gases the level of vibration and collisions between molecules is higher than the inter-molecular forces, so the molecules remain well separated (low density fluids). However, any sudden change in the pressure field may force the molecules to get closer or become more separated. This behaviour is measured by the fluid compressibility obtained by implementing Eq. (2-1), (Anderson 2003).

$$\tau = \frac{1}{\rho}\frac{d\rho}{dp} \quad \textbf{(2-1)}$$

Equation (2-1) can be rearranged into Eq. (2-2), where the change of fluid density ($d\rho/\rho$) is expressed as function of the compressibility and dp. As standard, the flow is assumed compressible if Eq. (2-2) gives a value over 0.05 (5%) during the evaluation of a particular process (Anderson 2003).

$$\frac{d\rho}{\rho} = \tau . dp \quad \textbf{(2-2)}$$

2.2 Useful definitions implemented in compressible flow:

2.2.1 Sound Wave

When a fluid registers perturbations of the pressure field, the molecules near the perturbation start moving normally to the gradient of pressure with an average velocity. This motion makes molecules collide and transmit the information to the neighbouring ones, which results in the conformation of waves.

Sound waves are reversible waves produced by the mechanism previously described after an infinitesimal disturbance in the pressure field. The velocity of

these waves is a fluid property known as the speed of sound. Therefore, sound waves move homogeneously from the perturbation source to the rest of the domain if the fluid crossed by the waves is stagnated and has a unique state.

2.2.2 The Shock Wave

Finite perturbations also generate waves but they are irreversible because a finite gradient of pressure is maintained across them. These waves are known as shock waves and they can be implemented to compress a fluid.

Figure 2-1 shows the effect of a shock wave in a fluid contained inside a shock tube as predicted by a numerical model based on particles. The initial condition comprises two zones; one zone is dense to represent the driver fluid (high pressure and temperature) and the other zone is sparse to represent the driven fluid (low pressure and temperature).

Both zones are initially separated by a diaphragm whose removal generates a shock wave that compresses the driven fluid; so, the particles' density increases.

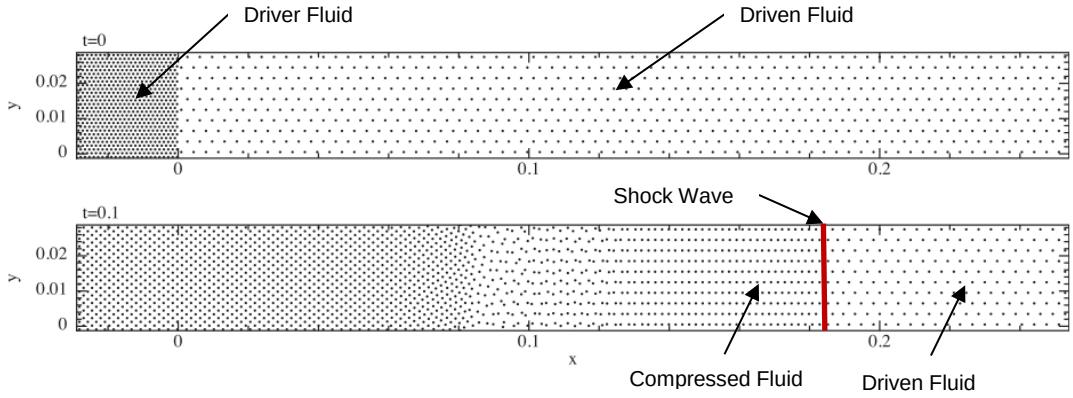

Figure 2-1 Shock tube evolutions, effect of the compression given by a shock wave (Price 2012)

2.2.3 Expansion Wave (Fan or Rarefaction waves)

After the diaphragm is removed in a shock tube, the driver fluid reduces its pressure as a consequence of the mass motion. The drop of pressure starts

near the diaphragm and propagates into the driver fluid through multiple sound waves in a serial arrangement, see Figure (2-2).

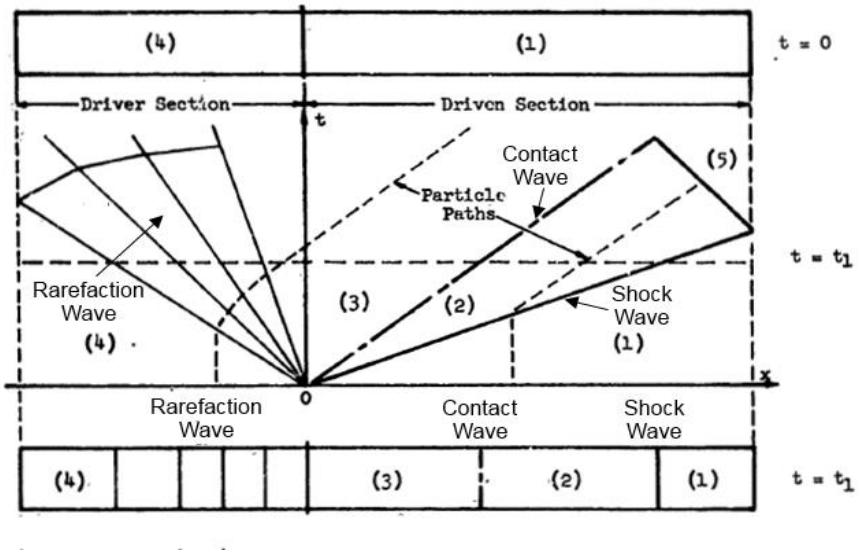

Figure 2-2 Wave's system in a shock tube (Martin 1958)

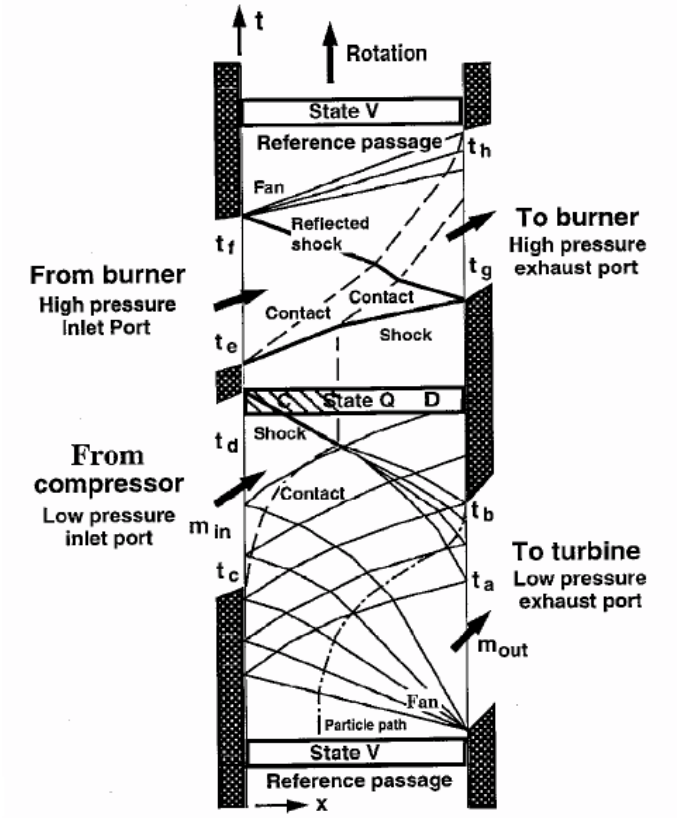

Figure 2-3 Wave diagrams for through-flow four port wave rotor (Akbari, Nalim & Mueller 2006)

The sound waves begin to separate from each other during their displacement through the tube making the fluid stretch. This group of sound waves is called an expansion wave.

The stretching effect arises as result of an increase of the flow velocity opposite to the waves' direction during the mass motion and a reduction of the speed of sound experienced by the fluid once it is crossed by the sound waves at the front of the expansion wave.

Expansion waves are produced not only by the process previously described but also due to the interaction between the fluid and the domain boundary conditions (see Figure 2-2), or by a sudden change in the flow angle which results in a stationary wave usually called Prandtl–Meyer expansion fan (see Figure 2-4).

The generation of an expansion wave due to the interaction of the boundary conditions is an important topic to be considered during the design of wave rotors, so it will be addressed later.

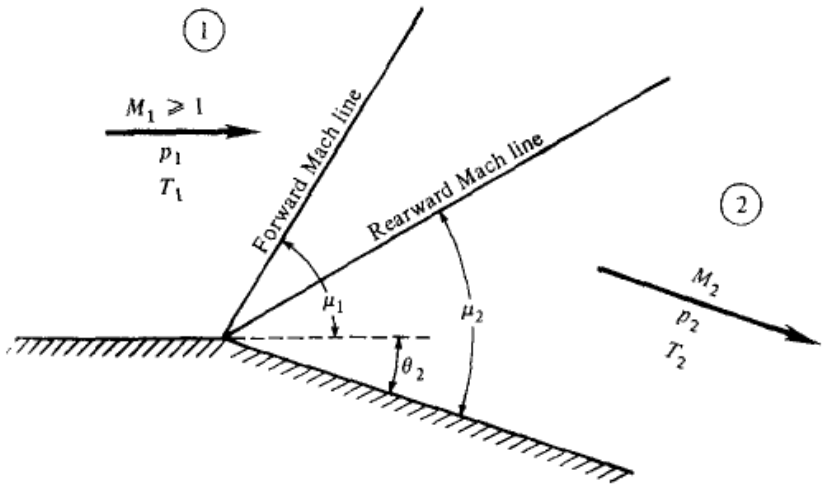

Figure 2-4 Prandtl–Meyer expansion fan (Anderson 2003)

2.2.4 Contact wave

The devices considered in this study need to manage burned gases and fresh reactants during their operation. Therefore, fluids with different properties are brought into contact during the transient process performed by them.

The interface between different fluids is called a contact wave and its tracking is usually implemented in the dimensioning of wave rotors and internal combustion wave rotors, as well as the detonation initiation in pulse detonation engines; these topics will be addressed later.

The pressure and velocity at both sides of the contact wave are the same during its displacement through the devices; this characteristic allowed Weber to obtain a design procedure for wave rotors based on the analytical solution of compressible flow; as will be presented in chapter 3 (Weber 1995).

2.3 One-Dimensional analysis of Shock Waves; the Hugoniot Equation

The compressibility effect of a shock wave that moves through a channel can be analytically evaluated by implementing conservative and constitutive equations to a control volume fixed to the moving shock wave; Figure 2-5 shows an example of this control volume.

The frame of reference at the shock wave makes the incoming fluid reach the control volume at the same speed as the shock wave in respect to the tube, when the velocity of the uncompressed fluid is zero in respect to the tube (fluid at the right side of the shock wave in Figure 2-5.),

The exiting fluid must move away at a lower velocity than the incoming fluid to ensure the mass conservation since its density increases due to the compression effect of the shock wave.

In order to obtain the analytical solution of the problem the following assumptions are considered valid during the compression process:

- Stationary flow
- The viscous effect is negligible

- The loss of heat through the walls in the control volume is negligible
- There is no change of flow transversal area
- Body forces in the control volume are negligible
- The working fluid is assumed to be an ideal gas with a constant value of specific heat.

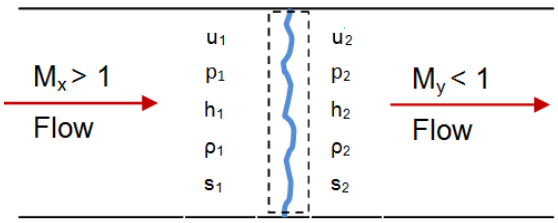

Figure 2-5 Control volume fixed on a shock wave (Cengel & Boles 2007)

With the previous suppositions the conservation equations of mass, momentum, energy and the equation of state acquire the shape of Eq. (2-3), Eq. (2-4), Eq. (2-5), and Eq. (2-6), respectively.

$$u_2 = u_1\left(\frac{\rho_1}{\rho_2}\right) \tag{2-3}$$

$$p_1 + \rho_1 u_1^2 = p_2 + \rho_2 u_2^2 \tag{2-4}$$

$$C_P.T_1 + \frac{u_1^2}{2} + q = C_P.T_2 + \frac{u_2^2}{2} \tag{2-5}$$

$$p = R.T.\rho \tag{2-6}$$

"q" in Eq. (2-5) represents the heat released or injected during the compression process, which in this case must be zero as it is stated in the second assumption.

Equation (2-7) results after manipulating Eq. (2-3) to Eq. (2-6) to evaluate a nonreactive process (q=0). This equation is called (Rankine-) Hugoniot (Kuo 2005) and gives the ratio between the fluid pressure and density before and after a shock wave crosses it, according to the conservation equations and the equation of state.

$$\frac{\gamma}{\gamma-1}\left(\frac{p_2}{\rho_2}-\frac{p_1}{\rho_1}\right)-\frac{1}{2}(p_2-p_1)\left(\frac{1}{\rho_1}+\frac{1}{\rho_2}\right)=0 \qquad \textbf{(2-7)}$$

Figure 2-6 shows the non-linear relationship between the fluid pressure and its density (specific volume) given by the Eq. (2-7). The working fluid is assumed to be air at 491.36 K and 101.325 kPa (conditions expected at the outlet of a gas turbine compressor with a pressure ratio of 10, in an airplane flying at 9000 meters of altitude). In this figure it is observed how an increase of pressure produces a reduction of the fluid specific volume.

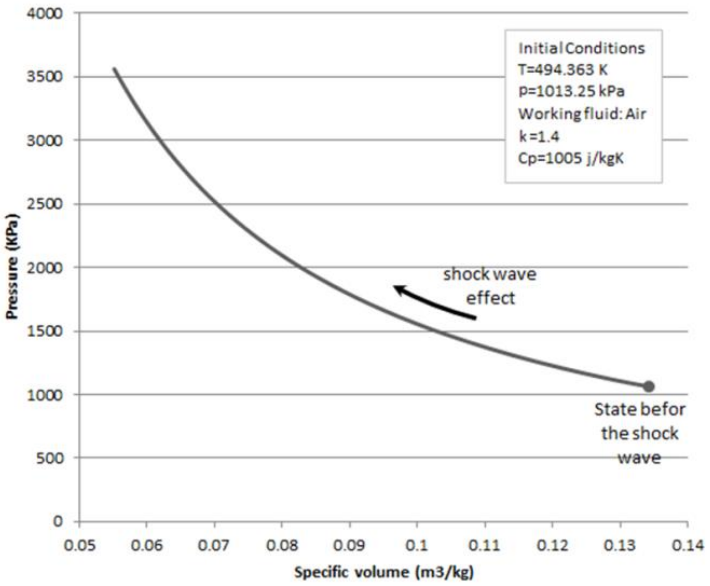

Figure 2-6 Shock Hugoniot curve (p-v diagram)

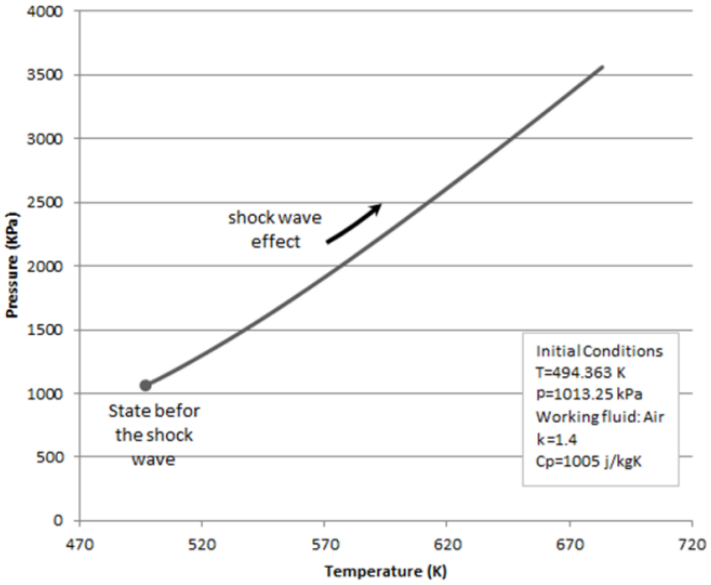

Figure 2-7 Shock Hugoniot curve (p-T)

Figure 2-7 presents the non-linear ratio between the temperature and the pressure of a fluid during a shock wave compression. The pressure and temperature of the fluid increase simultaneously to satisfy the equation of state of ideal gases. So, the shock waves can also be implemented to ignite a reactive mixture; a process called detonation that will be addressed next.

2.4 Detonation

The combustion process of a reactive mixture can be achieved with two distinct types of flame front, a deflagration front where a subsonic flame is driven due to the heat transfer given by the reaction, and a detonation front constituted by a shock wave coupled with a trailing reaction zone that moves at supersonic conditions (Helfrich 2006).

The detonation is a three dimensional process involving three types of shock waves. These waves are usually called Incident Shock, Mach Stem and Oblique Shock. Figure 2-8 presents a 2D representation of the phenomenon. In this figure the triple-point is also observed which is defined as the region where the three waves intersect each other.

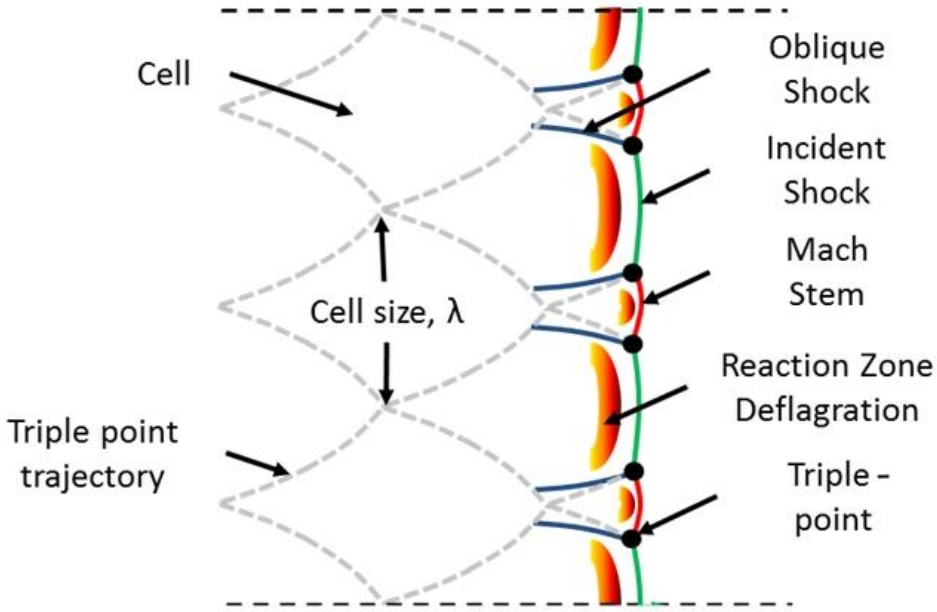

Figure 2-8 Cellular structure of detonation wave

Multiple triple-points are generated during the detonation process and their trajectories define a cellular structure with a fish scale shape. This structure can be captured by implementing soot foils, as shown Figure 2-9.

Figure 2-10 illustrates the transient process during the detonation. This process begins in frame (a) where the detonation structure is the same as that observed in Figure 2-8. The detonation zone shown in Figure 2-10 includes Incident Shocks (waves represented in green), Mach Stems (waves represented in red), and the trailing reaction zone (zone represented by a red-orange degradation).

Mach Stems have a closer reaction zone than Incident Shocks and therefore they are stronger. As a consequence, Mach Stems are projected forward as well as to each of their sides (See red arrows in Figure 2-10), while the main direction of Incident Shocks is forward. After a while, the movement of Mach Stems overcome the effect of neighbouring incident shocks during the development of the detonation.

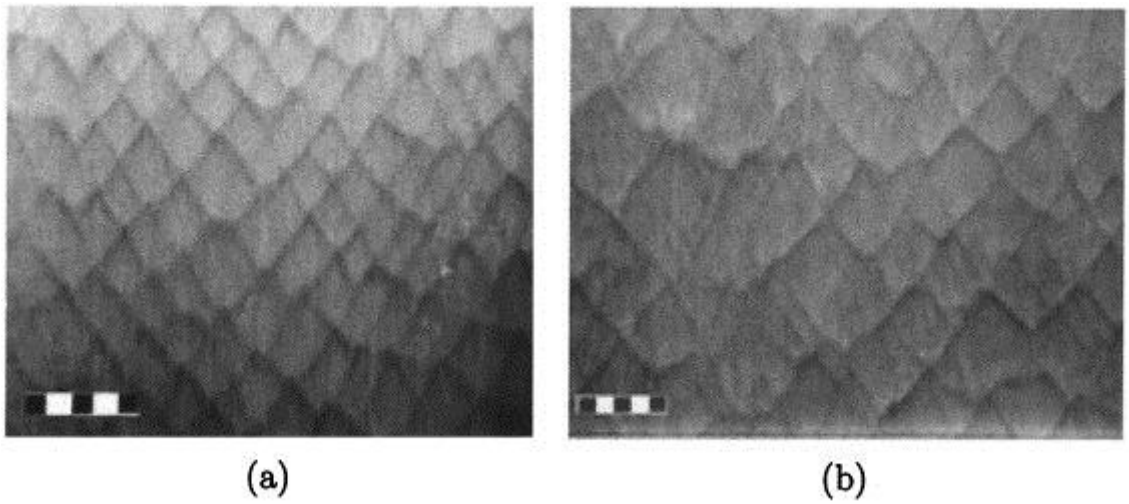

Figure 2-9 Soot foils obtained in a 280 mm diameter detonation tube for (a) 2H2-O2-12Ar and (b) 2H2-O2-4.5N2 (Pintgen et al. 2003)

The lateral movement of Mach Stems make them collide with their neighbours, as indicated by frame (b). At this condition, Mach Stems are turned into new Incident Shocks since the reaction zone gets farther from the shock waves. Moreover, the collision of Mach Stems produces hot spots that work as seeds of future Mach stems.

Oblique shock waves also appear during the transient process (waves represented in blue), these waves are a consequence of the complex interaction between a Mach Stem and its neighbouring incident shock; a process studied in depth by Sharpe (2001).

The transient processes described in frames (a) and (b) are repeated again in frames (c) and (d), and then in frames (e) and (f). The displacement of the detonation wave gives the resulting cellular structure previously mentioned.

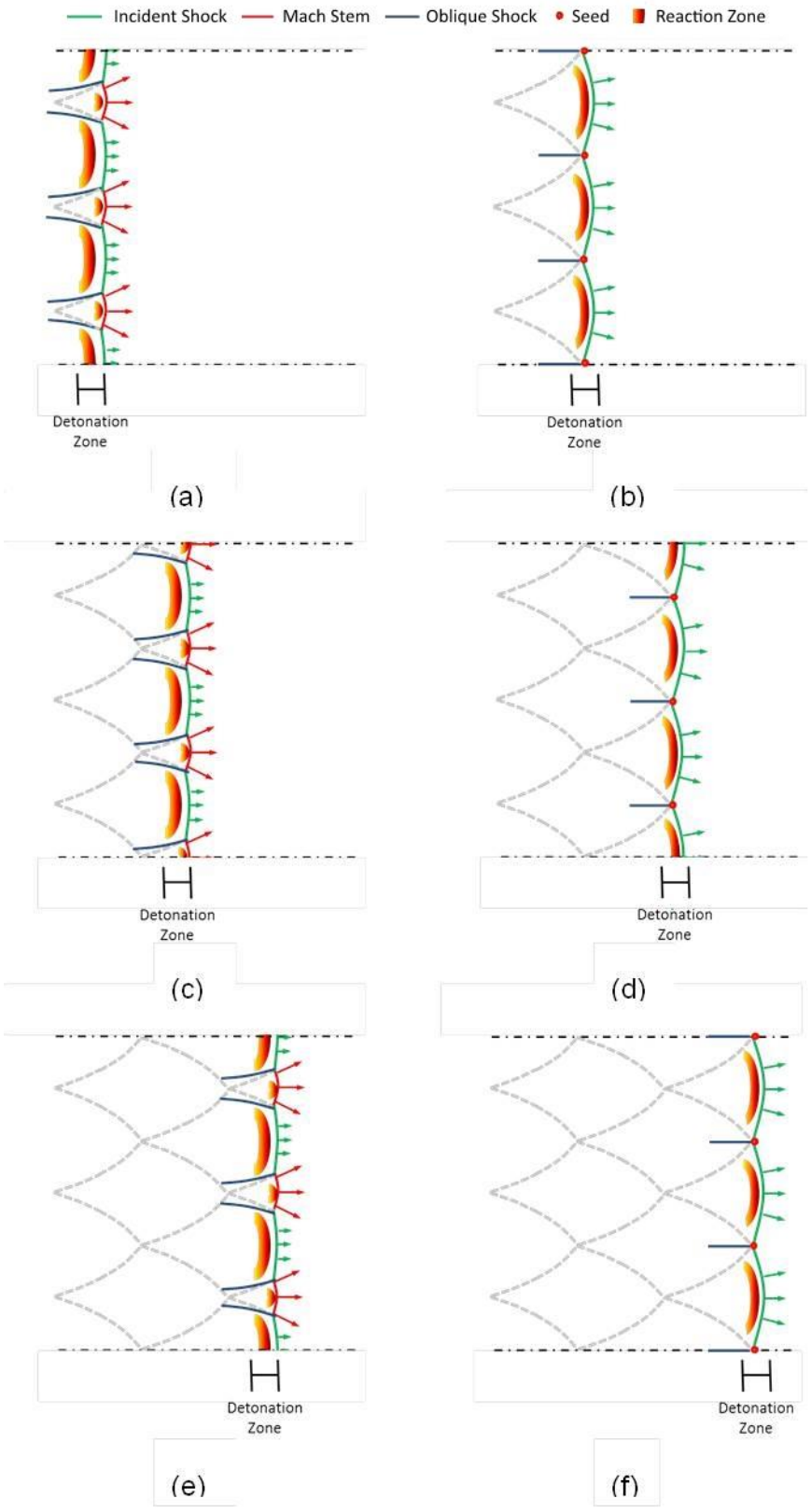

Figure 2-10 Transient process during the detonation

2.5 Rankine-Hugoniot Equation (analytical solution of detonation)

Despite the fact that detonation is a three dimensional phenomenon, valuable information can be obtained when simple representations are implemented; such as the planar-one-dimensional model of the detonation presented in Figure 2-11(b).

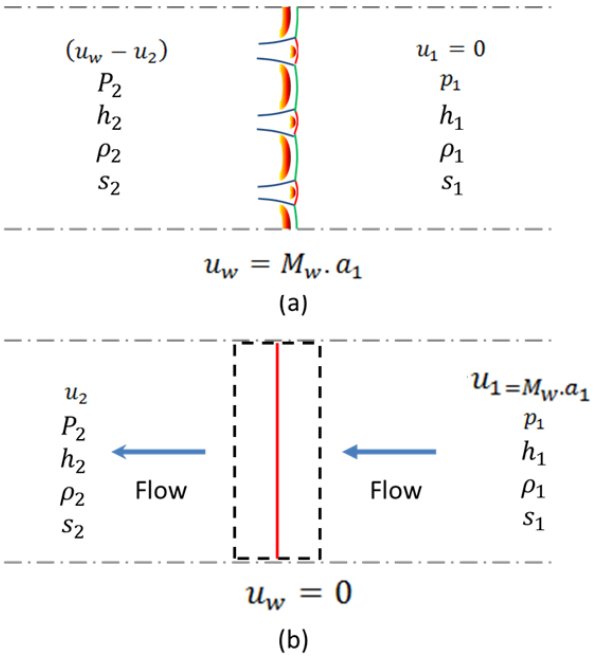

Figure 2-11 Detonation waves (a) transient 2D detonation (b) steady planar-one-dimensional detonation

In addition to the assumptions set during the simplified analysis of shock waves, the steady planar detonation model also includes the following suppositions (Wildon & William C. 2000):

- The flow is one dimensional
- The planar detonation front is a jump discontinuity (diffusion and radiation effects are neglected and the reaction is assumed to be complete instantaneously)
- Products emerging from the detonation are assumed to be in thermal equilibrium and behave as ideal gases
- The jump discontinuity is steady

Then Eq. (2-3) to Eq. (2-6) are manipulated to obtain the new Rankine-Hugoniot equation; a mathematics expression that gives the ratio between the pressure of a fluid and its density (specific volume) after a detonation process, once its initial state is known.

$$\frac{\gamma}{\gamma-1}\left(\frac{p_2}{\rho_2}-\frac{p_1}{\rho_1}\right)-\frac{1}{2}(p_2-p_1)\left(\frac{1}{\rho_1}+\frac{1}{\rho_2}\right)=q \qquad \textbf{(2-8)}$$

"q" represents the heat of reaction computed through Eq. (2-9), where $\Delta h^{o}_{f,i}$ denotes the enthalpy of formation of component i and Y_i its mass fraction.

$$q=\left(\sum_{i=1}^{N} Y_i \Delta h^{\circ}_{f,i}\right)_{reactants}-\left(\sum_{i=1}^{N} Y_i \Delta h^{\circ}_{f,i}\right)_{products} \qquad \textbf{(2-9)}$$

Figure 2-12 displays a section of the Rankine-Hugoniot curve called the detonation branch. In this region the density of burned gases is always above the density of reactants; an effect that only occurs after the participation of a detonation process. This figure also shows downward sloping lines that cross the fluid's initial state and intersect the Rankine-Hugoniot curve in one or two points (green dashed lines). These linear relationships between pressure and specific volume are called Rayleigh lines and are obtained from the integration of the continuity equation and the inviscid momentum equation, see Eq. (2-10) (Glassman & Yetter 2008).

$$p_2=\rho_1^2 u_1^2 v_1-\rho_1^2 u_1^2 v_2+p_1 \qquad \textbf{(2-10)}$$

Equation (2-10) can be turned into Eq. (2-11) to demonstrate the existence of a direct proportionality between the slope of the Rayleigh lines and the velocity of the detonation wave. u_1 is substituted by the velocity of the wave (u_w) during the manipulation, because both variables have the same magnitude, see Figure 2-11.

$${u_w}^2=\frac{1}{\rho_1^2}\frac{p_2-p_1}{v_1-v_2} \qquad \textbf{(2-11)}$$

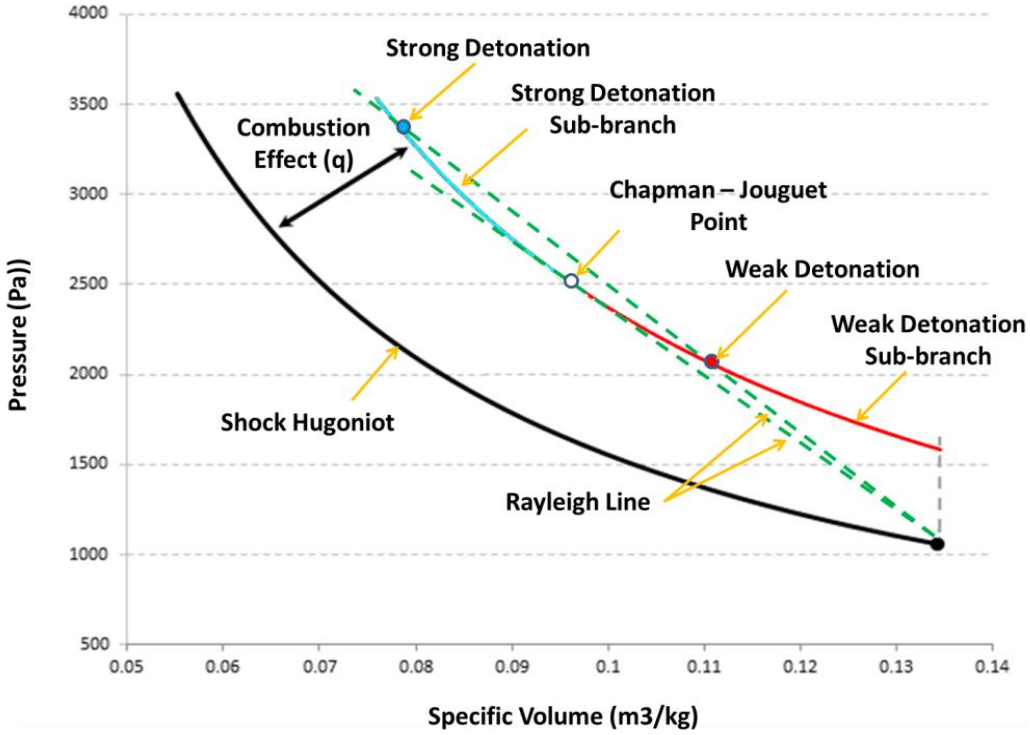

Figure 2-12 Shape of the Rankine-Hugoniot equation during a detonation process

The lowest speed reached by a detonation wave is called the upper Chapman-Jouguet velocity and results from intersecting the Rankine-Hugoniot curve with a Rayleigh line tangent to the curve (condition that gives the minimum u_w in Eq. (2-11)). The resultant intersection is known as the Chapman-Jouguet condition and makes the burned gases move away from the leading shock wave at the speed of sound (Kuo 2005).

If a detonation wave travels faster than the upper Chapman-Jouguet velocity, then the Rayleigh line will intersect the Rankine-Hugoniot curve at two points; one located in the strong detonation sub-branch and the other located in the weak detonation sub-branch (see Figure 2-12).(Kuo 2005).

Although these intersections represent states that satisfy the system of equations, some of them will be discarded later on after studying the piston problem.

2.5.1 The Piston problem

The piston problem consists of a detonation wave followed by a piston that moves due to an external force with a fixed velocity, as illustrated in Figure 2-13. This problem was proposed by Wildon & William C. (2000) and it offers an idea about the types of detonation waves that can be reproduced through experiments as well as the expected flow field for a fixed value of the piston velocity using as reference the Chapman-Jouguet (C-J) condition (Wildon & William C. 2000).

In this problem three cases are considered:

- Case (a) the piston moves faster than the C-J velocity
- Case (b) the piston moves at the C-J velocity
- Case (c) the piston moves slower than the C-J velocity

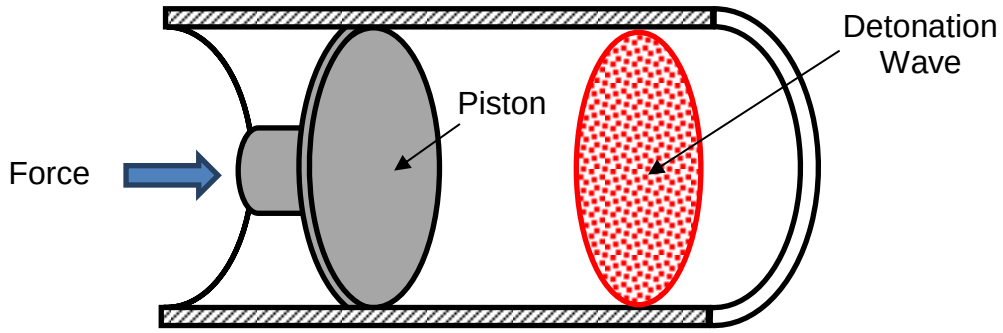

Figure 2-13 Scheme of a piston following a detonation wave in a rigid tube

In case (a) the fluid near of the piston increases its pressure and generates compression waves that travel downstream of the fluid until they collapse into a shock wave. The shock wave updates the downstream fluid with the new velocity and catches up with the detonation wave to transform it into a strong detonation wave.

Once the dynamic equilibrium is reached, the pressure field will display a simple jump discontinuity from the fluid initial pressure to the pressure reached by the

strong detonation wave (the upper-intersection between the Rayleigh line and the Rankine-Hugoniot curve), see Figure 2-14(a).

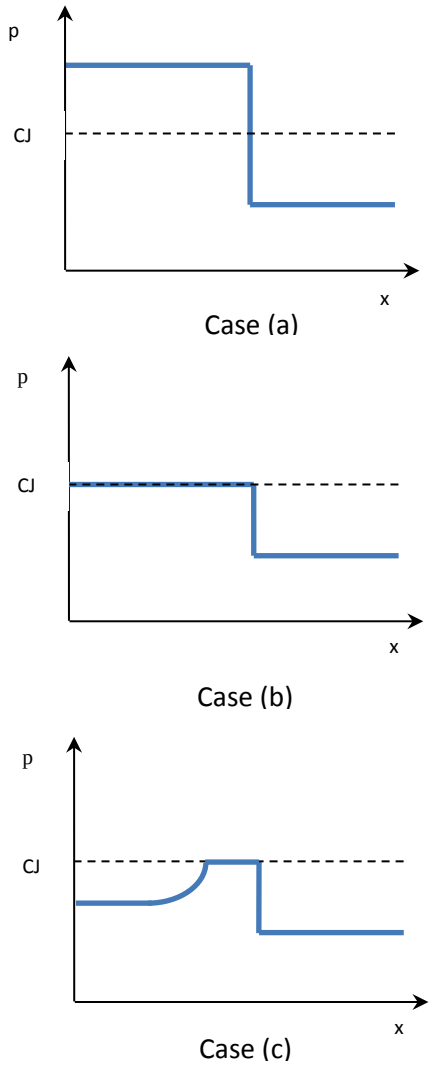

Figure 2-14 Instantaneous pressure field obtained in the piston problem

In case (b) the dynamic equilibrium also displays a simple jump discontinuity of the pressure field, but after the detonation the state reached by the fluid is defined by the C-J condition, see Figure 2-14(b).

In case (c) the detonation wave will move at the C-J velocity, so the dynamic equilibrium condition requires the generation of a rarefaction wave between the detonation wave and the piston to fit the velocity differences between both, see Figure 2-14.

Because burned gases move away from the detonation wave at sonic conditions, the rarefaction wave is unable to catch the detonation to modify its strength and therefore the wave cannot interact with the upstream fluid.

The internal combustion wave rotor and the pulse detonation engine are devices constituted by channels whose ends are closed during the detonation process. This condition matches with case (c) when the piston velocity is set equal to zero. Therefore, the detonation wave should move at the C-J velocity and the resultant gases must reach the C-J condition.

The C-J condition is a state that needs to be addressed during the preliminary study of the pressure rise combustion processes considered in this work.

2.5.2 The Chapman–Jouguet condition

In 1899, Chapman observed that in a shock tube, the burned gases commonly reached the C-J condition after the detonation. So, he stated that the C-J condition was achieved because it is a state that ensures a unique intersection between the Rayleigh line and the Rankine-Hugoniot curve (S. Browne & Shepherd 2008).

Later in 1905 Jouguet included the second law of thermodynamics into the analysis to prove that the C-J condition gives the maximum value of entropy expected during a detonation process and showed that the Rayleigh line tangent to the Rankine-Hugoniot curve not only represents the trajectory followed by the working fluid in which the entropy is constant but also the same of the C-J condition (S. Browne & Shepherd 2008).

The previous statement is demonstrated through the Eq. (2-12), in which the balance of entropy of the control volume shown in Figure 2-11(b) is computed (Glassman & Yetter 2008). In this equation H is used to emphasize a derivative along the Rankine-Hugoniot curve.

$$T_2\left[\frac{ds_2}{d(1/\rho_2)}\right]_H = \frac{1}{2}\left(\frac{1}{\rho_1}-\frac{1}{\rho_2}\right)\left\{\frac{p_1-p_2}{(1/\rho_1)-(1/\rho_2)}+\left[\frac{dp_2}{d(1/\rho_2)}\right]_H\right\} \quad \textbf{(2-12)}$$

Once $[ds_2/d(1/\rho_2)]_H$ is assumed to be zero to get the maximum entropy, Eq. (2-12) can be simplified into Eq. (2-13), where the left side represents the slope of the Rankine-Hugoniot curve and the right side represents the Rayleigh line tangent to the Rankine-Hugoniot curve (see Figure 2-12).

$$\left[\frac{dp_2}{d(1/\rho_2)}\right]_H = \frac{p_2 - p_1}{(1/\rho_2) - (1/\rho_1)} \quad \textbf{(2-13)}$$

In summary, the C-J condition is a unique solution in which product gases reach the maximum value of entropy during an adiabatic detonation. So, the generation of irreversibility is only due to the leading wave of the detonation (such as it was considered during the development of the Rankine-Hugoniot curve).

2.5.2.1 The Zel'dovich, Neumann, Döring (ZND) model

During the mid-twentieth century, Zel'dovich, Neumann and Döring worked independently to propose a one-dimensional detonation model able to satisfy the state given by the Chapman-Jouguet condition but with a more realistic structure of the detonation wave (Kuo 2005).

The resultant alternative was called the ZND model and it is based on four key assumptions (Wildon & William C. 2000):

- The flow is one dimensional
- The shock is a jump discontinuity, because diffusion and radiation effects are neglected
- The reaction rate is zero within the shock and finite behind it; also the reaction is irreversible.
- All thermodynamic variables other than the chemical composition are in local thermodynamic equilibrium everywhere

As consequence of the previous assumptions, the detonation structure comprises two fundamental processes, a compression process given by a thin shock wave and a combustion process called deflagration (integrated by an induction zone plus a reaction zone), see Figure 2-15.

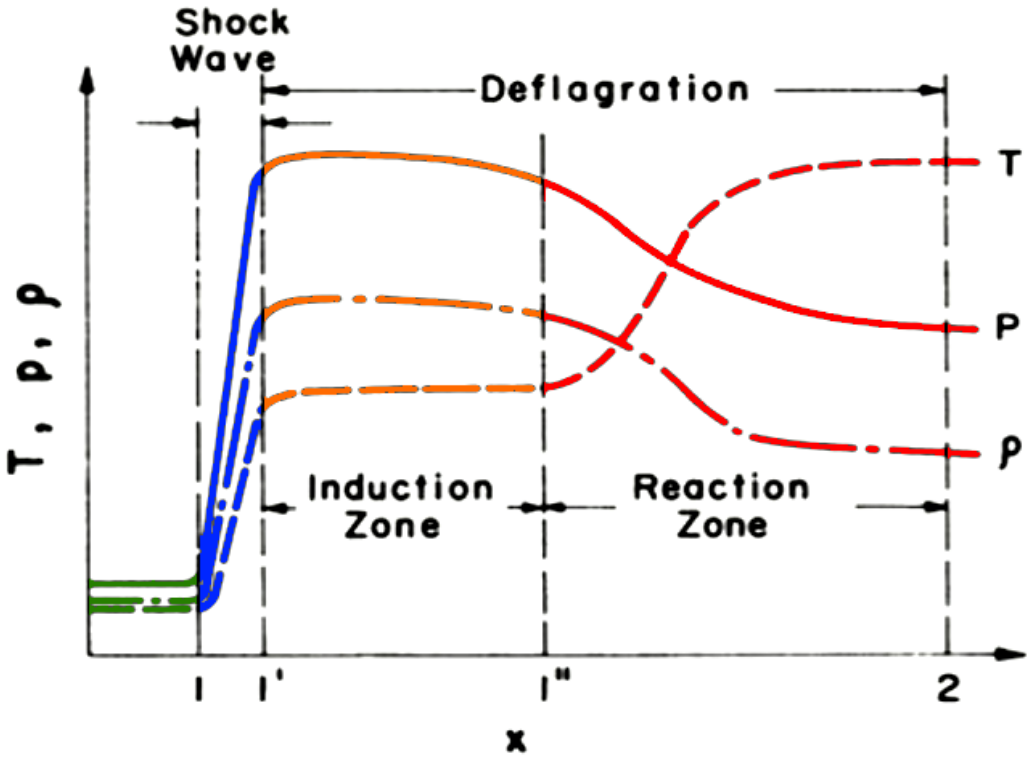

Figure 2-15 One dimensional structure of a detonation wave (Kuo 2005)

The compression process is a consequence of a thin shock wave and it produces an increase of the reactants' pressure, density and temperature along the Shock-Hugoniot curve till the von Neumann spike that is defined by the intersection between the Shock-Hugoniot curve and the Rayleigh line that crosses the C-J condition (Davis 1997). Figure 2-15 represents the compression process by blue lines.

The deflagration front is initiated by an induction zone, in which the reaction rate starts but the reaction process is performed slowly, so the thermodynamic properties remain almost constant. This effect is represented by orange lines in Figure 2-15 (Kistiakowsky & Mangelsdorf 1956).

Finally the reaction zone starts (red lines in Figure 2-15) and the fluid temperature is increased whilst its pressure and density decrease. The detonation process ends once the gases reach the equilibrium condition (C-J condition).

Figure 2-16 shows the detonation branch of the Rankine-Hugoniot curve and four alternative paths that end at the C-J condition (state u).

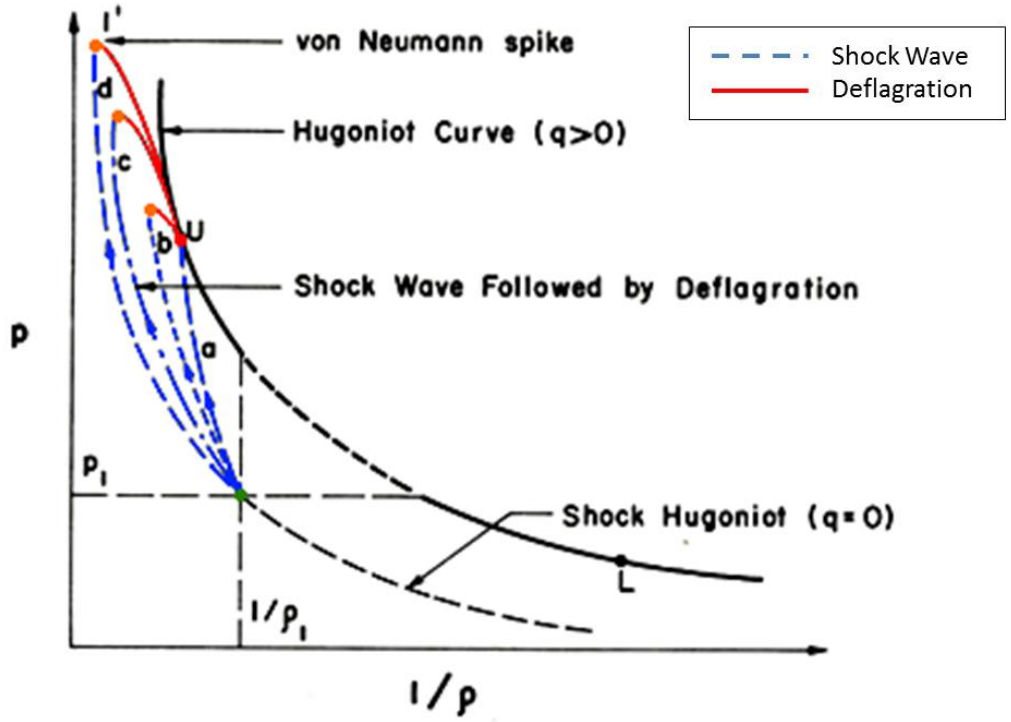

Figure 2-16 Rankine-Hugoniot curve with different detonation paths (Kuo 2005)

Path (a) is used to represent a thin detonation wave (the reaction is within the shock wave). This trajectory is less probable because there is little increase of pressure during the process and therefore the increase of temperature is not enough to initiate the reaction; the detonation wave is unsustainable at this condition.

Paths (b) and (c) represent a detonation with a reaction that starts within the shock waves and continues after the shock. In both paths the increase of temperature given by the compression process is enough to start the reaction, but they require fuels with fast chemical kinetic (case (b) has a faster chemical kinetic than case (c)).

Path (d) describes the ZND model. In this case the compression process is represented by the Shock-Hugoniot curve and finishes once the von Neumann

spike is reached. Then the deflagration process starts until gases reach the C-J condition.

The ZND mechanism (1D model) has been widely implemented during the preliminary design of devices in which a detonation process is involved, regardless of the three dimensional structure of the detonation waves (William & David 2002; Yuhui et al. 2003; Endo & Fujiwara 2002).

2.6 The Wave Rotor

The wave rotor is a pressure exchange device composed of multiple channels in a serial arrangement. These channels rotate about an axial axis, isolated by two plates set at each end. The plates have slots located in specific positions that let channels get in contact with multiple ports, see Figure 2-17. Each port operates by injecting or withdrawing the working fluid in a stationary condition at different states; the aforementioned characteristics allow the integration of the wave rotor as a component of different thermal cycles.

Despite the fact that the wave rotor has already been studied for multiple purposes, such as IC engine supercharging, refrigeration cycle, pressure divider & equalizer and wave super-heater (Akbari, Nalim & Mueller 2006), in this work attention will be centred on the wave rotor as a component of gas turbines.

The working fluid managed by this device is constituted by two streams, on one hand there is fresh air that comes from the compressor and is additionally compressed before being used to feed the combustion chamber, and on the other hand there are burned gases that come from the combustion chamber and are expanded before being used to feed the turbine.

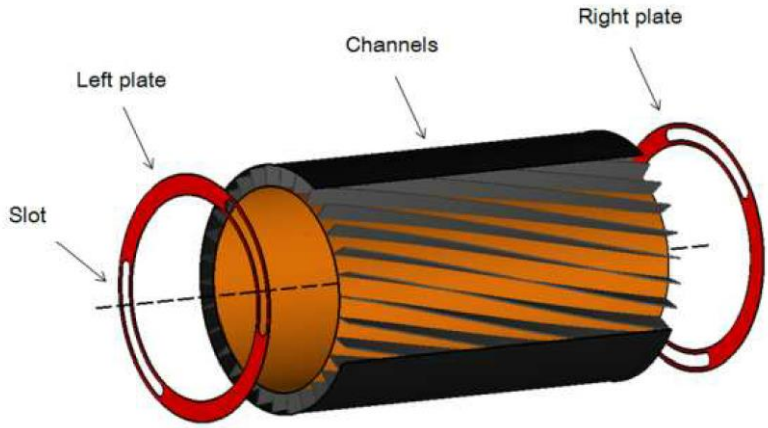

Figure 2-17 Schematic configuration of a typical Wave Rotor

Based on the streams configuration, the wave rotor can be classified in two basic arrangements: through-flow and reverse-flow wave rotors. In the first type, both the fresh air (cool fluid) and the burned gases (hot fluid) completely cross the channels and therefore the device offers a self-cooling capability, whilst in the second type both the hot and cold fluids leave the channel through the same side as their entry; achieving more efficient reduction of gas recirculation (Akbari & Müller 2003; Welch et al. 1995), see Figure 2-18.

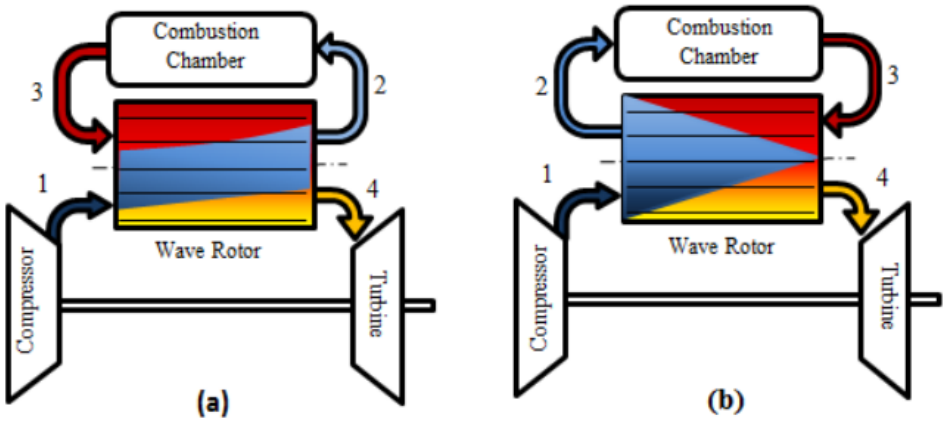

Figure 2-18 Wave Rotor flow configuration (a) through-flow Wave Rotor (b) reverse-flow Wave Rotor

Figure 2-19 shows the wave rotor cascades of a through flow and reverse flow configurations, the black arrows at the bottom specify the rotational direction of the channels whilst the arrows at each side of the arrangements are used to

indicate the injection and withdrawal of fresh air and gases through the ports of the device.

The operation of the Wave Rotor results from the interaction of three different waves during the cycle, as observed in Figure 2-19. Shock waves are implemented to compress the air that comes from the compressor before being injected into the combustion chamber. Rarefaction waves are implemented to expand product gases before being injected into the turbine, and contact waves that work as an interface between reactants and the combustion products. The following subsections explain the mechanism involved during the conformation of these waves based on the perspective of Weber (1995).

2.6.1 Generation mechanism of shock waves

Shock waves arise during the device rotation once the interaction between the channels and the ports that withdraw the working fluid culminates or when the interaction between the channels and the injection ports is started (sudden change of the channels' boundary condition).

The channels' end closure produces an increase of the local pressure due to a reduction of the kinetic energy experienced by the fluid when it arrives to the plate. This effect initiates the appearance of compression waves that travel backward through the channel and whose collisions form a shock wave.

Meanwhile, the pressure of the fluid in the injection ports must be higher than the pressure of the fluid contained in the channel prior to their interaction, to initiate the Wave Rotor feeding. So, the interaction between the injection port and the channel generates compression waves that travel through the channel and whose collision also forms a shock wave.

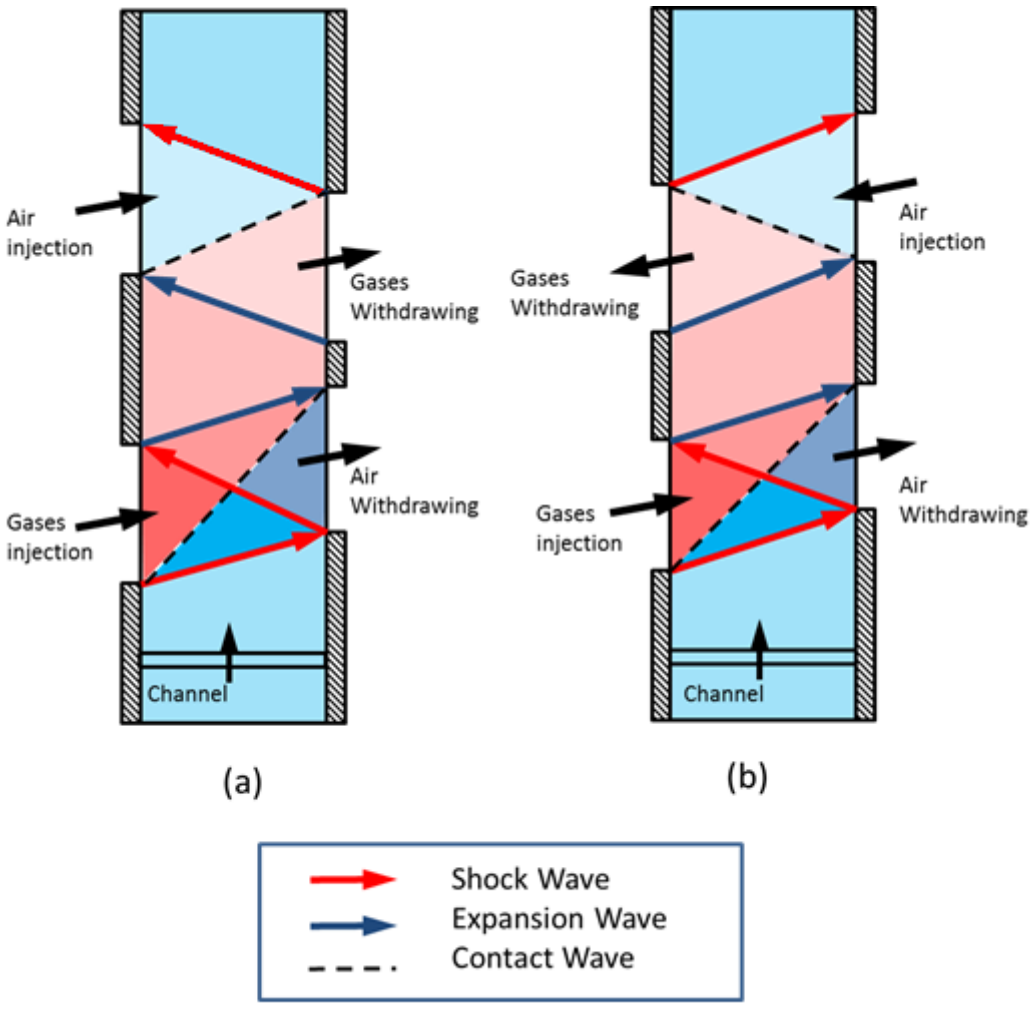

Figure 2-19 Cascade representation of the wave rotor (a) through flow (b) reverse flow (Iancu et al. 2008)

2.6.2 Generation mechanism of rarefaction wave

Rarefaction waves (Expansion waves) are also a consequence of the interaction between the channels' ends and the ports of the Wave Rotor during the device rotation, but in this case the waves appear inside the channels only if the channels finish interacting with the ports used to feed the wave rotor or if the channels start interacting with the ports used to extract the fluid contained in each of them.

In the first case, the wave emerges to link the state of the fluid that moves away from the port with the state of the fluid that keeps in contact with the plate; whose relative velocity must be zero.

In the second case, the rarefaction wave is generated due to a drop of the fluid pressure during the mass withdrawal. The pressure perturbation starts at the open end and moves toward each channel, in order to update the upstream fluid with the conditions at the port.

2.6.3 Generation mechanism of contact waves

The injection of air into the Wave Rotor is also used to scavenge the gases through the port that feeds the turbine whilst the injection of gases is used to push out the air through the port that feeds the combustion chamber. Therefore, during a cycle, at least two contact waves are observed.

The shape of the contact wave is affected by the non-instantaneous opening of the injection ports because a non-uniform tangential velocity field is generated (Akbari et al. 2013). Therefore a well-defined interface is not observed in an actual process.

2.7 The pulse detonation engine

The air-breather pulse detonation engine (PDE) is a device with an open cycle that uses the detonation to produce thrust during a transient process.

A PDE can be composed of one detonation tube or multiple detonation tubes in a parallel arrangement. Fresh air and fuel are injected into the tubes through a valve located at one of the tubes' ends, whilst the other end can be attached to a nozzle or a manifold (multi-tubes PDE) (Karki & Patankar 1989; Kailasanath 2003; Roy et al. 2004)

Figure 2-20 shows the detonation cycle performed by a single PDE. The cycle begins with the opening of the valve (left side of the tube) to feed the PDE with reactants (fuel and air). The pressure inside the PDE is lower than ambient pressure as consequence of the previous cycle.

Once the PDE is almost full of reactants the valve is closed and the detonation wave is generated either from a deflagration-detonation transition process (DDT) or directly from a strong initiation (F. R. Schauer et al. 2005).

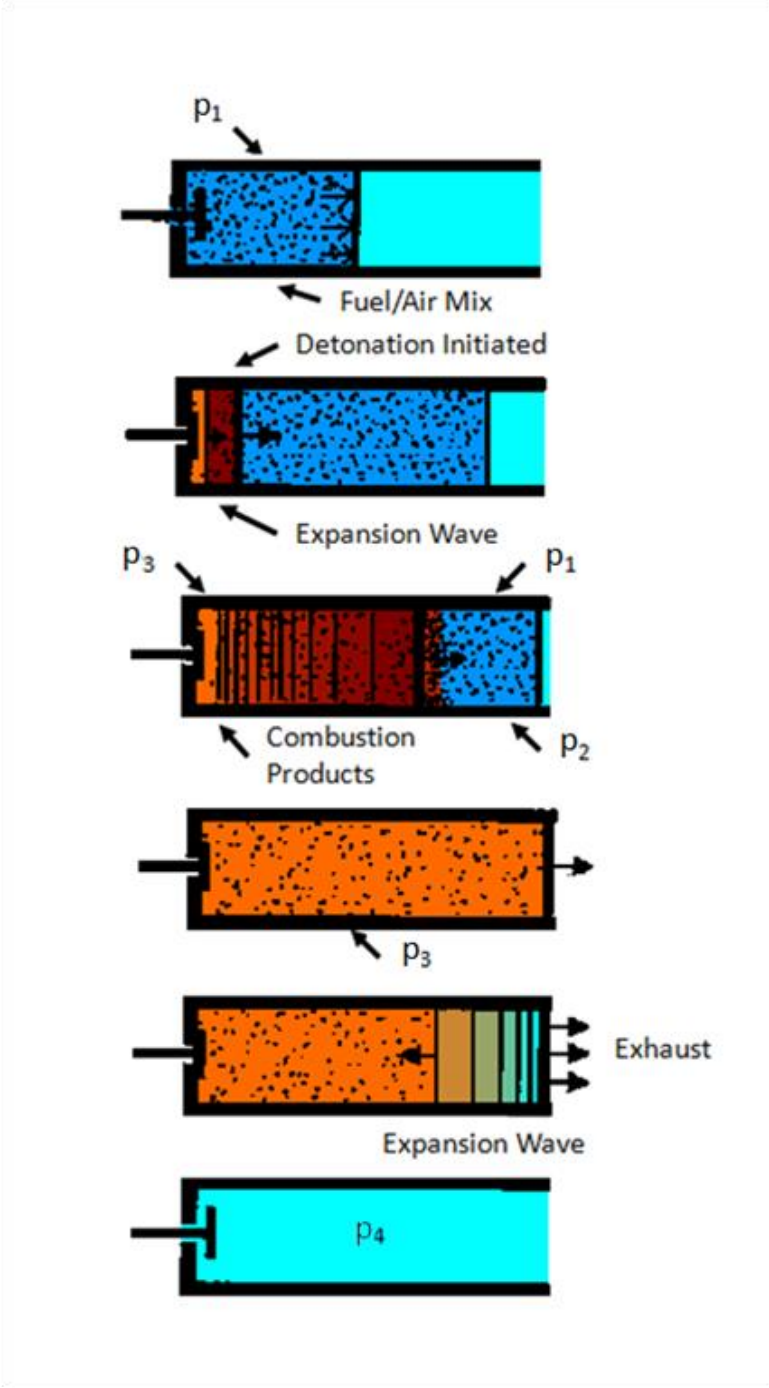

Figure 2-20 PDE combustion cycle (Hutchins & Metghalchi 2003)

The detonation is followed by a rarefaction wave, which results as consequence of the velocity difference between the fluid near the detonation wave and the stagnated fluid near the valve (see section 2.5.1).

Once the detonation wave reaches the open end of the PDE, the pressure at this end starts reducing as a consequence of the flow momentum. This effect is

followed by a rarefaction wave that moves backward through the whole chamber, whose reflection at the left end of the PDE causes the necessary drop of pressure which makes the injection of new reactant possible, so the cycle starts again.

2.7.1 Source of detonation in PDE

As was stated in the previous subsection, a detonation can result from a deflagrative flame, but this process is only possible if a turbulent combustion regimen is reached, which increases the reaction rate of the mixture and therefore the flame acceleration (Nalim 1995).

The deflagration detonation transition (DDT) is frequently achieved in a pre-detonation chamber attached to the PDE because a low-energy ignition is required (Kuznetsov et al. 2002).

The design process of DDT has to assess the best type of acceleration elements, its position and orientation inside of the chamber to ensure the combustion's acceleration. The diaphragm screens, the wire meshes and the Shchelkin spiral are some of the available options; their selection depends mainly on the type of fuel and fuel-air ratio (Vasil'ev 2002).

A strong detonation can be initiated from a sudden release of a high amount of energy such as an exploding wire source (Daniau et al. 2001). However, this alternative looks impractical in PDEs operating with multiple cycles (F. R. Schauer et al. 2005).

2.7.2 Pulse Detonation configurations in aircraft gas turbines

2.7.2.1 The Hybrid option

The Hybrid Pulse Detonation engine is an option where multiple pulse detonation engines are incorporated into a turbofan surrounding the main combustion chamber, as shown in Figure 2-21. Each PDE is fed with part of the by-pass air plus fuel and then it is detonated. All of this is done through an alternant process, so a rotary valve design type would be required (Kelly 2003; M A Mawid et al. 2003).

The hybrid pulse detonation engine not only requires simple engine mechanisms but also gives higher thrust during its operation than gas turbines with after-burner (Mawid et al. 2000; M. A. Mawid et al. 2003). Therefore this configuration is a prominent alternative for more efficient and environmentally friendly aircraft (GE Global Research 2013).

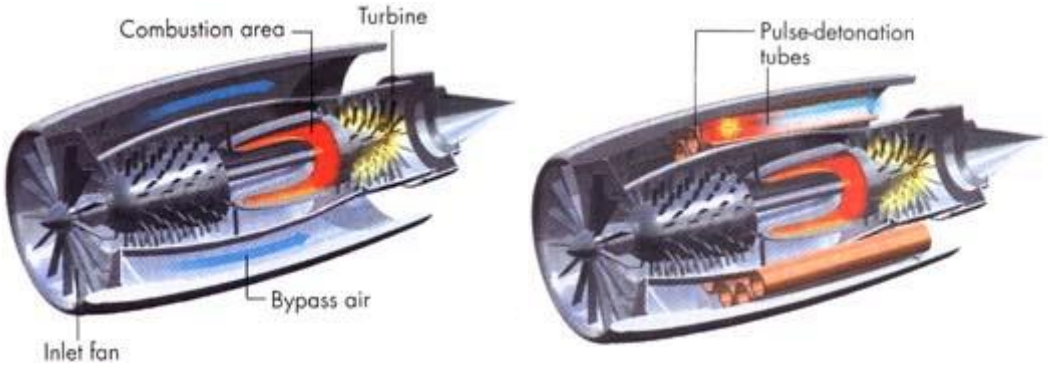

Figure 2-21 a) Standard turbofan engine b) Hybrid turbofan engine (Kelly 2003)

2.7.2.2 PDE as component of the gas turbine cycle

Another configuration able to increase the performance of gas turbines is obtained by incorporating a PDEs array inside of the gas turbine as combustion chamber. This type of array is also called pulse detonation chambers and it is able to increase the turbine efficiency by making the cycle get closer to the Fickett-Jacobs cycle; a topic that will be addressed in depth throughout the next section (pressure rise combustors).

Figure 2-22 is a schematic representation of a turbojet with a pulse detonation combustor.

2.7.3 PDE Performance - The Fickett-Jacobs cycle

The Humphrey cycle was introduced during chapter 1 to show the advantage of an isochoric combustion process as an option to substitute the Brayton cycle in future aircraft. However, Figure 2-16 indicates that a detonation process not only propitiates an increase of the fluid pressure during the combustion of gases but also a reduction of the fluid density and therefore the detonation trajectory differs from that followed by the Humphrey cycle.

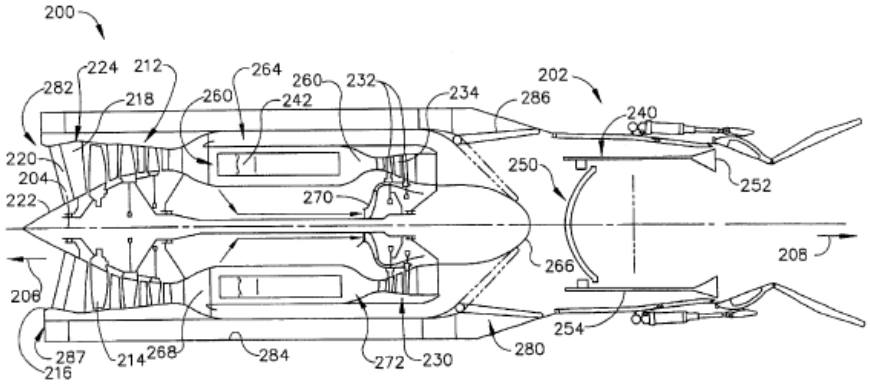

Figure 2-22 Turbojet with a pulse detonation combustor (Johnson et al. 2002)

A better alternative to evaluate the PDE performance is a conceptual thermal cycle called the Fickett-Jacobs (F-J) cycle. Figure 2-23 is a sketch of the F-J cycle which is composed of the following processes:

- Pre-compression of reactants initially at atmospheric pressure through an adiabatic and reversible process (a-b)
- Application of external work to move the left piston to the right side with a velocity u_p, the piston displacement will generate a detonation wave that moves rightward at the C-J velocity (u_{CJ}) (c)
- Instantaneous acceleration of the right piston until its velocity equals the left piston, once the detonation wave reaches the right side (d)
- Conversion of kinetic energy into external work through an adiabatic isochoric process, until both pistons reach repose (e)
- Expansion of products through an adiabatic and reversible process, until the atmospheric pressure is reached (f)
- Heat rejection at constant pressure, until product gases reach the atmospheric temperature (g)
- Conversion of products to reactants at constant temperature and pressure (h)

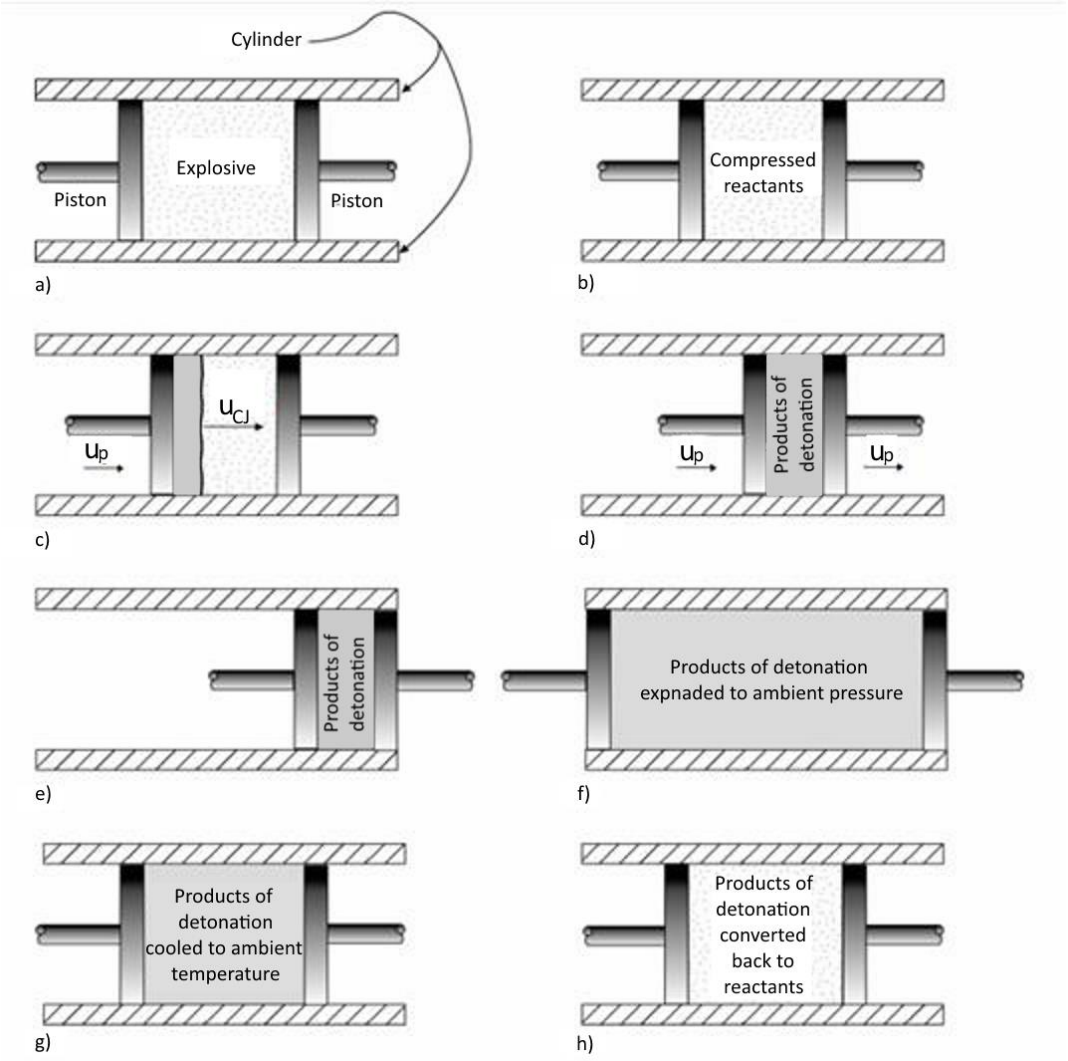

Figure 2-23 Physical steps followed by the Fickett-Jacobs cycle (Wintenberger & Shepherd 2004)

Figure 2-24 shows the p-v diagram of the Fickett-Jacobs cycle, the cycle trajectories are represented as follows:

- 1-1' Pre-compression of reactants
- 1'-2 Compression by a detonation wave
- 2-3 Change of kinetic energy into work
- 3-4 Expansion of the working fluid
- 4-5 Rejection of heat at constant pressure
- 5-1 Conversion of products into reactants

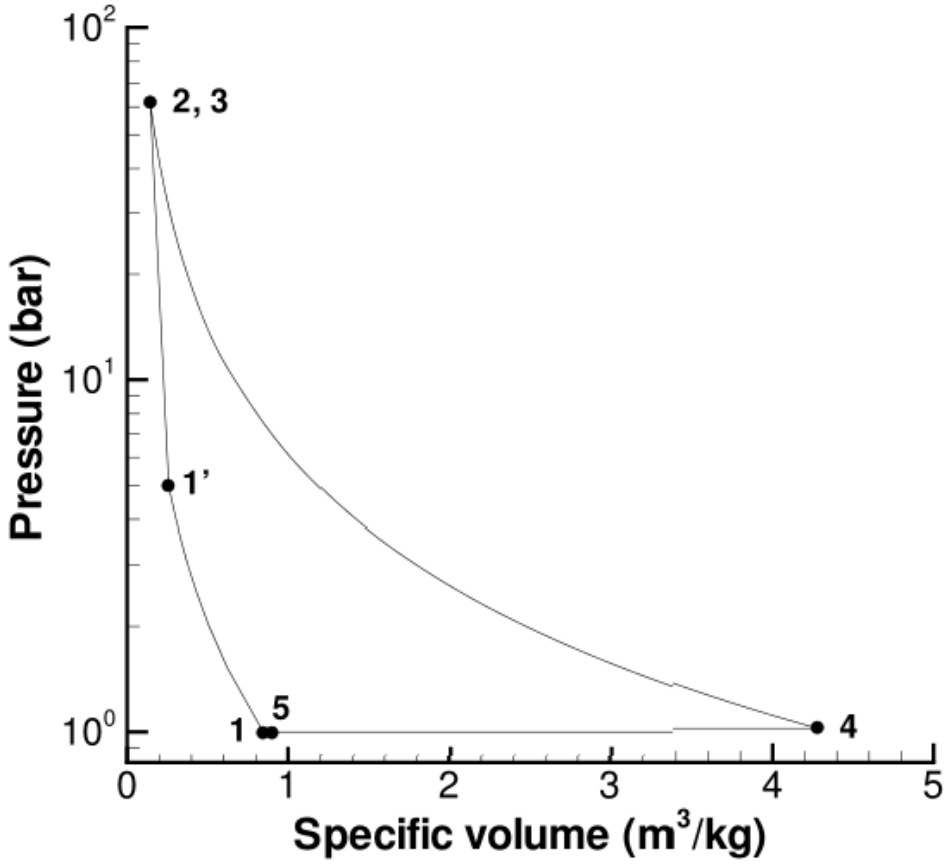

Figure 2-24 p-v diagram of the Fickett-Jacobs cycles (Wintenberger & Shepherd 2004)

Figure 2-25 shows differences between the FJ cycle, the Humphrey cycle and the Brayton cycle in a p-v diagram. The trajectory of a detonation process gives the maximum pressure and minimum specific volume during the heat injection, so it offers the maximum exergy.

The exergy increase experienced by the fluid after the detonation lets the Fickett-Jacobs cycle produce more work than the Humphrey or Brayton cycles for the same compressor pressure ratio and with a higher cycle thermal efficiency (see Figure 2-26) (Wintenberger 2004).

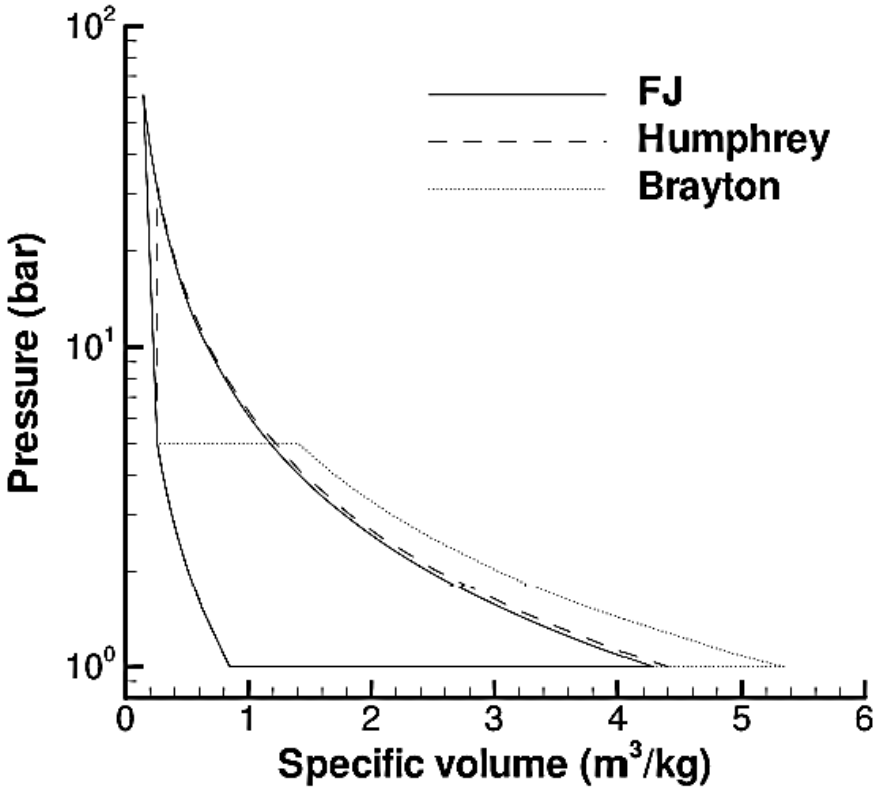

Figure 2-25 p-v diagram comparing the FJ, Humphrey, and Brayton cycles (Wintenberger & Shepherd 2004)

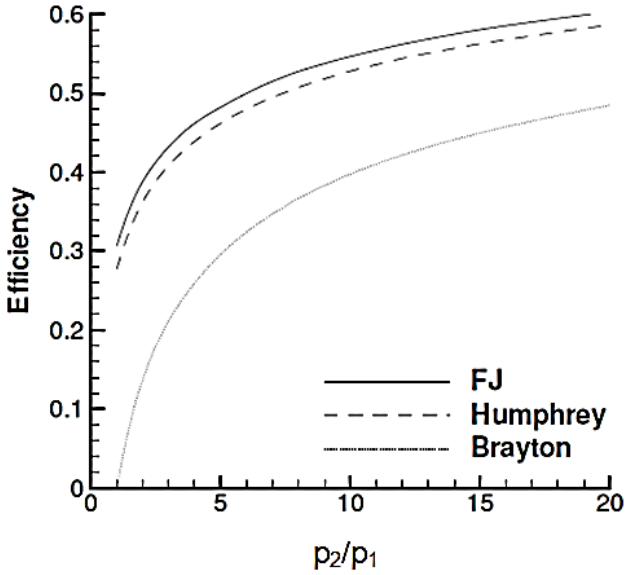

Figure 2-26 Thermal efficiency versus the compression pressure ratio for different cycles (Wintenberger 2004)

2.7.4 Internal combustion wave rotor (ICWR)

The Internal combustion wave rotor (ICWR) is a pressure rise combustion device composed of multiple channels in a serial arrangement in which the combustion process is conducted.

As for the WR, the channels rotate about an axial axis isolated by two plates set at each end. The plates have slots located in specific positions that let channels get in contact with multiple ports, see Figure 2-27.

As a pressure rise combustion device, the ICWR offers the following advantages (Nalim 1995; Lam et al. 2004; Snyder et al. 2002; M A Mawid et al. 2003; Akbari & Nalim 2006):

- The ICWR gives a pressure gain equal to or higher than the WR and it does not require ports to interact with an external combustion chamber. This configuration is compact and offers a uniform outflow as well as the reduction of flow losses
- The burned gases are expanded just after the detonation happens, so the residence time of the peak temperature is reduced as well as the NOx generation
- The ICWR obtains a higher pressure gain than the PDE due to differences in the fluid dynamics of the devices

As a type of WR, the ICWR also offers the following characteristics:

- It has its own self-cooling mechanism; reactants are injected into the channels at low temperature during each cycle to be burned. So, the average wall temperature is lower than the maximum temperature given by the combustion process
- It has a pre-compression process of incoming reactants as they are brought into rest

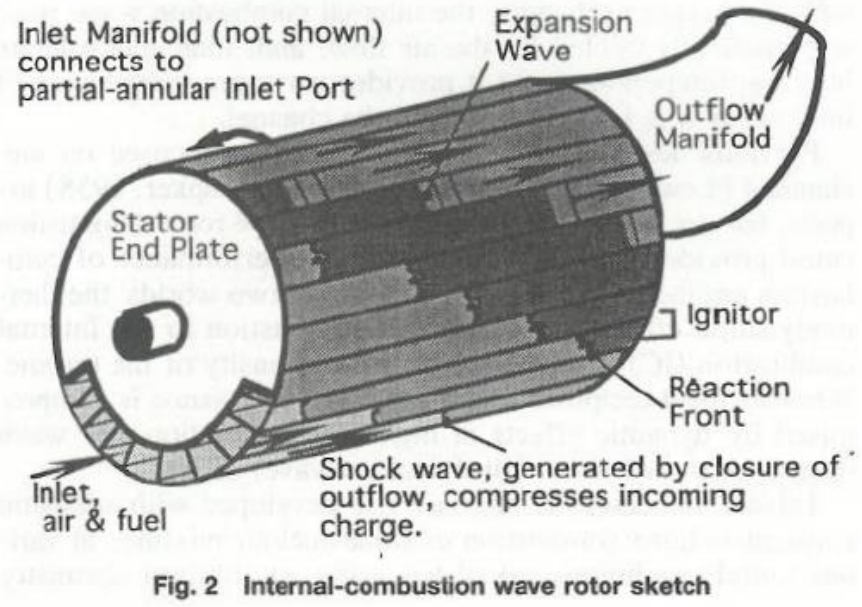

Figure 2-27 Internal-combustion wave rotor sketch (M. R. Nalim 1999)

Based on the previous characteristics, Nalim (1999) describes the ICWR as a device able to achieve the best out of the confined combustion given by isochoric combustion engines (see section 1.2.2) and the power density given by a gas turbine. Therefore this device is positioned as a suitable component of future gas turbines for the efficient propulsion of aircraft (Nalim & Izzy 2001; Akbari, Nalim & Li 2006).

2.7.4.1 The ICWR transient process

Figure 2-28 shows two types of ICWR, an ICWR with a detonation combustion process and an ICWR with a deflagrative combustion process. The channel located at the bottom of both ICWR represents the starting point implemented during the description of the transient process inside the devices.

At the reference point the channels are interacting with the withdrawal port to inject the working fluid into the turbine. The arrow at the bottom indicates the direction of the channels when they move through the cycle.

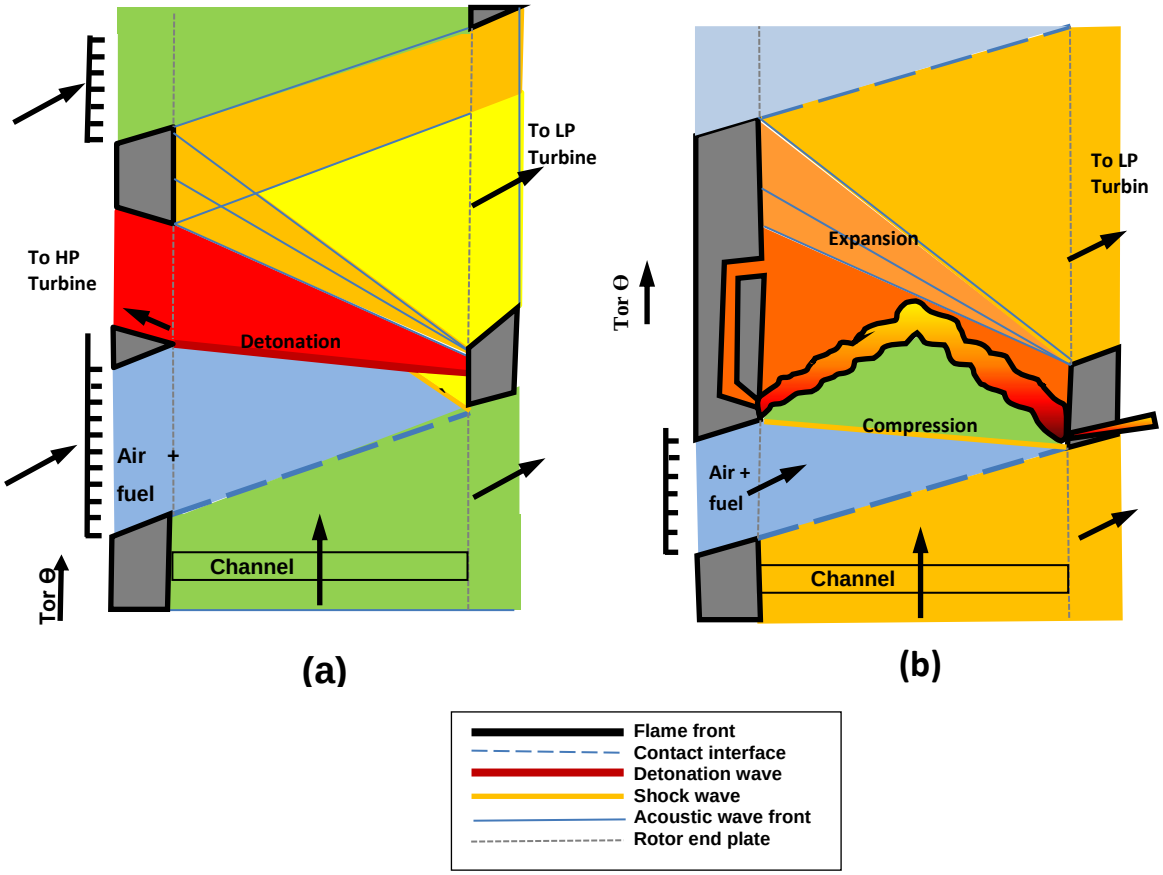

Figure 2-28 Simplified wave diagram for a) shock induced detonation mode b) deflagration mode (Nalim 1995; M. R. Nalim 1999)

Once interaction between the inlet port and channels begins, the injection of reactants into the channels is carried out; this condition generates a contact wave that moves from left to right.

The arrival of the contact wave to the right plate indicates the end of interaction between the channels and the withdrawal port to prevent the leak of reactants to the turbine. The sudden closure of the port initiates a local increase of the fluid pressure followed by compression waves travelling backward through the channels, whose collisions produce a shock wave.

A shock wave is able to produce the auto-ignition of most of the hydrocarbons through a detonation process if the temperature of reactants is above 800 K, as shown in Figure 2-28(a), otherwise a complementary ignition system will be

required such as the gases recirculation or a spark, see Figure 2-28(b) (Nalim 1995).

The detonation process releases an enormous amount of energy and therefore the withdrawal port must be split into two; the first port to feed a high pressure turbine and the second port to feed a low pressure turbine.

Before the channels start interacting with the low-pressure withdrawal port, the fluid is in repose, so the mass withdrawal produces a drop in the pressure field followed by a rarefaction wave that moves from the right end through the whole channel.

The expansion wave is reflected once it arrives at the left plate and generates an additional drop in pressure, which is enough to allow the future interaction between the injection port and the ICWR.

2.7.4.2 ICWR configurations

As for the WR, the ICWR has two flow configurations called the through-flow ICWR and the reverse-flow ICWR, see Figure 2-29. Both alternatives were evaluated by Nalim & Paxon (1997) by implementing numerical simulations. The results revealed some drawbacks of the reverse-flow configuration that could affect the ICWR's performance and therefore this configuration is not recommended.

The ICWR is also classified according the trajectory of the reaction into a forward or backward detonation or deflagration (see Figure 2-30). Among these options, the ICWR performs better with a backward propagation, since the residence time at peak temperature gets shorter (Akbari, Nalim & Snyder 2006) and a uniform velocity profile at the exhaust port is achieved (Pezhman et al. 2005).

2.7.5 Fuel stratification

As a component of a gas turbine, the ICWR must be able to drive the core flow of the thermal machine during its operation. However, a homogenous mixture of fuel and air inside each channel with the required amount of fuel to prevent the

turbine burning produces a low equivalence ratio, so the combustion process is unsustainable or impossible.

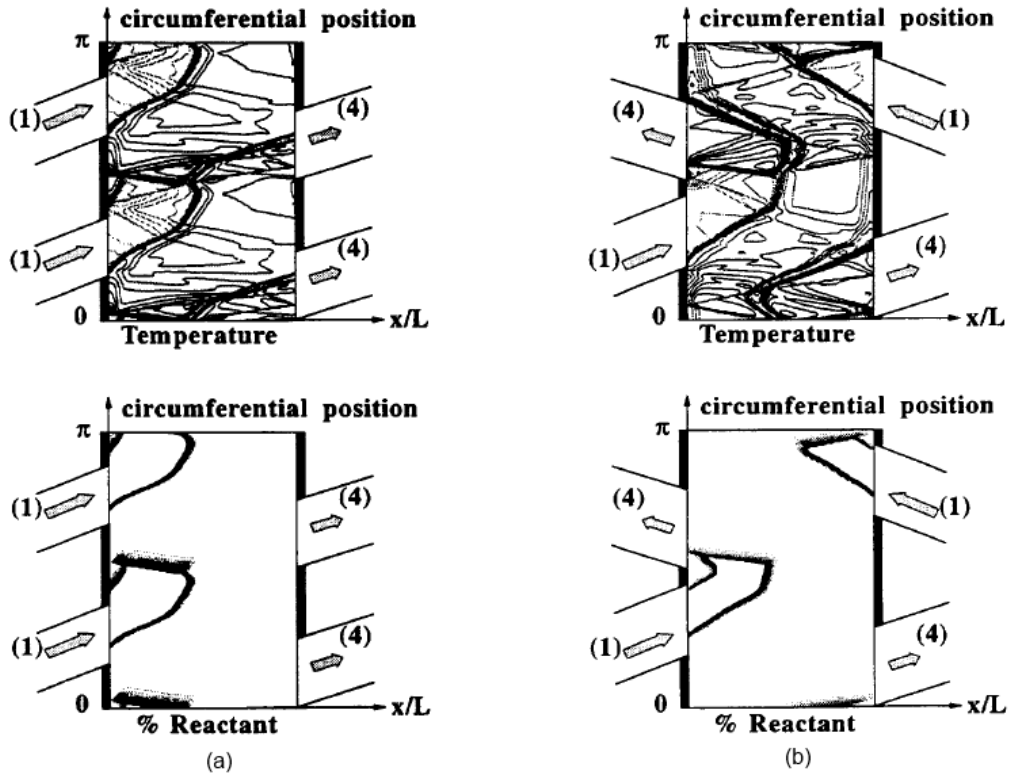

Figure 2-29 Flow configuration in an ICWR a) through-flow configuration b) reverse-flow configuration (Nalim & Paxson 1997)**; levels of temperature and percentage of reactants (%)**

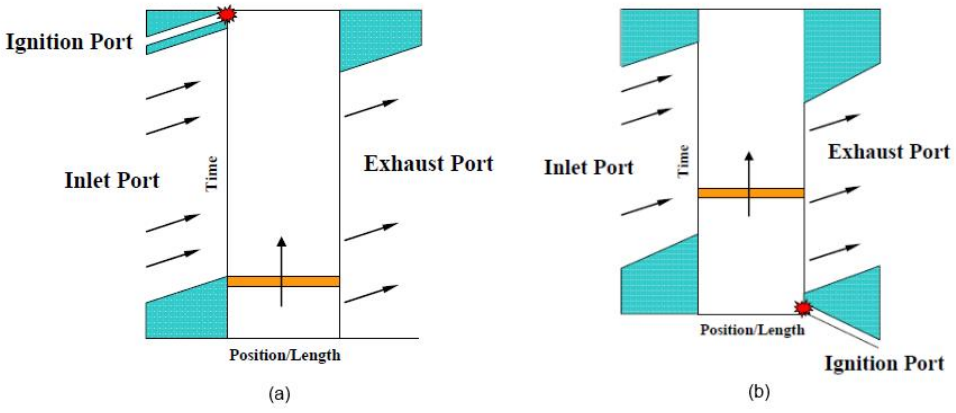

Figure 2-30 Detonation configuration a) Forward-propagation b) Backward propagation (Pezhman et al. 2005)

To sort out the problem the fuel is injected only into some regions of the injection port, so it is introduced into the channels by packages with the necessary equivalent ratio for the combustion process. This configuration is called fuel stratification and is shown in Figure 2-31 (Nalim 2000; Nalim 1997).

The fuel stratification confines the detonation process to a small region inside the channel. Once the reactants are burned, a shock wave starts moving in the same direction as the detonation wave to compress the remaining fluid.

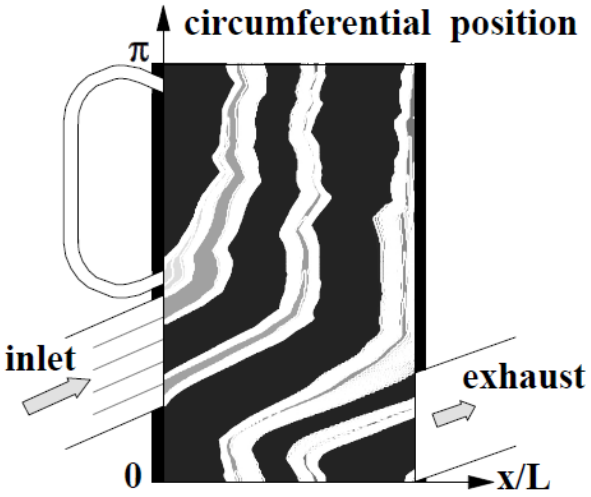

Figure 2-31 Fuel stratification inside of an ICWR

2.8 Review of the numerical methods implemented during the design and performance evaluation of the novel devices

Some relevant works performed by other authors are chronologically presented in the following subsections to provide a description about how the numerical techniques have been incorporated in the study of wave rotors, pulse detonation engines and internal combustion wave rotors.

2.8.1 Wave Rotor

In 1995, D. E. Paxson developed a 1D-CFD-based code able to design Wave Rotors by modelling the gas dynamics inside the devices. This code was validated with several experiments and later on in 1997 it was implemented in the design of the NASA Lewis 4-Port Wave Rotor (Paxson 1995; Wilson 1997).

In 2000, K. Okamoto presented a 2D CFD model to investigate the inner flow dynamics inside a Wave Rotor. The CFD code was based on the finite difference method and it was validated with experimental results. As part of the contribution the authors quantifying the influences of the ports “gradual opening effects” in the inner flow by changing the width of the channels. The model was able to reproduce the intensity and the propagation velocity of the shock waves reported by the experiment and a remarkable effect of the gradual opening was observed on the state of the contact discontinuity and the intensity of the shock wave generated by the hot gases that come from the combustion chamber (Okamoto 2000).

In 2003, K. Okamoto, Nagashima & Yamaguchi continued the assessment of the 2D-CFD code mentioned above, but in this case a micro-wave rotor was modelled. The post-processed data allowed quantifying the effect of the port adjustment upon the wave disturbances within the rotor cells. The analysis suggests a short distance (equal to the width of the channels) between the port that extract gases and the port that extract air, to prevent a large leaks, since the performance of the micro-WR is seriously deteriorated (Okamoto et al. 2003).

In 2004, Frackowiak et al. implemented FLUENT (CFD commercial software) to solve 2D and 3D models of a Wave Rotor. The authors state that FLUENT offers easy to implement tools that allow: building the geometry, setting the boundary conditions, selecting robust solvers and post-processing the solution. However, a huge computation effort is necessary during the WR simulation, so 2D and 3D models are appropriate in the last stage of the design but not during the initial geometry search or the geometry optimization. Instead, the authors recommend the implementation of 1D CFD codes (Frackowiak et al. 2004).

In 2005, Iancu, and Müller developed an analytical model to evaluate shock waves in micro-channels to explore the flow behaviour at that scale. The analytical model verification was performed by comparing the results obtained with a numerical model in ANSYS FLUENT®. As part of the observations, the CFD model predicted the dissipation of shock waves and their progressive

transformation into an array of compression waves during their way through the micro-channel due to the boundary layer (Iancu & Müller 2005).

In 2005, Iancu, Piechna and Mülle compared 2D and 3D models of a micro-wave-rotor in ANSYS FLUENT® with the outcomes given by an in-house 1D-CFD code. The CFD simulations of the commercial code confirmed the wave patterns as well as the compression and expansion processes during the device operation, regardless of some mismatches between the speed of the rotor and the speed of the waves. However, the authors agree that 1D-CFD codes are still valid to predict the device dimensioning and/or optimisation whilst 2D and 3D models are only recommended to fine tune the 1D code (Iancu et al. 2005).

In 2007, D. Paxson, Wilson and Welch developed a 1D-CFD code to evaluate a single channel that crosses the different ports of a wave rotor during a cycle. The ports of the WR were modelled by changing the model boundary conditions. The CFD result was quite a good approximation of the experiments performed (Paxson et al. 2007).

In 2010, Piechna, Cerpa, Marcin, Akbari, and Müller implemented a 3D model in ANSYS FLUENT® to validate the wave rotor dimensioning predicted by a 1D-CFD code. Among the differences, the Coriolis acceleration produced a strong skewing of the interface between the hot and cold gases through the radial axis, this effect was followed by a distortion of the moving compression waves only captured by the 3D model. Nevertheless, the main results predicted by the CFD models are in agreement with the wave rotor theory (Piechna et al. 2010).

2.8.2 Pulse Detonation Engine

In 1996, Pegg, Couch, and Hunter evaluated the preliminary design of a mixed-compression system to feed a PDEs array of a supersonic aircraft. The PDEs array had the aim to generate the necessary thrust to fly an airplane at high speed, up to a Mach number of 3. The evaluation was performed to study the effect of the hammer shock in the injection manifold as a consequence of the valves closure as well as the design capability to ensure a stable shock system inside the PDEs array. The results obtained demonstrated the successful

operation of the designed concept, since it satisfied the mass capture, the total pressure recovery and the operability requirements (Pegg et al. 1996).

In 2002, Ebrahimi & Merkle implemented a 2D model of a PDE with eight chemical species and 16 reaction steps to study the potential pre-combustion effect inside of a PDE during the cycle refilling process. The evaluation predicted the presence of reaction zones near the walls when the walls temperature was over 1500 K. However, these reaction zones were relatively benign at the operational condition of the evaluated PDE. Moreover, the pressure increased several times over the ambient pressure at the open end of the PDE as consequence of the fluid compression produced by the external shock wave and therefore the outflow was subsonic. Subsequently, the observed increase of pressure was followed by its reduction and therefore the fluid was throttled. This result suggested the implementation of a multidimensional correction model to improve the fidelity of one dimensional simulations (Ebrahimi & Merkle 2002).

In 2003, Mawid, Park, Sekar, & Arana implemented a multidimensional CFD model of a PDE to study the feasibility of substituting the afterburners of a turbofan engine by PDEs. The performance evaluation was achieved by comparing the thrust, specific thrust and specific fuel consumption reported by each configuration. The simulation was performed in STAR-CD with a single reaction step model of Hydrogen and air. The analysis demonstrated the benefit of PDEs as post-combustor, since they are capable to duplicate the thrust and specific thrust when they have an operation frequency near to 100 Hz. (M A Mawid et al. 2003)

In 2005, Choi and Yang performed a 2D-CFD simulation to study the gas dynamics inside of a PDE. The code implemented a chemical reaction scheme with a single-progressive variable. The authors reported a performance degradation of more than 6 % in respect to the baseline PDE as a consequence of the shape of the nozzle's exit and the internal flow losses associated with the shock dynamics. A reduction of the nozzle throat is favourable. Finally, large purge times decreased the specific thrust and increased the specific impulse produced by a PDE (Ma et al. 2005).

In 2006, Yungster, Radhakrishnan and Breisacher modelled a 2D PDE with a CFD code based on the Euler equations. The reaction mechanism implemented by the code consisted of 12 chemical species and 27 reactions steps whilst a multi-level dynamic adaptive mesh was implemented to solve the structure of the detonation front. The authors reported an elevated NOx formation when the reactants were near the stoichiometric condition. Therefore, they recommended a lean or rich fuel mixture and a short PDE to reduce the NOx formation ((Yungster et al. 2006).

In 2006, Canteins et al. performed some experiments to evaluate the increase of specific impulses obtained from a PDE with an ejector located downstream of the device. The ejector used the kinetic energy of the gases extracted from the PDE to suck external air, so an increase of the overall mass flux was obtained. The authors incorporated a CFD model into the analysis to get clues about the origin of the performance improvement. The implemented code solved the Euler unsteady transport equations in a 2D domain and modelled the detonation process with a single reaction step approach of air and C_2H_4. The authors reported an augmentation of 60 % of the turbine impulse as well as an overestimation of the impulse augmentation by 10 % predicted by the model since the heat losses through the domain boundaries were not included in the model. Finally the model analysis showed that 80 % of the improved impulse came from the expansion detonation through the annular surface between the PDE and the ejector (Canteins et al. 2006).

In 2007, Papalexandris, Thomas, Jacobs and Deledicque implemented a 2D CFD model to study the possible transition between a supercritical and critical detonation wave into a subcritical detonation wave. The first type of detonation has a reaction zone always attached to the shock wave, the second type of detonation has a reaction zone that is detached and reattached again during the shock wave displacement and the third detonation wave causes the reaction zone to be detached followed by the quenching of the flame. The control variables implemented in this work were the channels-width ratio (sudden expansion) and the fuel's activation energy. As a result, a detonation

transformation was achieved at sufficiently large values of any of the control variables (Papalexandris et al. 2007).

In 2009, Nikitin, Dushin, Phylippov and Legros performed 2D CFD models to study the possible reduction of the pre-detonation chambers with a successful deflagration to detonation transition (DDT). From all the studied cases, the author recommended a chamber's configuration to be able to generate shock waves from an annular region, since the coalescence of these shock waves at the centre of the PDE propitiates the appearance of a strong shock wave able to drive a stable detonation process (Nikitin et al. 2009).

In 2010, Al-Falahi, Yusoff, & Yusaf, developed a 2D-CFD model base on the Euler equations to study the performance of a newly built hypersonic test facility at the Universiti Tenaga Nasional "UNITEN" in Malaysia. The author emphasized the code's ability to estimate the speed of the shock wave, the shock wave compression and the overall gas dynamics after comparing the code's result with the analytical solution and some performed experiments (Al-Falahi et al. 2010)

2.8.3 Internal Combustion Wave Rotor

In 2002, Snyder, Alparslan and Nalim implemented a NASA one-dimensional non-steady CFD code to model a constant volume combustor (CVC). The modelled device was able to deliver a uniform outflow with an elevated pressure gain; so the device was considered suitable to reduce the SFC of future gas turbines. (Snyder et al. 2002).

In 2005, Pezhman, Berrak, Viktor and Raz implemented a quasi-one dimensional CFD code to predict the performance enhancement of a hydrogen-fuelled gas turbine with an ICWR that works as the combustion chamber. This study evaluated an ICWR with forward detonation propagation and an ICWR with backward detonation propagation. Even though a substantial increase of the pressure gain is obtained with all the ICWR, the backward detonation propagation produces a better velocity profile, and therefore this configuration is recommended to substitute the combustion chamber of future gas turbines (Pezhman et al. 2005).

In 2006, Akbari and Nalim compared the performance of an ICWR and a PDE as the combustion chamber of future gas turbines using a semi-one dimensional CFD model able to evaluate deflagrative and detonative combustion processes. As the results show, the ICWR has a more homogeneous flow than the PDE whilst the pressure gain is higher due to the additional compression effect achieved by the hammer shock. Therefore, the ICWR was considered a better option as a combustion chamber of new gas turbines (Akbari & Nalim 2006).

Simultaneously Akbari, Nalim, & Snyder implemented a 1D-CFD code to obtain the preliminary design of an ICWR for an innovative test rig. The selected design was numerically tested under different operating conditions such as the fuel distribution, the port timing, the rotational speed, and the exhaust back-pressure. As a result, the CFD model predicted a satisfactory performance of the designed device. (Akbari, Nalim & Snyder 2006).

In 2006, Khalid, Banerjee, Akbari and Nalim implemented a 2D-CFD model in STAR-CD to study the main loss mechanisms in a Wave Rotor; including viscous and heat transfer losses, flow leakage between channels and the gradual port opening and closure. The effect on the distribution of reactants inside the ICWR as a consequence of the large scale structures created by the ports' partial opening was also evaluated. The authors reported the necessity of implementing an air buffer between reactants and product gases to prevent an early ignition, as well as the necessity of more creative approaches to inject the reactants into the ICWR to avoid the presence of a highly skewed interface between reactants and air, because this effect and the gases diffusion make it difficult to have a mixture with the required ignitable composition in the right place (Khalid et al. 2006).

In 2007, Baronia, Nalim and Akbari evaluated the performance of the combustion-torch ignition technique (hot gases jet ignition) inside a single channel of an ICWR using a 2D-CFD model in STAR-CD. The aim of the work was the evaluation of some experimental results and the calibration of a simpler quasi-one-dimensional model. The 2D-CFD code implemented a hybrid reaction

model to consider the ignition delay. As the results show, the combustion process was highly sensitive to the ignition temperature rather than the turbulence kinetic energy and the equivalence ratio. The CFD model provided information about parameters such as the jet mixing Damkohler number, the density gradient in the early flame front, and the primary shock strength (Baronia et al. 2007).

In 2012, Nalim, Izzy and Akbari used a quasi-one-dimensional numerical model to design the basic geometry of a PDE with a rotary wave ejector. The new design was intended to suck external air using the kinetic energy of the PDE exhaust gases in order to increase the mass flux driven by the device, such as (Canteins et al. 2006). The results were compared with a single PDE (without ejector) to quantify the impulse augmentation given by the new proposal. The results show that the rotary wave ejector was able to increase the specific impulse up to 2.37 times the given by the baseline PDE. So the authors suggested the new design to make the technology highly efficient (Nalim et al. 2012).

2.8.4 Section summary

Based on the above, it is clear that 1D-CFD models have their limitations when predicting the fluid effect inside the studied devices. However, their implementation is still valid during the dimensioning process as well as the optimization process of future designs, since they offer simple solutions in a short period of time, with a reasonable level of accuracy.

Moreover, the implementation of multidimensional CFD models (2D and 3D) demand a huge computational effort, so they are recommended only when details of the transient process are required.

The usage of commercial software to verify the results predicted by the 1D-CFD codes has been commonly implemented. The verification process is valuable due to the long trajectory and the experience gained by the companies involved in the software development which have included multiple approaches that allow the numerical modelling of different engineering processes.

Finally, the numerical solution of the Euler transport equation has given reasonable results, able to evaluate the main phenomena inside a shock tube. Therefore, the implementation of this equation through a 1D-CFD code looks appropriate to predict the performance and dimensioning of devices such as WR, ICWR and PDE.

.

3 EVALUATION OF WAVE ROTORS AS A COMPONENT OF AIRCRAFT GAS TURBINES

The performance evaluation of a wave rotor connected to a gas turbine is often carried out by replacing the device for a compressor and a turbine whose efficiencies are assumed constant throughout the operating range of the thermal machine (Müller 2003; Akbari & Muller 2003; Wilson & Paxson 1993; Akbari, Nalim & Muller 2006).

However, a fixed value of the compression efficiency or the expansion efficiency during the device operation is inadequate when different thermal cycles are compared with each other, since fluids feeding the device have different properties and therefore the strength of shock waves and rarefaction waves is affected.

The gas dynamic analysis of wave rotors is an option that overcomes the problem stated above and it can be performed analytically through the Weber's algorithm, which is based on the one-dimensional theory of compressible flow (Anderson 2003) applied to a through-flow wave rotor with a double expansion port; suitable configuration for gas turbines with a high compressor pressure ratio (Weber 1995).

Moreover, in a wave rotor of this type the mass flux that crosses each of the expansion ports must be computed before the heat balance. So, the position of the slots and their length are also necessary. This information is part of the device's dimensioning and is strongly associated with the arrival of some compression and expansion waves to the channels' ends; a topic that will be addressed later on.

A 1D-CFD model is an alternative that enables tracking of the waves inside the wave rotor since it is based on the numerical solution of the transport equations (free of correlations) and its boundary conditions can be set from the analytical solution of the Weber's algorithm.

Based on the above, this chapter provides some tools able to assess the feasibility of implementing the wave rotor in a turbofan engine by integrating the fluid dynamic with the thermal analysis of the cycle through the Weber's algorithm. In addition, the development of a 1D-CFD code to estimate the dimension of the designed device is also included.

3.1 Through-flow wave rotor operation based on the model of Weber (two expansion process)

The wave rotor can be constituted by a single expansion port or multiple expansions ports according to the compressor pressure ratio achieved by the device. A double expansion wave rotor is a common configuration, if the maximum temperature of the cycle is two times higher than the temperature of the fresh air that feeds the wave rotor, because this configuration prevents the flow getting throttled at the channels' ends (minimum irreversibility) and at the same time it avoids obtaining complex designs (more than two expansions ports) (Weber 1995).

A wave rotor as a component of future gas turbines must have a significant participation in the compression process to achieve a substantial increase of the machine thermal efficiency. Based on the statement above, this work considers a double-expansion wave rotor integrated into an aircraft gas turbine.

Figure 3-1 is a schematic representation of a double-expansion through-flow wave rotor, in which the red continuous lines denote shock waves, the grey dotted-dashed lines denote contact waves, and the blue dashed lines denote rarefaction waves. Figure 3-2 presents a schematic representation of the wave rotor connected to a turbofan engine.

Throughout the cycle, the rotor channels are in contact with five ports, these are:

- Low pressure air port (LPA) feeds the rotor channels with fresh air that comes from a mechanical compressor.
- High pressure air port (HPA) feeds the combustion chamber with compressed air by the wave rotor.

- High pressure gases port (HPG) feeds the wave rotor with gases that come from the combustion chamber.
- Low pressure gases ports (LPG1 and LPG2) feed the high pressure and low pressure gas turbine respectively.

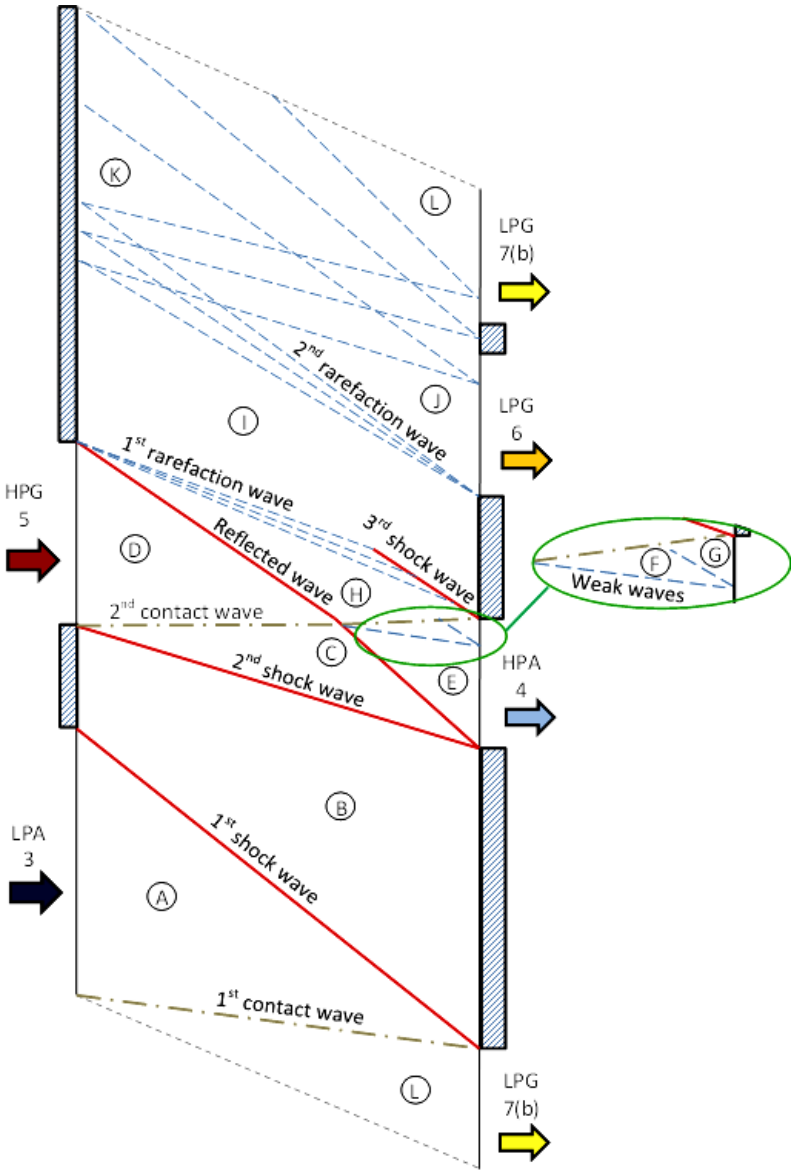

Figure 3-1 Representation of a double expansion through-flow wave rotor

As shown in Figure 3-1 there are two contact waves per cycle which separate the gases from fresh air, these two waves are generated when LPA and HPG ports are opened to fill the channels with air and burned gases respectively. Therefore their arrival to the right side is set as the time for closing the LPG2 and HPA ports.

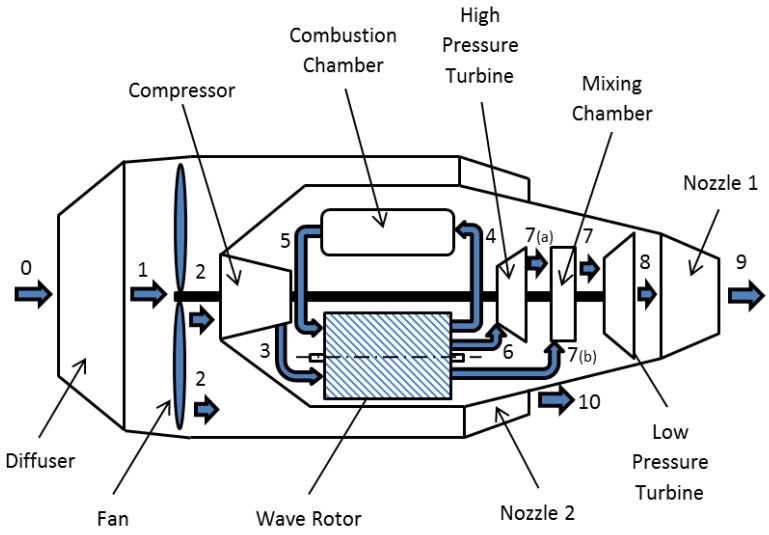

Figure 3-2 Schematic representation of a double expansion through-flow wave rotor connected to a turbofan engine

The first shock wave is called hammer shock and it is generated at the right side of the channels when the LPG2 port is closed due to the sudden reduction to zero of the flow velocity (condition established by the right-plate wall). This wave generates the first compression of the air inside the channels (first compression stage) and its arrival to the left side indicates the closure of the LPA port.

After the LPA port is closed the velocity of the flow normal to the wall is equal to zero, so a rarefaction wave is generated and it travels to the right side of the WR to compensate the velocity differences between the fluid located downstream of the channels and the fluid near to the wall. The collision between the rarefaction wave and the first shock wave makes them attenuate each other, so the fluid inside the channel reaches a homogeneous condition (state B).

The second shock wave is generated when the HPG port is opened due to the pressure difference between the channels and the combustion chamber. This wave travels to the right-end and is reflected once it arrives to the right plate. This situation causes the air to be compressed twice, once from state B to C and then from state C to D (second compression stage). The HPA port is

opened when air reaches state D; this condition allows the supply of air into the combustion chamber at state 4, see Figure 3-1.

The trajectory of the reflected shock wave crosses the second contact wave and starts compressing hot gases (State H). Once the collision occurs, the reflected wave increases its velocity while the velocity of the contact wave decreases. The collision also creates a weak rarefaction wave which expands the air to state F and then a weak shock wave that compresses the air to state G (instead of a weak shock wave, a weak rarefaction wave can be generated when a nozzle is included at the channels' end). The effect of these weak waves can be ignored (Iancu et al. 2008), but Weber decided to include it in his algorithm to provide a more accurate model (Weber 1995).

An instant after the ports HPA and HPG are closed the third shock wave is generated and the first rarefaction wave of the cycle. Based on Weber's criteria (Weber 1995), when the collision between both waves occurs they attenuate each other, so the fluid inside the channels reaches a homogeneous state I and is ready to be expanded by port LPG1.

Once the LPG1 port is opened the fluid starts moving outside (state 6) and generates the second strong rarefaction wave, which moves from right to left, then the wave is reflected by the left plate changing its direction. The LPG1 port is usually closed when half of the rarefaction wave arrives at the right end.

The last strong expansion of the cycle is achieved by opening the LPG2 port. This situation makes the remaining gases at state K change to state L inside the channels and then to state 7 outside the wave rotor. Once half of the rarefaction wave reaches the left side of the channels the LPA port is opened, starting the cycle again.

3.2 The algorithm of Weber

The algorithm of Weber is an alternative that enables the evaluation of the fluid properties through stage-to-stage ratios inside the wave rotor by implementing a one-dimensional analysis of compressible flow. It is based on the assumption that each channel is isolated (adiabatic walls), the viscous effect is negligible,

there is no source of irreversibility other than shock waves and the working fluid behaves as an ideal gas with constant specific heat values (Anderson 2003; Weber 1995; Cengel & Boles 2007); a full description of all the equations implemented within the subroutine is presented in appendix A.

In addition, Weber's algorithm comprises a system of equations derived from the following assumptions (Weber 1995; Weber 1992):

- Leakage from wave rotors is negligible
- The collision between a shock wave and a rarefaction wave makes them attenuate each other
- Compression waves are assumed to instantaneously coalesce into a shock wave
- Rarefaction waves are modelled by a single wave
- The angle of incidence between the fluid coming from the feeding ports and blades is zero

And the solution of the resultant system of equations is obtained once the following parameters are set:

- The Mach number at state A.
- The ratio between the static temperature of gases at HPG port and the static temperature of air at LPA port (T_5/T_3)
- The static pressure losses at the combustor (p_5/p_4)
- The channels' angle and HPG port's angle

The Weber technique splits the wave rotor process into three sections as follows: the first-stage compression (air compression from state A to state B), the second-stage compression, (air compression from state B to E), and the expansion processes (gases expansion from state H to J and then to L), see Figure 3-1.

The first stage compression is influenced by the sudden reduction of speed to zero experienced by the air when the LPG2 port is closed $(u_B = 0)$. Therefore, once the Mach number at state A is set, the ratio of properties between the state B and A can be obtained by implementing Eq. (A- 1) to Eq. (A- 7).

The second-stage compression requires a complex iterative process which includes:

- An external loop that links states B and C of Figure 3-1, once the Mach number of the first shock wave is given ($M_{x,B}$)
- An internal loop that connects states C, E and 4 (state at the HPA port) of Figure 3-1 able to ensure the pre-set value of pressure drop in the combustion chamber (pressure difference between states 5 and 6),
- An internal loop that links states C-E-F with states C-D-H of Figure 3-1 able to ensure the constraints imposed by the second contact wave ($p_H = p_E; u_H = u$) and T_D/T_C that is obtained from a pre-set value of T_5/T_3 and the temperature ratios computed through the first compression stage for a given M_{xB}.

Although the internal loops give a unique solution for each assumed value of $M_{x,B}$, the mass balance between LPA and HPG ports is used as the convergence criterion to conclude the external loop. Over the entire process the solution of Eq. (A- 1) to Eq. (A- 9) is necessary.

The mass balance is computed by tracking the second shock wave, the reflected wave and the second contact wave to estimate the dimensions of the HPA and HPG ports (a procedure thoroughly discussed in (Weber 1995)). The flow velocity should be referenced to the wave rotor and not to the ports; therefore, some trigonometric operations using the HPG port's angle and the blade angle are also required.

When the convergence criterion is reached in the second compression stage it is possible to compute the ratio between the tangential velocity of the wave rotor and the speed of sound in D because the angle on the HPG port, the Mach number in D and the blades' angle are all known. The tangential velocity will allow the rotation speed of the wave rotor to be obtained once the radius of the device is determined.

After modelling the second compression stage and before starting to model the expansion process, it is fundamental to get a link between state I and any other

state previously evaluated. This is done by solving some conservative equations in the control volume shown in Figure 3-3, which represents a section of the whole cycle, see Figure 3-1. During the evaluation of the control volume it is also important to consider a system of reference fixed to the channels.

The establishment of the control volume in Figure 3-3 is a key factor of the algorithm and is based on the assumption that there is an instant of time where the fluid inside the channels reaches a homogeneous state B and another where it reaches a homogeneous state I, see section 3.1.

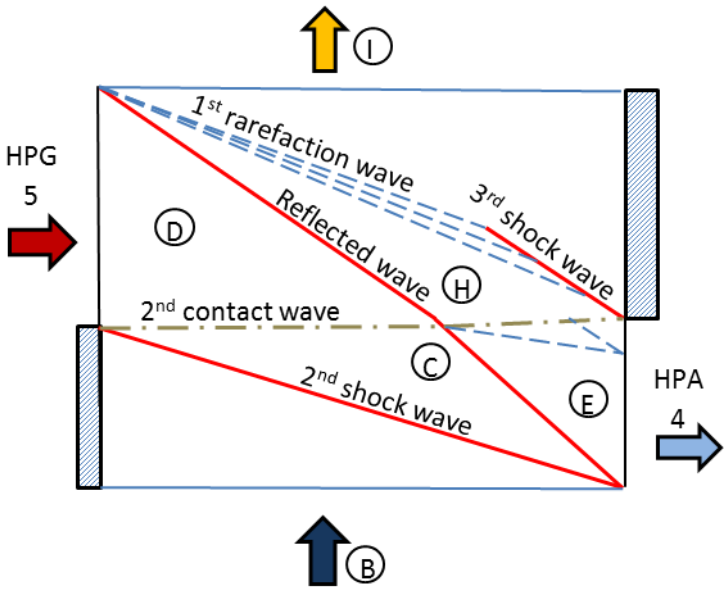

Figure 3-3 Control volume set to calculate the state 10

Finally, the expansion process is modelled by evaluating the Mach number in state L, considering that the pressure ratio between I to A is the same as I to L and that the overall expansion process is isentropic. Then, based on the fact that the Mach number at state K is zero, the remaining states are obtained by implementing an iterative loop that guesses the Mach number at state J until the suppositions satisfy Eq. (A- 4) to Eq. (A- 6).

Once Weber's algorithm provides the property's ratios, the polytropic efficiency of the compression and expansion process inside the wave rotor are estimated by means of Eq. (3-1) and Eq. (3-2) respectively.

$$\eta_{Pc} = \frac{ln\left(\frac{p_{04}}{p_{03}}\right)^{\frac{k-1}{k}}}{ln\left(\frac{T_{04}}{T_{03}}\right)} \quad \textbf{(3-1)}$$

$$\eta_{Pe} = \frac{ln\left(\frac{T_{06}}{T_{05}}\right)^{\frac{k-1}{k}}}{ln\left(\frac{p_{06}}{p_{05}}\right)} \quad \textbf{(3-2)}$$

Fluid states 3, 4, 5 and 6 in the above two equations are computed at the LPA, HPA, HPG and LPG ports of the wave rotor, see Figure 3-1. Therefore, the compression polytropic efficiency (η_{Pc}) is a measure of the irreversibility associated with the compression between LPA and HPA ports while the expansion polytropic efficiency (η_{Pe}) is a measure of the irreversibility associated with the expansion between HPG and LPG1 ports; the expansion process between LPG1 and LPG2 ports is isentropic because Weber's model considers only the presence of rarefaction waves, which are reversible by nature.

3.3 Thermal Analysis of the Gas Turbine with a Wave Rotor

The thermal evaluation of a turbofan with a wave rotor requires the performance of the turbine components to be estimated separately, including the wave rotor. Therefore, parameters such as the isentropic efficiency of the diffuser and the nozzle as well as the polytropic efficiency of the fan, the compressor and the turbine are necessary. The states reached by the fluid inside the wave rotor can be computed with Weber's algorithm.

The thermal evaluation of the novel cycle is performed by computing the efficiency of energy conversion (η_e), the specific thrust (F_s) and the specific fuel consumption. These values are compared with those obtained by the baseline turbofan used in business jets.

The efficiency of energy conversion η_e quantifies how much of the energy given by the combustion process is converted into potentially useful kinetic energy, and is obtained through Eq. (3-3).

$$\eta_e = \frac{(u_j^2 - u_a^2)/2}{m_f . Q_{net,p}} \quad \textbf{(3-3)}$$

The specific thrust F_s gives the ratio between the thrust generated by the propulsion system and the mass flow required. This parameter is computed by means of Eq. (3-4).

$$F_s = (u_j - u_a) + \frac{A_j}{\dot{m}} . (p_j - p_a) \quad \textbf{(3-4)}$$

In the equations above u_j and u_a represent the average velocity of the jet plume at the turbine's nozzle and the velocity of the airplane; both values relative to earth, whilst p_j and p_a represent the static pressure at the turbine's nozzle and the ambient pressure (the pressure values differ from each other only when the nozzle is throttled).

The specific fuel consumption "SFC" gives the ratio between the fuel-air ratio required by the turbine and the generated thrust, this parameter is obtained through Eq. (3-5)

$$SFC = \frac{f}{F_s} \quad \textbf{(3-5)}$$

F_s and SFC are usually implemented during the gas turbine optimisation, just because they give an idea about the airflow, the fuel flow and the nozzle area; three variables are strongly related to the sizing of the gas turbine (Saravanamuttoo 2008).

3.4 Performance evaluation of a wave rotor connected into a gas turbine (analytical solution).

In order to evaluate the performance of a wave rotor as a component of a gas turbine, a subroutine was developed to predict the wave rotor's behaviour using

Weber's algorithm, as well as a main program that uses this information to perform a thermal analysis of the turbine cycle.

The thermal analysis of the cycle and gas dynamic analysis of the wave rotor are obtained by disregarding the reduction of work experienced by the turbine due to the extraction of compressed air to the cooling system.

To simplify the analysis, the working fluid is assumed to be standard air (R equal to 287 J / kg K), and the air is assumed to be cold and hence Cp is equal to 1,005 J / kg and k = Cp / Cv is equal to 1.4 (Cengel & Boles 2007).

Although in a gas turbine the working fluid undergoes great changes in its temperature, Saravanamuttoo (2008) agrees that a fixed value of the specific heat is valid during the performance evaluation of gas turbines, because Cp behaves inversely proportional to k (Cp/Cv) when the fluid temperature changes and therefore an underestimation of Cp is compensated by an overestimation of k, so the thermal analysis is achieved without the presence of big inaccuracies (Saravanamuttoo 2008). However, the model of standard air is susceptible to errors since the value of specific heat and the value of specific heat ratio differ between the air and the burned gases in a common gas turbine.

The baseline machine selected in this work is a turbofan engine whose operational range is equivalent to the Rolls Royce AE3007 series gas turbine (Roll Royce 2011) implemented in the propulsion of business jets. This turbine is selected to perform the analysis, since the CLEANSKY project includes the improvement of technologies for regional flights as part of its targets (middle range aircraft).

The performed procedure can be implemented in the study of shorter or larger turbines since it only requires general information of the cycle to describe the trajectory of the processes that follows the working fluid through the gas turbine.

Some of the turbine operational parameters of the selected gas turbine were obtained from its datasheet. However, parameters such as the polytropic and isentropic efficiencies of the gas turbine components were estimated from a type of problem illustrated by Saravanamuttoo (Saravanamuttoo 2008), due to

the lack of information in the main source. The data sheet of the engine is shown in Table 1.

Table 1 Specifications of the baseline turbofan

Variable	Value
Thrust (kN)	42
Turbine maximum temperature (K)	1110
Bypass ratio	5
Fan Pressure Ratio	1.36
Compressor Pressure Ratio	16.91
Altitude (m)	10000
Airplane Mach number	0.8
Polytropic fan efficiency	0.9
Polytropic compressor efficiency	0.9
Polytropic turbine efficiency	0.9
Isentropic intake efficiency	0.93
Isentropic propelling-nozzle efficiency	0.9
Mechanical transmission efficiency *	0.99
Combustion efficiency	0.98

* The mechanical transmission efficiency is define as the ratio between the power consumed by the compressor and/or fan and the power produced by the turbine

The evaluation of the wave rotor integrated to the turbofan was achieved by comparing four possible design configurations with the baseline engine. These designs keep some characteristics of the baseline turbofan, as Table 2 indicates.

These configurations were previously studied by (Akbari & Müller 2003; Müller 2003), who evaluated the possibility of coupling a reverse flow wave rotor and a through flow wave rotor into a gas turbine for power generation.

Table 2 Similarities between the evaluated cases and the base line gas turbine

Cases	Similarities between the studied case and the base line engine
Case (a)	The cycle keeps the same compressor pressure ratio and turbine inlet temperature
Case (b)	The cycle keeps the same overall pressure ratio and turbine inlet temperature.
Case (c)	The cycle keeps the same temperature level in the combustion chamber
Case (d)	The cycle keeps the same compressor pressure ratio and combustion end temperature

In cases (a) and (d) the state at the compressor discharge is the same as the baseline engine in order to achieve the same compressor pressure ratio. Meanwhile, in case (b) and (c) the state at the compressor discharge is assumed and then improved by an iterative process until Eq. (3-6) is satisfied, were $PR_{c,BL}$ represents the compressor pressure ration of the vase line engine and $PR_{c,WR}$ represents the compression pressure ration delivered by the Wave Rotor. The iterative process is performed in order to maintain the overall pressure ratio of the cycle.

$$PR_{c,BL} = \frac{p_{03}}{p_{02}} . PR_{c,WR} \quad \textbf{(3-6)}$$

An increase of η_e is expected during the evaluation of the novel cycles, which in some circumstances can generate the throttling of the nozzle located downstream of the gas turbine. In order to do a fair comparison of all the studied cases, the performance will be computed assuming a full expansion process; therefore a divergent nozzle will be included when necessary.

In section 3.2, the necessity of defining some parameters before running the algorithm was emphasized. Among the parameters, this study focused on observing the effect of M_A and T_5/T_3, due to their direct influence on the first and second compression stage, and therefore they are alternated in a range from 0.2 to 1 and from 1.5 to 3.5 respectively. The remaining parameters were fixed based on Weber's criterion to obtain the optimal condition (Weber 1995), see Table 3.

Table 3 Parameters fixed before executing Weber's algorithm

Variable	Value
Pressure ratio between states 5 and 4 of Figure 3-1	0.95
Angle of the HPG port according to the turbine axial direction (θ_{HPG}); see Figure 3-4	0°
Channels' angle according to the turbine axial direction (β); see Figure 3-4	45°

The Mach number reached by the fluid in each state within the wave rotor can be obtained after executing Weber's algorithm, since the Mach number is also a ratio of properties.

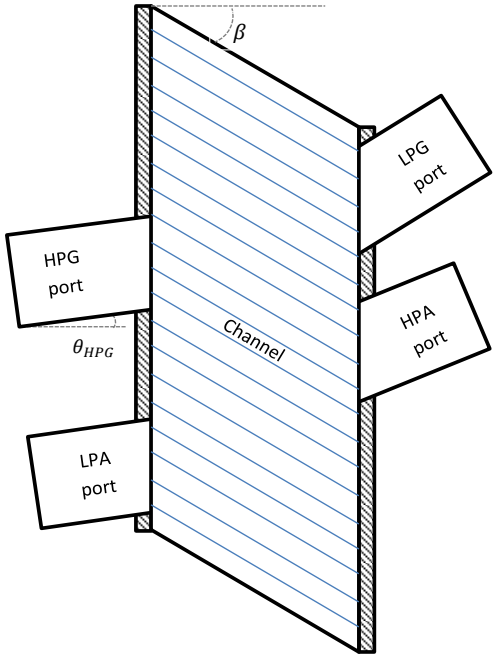

Figure 3-4 Representation of a Wave Rotor, the angel of the HPG port ($\boldsymbol{\theta_{HPG}}$) and the channels' angle ($\boldsymbol{\beta}$)

All the states in the domain can be computed once the stagnation properties are set in a specific location inside the domain. This work set the stagnation properties in the LPA port directly or by an iterative loop, as it was previously described.

3.5 Results of the performance evaluation (analytical solution)

Figure 3-5 and Figure 3-6 show the wave rotor's operating maps computed from the gas dynamic evaluation. The constrained area observed in these maps is a zone in which the gas turbine is unable to operate autonomously, since the power produced by the turbine is lower than that required by the compressor and fan.

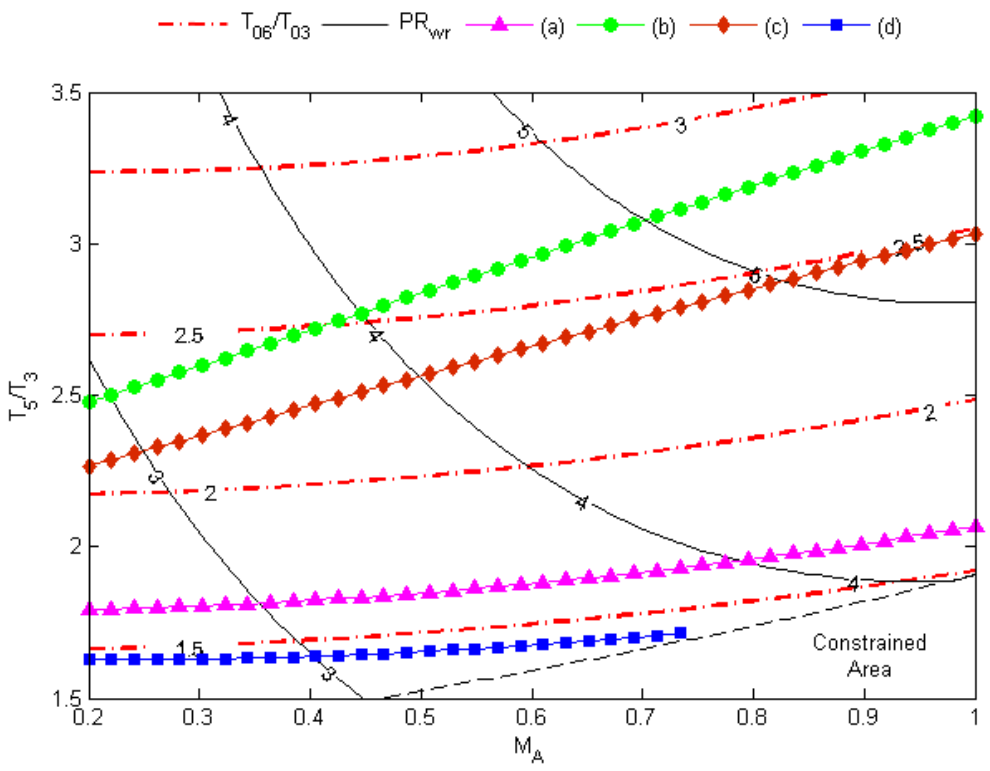

Figure 3-5 Map of wave rotor pressure ratio and T_{06}/T_{03} at different values of M_A and T_5/T_3; the states numbering is based on Figure 3-1

These maps also show the ratio between the maximum and minimum temperatures of the working fluid driven by the device (T_5/T_3) as a function of M_A for each of the cases presented in Table 2; the first variable is a measure of the thermal jump experienced by the WR whilst the second variable is associated with the pressure jump given by the first compression stage. All of them must be pre-set before implementing the Weber's algorithm (Weber 1995).

One of the maps displayed in Figure 3-5 is the ratio between the stagnation temperature at the LPG1 port and the stagnation temperature at LPA port (T_{06}/T_{03}) (see Figure 1-1), which is represented by red dotted lines. Such as (T_5/T_3) and M_A, this ratio of stagnation temperatures needs to be pre-set before implementing the Weber's algorithm and therefore it is significant. In addition, Figure 3-5 shows the map of the pressure ratio delivered by the WR (p_{04}/p_{03}) to give an idea about the contribution of the wave rotor in the overall pressure ratio. This map is represented by black solid lines.

A direct proportionality between T_5/T_3 and M_A is observed in all the studied cases shown in Figure 3-5, whilst T_{06}/T_{03} only display a similar behaviour in cases (b) and (c); T_{06}/T_{03} is almost constant in case (a) and behaves inversely proportional in case (d). The highest value of T_5/T_3 and T_{06}/T_{03} is obtained in case (b) and then in case (c) when M_A is equal to one. These conditions also achieve the maximum pressure ratio in the WR.

The main similarity between cases (b) and (c) lies in the fact that the overall pressure ratio is maintained equal to the baseline engine, thus an increase of the pressure ratio delivered by the wave rotor demands a reduction of the pressure ratio in the mechanical compressor (the compressor requires less work), so the temperature of the fluid that feeds the LPA port (T_3) becomes lower and T_5/T_3 higher.

Finally, it is noteworthy that each of the studied cases has a unique value of T_5/T_3 and T_{06}/T_{03} for each value of M_A. The observed behaviour is simple to model since it is almost linear or parabolic.

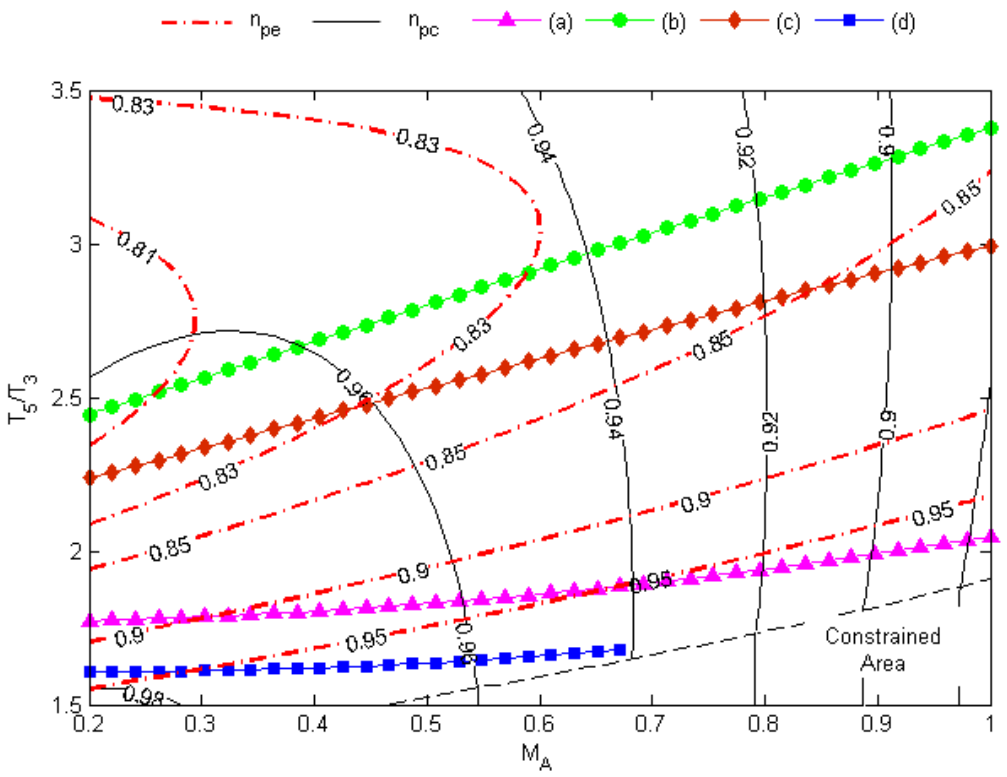

Figure 3-6 Map of wave rotor polytropic compression efficiency η_{p_c} and polytropic expansion efficiency η_{p_e} at different values of M_A and T_5/T_3; the states numbering is based on Figure 3-1

Figure 3-6 presents the maps of polytropic compression efficiency (η_{p_c}) between LPA and HPA ports, as well as the expansion polytropic efficiency (η_{p_e}) between HPG and LPG1 ports. The performance of studied cases indicates that an increase of M_A reduces η_{p_c}, up to a value that could be lower than the compression polytropic efficiency of the baseline turbine. This trend is a consequence of a compression process that is comprised by shock waves whose intensity grow when M_A increases; so the compression process is less reversible.

In contrast, Figure 3-6 shows that an increase of M_A causes an increase of η_{p_e}, which could be more than 9% lower than the efficiency achieved by the baseline turbine at low M_A values. This effect must be ascribed to a change in the strength of the third shock wave shown in Figure 1-1, since the irreversibility

produced by that shock wave only has an effect in the expansion process (fresh air does not cross the third shock wave during the compression process).

Figure 3-7 is included to clarify the behaviour described above through a T-s diagram of the compression and expansion processes in a gas turbine with a WR that follows case (c) with different injection Mach numbers (M_A). The fluid states in these diagrams follow the same numbering as in Figure 3-2.

Case (c) is selected from the other options since its cycle can be overlapped with that obtained from the baseline gas turbine to make comparison easier; both cycles have the same value of maximum and minimum pressure as well as the maximum temperature of burned gases.

The compression diagram (left side of Figure 3-7) shows a compression process inside the WR that gets closer to the isentropic trajectory if M_A is near to 0.2. This effect results in a lower temperature at the HPA port, regardless of whether this causes a greater participation of the mechanical compressor in the overall pressure ratio of the turbine, so the $\eta_{p_c}$is increased.

Moreover, the expansion diagram (right side of Figure 3-7) shows that at low M_A the stagnation pressure and temperature are higher at LPG1 port (state 6) but the entropy change (Δs_{6-5}) is also higher and therefore the irreversibility increases. This behaviour matches with the reduction of the expansion polytropic efficiency observed at low M_A.

Figure 3-8 displays the T-s diagram of the whole studied cycle when M_A is equal to 0.4 in which the fluid states follow the same numbering as in Figure 3-2. Case (d) is unable to expand the fluid to the ambient condition through nozzle 1, shown in Figure 3-2, because the compressor requires more work than is delivered by the turbine and therefore state (9d) does not appear. The behaviour is repeated during the evaluation of the whole range of M_A.

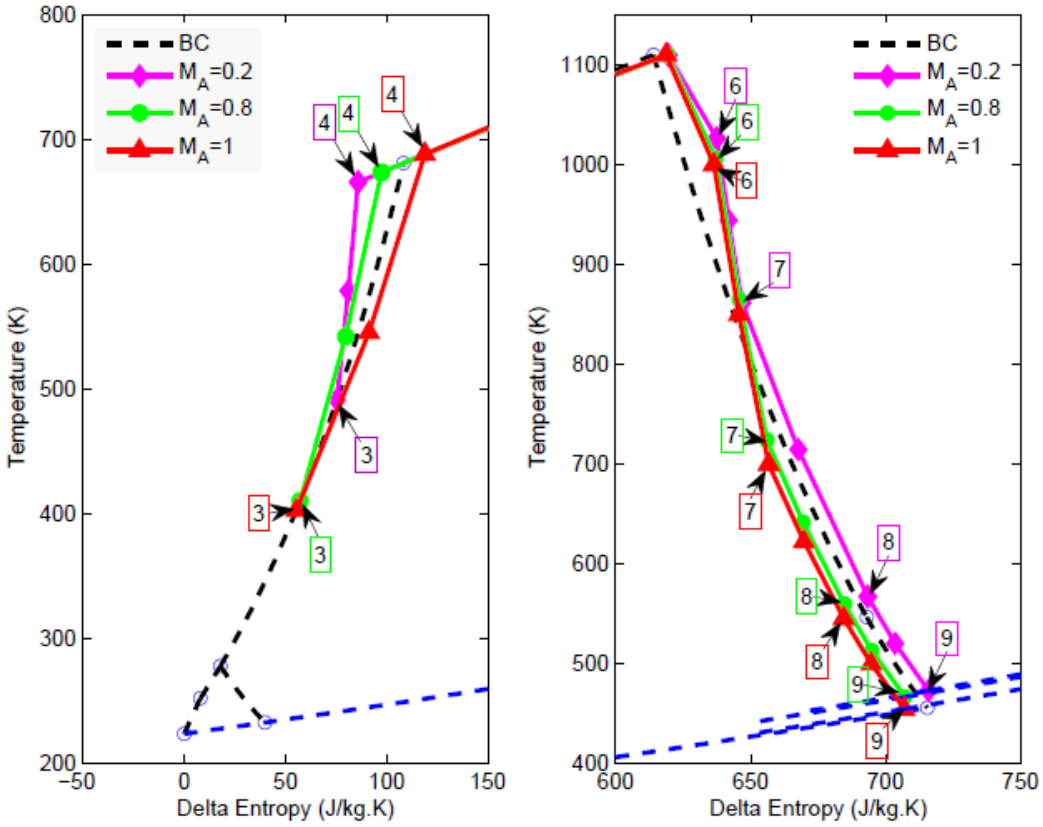

Figure 3-7 Effect of M_A in the compression and expansion process of the gas turbine (case ©); the states numbering is based on Figure 3-1

The situation described above is a consequence of an elevated bypass ratio that increases the work required by the fan, as well as an elevated global pressure ratio and a low value for the maximum cycle temperature, whose combination limits the injection of heat into the cycle. So, case (d) is discarded as an option for the propulsion of future aircraft.

The effect described above is also observed in case (a) since it has the same compressor pressure ratio. However, only a small expansion is possible through the nozzle 1 shown in Figure 3-2, because this case has a cycle with a higher maximum temperature than in case (d).

Figure 3-9, Figure 3-10 and Figure 3-11 show the η_e, F_s and SFC of cases (a), (b) and (c) at different values of M_A. Case (a) achieves higher values of η_e and SFC than the baseline engine if M_A is lower than 0.28 and 0.36 respectively.

However, F_s is kept lower throughout the range of M_A due to the small expansion through the nozzle 1 of Figure 3-2, as mentioned above.

Case (b) achieves the maximum F_s and η_e with a best performance attained when M_A is between 0.52 and 0.62, whilst case (c) offers a lower SFC than the baseline engine all over the range of M_A.

Despite case (a) offering the lowest SFC, this option is discarded for future aircraft gas turbines due to the following reasons:

- A low value of F_s demands an increase of the turbines size (increase on the turbine mass flow), to keep the same thrust of the baseline engine.
- The first contact wave will move at low velocity if M_A is near to 0.2 (maximum η_e and SFC), so the LPA port needs to be longer to drive the required airflow. This results in a larger and heavier wave rotor.
- η_e and SFC are sensitive to small changes of M_A, so the off-design operation is more complex.

Table 4 shows the conditions that bring the maximum F_s, maximum η_e and minimum SFC in cases (b) and (c), as well as the performance improvement in respect to the baseline engine; in this table BL represents the baseline gas turbine.

In general, both cases (b) and (c) perform better than the baseline turbofan. However, case (b) looks suitable for the propulsion of faster aircraft since it reaches the maximum values of η_e and F_s; turbine thrust increases when its η_e is above the η_e of the baseline engine and the fuel consumption is the same, whilst a higher value of F_s enables smaller engines to be designed which are able to reduce the drag of the aircraft.

Moreover, case (c) reaches the lowest fuel consumption, so it looks suitable for the reduction of emissions in future gas turbines.

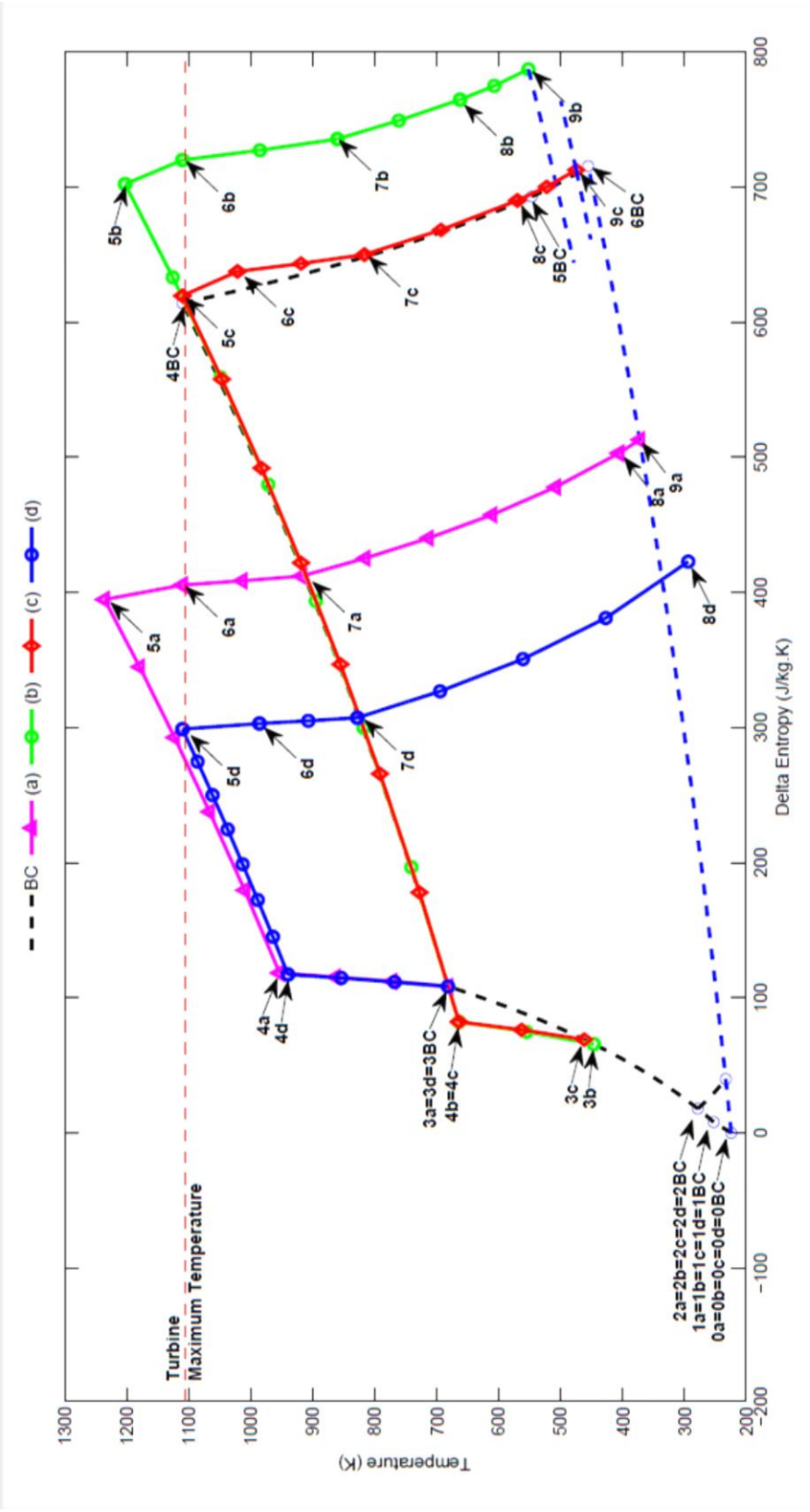

Figure 3-8 Representation of the baseline cycle and four different wave-rotor configurations in a T-s diagram; the states numbering is based on Figure 3-1

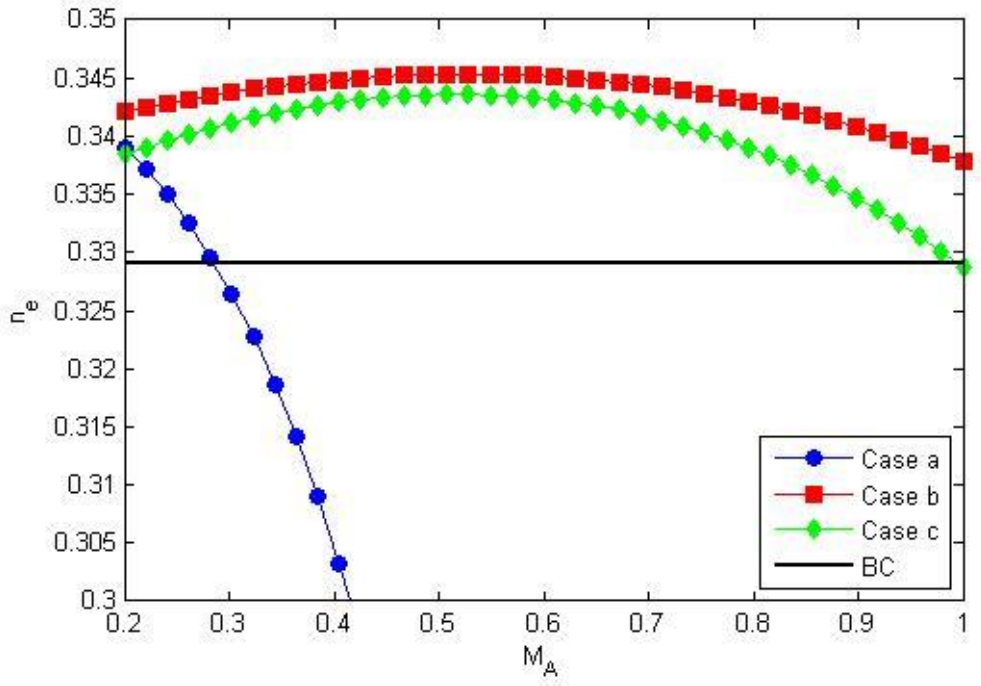

Figure 3-9 η_e of a gas turbine topped with a wave rotor operating at different values of M_A, in cases (a), (b) and (c)

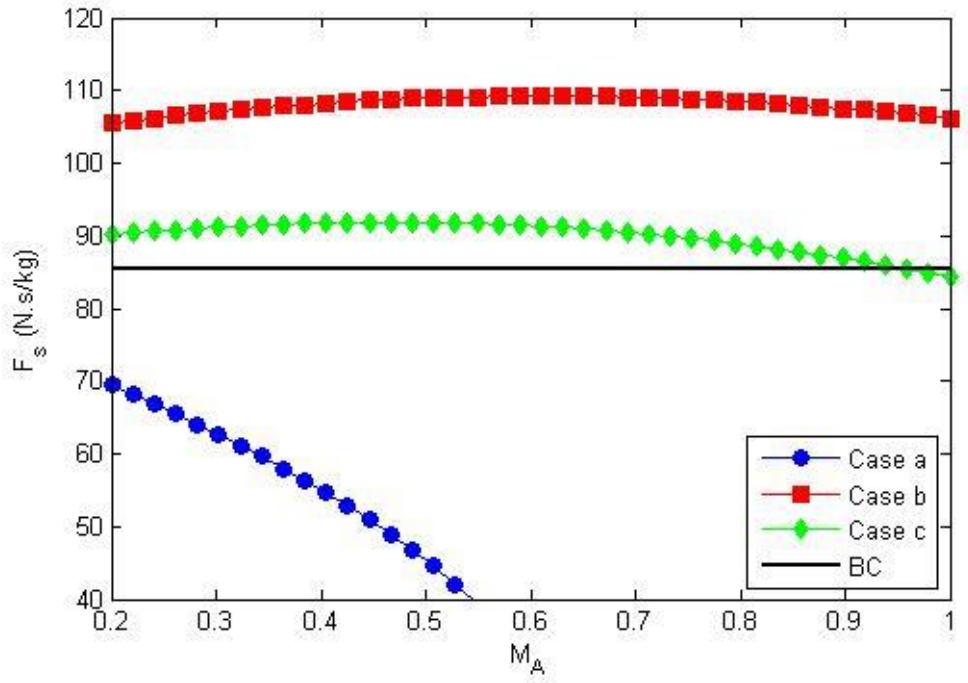

Figure 3-10 Specific thrust of a gas turbine topped with a wave rotor, operating at different values of M_A, in cases (a), (b) and (c)

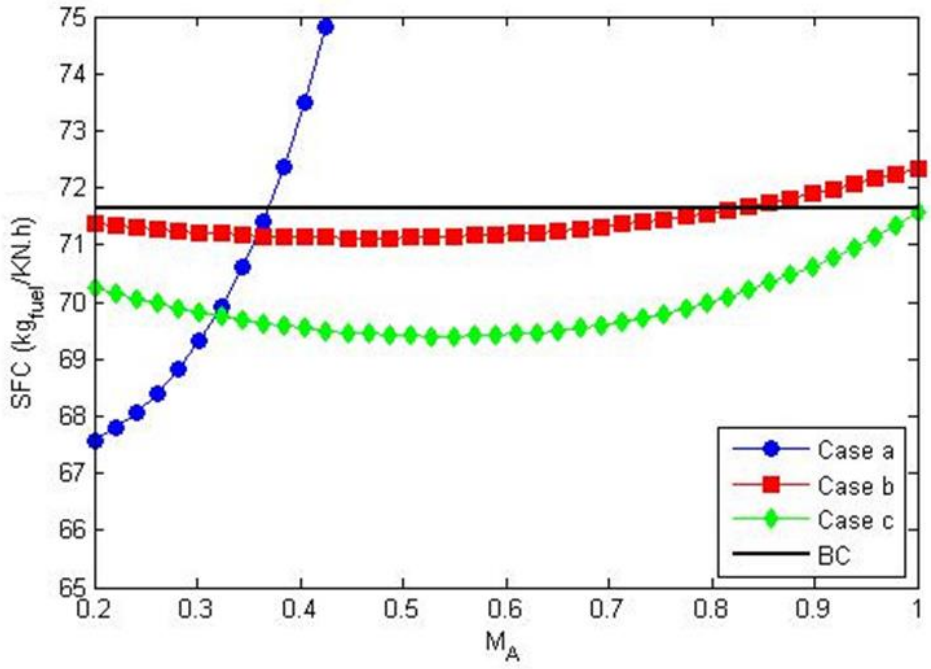

Figure 3-11 SFC of a gas turbine topped with a wave rotor, operating at different values of M_A, in cases (a), (b) and (c)

Weber stated that wave rotors with sloped blades (the angle β in Figure 3-4 is different than zero) are able to produce work. However, the cases studied displayed the opposite behaviour; Figure 3-12 indicates that the wave rotor in cases (b) and (c) require an input work for its operation; the minus sign represents an input work.

The high pressure gas turbine is able to deliver work to the wave rotor and to the compressor if M_A is higher than 0.55 in case b and 0.95 in case c, as illustrated in Figure 3-13. Otherwise, part of the necessary work must be taken from the low pressure gas turbine and therefore other options such as the splitting of the low pressure turbine into two separate turbines should be considered.

Table 4 Conditions that achieve the maximum efficiency of energy conversion, maximum specific thrust and minimum SFC, in a turbofan topped with a wave rotor, in cases (b) and (c)

CASE	M_A	η_e	$F_s\left(\frac{N.s}{kg}\right)$	$SFC\left(\frac{kg}{kN.h}\right)$	Maximum improvement respect to the BL(**)
	0.53	0.345(*)	109.1	71.17	0.0159
(b)	0.61	0.345	109.2(*)	71.2	23.74 (N.s/kg)
	0.46	0.345	108.8	71.12(*)	-0.53 (kg/kN.h)
	0.52	0.344(*)	91.81	69.405	0.0149
(c)	0.47	0.343	91.88(*)	69.44	6.42 (N.s/kg)
	0.53	0.344	91.74	69.4(*)	-2.21 (kg/kN.h)
BL	(N/A)	0.3291	85.46	71.65	(N/A)

$(*)$ *Minimum value of SFC and maximum value of F_s and η_e in cases (b) and (c)*
(**) Minimum value of SFC and maximum value of F_s and η_e minus their equivalents achieved by the baseline engine

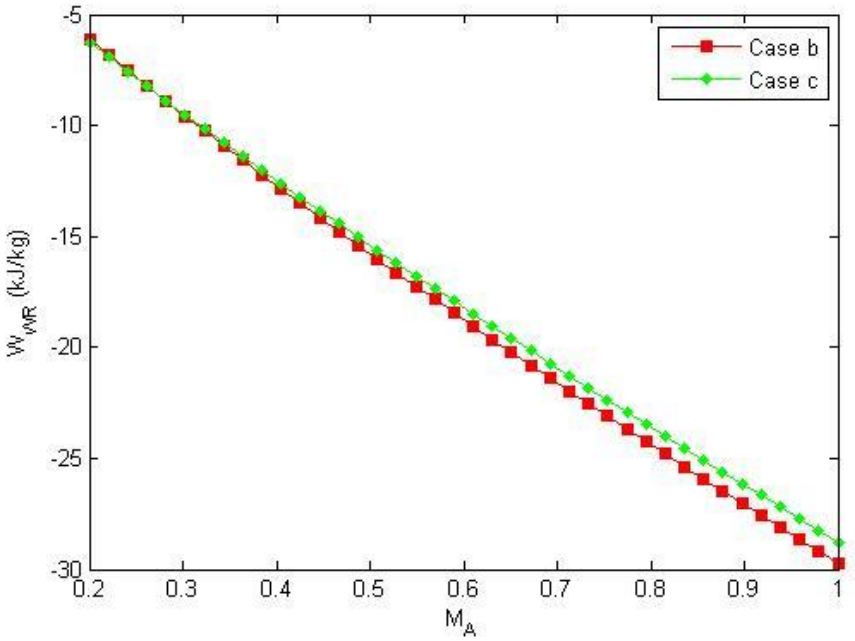

Figure 3-12 Work delivered by the wave rotor, in cases (b) and (c)

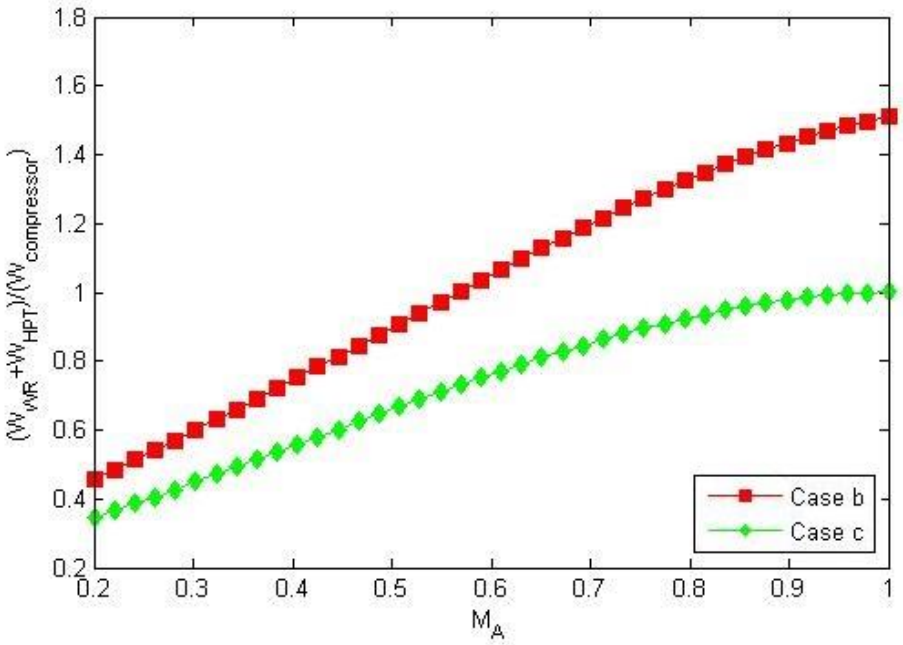

Figure 3-13 Ratio between the work delivered by the high pressure turbine and wave rotor by the work received by the compressor, in cases (b) and (c)

Table 5 shows the properties at the wave rotor's ports as well as the ports' angle predicted by the code in cases (b) and (c) for three different values of M_A; the evaluation points are set as the end values of the range in which M_A was changed ($M_A = 0.2$ and $M_A = 1$), as well as the Mach number that produced the minimum SFC (condition of low emissions). This information will be used during the wave rotor dimensioning.

3.6 Wave Rotor Dimensioning

The opening and closure of the wave rotor's ports are commonly linked with the arrival of some waves to the end plates during the transient process, as was explained in section 3.1. Therefore, Weber proposed the tracking of these waves by assuming a linear behaviour of their trajectory as a simplified technique to set the position of the ports (Weber 1995).

Table 5 Results provided by the developed program in cases (b) and (c) for different values of M_A

Parameters	Case (b)			Case (c)			units
PRESET VARIABLES							
M_A	0.2	0.46	1	0.2	0.53	1	$(--)$
β	-45	-45	-45	-45	-45	-45	$(^\circ)$
θ_{HPG}	0	0	0	0	0	0	$(^\circ)$
T_{HPG}/T_{LPA}	2.48	2.79	3.42	2.27	2.59	3.03	$(--)$
p_{HPA}/p_{LPA}	2.92	4.06	5.68	2.8	4.12	5.25	$(--)$
RESULTS							
$\dot{m}_{core}$	65.3	63.43	65	76.96	75.59	83.09	$(\mathrm{kg/sec})$
u_t	180.09	181.44	182.16	170.54	170.66	169.15	(m/sec)
ρ_A	2.08	1.64	1.07	2.16	1.61	1.12	(kg/m^3)
u_A	87.45	190.01	376.89	88.14	218.37	380.98	(m/sec)
$T_{0,LPA}{}^{*}$	479.67	444.5	424.23	487.18	446.21	433.49	(K)
$p_{0,LPA}{}^{*}$	292.7	232.5	205.1	307.7	236.1	219.2	(kPa)
$T_{0,HPG}{}^{*}$	1194.49	1204.98	1225.79	1109.99	1109.99	1109.99	(K)
$p_{0,HPG}{}^{*}$	860.5	859.7	860.9	864.6	864.5	866.3	(kPa)
$T_{0,LPA}{}^{**}$	484.73	436.62	392.42	491.08	434.47	402.36	(K)
$p_{0,LPA}{}^{**}$	303.7	218.5	156.1	316.4	215.1	168.9	(kPa)
$T_{0,HPG}{}^{**}$	1194.49	1204.99	1225.79	1110	1110	1110	(K)
$p_{0,HPG}{}^{**}$	821.0	820.0	821.5	826.3	826.1	828.5	(kPa)
T_{HPA}	652.59	649.65	674.07	653.75	651.82	676.22	(K)
p_{HPA}	824.0	822.8	824.6	830.7	830.5	833.5	(kPa)
T_{LPG1}	1096.9	1094.05	1090.13	1016.47	1003.39	987.22	(K)
p_{LPG1}	572.4	549.6	511.9	570.4	545.0	516.8	(kPa)
T_{LPG2}	898.44	821.13	699.48	845.35	748.1	643.91	(K)
p_{LPG2}	284.7	201.3	108.3	299.2	195.0	115.8	(kPa)
θ_{LPA}	62.39	19.31	-17.56	60.06	6.01	-20.41	$(^\circ)$
θ_{HPA}	5.07	5.02	5.09	5.35	5.34	5.47	$(^\circ)$
θ_{LPG1}	6.73	0.79	-4.86	13.94	6.96	3.66	$(^\circ)$
θ_{LPG2}	62.39	19.31	-17.56	60.06	6.01	-20.41	$(^\circ)$

Note: angles are given according to the first quadrant of the coordinate plane (*) means property relative to the rotor (**) means property relative to the stator, subscripts LPA, HPA, HPG, LPG1 and LPG2 are implemented to identify the ports of the wave rotor (see Figure 3-1*), subscript 0 indicates stagnation properties*

Weber's approach is based on the fact that during the transient phenomenon, the fluid's states inside the wave rotor are a consequence only of the participant waves. Therefore, correlations are required to estimate the nonlinear trajectory of the waves given by distinct variables, such as the non-instantaneous opening and closure of the channels' ends, the reduction of the flow velocity given by the closed ends, the acceleration experienced by the fluid when the ends of the channels are opened, amongst others.

Some of the variables' effects described above can be predicted by 1D CFD models to avoid implementing correlations. In addition, 1D-CFD models only require the setting of the channels' length as an input parameter to define the domain geometry and therefore the computational effort is lower than 2D or 3D models (see Section 2.8).

A 1D CFD code is developed in this work to predict the dimensions of a wave rotor. The proposed code implements the SIMPLE algorithm to solve the Euler equations of mass, momentum and energy (inviscid conservation equations), a topic that will be addressed later on.

The form of the Euler conservation equations is presented in Eq. (3-7), where the first left-term models the transient behaviour, the second left-term models the transport of ϕ due to flux, and the right term is the source term to include any other factors such as the surface and/or body forces in the momentum equation.

$$\frac{\partial \phi}{\partial t} + \frac{\partial \rho u \phi}{\partial x} = S_c \qquad \textbf{(3-7)}$$

Equation (3-8) is the discretised form of the conservation equations that results from integrating Eq. (3-7) in each cell of a discretised control volume, such as that observed in Figure 3-14. The coefficients a_p and a_{nb} give the relationships between the scalar value at node p (ϕ_p) and at neighbouring nodes (ϕ_{nb}) due to transient and convection terms.

$$a_P \phi_P = \sum a_{nb} \phi_{nb} + S_c \quad \textbf{(3-8)}$$

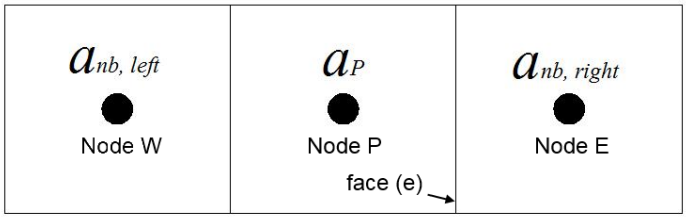

Figure 3-14 Representation of a 1D discretization that shows the nodes considered on Eq. (3-8)

The SIMPLE algorithm was initially developed to simulate incompressible flow by means of a pressure correction equation obtained from manipulating the mass conservation equation and the equation of state (Versteeg & Malalasekera 2007). However, Karki and Patankar (1989) incorporated a hyperbolic term into the mass conservation equation to make the modelling of problems that involve compressible flow possible.

Equation (3-9) represents the flux per unit of mass that crosses the east face of a cell and its value is part of the convection term of the mass conservation equation. The new hyperbolic term is represented by the third term at its right.

Superscript (^{o}) in Eq. (3-9) is used to represent the values obtained during the previous iteration, d_e is a term that comes from manipulating the momentum equations and superscript (') is used to identify the pressure correction. Moreover, subscripts P and E denote central and east nodes whilst subscript e denotes the east face of a cell as indicated in Figure 3-14, see (Versteeg & Malalasekera 2007).

$$F_e = (\rho u)_e = (\rho u)_e{}^{o} + \rho_e{}^{o} d_e (p_P' - p_E') + u_e{}^{o} K_P p_P' \quad \textbf{(3-9)}$$

In the hyperbolic term, Kp represents the change of density in respect to the fluid pressure, so it is a function of the process trajectory; Kp is inversely proportional to the speed of sound when the trajectory is assumed isentropic, see Eq. (3-10) (Karki & Patankar 1989).

$$K_P = \left(\frac{\partial \rho}{\partial p}\right)_s = \frac{1}{a} \quad \textbf{(3-10)}$$

The trajectory selected to model Kp does not affect the final result because the pressure correction approaches zero once the iterative process converges into the expected solution.

The momentum equation is computed in a staggered mesh to avoid the interpolation of the pressure field, the convective term is estimated by implementing UMIST (high order TVD scheme) through a deferred correction technique (Versteeg & Malalasekera 2007), and the transient phenomenon is modelled by implementing a full implicit scheme that offers a stable iterative process regardless of the values of the Péclet number.

Finally, the transient solution is achieved by incorporating the external loop that is shown in Figure 3-15. A comprehensive description of this alternative is given by Versteeg and Malalasekera (2007).

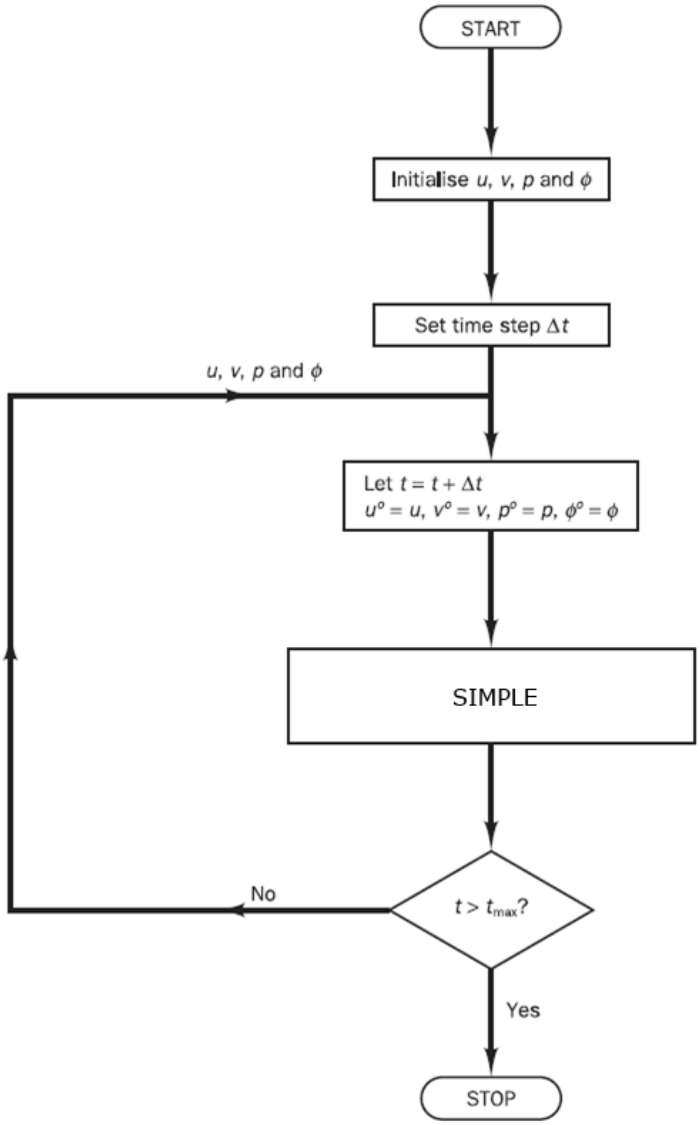

Figure 3-15 Transient flow algorithm (Versteeg & Malalasekera 2007)

3.6.1 Boundary conditions

The simulation of the transient phenomenon inside the wave rotor requires defining three types of boundary, as follows: "*Wall"* to model the closure of the channels' ends, *"Stagnation properties at the inlet"* to model ports LPA and HPG (see figure 2), and "*Static properties at the outlet"* to model ports HPA, LPG1 and LPG2.

This section briefly presents how the Euler equations must be closed to establish the desired boundary conditions, either by setting a Dirichlet boundary

condition (prescribed scalar value) or a Neumann boundary condition (prescribed derivative) and the strategies followed to solve these equations with SIMPLE, as appropriate. A further discussion of each case is presented by Versteeg and Malalasekera (2007) and Ferziger and Perić (1997).

It is important to note that when an equation is constrained by the Neumann boundary condition (it has fixed the value of the scalar derivative) the scalar value at the edge is not obtained directly from the solution of the system of equations, and therefore an extrapolation function is required to estimate it. A simple and accurate alternative is the selection of a second order polynomial fitted to the values of the two neighbouring nodes and to the pre-set value of the derivative at the boundary.

3.6.1.1 Wall boundary condition

To set the wall boundary condition the Dirichlet boundary condition is implemented in the momentum equation with a velocity value equal to 0, and the Neumann boundary condition is used in the energy equation and the pressure correction equation assuming a derivative value equal to zero.

3.6.1.2 Stagnation pressure and temperature at the inlet

Stagnation properties at the inlet are associated with the static properties by means of Eq. (3-11) and Eq. (3-12); which result from the one-dimensional analysis of compressible flow (Ferziger & Perić 1997).

$$p_0 = p\left(1 + \frac{k-1}{2}\frac{u^2}{kRT}\right)^{\frac{k}{k-1}} \quad \textbf{(3-11)}$$

The momentum equation is solved by imposing the Dirichlet boundary condition and the velocity value is obtained by assuming static pressure at the inlet through Eq. (3-11). Then, during the iterative process this velocity is modified by extrapolating the pressure correction and the velocity correction at this edge.

$$T_0 = T\left(1 + \frac{k-1}{2}\frac{u^2}{kRT}\right) = \left(\frac{\partial \rho}{\partial p}\right)_s = \frac{1}{a} \quad \textbf{(3-12)}$$

The Dirichlet boundary condition is also implemented to solve the pressure correction equation and the energy equation. The pressure correction value is set to zero at the boundary and the temperature is computed by applying Eq. (3-12).

Once the pressure-correction is obtained it is possible to modify the static pressure set at the beginning of the simulation by implementing a linear extrapolation fitted to the pressure corrections obtained at the neighbouring nodes. The value of the pressure correction at the edge is also used to compute the velocity correction at the boundary node through Eq. (3-13).

$$u' = \left(\frac{\partial u}{\partial p}\right)_b p_b' = C_u p_b' \tag{3-13}$$

Cu is computed by using Eq. (3-14) that results from the manipulation of Eq. (3-11), and in which subscript b indicates “node at the edge” and subscript nb indicates “neighbouring node”.

$$C_u = -\frac{kRT_b}{p_{0,b} u_{nb} k \left(1 + \frac{k-1}{2}\frac{{u_{nb}}^2}{kRT_b}\right)^{\frac{1-2k}{k-1}}} \tag{3-14}$$

Once the pressure is corrected at the boundary and before the energy equation is solved, the temperature and density must be updated by implementing the isentropic flow equations and the equation of state.

3.6.1.3 Static pressure at the outlet

This new condition indicates that the pressure correction at the outlet is zero, but the speed should be obtained by extrapolating its value from the neighbouring nodes following an idea similar to the collocated grids (Demirdžić & Lilek 1993). The process is performed through Eq. (3-15), where A is the cells transversal area, $a_{P,m}$ is a coefficient of the momentum equation in the node P and p_{nb}' is the pressure correction at the neighbouring node.

$$u_b' = -2\left(\frac{A}{a_{P,m}}\right)_{nb} p_{nb}' \tag{3-15}$$

The energy equation is solved by using a Dirichlet boundary condition where the temperature value at the outlet is extrapolated from the neighbour nodes. To simplify the CFD code, the edge's temperature is set equal to the temperature of the upstream node (upwind scheme).

3.6.2 Additional Considerations

The CFD program requires knowing details of the channels' length in advance to define the computational domain, as well as having a procedure to switch the boundary conditions opportunely to reproduce the transient process experienced by the fluid. Therefore in the following subsection a discussion of each one of these topics is presented.

3.6.2.1 Channels Length

To keep the design of the wave rotor simple this work only considers devices with one cycle per revolution, therefore the mass flow required by the turbine is equal to the mass flow that crosses LPA port and can be computed by Eq. (3-16), which assumes that the LPA port always presents a uniform state (Weber 1995; Weber 1992). In this equation, trigonometric operators are used to compute the velocity in the axial direction, as is shown in Figure 3-16 and Eq. (3-16).

$$\dot{m}_{LPA} = \rho_A u_A \cos(\beta) h Y_{LPA} \quad \textbf{(3-16)}$$

The channel length is also equal to the tangential velocity at the pitch line (u_t) times the time in which a channel is in contact with LPA port Δt_{LPA}, see Eq. (3-17).

$$Y_{LPA} = u_t \Delta t_{LPA} \quad \textbf{(3-17)}$$

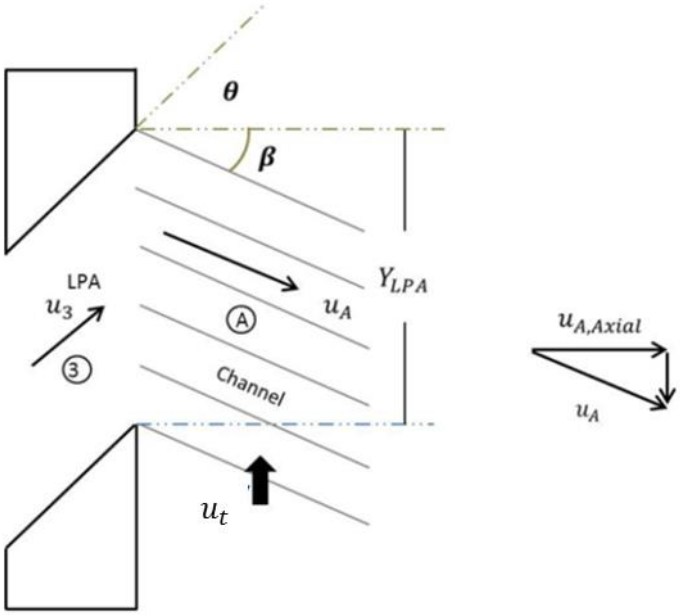

Figure 3-16 Scheme of the LPA port

Because Δt_{LPA} is also equal to the time required by the first contact wave to reach the right channel's end plus the time required by the first shock wave to reach the left channel's end (see Figure 3-1), then it is possible to represent Y_{LPA} by means of Eq. (3-18).

$$Y_{LPA} = u_t \left(\frac{L}{\bar{u}_A} + \frac{L}{\bar{u}_{SW}} \right) \tag{3-18}$$

The substitution of Eq. (3-18) into Eq. (3-16) followed by its manipulation leads to Eq. (3-19).

$$\dot{m}_{LPA} = \rho_A \cos(\beta) h u_t L \left(1 + \frac{1}{\frac{M_{x,A}}{M_A} - 1} \right) \tag{3-19}$$

The channel length is computed from Eq. (3-19) once the value of h is set; the other variables are given in section 3.5.

3.6.2.2 Mass handled by the wave rotor's channels

During the transient process the air and gases that interact with the device are kept separate by means of contact waves. These contact waves are generated

once LPA and HPG ports are opened and their arrival to the channels' right end indicates the closure of LPG2 and HPA ports (see Figure 3-1).

Based on the previous statement, as well as the fact that the mass is a conservative quantity, it follows that the mass entering through LPA port must be equal to the mass exiting HPA port, and the mass entering through HPG port must be equal to the mass exiting LPG1 port plus the mass exiting LPG2 port.

In addition, because in gas turbines the amount of fuel injected in the combustion chamber is negligible in comparison with the mass flow of air, then the mass flow of air that crosses LPA port must be approximately the same as the mass flow of burned gases that crosses HPG port to reach the dynamic equilibrium in the device.

On the basis of the mass conservation the wave rotor dimensioning can be achieved by monitoring the mass flow that crosses the device's ports, which must match with the mass flow given by the thermal analysis presented at the beginning of this chapter. However, when a one-dimensional model is performed the mass flow by itself is not useful because the ports' transversal area is not known in advance.

To solve the problem this work considers a new parameter that computes the ratio between the mass entering through each channel when it crosses the device's ports during a cycle and the channel width; in the case of LPA port this new parameter is obtained by implementing Eq. (3-20).

$$\frac{m_{CH-LPA}}{s} = \rho_A \cos(\beta) u_A h \Delta t_{LPA} \tag{3-20}$$

In order to express Eq. (3-20) as a function of the same variables as Eq. (3-19), Δt_{LPA} is then substituted by the ratio given in Eq. (3-16) followed by Eq. (3-18). Now by rearranging, Eq. (3-21) is obtained.

$$\frac{m_{CH-LPA}}{s} = \rho_A \cos(\beta) Lh \left(1 + \frac{1}{\frac{M_{x,A}}{M_A} - 1} \right) \tag{3-21}$$

By comparing Eq. (3-16) with Eq. (3-21), it is easy to notice that $\dot{m}_{LPA}$ and m_{CH-LPA}/s are linked only by u_t (see Eq. (3-22)), which is constant because the wave rotor operates in a stable condition.

$$\dot{m}_{LPA} = \frac{m_{CH-LPA}}{s} u_t \tag{3-22}$$

The advantages of this formulation is that Eq. (3-8) also has a discrete shape defined by Eq (3-23), in which n represents the number of time steps calculated. This equation can be implemented by a 1D CFD code and the accumulated value can be used as a criterion to close the LPA port once Eq. (3-22) is satisfied.

$$\frac{m_{CH-LPA}}{s} = \cos(\beta) h \sum_{i=1}^{n} \rho_{A,i} u_{A,i} \Delta t_{step} \tag{3-23}$$

The previous analysis is done in each port of the wave rotor by using the mass flow that crosses the LPA port as constrainer.

3.6.2.3 Boundary conditions interaction

To start the simulation, a channel located at the bottom of the scheme shown in Figure 3-1 was selected (origin of the cycle). At this condition the channel's ends are open, one in contact with LPA port and the other with LPG2 port, therefore the model is set by fixing the boundary conditions: *"stagnation properties"* at the left side and *"static properties"* at the right side.

Once the program starts, an additional transport equation is solved to track the contact waves generated during the cycle, the resultant scalar value is normalised, using 1 to represent air and 0 to represent burned gases. In addition, the accumulated value of Eq. (3-23) is computed in each port of the device during the channel's trajectory through the cycle. The results obtained from these procedures are then used as a guide to close the device's ports opportunely as well as to set the cycle end; both aspects will be discussed later.

Since the procedure developed in this work is derived from the Weber's algorithm, there is no criterion to quantify the distance between the LPA port

closing and HPG port opening or between the HPA port closure and the LPG2 port opening. The channels located in these areas contain a homogeneous fluid which results from the previous attenuation of the shock waves after colliding with rarefaction waves, as well as the purge of burned gases or air carried out by LPG2 and HPA ports, see Figure 3-1. So, once LPA or HPA are closed the working fluid is ready to interact with the following port.

However, short distances between these ports can produce the leakage of fluid from one port to the other due to the difference of pressure, whilst long distances can make the pitch line diameter of the device impractical. In this analysis the distance is fixed as equal to the width of three channels (this criterion ensures that during the transient process at least two channels will be completely closed) to isolate the ports.

Equation (3 24) is implemented to convert the selected distance into the number of time steps executed by the CFD code to change the boundary conditions. The opening of the LPG2 port is also defined by the same criterion.

$$NDt = \frac{3.s}{\Delta t_{step}.u_t} \quad \textbf{(3-24)}$$

The objective now is to define the times to change the boundary conditions from the starting point of the cycle; therefore the following procedure is implemented:

- LPG2 port is closed once the passive scalar reports a value of 1 in the neighbour node.
- LPA port is closed upon either of the following design criteria. Firstly the accumulated value of m_{CH-LPA}/s is equal to $\dot{m}_{LPA}/u_t$, the latter computed from the results presented in section 3.5. Secondly, when the velocity at this end is opposite to the flow entering through LPA port, to prevent the compressor being affected by the first shock wave; in this case the value of m_{CH-LPA}/s is changed by the accumulated value given by Eq. (3-23)
- HPA port is opened once the second shock wave reaches the right side; a condition in which the neighbour node reports a sharp increase of the static pressure.

- HPA and HPG ports are closed once the accumulated value of m_{CH-HPA}/s and m_{CH-HPG}/s are equal to $\dot{m}_{LPA}/u_t$.
- LPG1 port is opened NDt time steps after LPA port is closed.
- LPG1 port is closed and LPG2 port is opened once the flow velocity in the boundary reaches a negative value to avoid backflow in LPG1 port.

The cycle ends once the accumulated value of $m_{CH-LPG1}/s + m_{CH-LPG2}/s$ is equal to $\dot{m}_{LPA}/u_t$.

Since the initial conditions implemented in the model are assumed, it is important to solve at least four cycles to achieve the dynamic equilibrium. At the end of the run the ports location and their dimensions are obtained and therefore the preliminary design process concludes.

3.6.2.4 Transformation of the coordinate system

The 1D-CFD code stores its results by using time and cell position through the channel as a coordinate system; therefore the system of reference needs to be converted into a new one able to include the angle of the blades to get the dimensioning of the device.

The proposed axes of the new system of references are the cell's position in the pitch line perimeter and the cell's position in the wave-rotor axial direction; both axes are computed through Eq. (3-25) and Eq. (3-26) in each node of the computational domain. β and u_t are parameters previously defined.

$$l_x = l * \sin(\beta) \quad \textbf{(3-25)}$$

$$l_y = t * u_t - l_x \quad \textbf{(3-26)}$$

3.6.3 1D CFD code validation (compressible flow)

The validation of the 1D-CFD code is performed by modelling a shock tube experiment cited by (Shapiro 1954), see Figure 3-17. The shock tube has a length of 80 inches and it is split by a diaphragm into two sections, one section contains the driver fluid (32 in) and the other section contains the driven fluid

(48 in). The whole tube is filled with air at 293.11K (speed of sound equal to 1126 ft./sec.), but the driver section has an initial absolute pressure of 1 atm and the driven section has an initial absolute pressure of 2 atm.

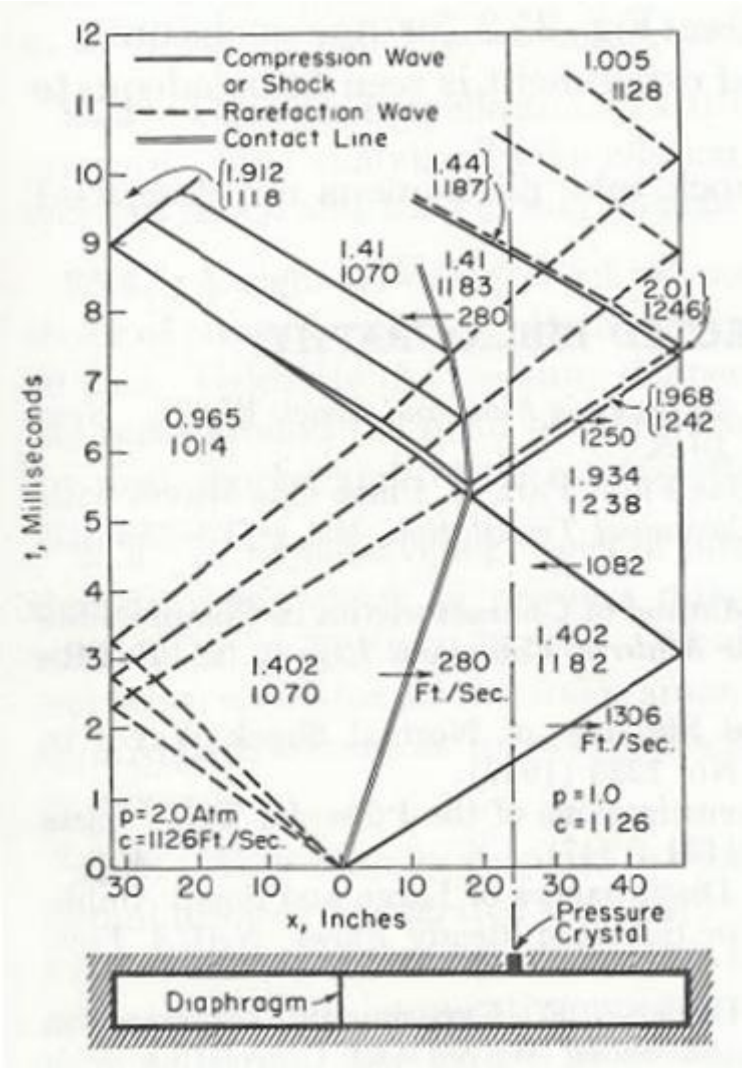

Figure 3-17 Shock tube - experimental results (Shapiro 1954)

3.6.3.1 Shock tube simulation

The CFD simulation is performed with three different resolutions of the mesh and three different time steps, in order to quantify the false diffusion effect. The mesh resolutions implemented are 80 cells per meter, 160 cells per meter and 320 cells per meter, whilst the implemented time steps are 18e-6 sec, 9e-6 sec and 4.5e-6 sec.

The shock wave is the fastest wave inside the shock tube during the transient process and its velocity is equal to 383 m/s (estimated from Figure 3-17). Therefore, the Courant number computed from Eq. (3-27) changes between 0.276 and 1.10 during the sensitivity analysis.

$$\text{Courant Number} = \frac{Velocity\ of\ the\ Shock\ Wave}{\frac{mesh\ resolution}{time\ step}} \quad \textbf{(3-27)}$$

Figure 3-18 and Figure 3-19 show the pressure history predicted by the 1D-CFD code at 22 inches from the diaphragm in the driven zone for different mesh resolution and time steps. Frame (a) of these figures presents the pressure history whilst Frames (b) and (c) are a closer view of the first two jump discontinuities captured by the simulation.

The CFD code is able to track the shock waves inside the shock tube with a reasonable level of accuracy when the mesh density is over 160 cells per meter. A mesh density of 80 cells per meter is not appropriate since the position of the first shock wave is predicted with a small delay (see Figure 3-18(b)).

The false diffusion effect is not dissipated when the mesh density is changed during the analysis (see Figure 3-18). This behaviour could be a consequence of the implementation of high order resolution schemes through the deferred correction technique (see Section 3.6), as well as the implementation of a Cartesian grid (main characteristic of one-dimensional domains).

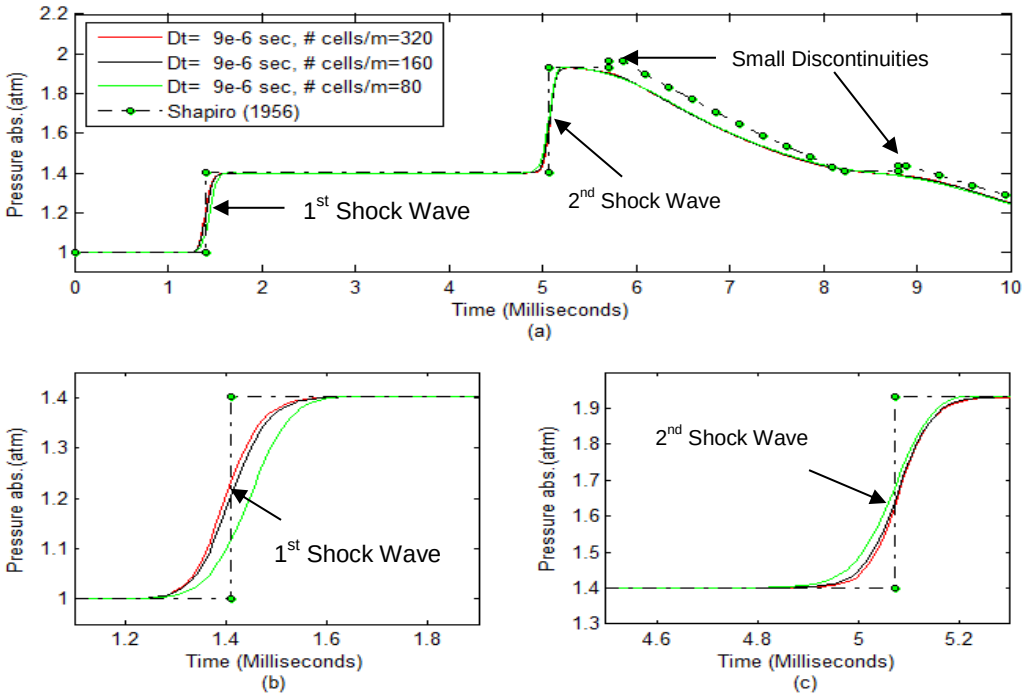

Figure 3-18 Pressure history at the centre of the driven tube (24 inches from the diaphragm at its left), predicted by the CFD code for different mesh resolutions

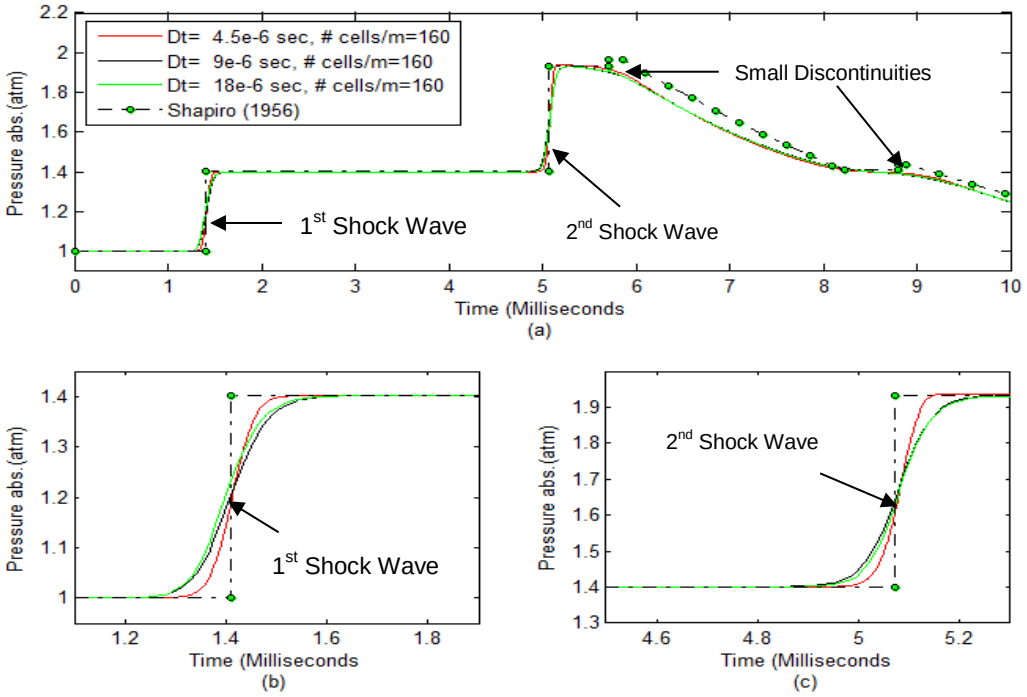

Figure 3-19 Pressure history at the centre of the driven tube (24 inches from the diaphragm at its left) predicted by the CFD code for different time steps

In contrast, the CFD simulation is enhanced when the time step is reduced (see Figure 3-19) because the false diffusion effect is dissipated. This result shows that the major source of false diffusion generated by the CFD code is inherent to the implicit interpolation scheme implemented during the time integration.

The CFD code is unable to capture some small jump discontinuities observed in the experiment during the sensitivity analysis. This result is expected since small discontinuities are strongly affected by false diffusion (see Figure 3-18 and Figure 3-19).

Figure 3-20 and Figure 3-21 present the level of accuracy of the CFD code for different mesh resolutions and time steps. Frame (a) displays the error of the pressure history predicted by the code relative to the experimental results while Frame (b) displays the relative difference of the pressure history in respect to the maximum resolution of the mesh and minimum time step implemented during the analysis.

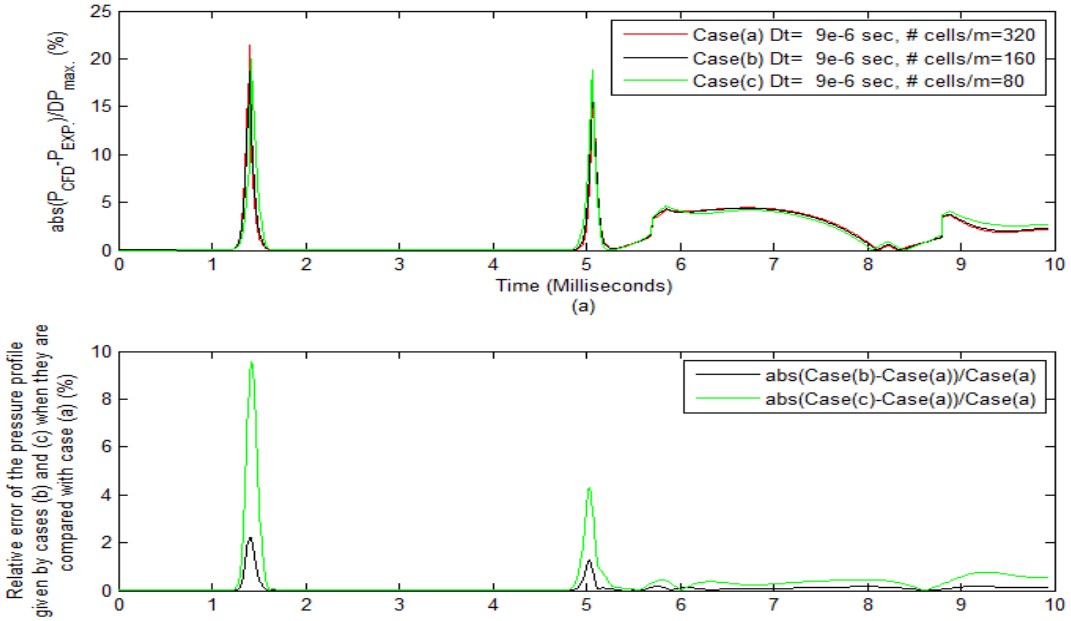

Figure 3-20 Frame(a) absolute error of the pressure profile at 22 inches from the diaphragm in the driven zone, achieved by different mesh resolutions, Frame (b) relative error of cases (b) and (c) when compared with case (a)

The maximum errors of the CFD code are observed over the shock waves such as peaks whose width and height are reduced when the time step is decreased, see Figure 3-21 (a).

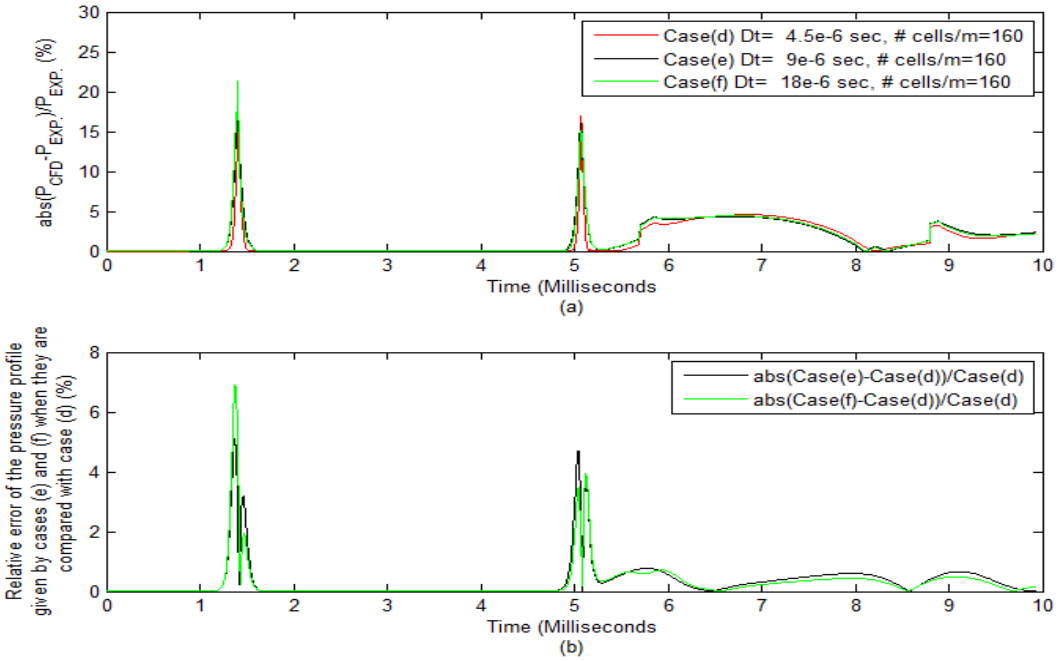

Figure 3-21 Frame(a) absolute error of the pressure profile at 22 inches from the diaphragm in the driven zone, achieved by different time steps, Frame (b) relative error of cases (b) and (c) when compared with case (a)

The absolute error reaches a maximum value near but less than 25 %, since the sharp shape of the shock wave is modelled by a smooth curve. However, the fluid's state after the compression is accurately estimated, so the error drops near to zero once the compression occurs.

Frame (b) in Figure 3-20 and Figure 3-21 indicates that a cell resolution of 160 cells per meter and a time step of 9e-6 seconds are able to obtain relative differences under 2.2 % and 5.1%, whilst a discretisation of 80 cells per meter and a time step of 18e-6 second reported a difference under 9.6% and 6.9% respectively.

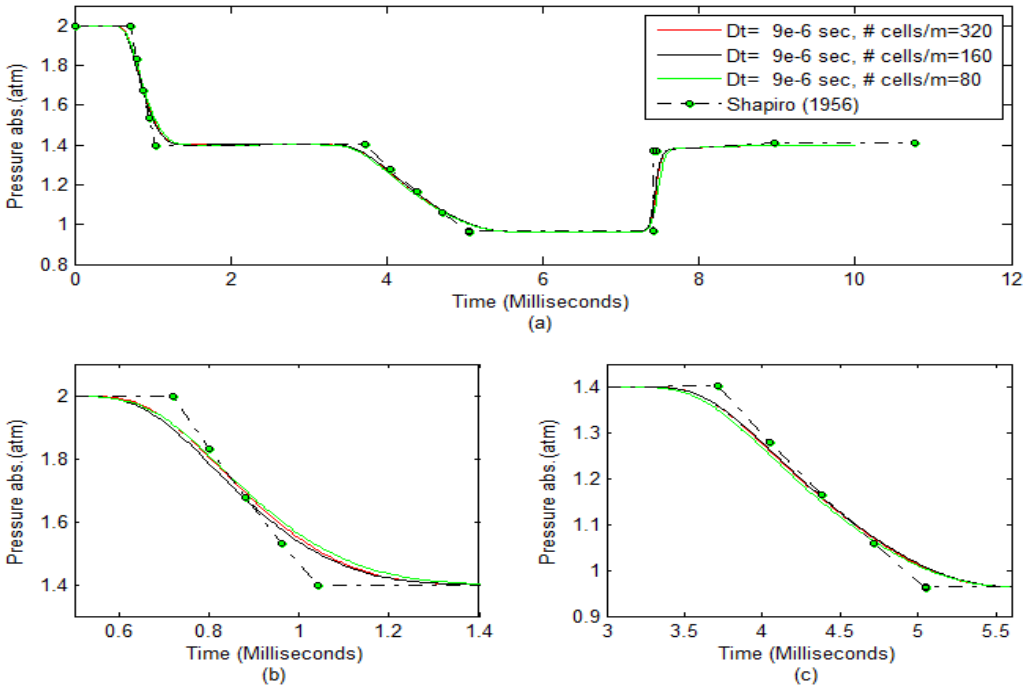

Figure 3-22 Pressure history at 10 inches of the diaphragm in the driver zone, predicted by the CFD code for different mesh resolutions

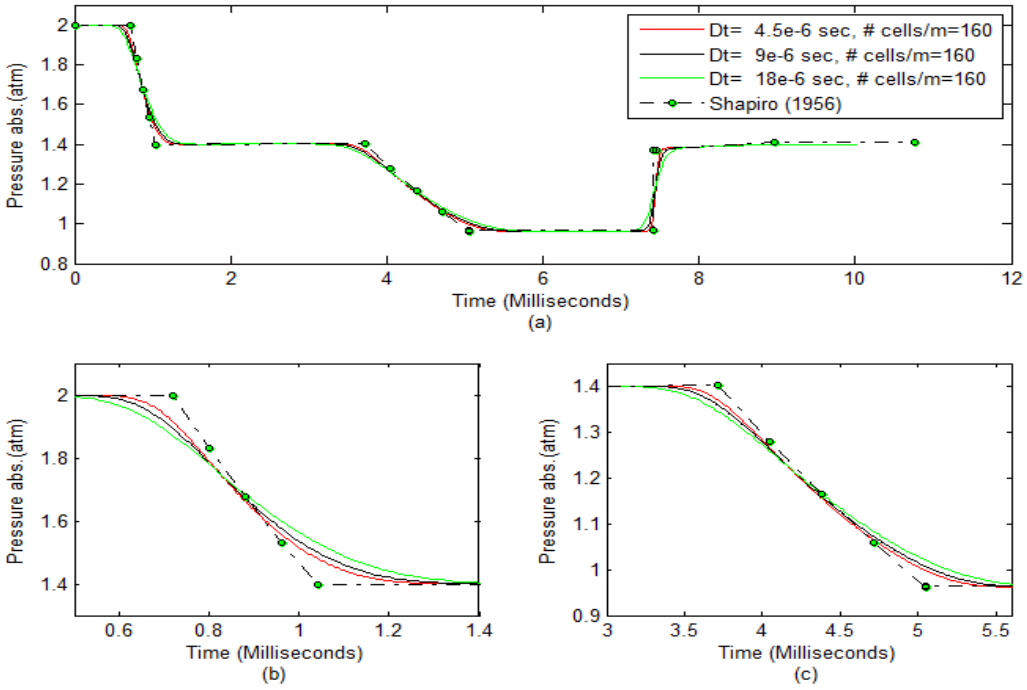

Figure 3-23 Pressure history at 10 inches of the diaphragm in the driver zone, predicted by the CFD code for different time steps

Frame (a) in Figure 3-22 and Figure 3-23 shows the pressure history predicted at 10 inches from the diaphragm in the driver zone while Frames (b) and (c) show the expansion processes in detail.

The CFD code is able to reproduce the expected process when the driver zone is modelled. However, the false diffusion effect also affects the shape of the expansion waves since the pressure profile is smoother than in the experiment.

The mesh density does not have a significant influence in the reduction of false diffusion as indicate Figure 3-22 but the time step reduction improves the pressure profile predicted by the model, such as in the driven zone (see Figure 3-23).

Figure 3-24 and Figure 3-25 are included in this section to quantify the level of error achieved by the CFD simulation of the driver zone. Frame (a) displays the error of the model prediction in respect to the experimental results and Frame (b) displays the relative error of the model prediction in respect to the denser mesh and the shorter time step implemented during the analysis.

The absolute error reaches a maximum value near but under 29 % as a consequence of the shock wave arrival to the driver zone, this error has a peak shape that behaves in the same way as the peaks observed in the driven zone at different mesh densities and time steps. Nevertheless, the fluid state after the compression reaches the values reported by the experiment with a good level of accuracy (see Figure 3-24(b)).

Frame (b) in Figure 3-24 and Figure 3-25 indicates that a resolution of the mesh of 160 cells per meter and a time step of 9e-6 seconds are able to achieve relative differences under 2.26 % and 5.5%, whilst a resolution of the mesh of 80 cells per meter and a time step of 18e-6 second reported a difference under 6.29% and 11.15% respectively.

Base on the obtained results, a mesh density of 160 cells per meter and a time step of 9e-6 seconds were selected to perform the simulation. Since they offer a relative difference under 2 % in average in respect to the densest mesh and the shortest time step, the highest errors are near to 5% and they only occur when

the shock wave compresses the fluid (short period of time) but the properties after the compression process are in a good agreement with the experiments. Finally, these parameters keep a reasonable computational effort of the 1D-CFD code.

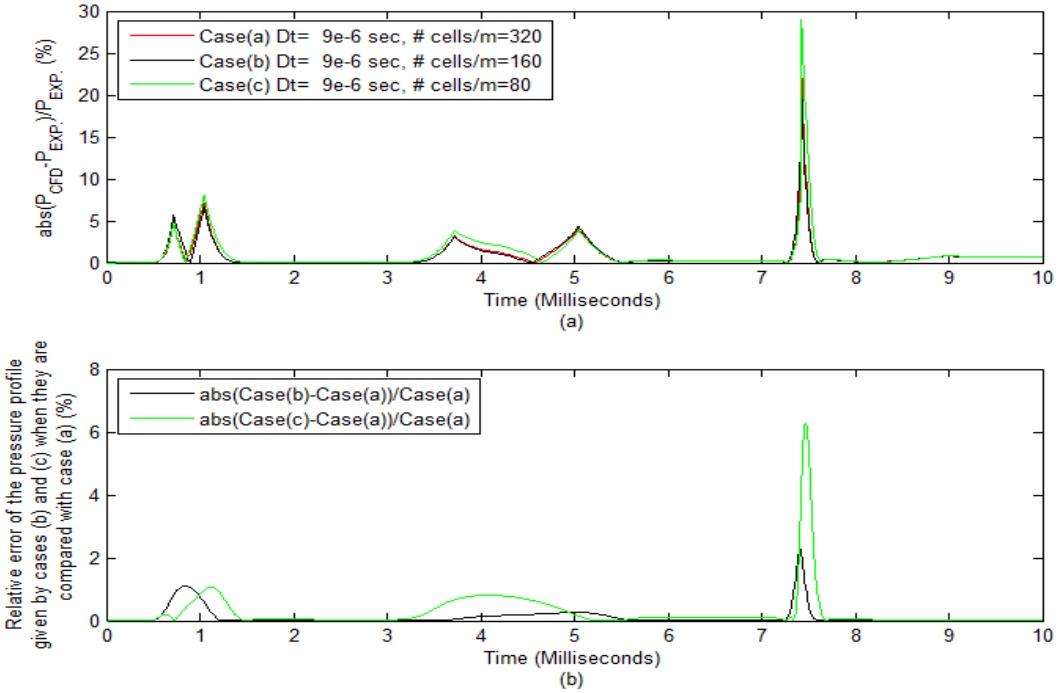

Figure 3-24 Fame(a) absolute error at 10 inches from the diaphragm at the driver zone, achieved by different mesh resolutions, Frame (b) relative error of cases (b) and (c) when compared with case (a)

Figure 3-26 presents a general panorama of the CFD code capability to model a transient compressible flow. This figure overlaps Figure 3-17 with the field of speed of sound predicted by the code when the mesh density is 160 cells per meter and the time step is 9e-6 seconds; the speed of sound is selected since all the waves inside the device, including the contact wave are able to be observed.

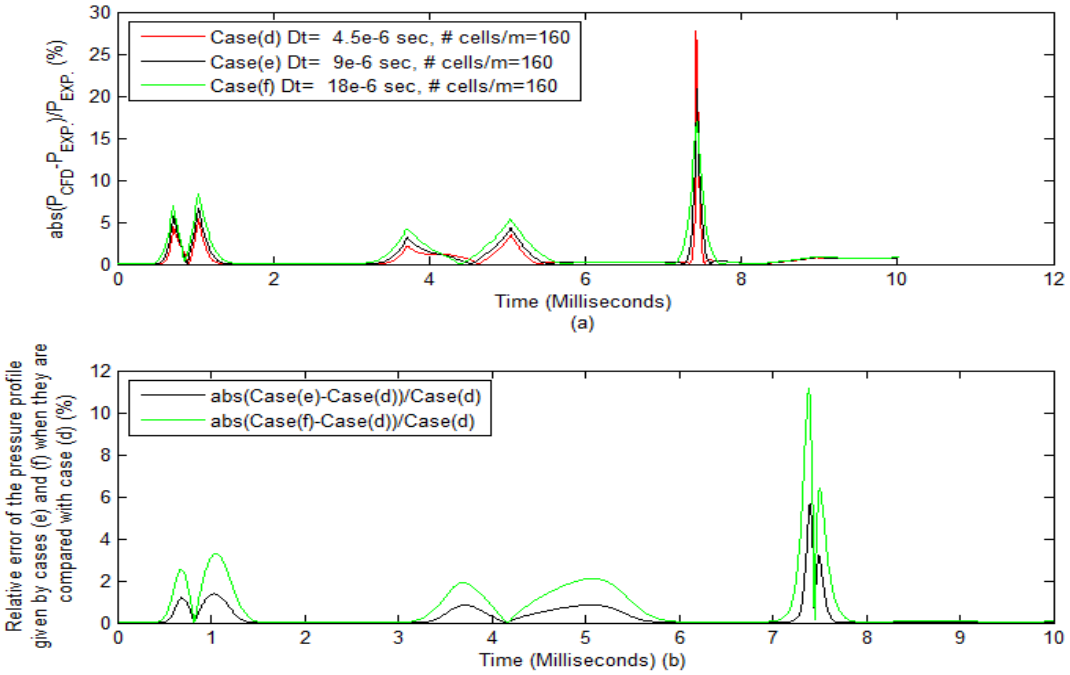

Figure 3-25 Fame (a) absolute error at 10 inches from the diaphragm at the driver zone, achieved by different time steps, Frame (b) relative error of cases (b) and (c) when compared with case (a)

Table 6 shows the values of pressure and speed of sound given by the numerical model and by the experiment at different states of the fluid through the transient process (see Figure 3-26), as well as the model absolute error, whose maximum is given in states g, h, i and j, the first three states are measured over the small discontinuities which are not captured by the CFD code as stated above, whilst the effect in state j must be a consequence of an accumulated error.

The 1D-CFD code is able to track the main waves inside the shock tube as well as their effect on the working fluid states after the compression and expansion processes), therefore this option looks suitable for the WR dimensioning.

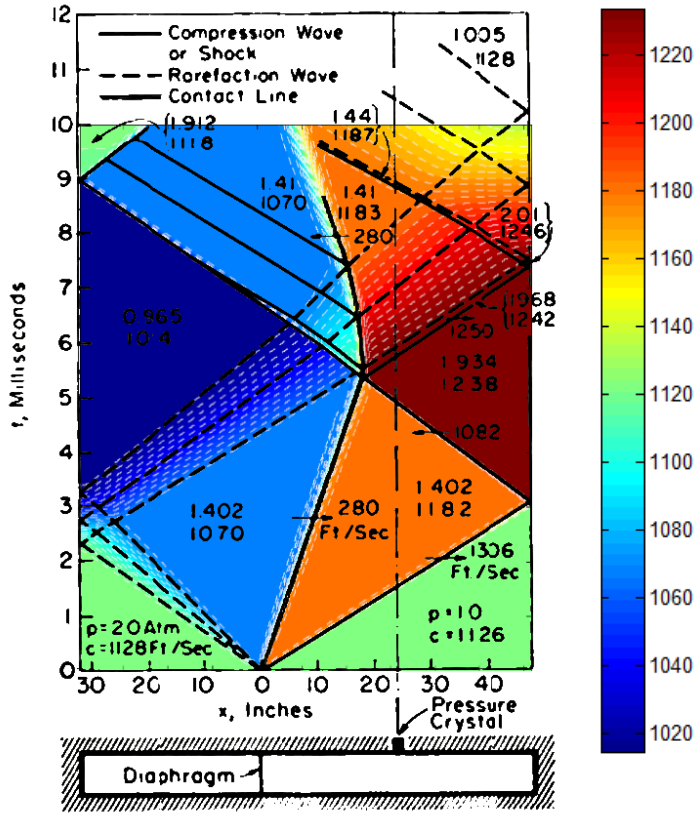

Figure 3-26 Overlap of the contour of speed of sound (ft/sec) predicted by the CFD code and the theoretical results presented in Figure 3-17

Table 6 Pressure and speed of sound predicted by the 1D-CFD code and the theoretical solution of the states represented in Figure 3-26

State	Model (M) p (atm)	Experiment (E) p (atm)	$\frac{(M-E)}{E}$ (%)	Model (M) a(ft/sec2)	Experiment (E) a (ft/sec2)	$\frac{(M-E)}{E}$ (%)
a	2	2	0	1126	1126	0.000
b	1	1	0	1126	1126	0.000
c	1.402	1.402	0	1070	1070	0.000
d	1.401	1.402	-0.07	1182	1182	-0.000
e	0.963	0.965	-0.21	1015	1014	0.099
f	1.935	1.934	0.05	1238	1238	-0.000
g	1.924	1.968	-2.24	1237	1242	-0.403
h	1.901	2.01	-5.42	1235	1246	-0.883
i	1.970	1.912	3.03	1125	1118	0.626
j	1.3905	1.44	-3.44	1181	1187	-0.505

3.6.3.2 Boundary conditions evaluation

After the analysis presented in the previous section, it is easy to state that the boundary condition “wall” is operating properly, since the gas dynamics predicted by the CFD simulation has the same pattern as in the experiment and the states reached by the fluid are similar in both cases.

Meanwhile, “ the stagnation properties at the inlet” and “the static properties at the outlet” as boundary conditions are evaluated by modelling the driven zone and driver zone independently from each other during the first 4.5 milliseconds, because the fluid properties near to the diaphragm are constant during that interval of time as indicated in Figure 3-17.

Figure 3-26(b) and Figure 3-26 (c) show the two new domains. The boundary conditions of these models are set by post processing the results obtained from the simulation of the whole shock tube that is performed in the previous subsection.

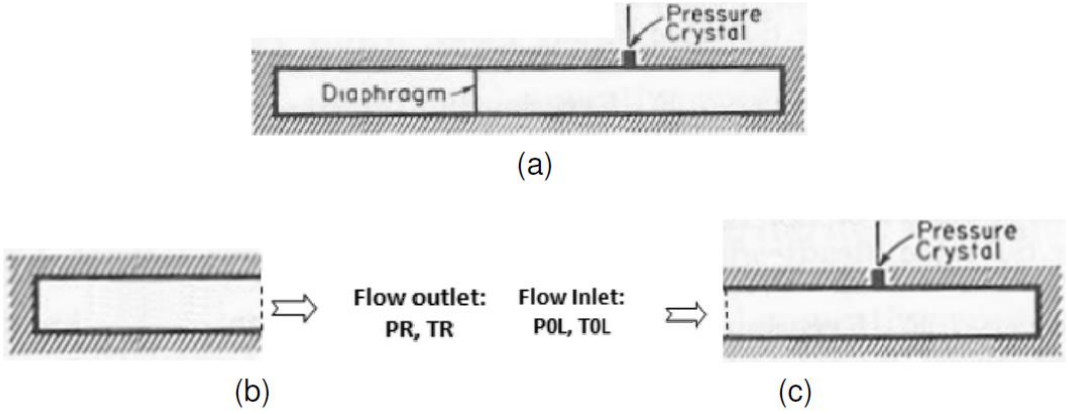

Figure 3-27 Computational domains implemented in the evaluation of the code boundary conditions, as follows: (a) wall (b) static properties at the outlet (c) stagnation properties at the inlet

The stagnation properties at the inlet:

Figure 3-28(a) and Figure 3-28(b) show the solution obtained after the simulation of this case. The mesh density is equal to160 cells per meter whilst

the total pressure and temperature employed are 148.68 kPa and 268.84 K; both values were post-processed from the previous simulation.

The solution pattern is similar to that obtained in the driven zone during the first 4.5 milliseconds when the whole tube is modelled (see Figure 3-18 and Figure 3-19), then some differences are observed since this case is unable to capture the arrival of the rarefaction wave reflected by the left end of the shock tube.

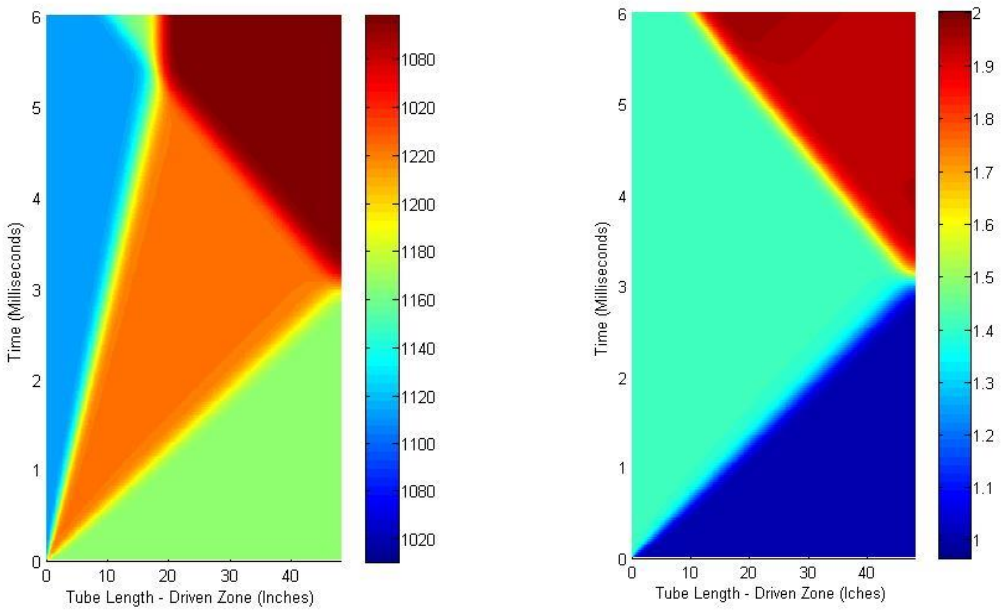

Figure 3-28 Validation of the CFD code - Stagnation properties at the inlet: a) Speed of sound (ft/sec) b) Pressure (atm)

Figure 3-29 shows the pressure history capture by the model at 22 inches of the diaphragm in the driven zone as well as the simulation of the whole shock tube and the experimental results. The CFD results are similar during the first 5.7 milliseconds. Then, the effect of the reflected rarefaction wave makes them differ from each other as expected. This behaviour clearly indicates that the evaluated boundary condition is working properly.

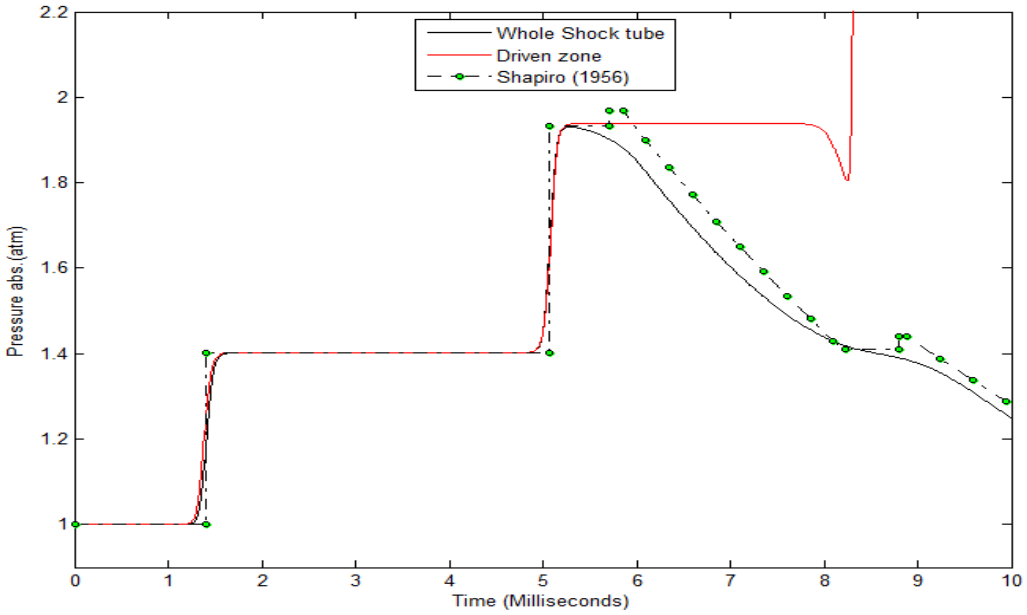

Figure 3-29 Validation of the CFD code - pressure profile at 22 inches of the diaphragm in the driven zone

Static properties at the inlet:

Figure 3-30(a) and Figure 3-30(b) show the solutions obtained when the boundary condition "*static properties at the outlet"* is implemented to model the driven zone. The mesh density implemented in this case is 160 cells per meter, such as in the previous evaluations.

The solution follows the same pattern observed in the experiment during the first 4.5 milliseconds. Then, some differences are detected firstly because the model produces a reflection of the expansion wave at its open end and secondly because the model is unable to track the arrival of the shock wave reflected at the right end of the shock tube.

Figure 3-31 shows the pressure history captured by the model at 10 inches of the diaphragm in the driver zone, as well as the results given by the simulation of the whole shock tube and the experiment. The CFD results are similar to each other during the first 4.5 milliseconds as expected. This corroborates the suitable operating of "*static properties at the outlet"* as a boundary condition.

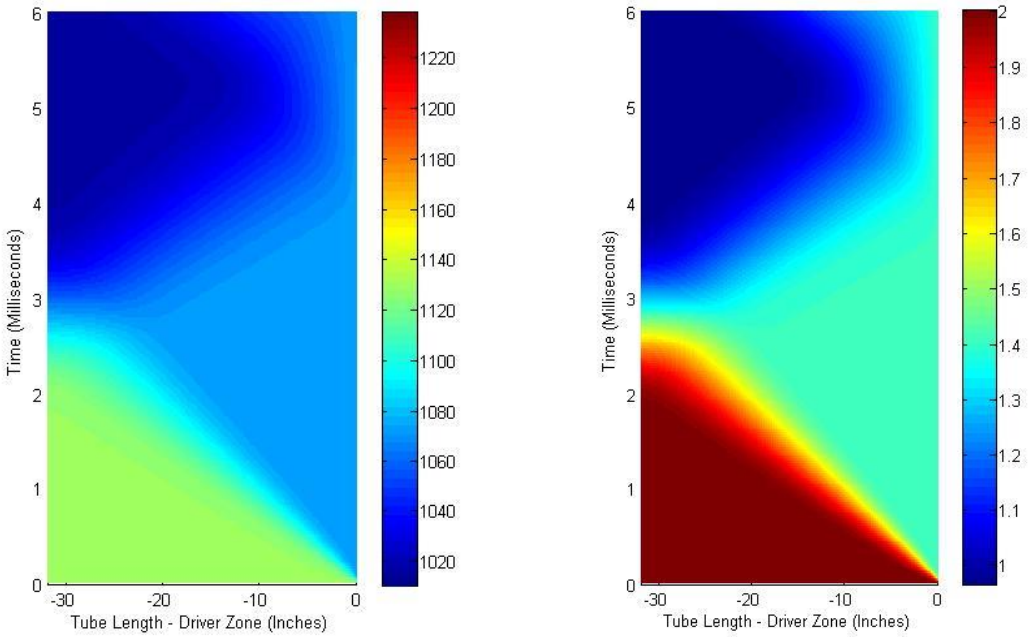

(a) (b)

Figure 3-30 Validation of the CFD code - Static properties at the inlet a) Speed of sound (ft/sec) b) Pressure (atm)

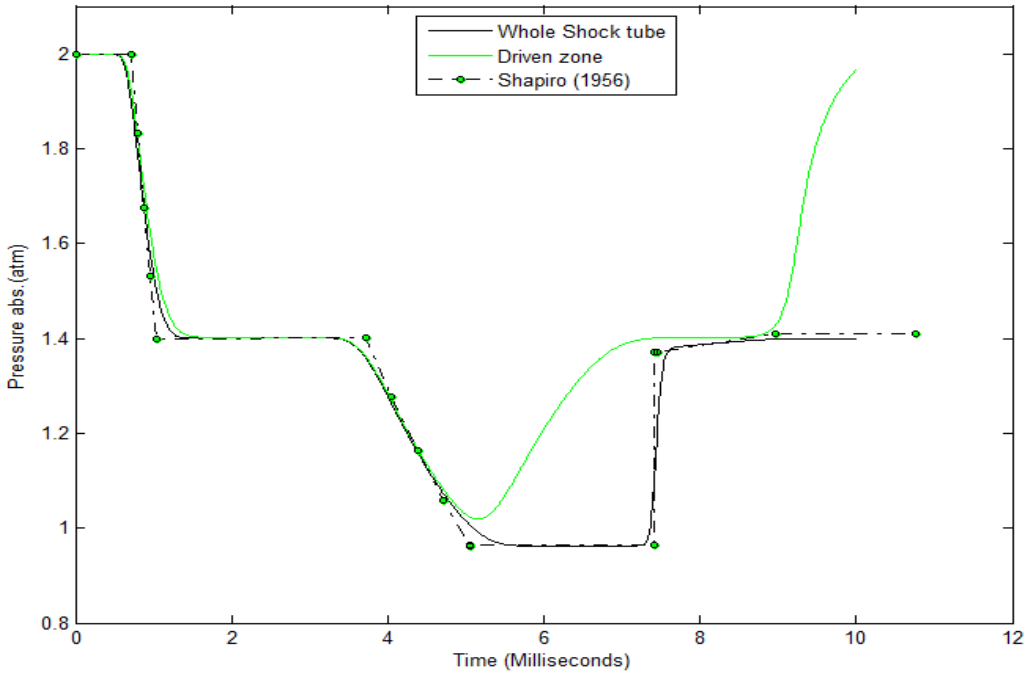

Figure 3-31 Validation of the CFD code - pressure profile at 10 inches of the diaphragm in the driver zone

Comments

After the validation of the in-house CFD code the following comments are presented:

- The CFD code is able to track the main waves generated inside the shock tube during the transient process whilst the fluid properties are estimated with a reasonable level of accuracy during the transient process
- Small jump discontinuities are unable to be captured by the CFD code with the mesh resolutions and the time steps implemented during this evaluation. However, their effect in the gas dynamics of the wave rotor is negligible and therefore the Weber's algorithm does not include them into the design process.
- The boundary condition required to simulate a wave rotor were successfully evaluated
- The sensitivity analysis indicates that a mesh density of 80 cells per meter is unable to track the position of the shock waves
- A mesh density of 160 cells per meter and a time step of 9e-6 seconds produce relative errors up to 5.6 % in respect to a model two times denser or a model with half of the time step implemented. Nevertheless, the code is able to give an accurate prediction of the waves' position as well as the correct prediction of states reached by the fluid during the gas dynamics. Therefore, this discretisation is selected to perform the WR dimensioning

3.6.4 1D-CFD code for the wave rotor dimensioning

The feasibility of fitting a wave rotor into a gas turbine for business jets was studied in section 3.5 by performing the thermal analysis of the novel cycle and the gas dynamic analysis of the wave rotor.

As a result, it was found that only two of the studied configurations were possible:

- Case 1- The novel cycle kept the same overall pressure ratio and turbine inlet temperature as the baseline cycle.
- Case 2- The novel cycle kept the same temperature level in the combustion chamber as the baseline cycle.

The performance evaluation of both cases was obtained by changing the flow velocity at state A (see Figure 3-1), in a range between 0.2 and 1 times the speed of sound $(0.2 \leq M_A \leq 1)$. The minimum SFC was achieved when M_A was equal to 0.47 in case 1 and 0.53 in case 2. Now, this section implements a 1D-CFD code that uses the information given by previous sections in order to obtain the wave rotor's dimensioning.

The wave rotor dimensioning is performed by setting three operational conditions for each case, the first when $M_A = 0.2$, the second when the minimum SFC is achieved ($M_A = 0.47$ in case 1 and $M_A = 0.53$ in case 2) and the third when $M_A = 1$.

The channels' height is assumed equal to 20 cm to start running the simulation and then it is corrected at the end of the simulation by comparing the theoretical mass flow rate predicted from the Weber's algorithm ($\dot{m}_{core}$) and the mass flow rate predicted by the CFD code through Eq.(3-28); Y_{LPA} represents the length of the LPA port, $\bar{u}_{inj}$ the average injection velocity of fresh air (computed at the LPA port) and $\bar{\rho}_{inj}$ its average density. The assumed height does not have an effect on the gas dynamics inside the device since the fluid is inviscid.

$$\mathrm{h} = \frac{\dot{m}_{core}}{\bar{\rho}_{inj} \cdot \bar{u}_{inj} \cdot Y_{LPA}} \qquad \textbf{(3-28)}$$

The aspect ratio between the channel's height and its width (h/s) changes from one WR to the other. Paxson (1995) evaluated three different wave rotors with aspect ratios equal to 1.45, 5.76 and 2.39, while Frackowaiak et al. (2004) evaluated a WR with an aspect ratio of 6.36.

Low values of h/s are not suitable in a WR that drives a large amount of mass; such as the core flow of a gas turbine, because the pitch line diameter of the WR turns impractical. An aspect ratio (h/s) of 5.0 is selected to perform the simulation of the WR, so the width of the channels is 4 cm when their height is 20 cm. The selected aspect ratio changes when the channels' height is corrected. However, it is expected a final value lower than the maximum aspect ratio found in the literature.

Equation (3-19) is used to compute the length of the channels for each studied case by implementing the results obtained in section 3.5. The required information is shown in Table 7 and Table 8.

Table 7 Boundary conditions implemented in the CFD model for three different values of M_{LPA}- case 1, see section 3.5

Parameter	Case 1			Units
M_A	0.2	0.46	1	$(--)$
u_t	180.09	181.44	182.16	m/s
h	0.2	0.2	0.2	m
L	1.01	0.98	1.03	m
$\dot{m}_{LPA}$	65.3	63.43	65.00	kg/s
$T_{0,LPA}$	479.67	444.50	424.23	K
$p_{0,LPA}$	292.72	232.6	205.06	kPa
$T_{0,HPG}$	1194.49	1204.98	1225.79	K
$p_{0,HPG}$	860.51	859.71	860.9	kPa
T_{HPA}	652.59	649.65	674.07	K
p_{HPA}	824.03	822.78	824.64	kPa
T_{LPG1}	1096.9	1094.05	1090.13	K
p_{LPG1}	572.43	549.62	511.91	kPa
T_{LPG2}	898.44	821.13	699.48	K
p_{LPG2}	284.67	201.31	108.33	kPa

The domain implemented has a density of 160 cells per meter of length of the channel and the simulation is performed with a time step of 9e-6 seconds throughout the simulation, since these values offered a suitable performance of

the CFD code during its validation (see section 3.6.3). The code is executed during four cycles of the device to ensure the dynamic equilibrium of the model.

Table 8 Boundary conditions implemented in the CFD model for three different values of M_{LPA}- case 2, see section 3.5

Parameter	Case 2			Units
M_A	0.2	0.53	1	$(--)$
u_t	170.54	170.66	169.15	m/s
h	0.2	0.2	0.2	m
L	1.22	1.19	1.35	m
$\dot{m}_{LPA}$	76.96	75.59	83.09	kg/s
$T_{0,LPA}$	487.18	446.21	433.49	K
$p_{0,LPA}$	307.67	236.14	219.22	kPa
$T_{0,HPG}$	1110	1110	1110	K
$p_{0,HPG}$	864.64	864.49	866.27	kPa
T_{HPA}	653.75	651.82	676.22	K
p_{HPA}	830.73	830.48	833.54	kPa
T_{LPG1}	1016.47	1003.39	987.22	K
p_{LPG1}	570.40	544.98	516.77	kPa
T_{LPG2}	845.35	748.10	643.91	K
p_{LPG2}	299.21	195.02	115.81	kPa

Figure 3-32 and Figure 3-33 show the code's estimations of the pressure and temperature fields reached within the channels during their trajectory throughout the cycle. In these figures it is noted that smaller peripheral distances are obtained at intermediate values of M_A.

Table 9 shows the ports' position through the pitch line perimeter predicted by the 1D CFD code using as reference the LPA port opening, the perimeter of the wave rotor and the angular velocity required on each evaluated condition. This table shows that case b not only requires a smaller wave rotor but also wave rotors with a higher angular velocity.

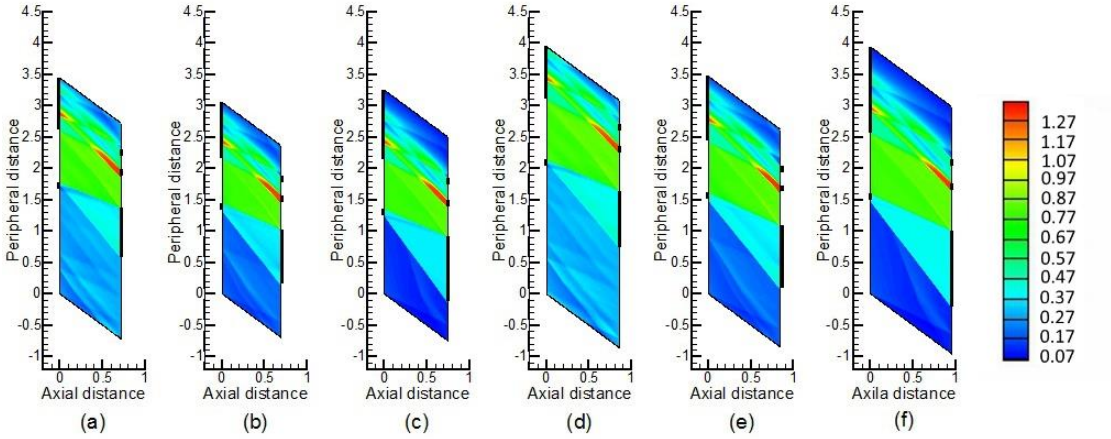

Figure 3-32 Contour of pressure in MPa given by the 1D CFD model: a) case 1 with $M_A = 0.2$ b) case 1 with $M_A = 0.46$ c) case 1 with $M_A = 1$ d) case 2 with $M_A = 0.2$ e) case 2 with $M_A = 0.53$ f) case 2 with $M_A = 1$

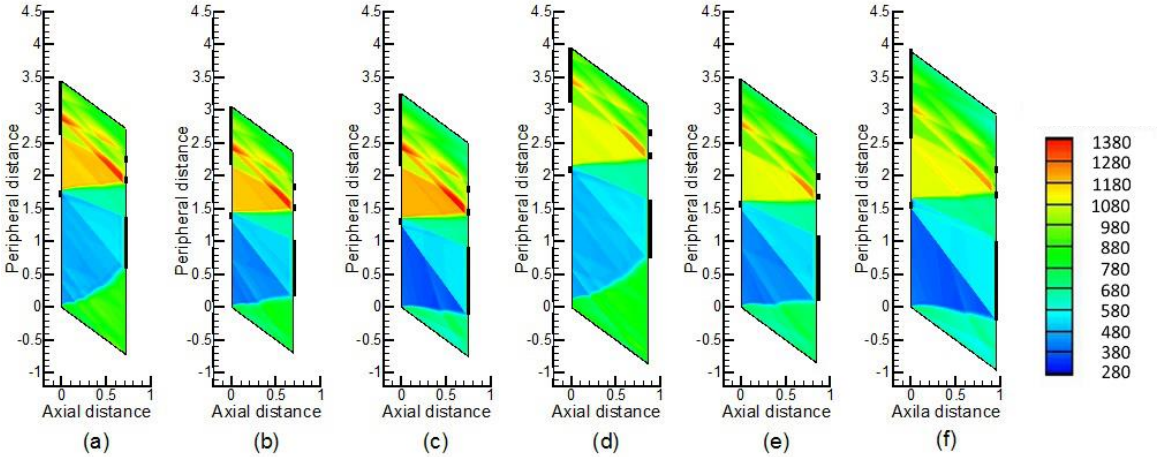

Figure 3-33 Contour of temperature in Kelvin given by the 1D CDF model: a) case 1 with $M_A = 0.2$ b) case 1 with $M_A = 0.46$ c) case 1 with $M_A = 1$ d) case 2 with $M_A = 0.2$ e) case 2 with $M_A = 0.53$ f) case 2 with $M_A = 1$

Table 9 Prediction of the developed 1D-CFD code; dimensions are measured through the peripheral distance and the reference system is set at the opening of the low-pressure air port (LPA port), see bottom of Figure 3-1

Parameter/State	Case 1			Case 2			Units
M_A	0.200	0.460	1.000	0.200	0.530	1.000	$(--)$
Pitch-line perimeter	3.441	3.057	3.251	3.945	3.468	3.938	m
RPM	3140	3561	3362	2594	2952	2577	rev/min
Diameter	1.095	0.973	1.035	1.256	1.104	1.254	m
LPG2 port closure	0.571	0.137	-0.137	0.728	0.071	-0.222	m
LPA port closure	1.653	1.324	1.231	2.024	1.490	1.475	m
HPG port opening	1.773	1.444	1.531	2.144	1.610	1.594	m
HPA port opening	1.367	1.028	0.910	1.637	1.091	1.005	m
HPA port closure	1.857	1.450	1.379	2.235	1.610	1.640	m
HPG port closure	2.598	2.147	2.130	3.093	2.416	2.555	m
LPG1 port opening	1.977	1.569	1.499	2.355	1.729	1.759	m
LPG1 port closure	2.184	1.752	1.725	2.585	1.923	2.027	m
LPG2 port opening	2.304	1.871	1.845	2.705	2.043	2.146	m

3.6.5 Comparison between the Weber's model and the 1D-CFD model

Figure 3-34 and Figure 3-35 present a comparison between Weber's model and the 1D-CFD simulation. To make the evaluation easier, the contours of pressure and temperature are shown with the same colour scale in both figures.

Among the differences, the following are the most significant:

- The first contact wave does not follow a linear trajectory. This effect is accentuated at low values of M_A and its source can be ascribed to the inertia that air has to overcome to push the gases outside of the channels and the velocity reduction produced by the rarefaction waves generated during the opening of LPG1 and LPG2 ports
- The CFD value of $\dot{m}_{LPA}$ is lower than that predicted by Weber's model, due to the early closure of LPA port. This effect is a consequence of an earlier arrival of the first shock wave to the left end of the channels; so the channels' height should be corrected

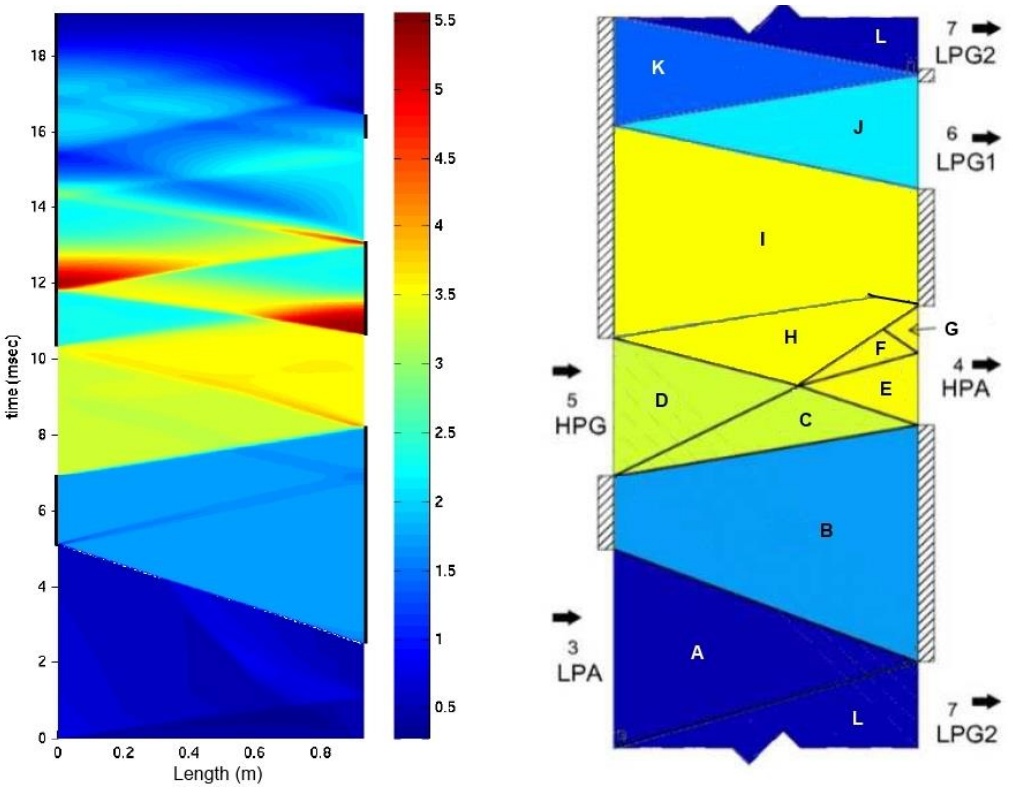

Figure 3-34 Comparison between the absolute pressure fields in MPa predicted by the 1D-CFD model (left side) and by the Weber's algorithm (right side)

- In all the studied cases it was observed that the first shock wave is reflected followed by a thin rarefaction wave. This effect generates a small distortion of the properties reached by the fluid and becomes more remarkable at high values of M_A. Consequently, the working fluid never reaches a homogeneous state B
- The collision between the third shock wave and the first rarefaction wave does not cause them to dissipate; instead both waves keep their strength and therefore the working fluid never reaches a homogeneous state I
- Because the first rarefaction wave is not attenuated during its collision with the third shock wave, its arrival to the right end of the channels forces the early closure of LPG1 port, to prevent reverse flow. Therefore the mass flow through LPG1 port is smaller than that estimated by Weber's algorithm
- At high values of M_A the reflected shock wave reaches the HPG port before its closure

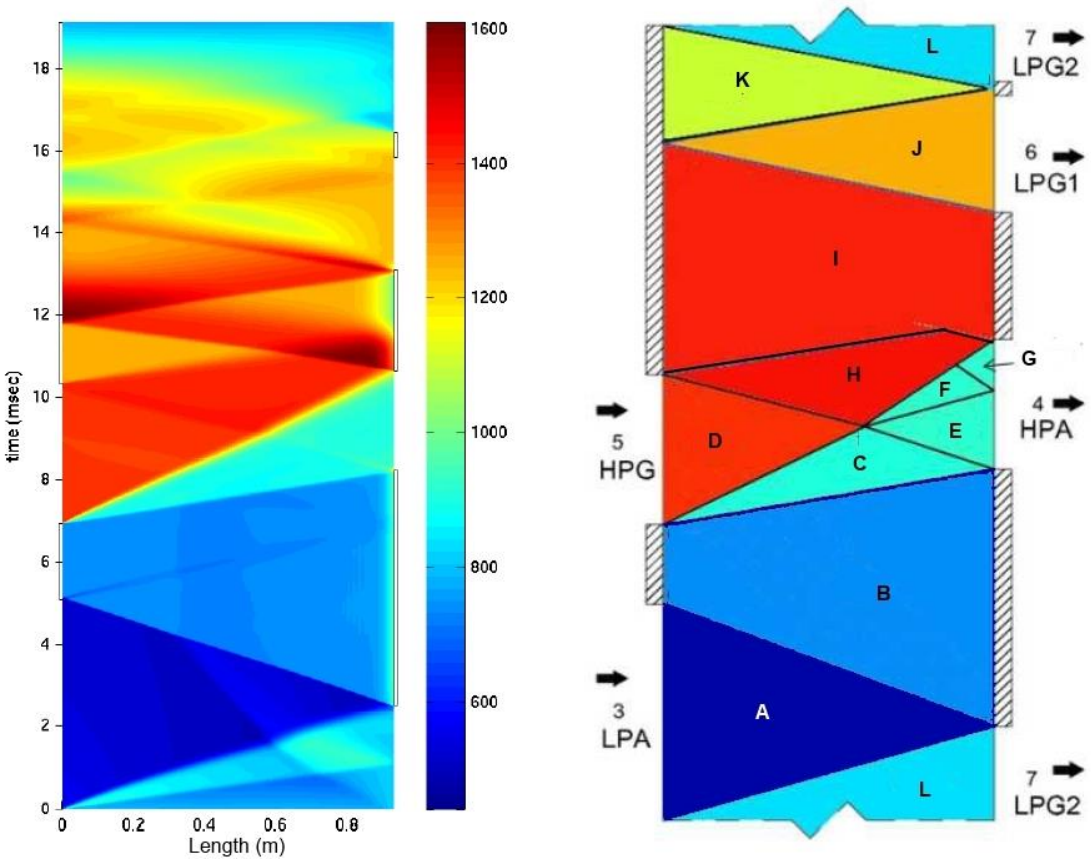

Figure 3-35 Comparison between the temperature fields in Kelvin predicted by the 1D-CFD model (left side) and by the Weber's algorithm (right side)

3.6.6 Performance correction

Table 10 and Table 11 allow the comparison between Weber's model and the 1D-CFD model. The mass flow through LPG2 port gets reduced in all the CFD simulations and therefore the work generated by the high pressure gas turbine decreases.

However, the simulations predict an efficient production of work from the wave rotor, in a way that the total work (work generated by the high pressure turbine plus the wave rotor) becomes higher than that obtained from Weber's model. So, gas turbines with the new configuration have a better performance that improves at higher values of M_A, see Table 12.

Table 10 Estimations of the Weber's algorithm: Mass flow driven by the LPG1 and LPG2 ports shown in Figure 3-1 ($\dot{m}_{LPG1}$and $\dot{m}_{LPG2}$), work delivered by the wave rotor work (w_{WR}) and work delivered by the high pressure turbine (w_{HPT})

		Mx_A	$\dot{m}_{LPG1}$ (kg/seg)	$\dot{m}_{LPG2}$ (kg/seg)	w_{WR} (J/kg)	w_{HPT} (J/kg)	$w_{WR} + w_{HPT}$ (J/kg)
	a	0.2	5.50E-01	4.50E-01	-6.11E+03	1.02E+05	9.56E+04
case b	b	0.46	5.79E-01	4.21E-01	-1.46E+04	1.48E+05	1.34E+05
	c	1	5.96E-01	4.04E-01	-2.97E+04	2.04E+05	1.75E+05
	a	0.2	5.09E-01	4.91E-01	-6.26E+03	8.03E+04	7.41E+04
case c	b	0.53	5.35E-01	4.65E-01	-1.62E+04	1.25E+05	1.09E+05
	c	1	5.33E-01	4.67E-01	-2.88E+04	1.55E+05	1.26E+05
Brayton		N/A	N/A	N/A	N/A	N/A	N/A

Note: the work is computed per unit of mass of air that crosses the turbine (core flow)

Table 11 Estimations of the 1D-CFD code: Mass flow driven by the LPG1 and LPG2 ports shown in Figure 3-1 ($\dot{m}_{LPG1}$ and $\dot{m}_{LPG2}$), work delivered by the wave rotor work (w_{WR}) and work delivered by the high pressure turbine (w_{HPT})

		Mx_A	$\dot{m}_{LPG1}$ (kg/seg)	$\dot{m}_{LPG2}$ (kg/seg)	w_{WR} (J/kg)	w_{HPT} (J/kg)	$w_{WR} + w_{HPT}$ (J/kg)
	a	0.2	2.36E-01	7.64E-01	5.78E+04	4.36E+04	1.01E+05
case b	b	0.46	2.18E-01	7.82E-01	8.66E+04	5.58E+04	1.42E+05
	c	1	2.44E-01	7.56E-01	1.02E+05	8.37E+04	1.85E+05
	a	0.2	2.27E-01	7.73E-01	4.28E+04	3.58E+04	7.86E+04
case c	b	0.53	1.94E-01	8.06E-01	7.13E+04	4.53E+04	1.17E+05
	c	1	2.22E-01	7.78E-01	6.98E+04	6.44E+04	1.34E+05
Brayton		N/A	N/A	N/A	N/A	N/A	N/A

Note: the work is computed per unit of mass of air that crosses the turbine (core flow)

3.6.7 2D Verification

The verification of the wave rotor's design is performed by comparing the 1D-CFD model of case 1(b) with a 2D simulation performed with ANSYS FLUENT®. The boundary conditions implemented in the 2D model are the same as the ones used in the 1D model, except the stagnation properties in LPA and HPG ports, because there is a change in the reference frame (the

stagnation properties at the stator are different than at the rotor); the new values are shown in Table 13.

Table 12 Performance comparison between the model of Weber and the 1D-CFD model

			Model of Weber				1D-CFD model			
		M_A	η_e	η_o	SFC	F_s	η_e	η_o	SFC	F_s
case b	a	0.2	3.42E-01	2.80E-01	71.4	105	3.46E-01	2.83E-01	70.7	106
	b	0.46	3.45E-01	2.81E-01	71.1	109	3.51E-01	2.85E-01	70.2	110
	c	1	3.38E-01	2.77E-01	72.3	106	3.45E-01	2.82E-01	70.9	108
case c	a	0.2	3.38E-01	2.85E-01	70.2	90.1	3.42E-01	2.87E-01	69.7	90.9
	b	0.53	3.44E-01	2.88E-01	69.5	91.8	3.50E-01	2.93E-01	68.3	93.3
	c	1	3.29E-01	2.80E-01	71.6	84.3	3.38E-01	2.86E-01	70.0	86.2
Brayton		N/A	3.29E-01	2.79E-01	71.6	85.5	3.29E-01	2.79E-01	71.6	85.5

Table 13 Case 1(b)-stagnation properties relative to the stator, see section 3.5

Port	$p_0(\mathrm{k}Pa)$	$T_0(K)$
LPA	218.5	436.62
HPG	820.0	1204.99

The geometry of the model is built from the data given by the 1D CFD code and the ports are projected based on the analytical solution obtained in section 3.5, (see Table 14). Seventy-eight channels are used to cover the pitch-line perimeter of the WR predicted by the 1D-CFD code; the number of channels is related to the channels' width selected in section 3.6.4

Some instabilities are obtainable in ANSYS FLUENT® when the time step is equal to 9e-6 seconds (time step implemented by the 1D-CFD code). The instabilities occur between the ports and the rotor (sliding edges of the domain) as a consequence of the variables initialization and the interpolation scheme implemented by the sliding mesh technique. Fortunately, the instabilities observed disappear for a time step equal to 4.5e-6 seconds (half of the time step initially implemented).

The reduction of the time step must improve the model prediction because the error of the time integration is reduced and the computational effort is not significantly affected because 2D models are able to dissipate the noise of the variable initialization faster than 1D models, since the whole array of channels is interacting during the simulation; the dynamic equilibrium of the fluid is obtained after the simulation of two cycles.

Table 14 Case 1(b) - ports angle based on the first quadrant of the coordinate plane, see section 3.5

Port	Angle θ
LPA	$19.31°$
HPG	$0°$
HPA	$5.02°$
$LPG1$	$0.79°$
$LPG2$	$19.31°$

Figure 3-36 and Figure 3-37 present the contour of pressure and temperature given by the 1D and 2D results respectively when case 1(b) is modelled. Both solutions are similar, however a small difference is observed in the position of the first contact waves. The difference in the contact wave position can be ascribed to the inability of one dimensional models to reproduce the non-instantaneous port opening among other 3D effects.

Moreover, Figure 3-38 shows the values of temperature and pressure reached by a cell located in the middle of the channels during a cycle of the wave rotor estimated by the 1D and 2D CFD simulations. Both models are reproducing similar values with small differences in the temperature contour due the differences in position of the first contact wave (an effect that was previously mentioned).

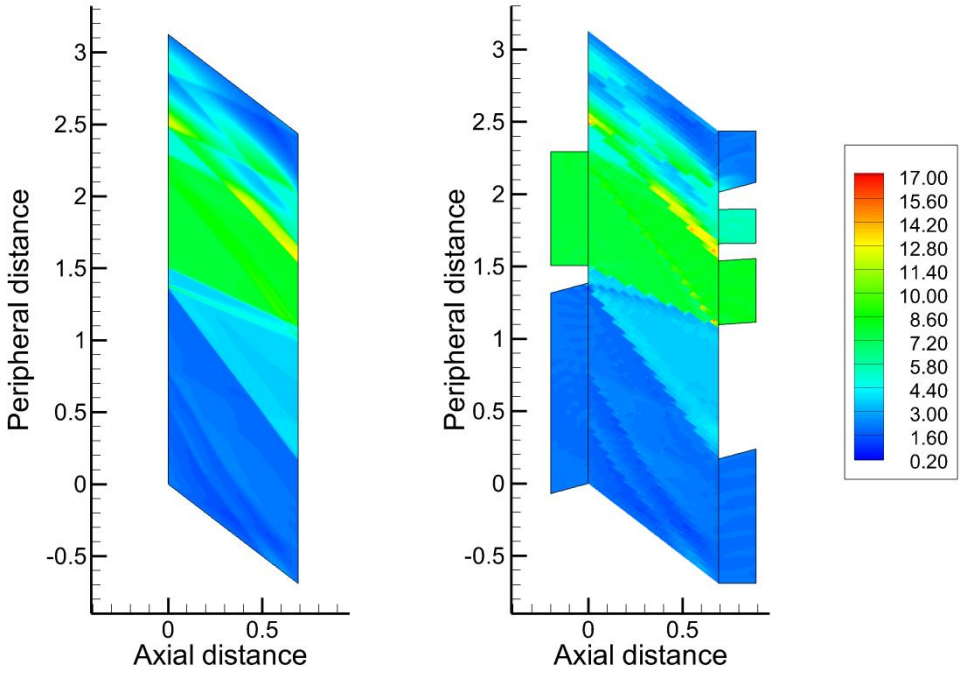

Figure 3-36 Contour of static pressure in atm. Predicted by the 1D-CFD code (left side) and the 2D-CFD code (right side) of case (1) at M_A equal to 0.46

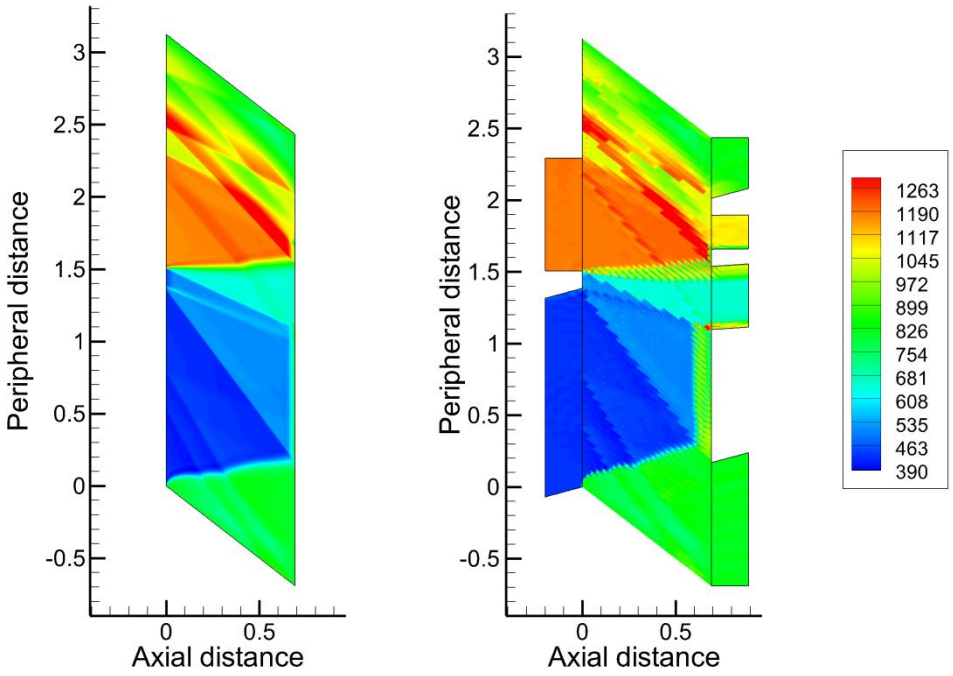

Figure 3-37 Contour of temperature in Kelvin predicted by the 1D-CFD code (left side) and the 2D-CFD code (right side) of case (1) at M_A equal to 0.46

Table 15 presents the mass flow predicted by the 1D and 2D CFD simulations in each port of the device. These values are lower than those presented in Table 7, because the first shock wave arrives at the left plate earlier than expected during the simulation; a situation that forces the prompt closure of LPA port.

Consequently, the height of the channels (initially assumed equal to 0.2 m, see section 3.6.4) is corrected by a factor of 1.038. The correction is obtained by dividing the mass flow predicted in section 3.5 and that obtained from the 1D-CFD simulation.

The contour of pressure given by both cases is similar. However, the mass flow crossing through the LPA port achieves the maximum differences between the models (see Table 7). This effect is also expected due to the overestimation of the contact waves' velocity given by the 1D-CFD simulation when it is compared to the 2D-CFD simulation; an effect that was appreciated during the evaluation of the temperature contours.

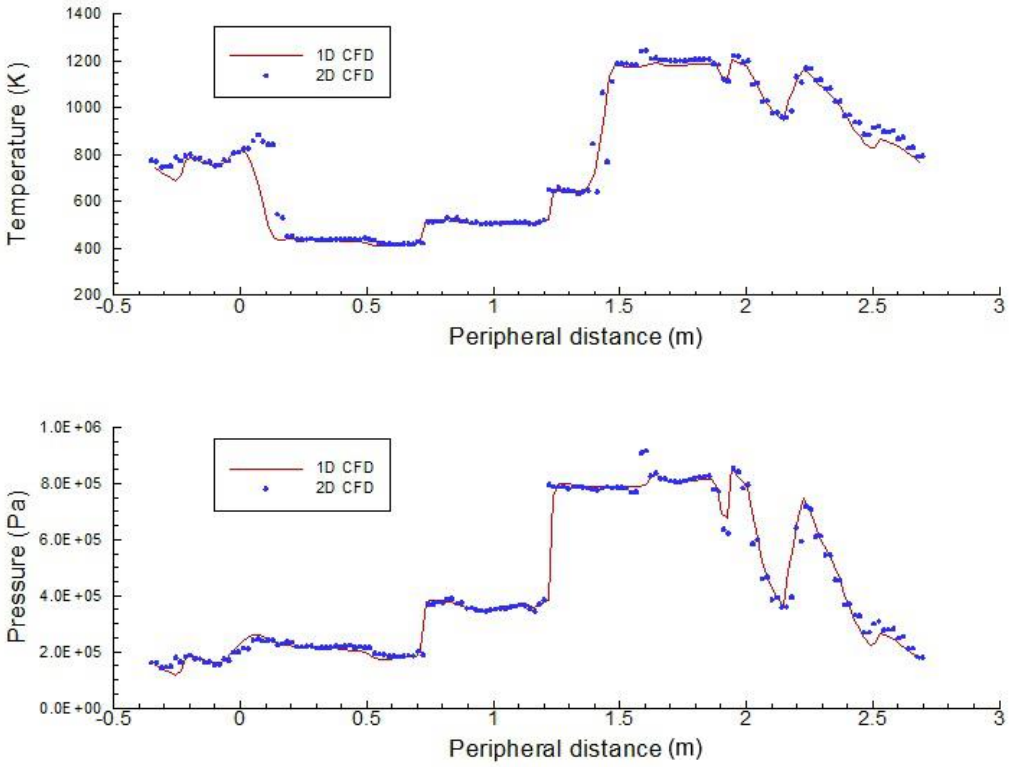

Figure 3-38 Pressure and temperature values predicted by the 1d and 2d model, measured in the middle of the channels during the entire cycle of the wave rotor

Table 15 : Mass flow in (kg/sec) discrepancies between the 1d and the 2d CFD simulation, reported in each port of the device

Port	1D CFD	2D CFD	Difference (%)
$\dot{m}_{LPA}$	63.43	58.6337	7.562
$\dot{m}_{HPA}$	63.43	63.7291	0.472
$\dot{m}_{HPG}$	63.43	62.0274	2.211
$\dot{m}_{LPG1+LPG2}$	63.43	60.5053	4.611

3.7 NO_X emissions inside the wave rotor (Thermal NO_X)

The maximum temperature of gases within the WR is near or equal to 1100K at the HPG port, since this value of temperature is obtained at the outlet of the combustion chamber of the baseline gas turbine and there is no other exothermic reaction process inside the WR that leads to a future increment of the fluid temperature.

Meanwhile, the rate of formation of NOx is important when the gases temperature is over 1800 K, because the strong triple bond of nitrogen molecules must be broken (dissociation energy of 941 kJ/mol), so the evaluated WR does not allow the formation of thermal NOx (ANSYS 2013).

Based on the above, the NOx concentration at the LPG port must be equal to that measured at the exhaust of the combustion chamber and therefore this value is linked with the technology involved in the combustion process, a topic that is not considered by this work.

3.8 Chapter summary

This section presents a procedure to evaluate the performance of wave rotors as components of the gas turbine. The procedure starts by implementing the Weber's analytical model of a WR to complete the thermal evaluation of the novel cycle and concludes by building an executing a 1D-CFD code based on the finite volume method to predict the dimensions of the device as well as the position and length of the different ports. The dimensioning is performed by tracking the waves generated during a cycle.

As part of the results, it is observed that cycles with the same overall pressure ratio than the baseline engine perform better since the turbine is able to deliver the work required by the compressor, fan and wave rotor through all the evaluation range, whilst an increase of the specific thrust and a reduction of the SFC in respect to the baseline engine are achieved.

The injection of air has an impact on the compression and expansion processes inside the wave rotor; a low injection Mach number benefits the compression process but reduces the efficiency of the expansion process whilst a high injection Mach number produces an opposite effect. Therefore an injection Mach number between 0.46 and 0.53 is recommended.

The developed 1D-CFD code has been executed to model a WR able to reproduce the same condition at each port of the device predicated by the analytical solution. The temperature and pressure profiles were compared between these two models to observe their discrepancies.

Among the differences remarked in section 3.6.5, the CFD model does not reproduce the waves dissipation stated by Weber when a shock wave collides with a rarefaction wave and therefore the prompt closure of the LPG1 ports shown in Figure 3-1 is essential to prevent a reverse flow as a consequence of the arrival of the first rarefaction wave.

The effect described above causes a reduction of the mass that crosses through the LPG1 port and therefore the performance of the gas turbine predicted by the analytical solution can be affected (the distribution of mass through the LPG1 and LPG2 ports is different).

4 PERFORMANCE OF PULSE DETONATION ENGINES AS COMPONENTS OF AIRCRAFT GAS TURBINES

4.1 Factors to consider in the modelling of PDE

The performance of PDEs as component of gas turbines can be predicted with a good level of accuracy if the different waves that participate in the transient process inside a PDE are appropriately modelled (see section 2.7). Among the factors that must be considered, remarkable ones are as follows:

Rarefaction waves become wider when they move along a large PDE. So, the pressure profile of the fluid within the device changes smoothly between the pressure at the closed end and the pressure at the von-Neumann spike when the detonation wave arrives to the open end of the PDE, as Figure 4-1 indicates.

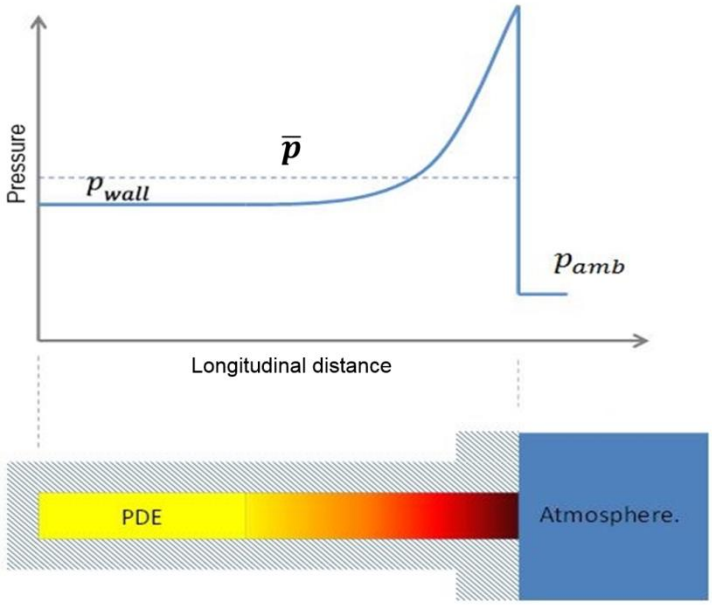

Figure 4-1 Pressure distribution in the PDE an instant of time after the reactants are consumed

At the end of the detonation a strong shock wave is generated. This wave continues travelling outside the PDE to compress the external fluid. Its propagation produces a distortion in the external pressure field such as the oval-shape observed in Figure 4-2. This distortion increases the external

pressure near the open end during a short period of time that prevents the fluid choke unless it travels at supersonic conditions.

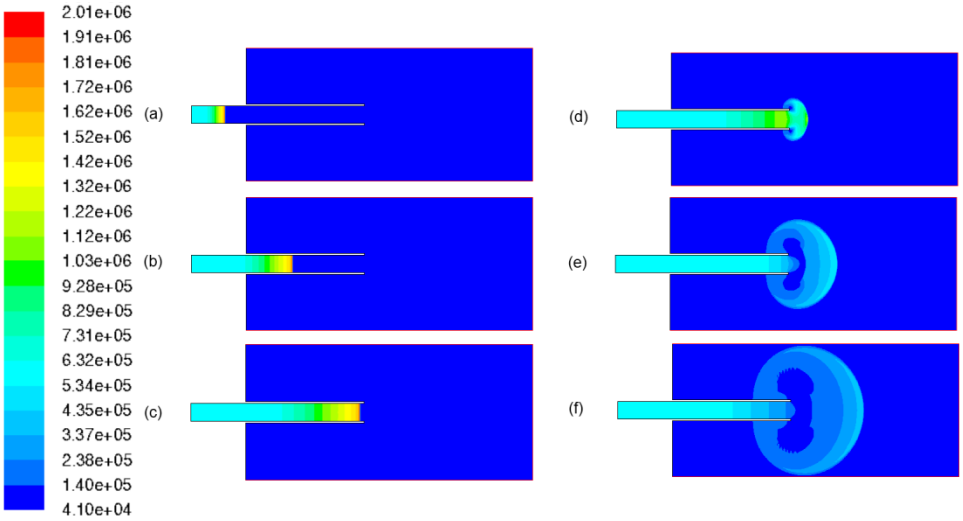

Figure 4-2 Pressure field during a PDE transient process (Pa)

Moreover, the rarefaction wave behind the detonation moves out of the PDE and then it is reflected by the interface between product gases and external air (Wintenberger et al. 2003). The reflected wave overcomes the outflow velocity and starts interacting with the fluid contained inside the PDE when the flow is not throttled at the open end (see Figure 4-3).

The flow at the open end reaches a throttling condition once the external pressure is recovered; whose value is affected by the compression effect of the shock wave. In most of the cases, the throttling condition occurs in a small fraction of the whole time required by the cycle.

The throttling condition can end as a consequence of the arrival of the remaining rarefaction wave contained inside the tube or due to the arrival of the second rarefaction wave after its reflection at the closed end of the PDE (see section 2.7). Both options produce a non-linear drop of pressure due to the stretching of the wave.

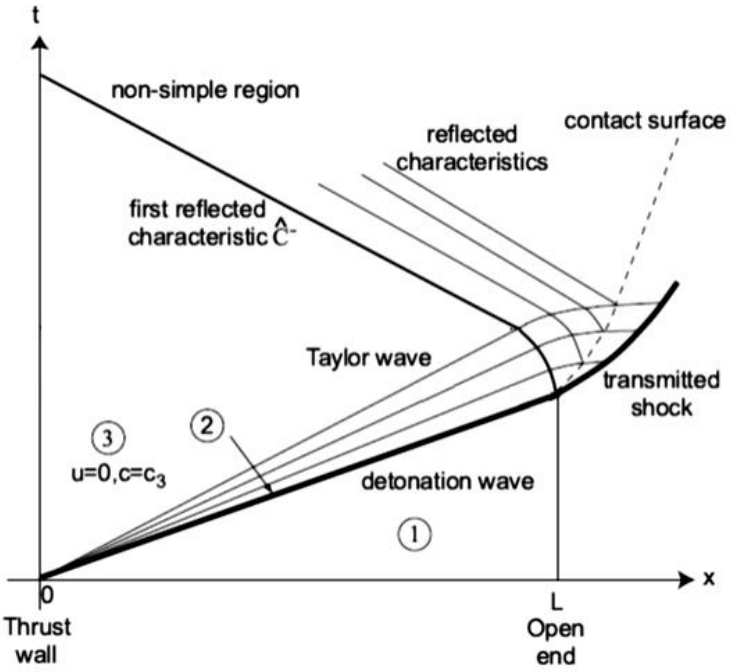

Figure 4-3 Taylor wave's reflection - space-time diagram (Wintenberger et al. 2003)

4.2 PDE evaluation - Method of the characteristics

In a PDE, the detonation time can be computed as the length of the PDE divided by the velocity of the detonation wave; the last parameter is given by the Chapman-Jouguet condition (see section 2.5.2).

Once the detonation wave arrives to the open end of the PDE, the transient process that follows is mainly driven by different rarefaction waves. Thus, Endo and at (2004) have implemented the method of characteristics to produce a good estimate of the pressure profile during the transient process.

The method of characteristics is a technique that allows the conversion of hyperbolic partial differential equations into ordinary differential equations. The resultant equations can be integrated from an initial value to produce a hyper-surface.

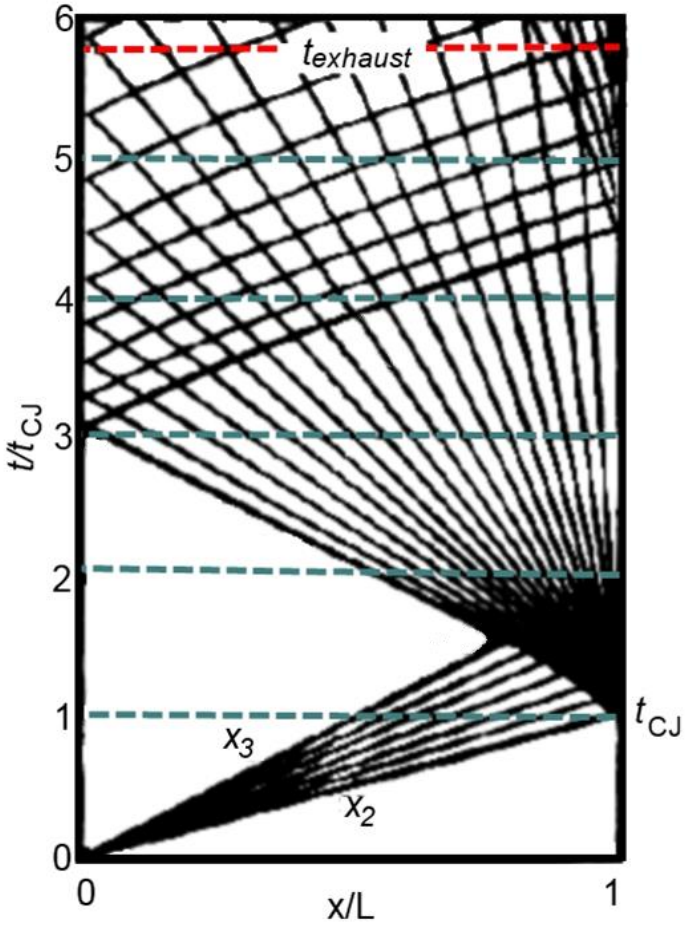

Figure 4-4 Schematic space-time (x-t) diagram of characteristic in a simplified PDE (Endo et al. 2004)

Figure 4-4 is an example of a PDE evaluated with the method of characteristics. This work was carried out by Endo et al (2004) to compute the time implemented by the expansion waves to move through the device, as well as the position of the waves' interception and the states reached by the fluid during the process. The open end of the PDE is at the right side, while the waves position is represented by X and the times by t.

Equations (4-1) and (4-2) are the differential form of mass and momentum conservation equations implemented to model the trajectory followed by the rarefaction waves during the PDE transient process. The momentum equation neglects body forces and viscous dissipation (Euler equation).

$$\frac{D\rho}{Dt} + \rho\frac{\partial u}{\partial x} = 0 \quad \textbf{(4-1)}$$

$$\rho\frac{Du}{Dt} = -\frac{\partial P}{\partial x} \quad \textbf{(4-2)}$$

The partial differential equations above are transformed into ordinary differential equations through Eq. (4-3), which gives the distance travelled by a sound wave in a moving media.

$$dx = (u + a)dt \quad \textbf{(4-3)}$$

The transformation procedure is thoroughly discussed by Anderson (2003) and it gives as result the C+ characteristic and C- characteristic (see Eq. (4-4) and Eq. (4-5)).

$$du + \frac{dp}{\rho a} = 0 \quad \textbf{(4-4)}$$

$$du - \frac{dp}{\rho a} = 0 \quad \textbf{(4-5)}$$

The Riemann invariants, J+ and J-, are constants that follow each of the C+ and C- characteristics. They are obtained when Eq. (4-4) and/or Eq. (4-5) are integrated along the C+ and/or C- characteristics. Eq. (4-6) and Eq. (4-7) are the Riemann invariants for fluids that behave like an ideal gas.

$$J_+ = u + \frac{2a}{k-1} = const. \quad \text{(along a C+ characteristic)} \quad \textbf{(4-6)}$$

$$J_- = u - \frac{2a}{k-1} = \text{const.} \quad \text{(along a C- characteristic)} \quad \textbf{(4-7)}$$

The speed of sound and the fluid velocity can be computed through equations (4-8) and (4-9) when a C+ characteristic intersects a C- characteristic and their Riemann invariants are known. These equations result from manipulating Eq. (4-6) and Eq. (4-7).

$$a = \frac{k-1}{4}(J_+ - J_-) \tag{4-8}$$

$$u = \frac{1}{2}(J_+ + J_-) \tag{4-9}$$

Then, the pressure, temperature and density reached by the fluid throughout the expansion wave are computed by implementing equations from Eq. (A- 7) to Eq. (A- 9) and the equation of state. This process requires the knowledge of the fluid state before or after the expansion wave.

Figure 4-5 shows an expansion wave in an x-t diagram. The red dotted lines represent different C+ characteristics whilst the blue continuous lines represent different C- characteristics, each of them with their own J+ or J- invariants. In this scenario, state c must be equal to d but different to e to satisfy Eq. (4-8) and Eq. (4-9). In the same way, state f must be equal to e but different to d.

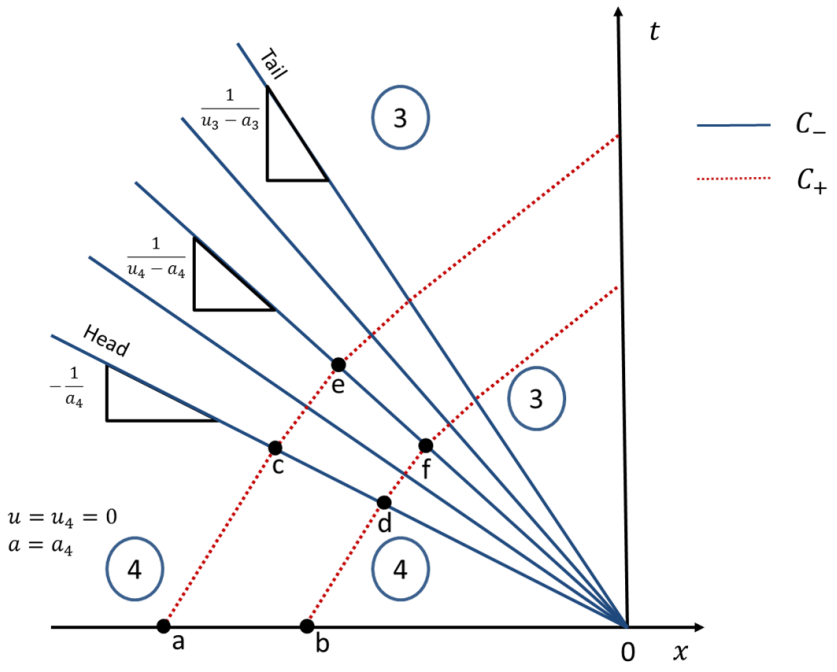

Figure 4-5 The C+ and C- characteristics for a cantered expansion wave (on an x t diagram)(Anderson 2003)

4.3 Thermal performance of aircraft gas turbines with PDEs as components of the cycle

Section 2.7.2 defined two options to attach PDEs into a turbofan. The first option involves an array of PDEs set downstream of the fan but outside the turbine's main cycle, whilst the second configuration implements an array of PDEs that substitutes the combustion chamber of the gas turbine.

The first option achieves an improvement in aircraft efficiency when compared with turbine cycles with after-burner, due to the advantage of isochoric combustion processes presented in section 1.2.2 (Mawid et al. 2000; M. A. Mawid et al. 2003). However, the kinetic energy of the fluid gets higher at the outlet of the gas turbine and therefore this configuration counteracts the advantages of turbofan engines with high by-pass ratios (Saravanamuttoo 2008). So, this option seems inadequate in civil aircraft.

Moreover, the second option gives a gas turbine's cycle closer to the Fickett-Jacobs cycle and therefore machines with better performance (see section 2.7.3). However, additional drawbacks must be solved; such as the conversion of kinetic energy from a pulsating source into pressure through a compact device, or the mixture of burned gases with dilution air in a manifold located upstream of the turbine to prevent damages due to thermal stress.

Based on the above, this work considers only the thermal evaluation of the second option. Therefore it is assumed that kinetic energy is transformed into pressure throughout a diffuser, the dilution air is well mixed with burned gases in a manifold located downstream of the PDEs array and an additional compressor is implemented to inject dilution air into the manifold.

The performance parameters considered during the evaluation are the efficiency of energy conversion, the specific thrust and the specific fuel consumption (see section 3.3).

The heat of combustion ($Q_{net,p}$) implemented to compute the efficiency of energy conversion is equal in magnitude to the enthalpy of combustion of

Kerosene, since the correction factor for isochoric trajectories is less than 0.2%, as demonstrated in Appendix B.

4.4 Developed code to evaluate the PDE performance

The in-house code implemented during the performance evaluation of PDE is constituted by three fundamental stages. The first stage is the main routine developed to compute the states reached by the working fluid during the turbine cycle through a thermal analysis of the process. Therefore, some operational parameters of the turbine's components are required during this stage.

The second stage is given by a sub-routine that interacts with NASA CEA code (Anon 2004) to predict the behaviour of the detonation process, the subroutine modifies an input file (*.inp) such as that observed in Figure 4-6, by including the fluid pressure and temperature expected during the injection of the reactant into the PDE, the required information is computed during the first stage.

```
prob
case=detonation  phi,eq.ratio=1 det t,k=1400.2 p,bar=1.2
react
  fuel=Jet-A(g)
  oxid=Air
output
     siunits massf transport
    plot rho p t gam son detvel gam1 t1 son1 u mw

end
```

Figure 4-6 Input data of CEA-NASA code

By default, the input data not only includes the reactants' temperature and pressure, but also the type of reactants, the trajectory of the combustion process (e.g. isochoric or isobaric trajectory) and the equivalence ratio. However, kerosene and air were set as reactants, since both fluids are commonly implemented in aircraft gas turbines. The equivalence ratio was set equal to 1 to ensure a stable detonation with low specific fuel consumption (Mawid et al. 2000; M. A. Mawid et al. 2003; Wintenberger et al. 2002; F. R. Schauer et al. 2005), and the ZND model was set to define the detonation trajectory (see section 2.5.2.1).

The third stage starts once the detonation is modelled by the NASA CEA code. In this stage the fluid's properties after the expansion that follows the detonation are computed through equations from Eq. (A- 7) to Eq. (A- 9). Then, the in-house code implements the method of characteristics to track the expansion wave attached to the detonation. In this case the Riemann invariant of the front C+ characteristic is computed using the fluid's properties after the detonation whilst the Riemann invariant of the rear C+ characteristic is computed with the fluid's properties after the expansion, such as was done by (Endo et al. 2004).

The arrival of the front C+ characteristic to the open end of the PDE defines the detonation time. At this condition, the code discriminates the sudden expansion process into three sub-stages as follows:

- *Sub-stage 1:* Fluid expansion with an outlet pressure higher than ambient due to the compression effect of the driven shock wave, as seen by (Wintenberger et al. 2003)
- *Sub-stage 2:* Fluid expansion and its throttling due to the recovering of external pressure
- *Sub-stage 3:* Fluid expansion and its throttling as consequence of the arrival of the rarefaction wave that remains inside the PDE.

Each of the sub-stages mentioned above generate a family of C- characteristics used to track the second expansion wave; an issue that will be discussed later on in this chapter.

At the closed end of the PDE the reflection of the rarefaction wave is modelled by fixing the fluid velocity equal to zero whilst the non-simple zone is estimated by computing the state of the fluid on the intersections of the characteristic lines. Both processes are addressed in detail by Anderson (2003).

The injection of new reactants starts when the pressure at the closed end is equal to the injection pressure previously defined by the fluid properties at the compressor discharge and the desired injection Mach number. The elapsed time from the cycle initiation to the injection of reactants is obtained by

implementing the pressure profile at the closed end of the PDE computed by the method of characteristics.

During the injection of new reactants, the temperature of the fluid inside the channel is assumed to be an average value between the burned gases and fresh reactants. Since the injection of new reactants starts with the whole PDE filled with burned gases at high temperatures and ends with reactant at low temperature.

Figure 4-7 shows the gas dynamic of a PDE predicted by the method of characteristics. The front of the rarefaction wave is denoted by a red line while the rear is represented by a green line. In addition, blue dots are used to indicate the intersection of the characteristic lines in the computational domain.

The average value of the fluid properties at the PDE discharge is calculated by post-processing the transient profile displayed by each of them through the mass-weighted average or the area-weighted average according to the type of property.

Once the average properties at the PDE discharge are obtained, the thermal analysis concludes by computing parameters such as the specific thrust, the specific fuel consumption, and the efficiency of energy conversion through equations from Eq. (3-3) to Eq. (3-5).

The main code is able to compute the PDE mass flow rate to estimate the number of PDEs able to drive the core flow of the gas turbine, if the PDE’s diameter or transversal area is defined.

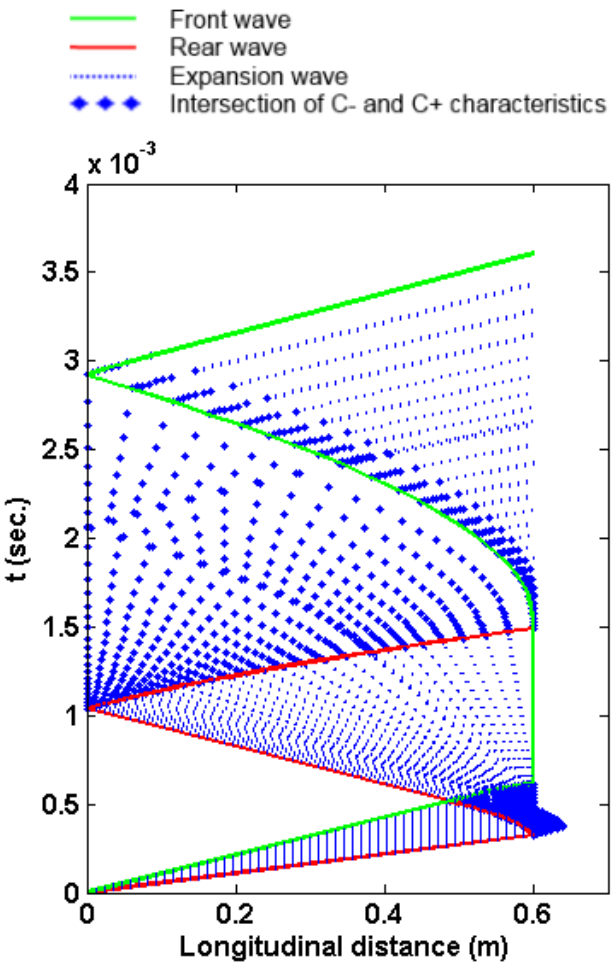

Figure 4-7 PDE gas dynamic evaluated through the method of characteristics

Moreover, the minimum diameter required by the array of PDEs to enclose the turbine shaft is computed from Eq. (4-10), where: $\emptyset_{in}$ represents the internal diameter of the PDEs array, $\emptyset_{PDE}$ the diameter of each PDE, and $\#_{PDE}$ the number of PDEs (see Figure 4-8).

$$\emptyset_{in} = \emptyset_{PDE} \cdot \frac{\left(1 - sin\left(\frac{\pi}{\#_{PDE}}\right)\right)}{sin\left(\frac{\pi}{\#_{PDE}}\right)} \quad \textbf{(4-10)}$$

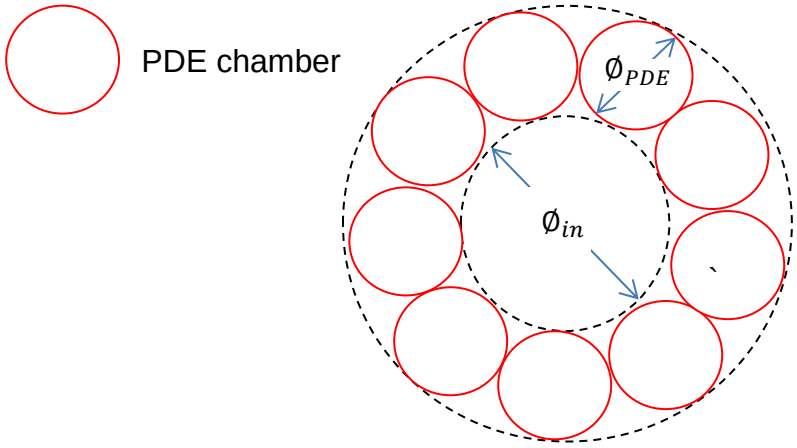

Figure 4-8 Representation of a PDEs array enclosing the gas turbine shaft

4.4.1 Sub-stage 1: Fluid expansion with an outlet pressure higher than ambient due to the compression effect of the driven shock wave

This sub-stage is implemented if the Mach number of burned gases is less than one for a reference system located at the wall of the PDE.

The code tracks the position and velocity of the contact surface to estimate the place where the outgoing rarefaction wave is reflected as well as the speed of sound reached by the C+ characteristic that arrives at the contact surface.

The values of velocity and speed of sound obtained at the contact surface are implemented to compute the Riemann invariants of the reflected C- characteristic, whose intersection with the outgoing C+ characteristic defines the non-linear zone represented by red dots in Figure 4-9.

Figure 4-10 illustrates the procedure followed by the in-house code to track the contact surface represented by the black dashed line that crosses states a, f and k. The fluid velocity and Mach number at state “a” are given by the Chapman-Jouguet condition. Then, these properties are calculated in state “f” by weighting states “a” and “b”. The surface's position is given by the C+ characteristic that crosses states “b” with a line that starts at state “a” whose slope is equal to the inverse of the computed velocity at the state f.

The process described above is performed to compute all the states that are over the contact surface until the elapsed time of sub-stage 1 is equal or higher than the time in which the pressure at the open end is equalised to the ambient pressure.

The fraction of time in which the rarefaction waves is reflected by the contact wave is estimated by implementing CFD models of a PDE based on the finite volume method, see section 4.5. The CFD models gave the result that less than 0.7% (in average) of the rarefaction is reflected and therefore the in-house code uses this value by default.

4.4.2 *Sub-stage 2:* Fluid expansion and its throttling due to the recovering of external pressure

This sub-stage starts by calculating the fluid's state at the open end after its expansion to the throttling condition and then the Riemann invariants for the gamma of C- characteristics that comprise the expansion wave.

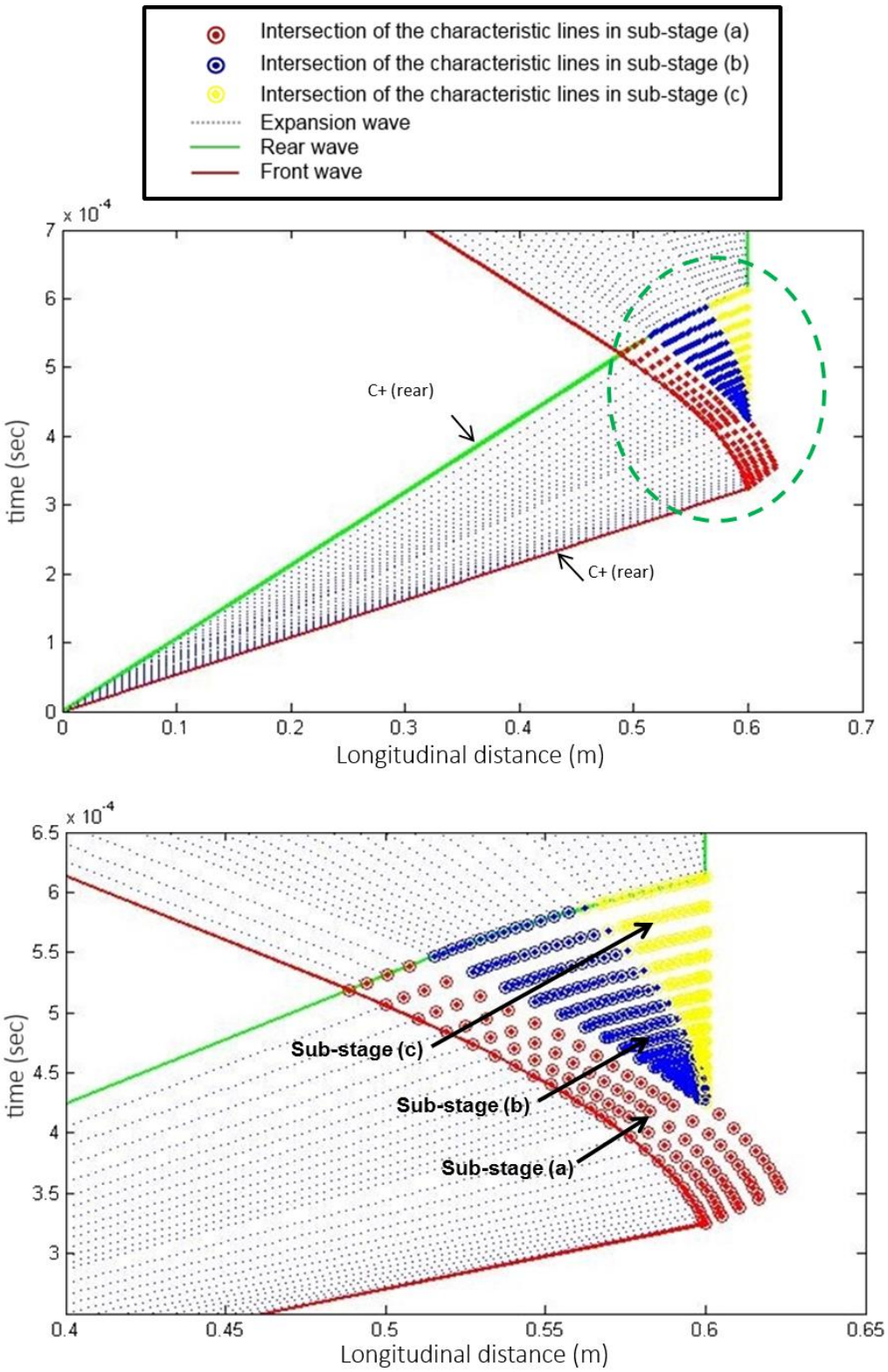

Figure 4-9 Sub-stages implemented by the in-house code to predict the fluid's sudden expansion

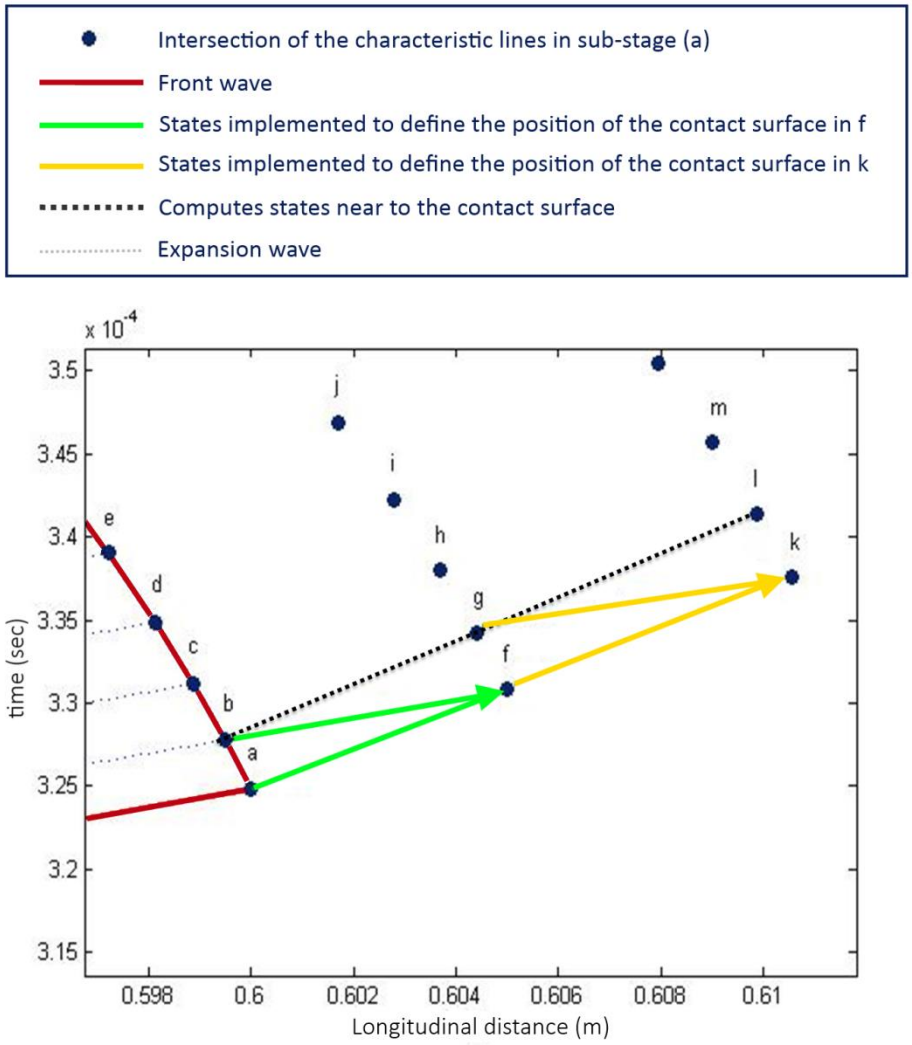

Figure 4-10 States implemented by the in-house code to estimate the contact surface

If the first sub-stage is computed then the initial state is obtained from an interpolation or an extrapolation of the distinct states located along the last C-characteristic of the first sub-stage. The interpolation is implemented if at least one state is located at each side of the PDE's open end while the extrapolation is implemented when states are outside the PDE, as indicated in Figure 4-11.

If sub-stage 1 is not computed as a consequence of an elevated Mach number of burned gases (Mach number higher than 1), then sub-stage two assumes the fluid's state to be equal to the C-J condition given by the NASA-CEA code,

neglecting the effect of the supersonic flow, such as the model proposed by (Endo et al. 2004).

Figure 4-12 shows the rarefaction wave generated during sub-stage 2. The front wave moves along the C- characteristic with subscript “a” which has the same Riemann invariant as the last C- characteristic of sub-stage 1. Whilst the rear-wave moves along the C- characteristic with subscript “z”, whose initial trajectory is vertical due to the fluid throttling, it starts penetrating the PDE once the following C+ characteristic of the first rarefaction wave arrives at the open end. The blue dotted zone in Figure 4-9 represents the sub-stage 2.

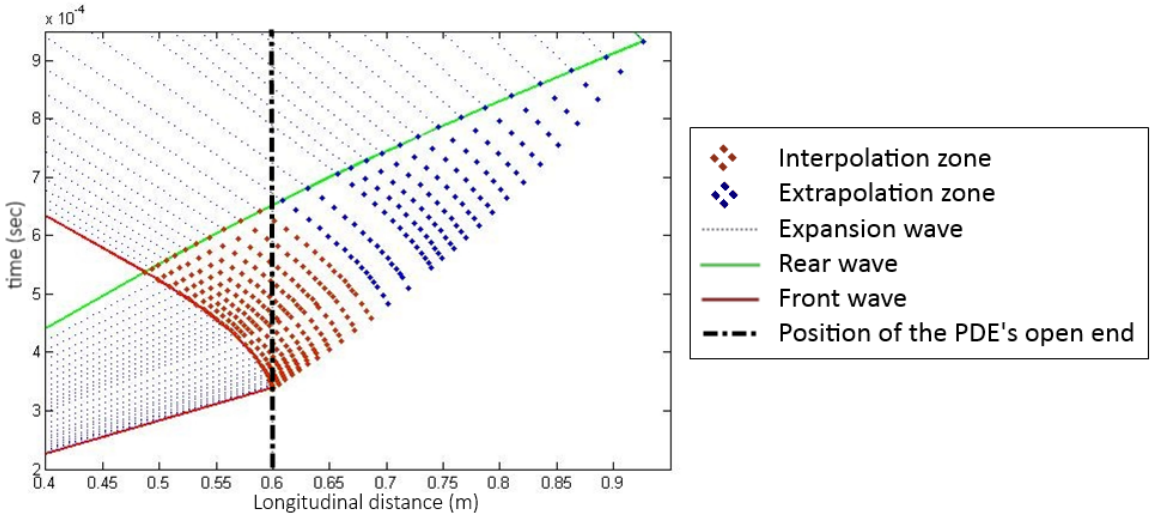

Figure 4-11 Interpolation zone (red dots) and extrapolation zone (blue dot) to compute the source state of the rarefaction wave (second sub-stage)

4.4.3 *Sub-stage 3:* Fluid expansion and its throttling as consequence of the arrival of the rarefaction wave that remains inside the PDE.

The arrival of the remaining rarefaction wave to the open end produces a pressure drop. The in-house code models this condition assuming an infinitesimal period of time where the flow is throttled again through a micro-expansion process. The state is defined by the intersection of the vertical C-

characteristic that comes from the previous expansion and the C+ characteristic that arrives at the open end.

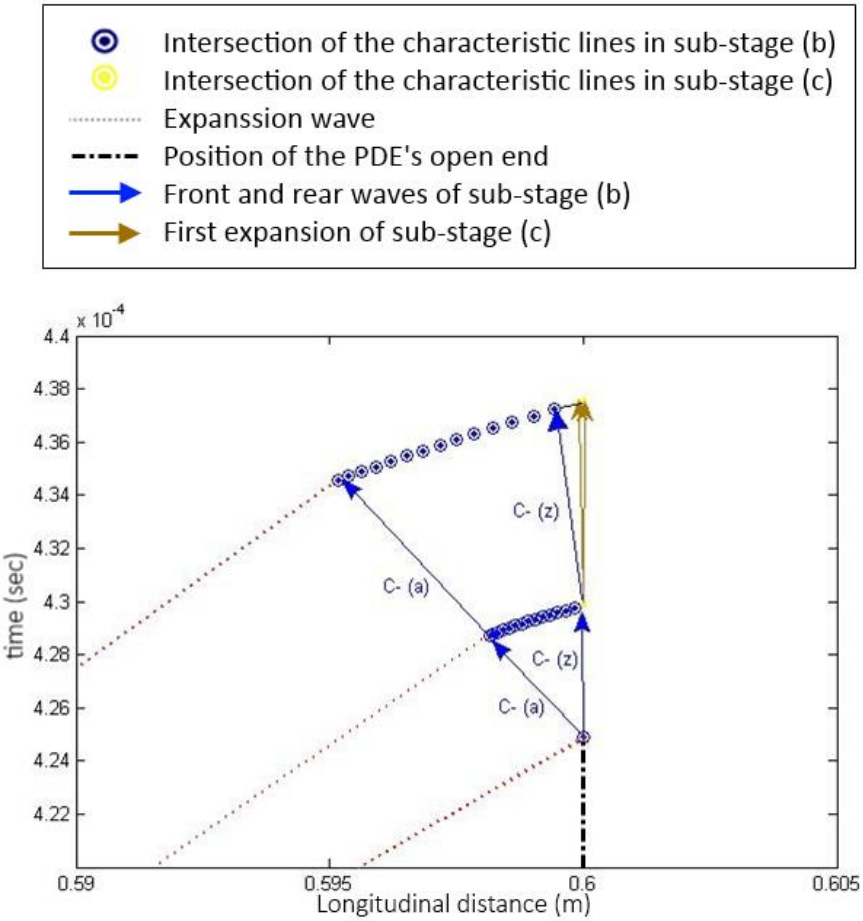

Figure 4-12 Representation of the second sub-stage

An infinite number of C- characteristics are generated during the micro-expansion. However, the in-house code only considers the front and rear waves of the rarefaction wave to avoid increasing the resolution of C- characteristics in this sub-stage (see Figure 4-13).

The Riemann invariant of the vertical C- characteristic is obtained after computing the speed of sound at the throttled end through equations from Eq. (A- 7) to Eq. (A- 9). The yellow dotted zone in Figure 4-9 represents the sub-stage 3.

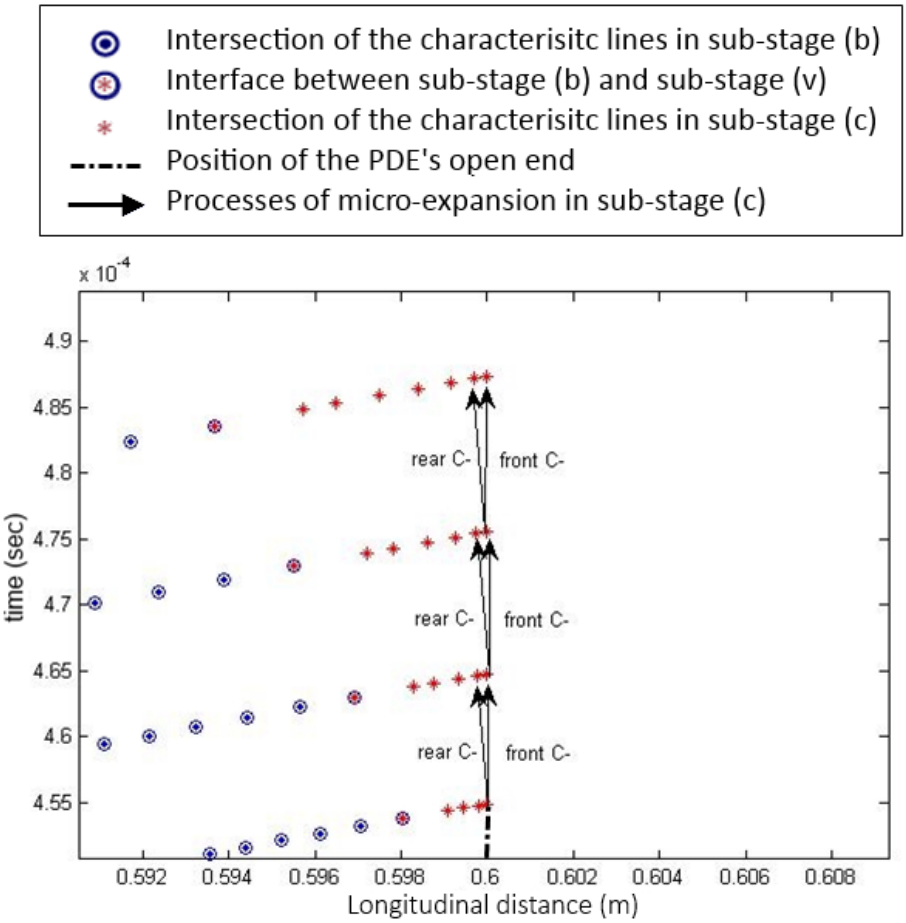

Figure 4-13 C- Characteristics considered at the open end of the PDE to model the last sub-stage

4.5 In-house code calibration

Based on the theoretical analysis of PDE, once the detonation wave arrives to the open end of the PDE, the outgoing rarefaction wave is reflected by the contact wave and it starts interacting with the fluid inside the PDE if the condition at the open end of the device is not throttled; model proposed by Wintenberger et al. (2003) and studied in section 4.4.1.

The in-house code is able to model the effect described above, however, there is no criterion able to define the interval of time in which these conditions happen during the whole PDE's cycle because the reflection of the rarefaction wave is linked to the pressure perturbations that occur outside of the PDE.

It is important to know the conditions of the fluid that propitiate a detonation with a subsonic flow behind it to start gaining experience about the reflection of the rarefaction wave at the contact surface,. Therefore, different simulations are performed in the NASA CEA code in which the compressor pressure ratio is changed between 1 and 16, the injection Mach number is changed between 0.2 and 0.8 and the PDE length is changed in a range between 0.3 and 0.6.

Figure 4-14 presents the flow condition behind the detonation predicted by the NASA CEA code, 1 indicates supersonic flow and 0 indicates subsonic flow. The simulation demonstrated that only an injection Mach numbers near to 0.2 is able to produce a subsonic condition behind the detonation and therefore the reflection of the rarefaction wave is limited only to that condition.

A better comprehension of the phenomena is intended to be achieved by modelling the PDE in ANSYS FLUENT®. A sensitivity analysis is performed before the evaluation to ensure independent results from the space and time discretisation. Section 0 describes in depth the procedure followed and the final model, while Table 16 and Table 17 show the properties implemented to inject dilution air and reactants into the domain with a Mach number equal to 0.2 (boundary conditions “inlet2” and “inlet1” in Figure 4-33).

Figure 4-15 shows the pressure profile at the open end of the PDE predicted by ANSYS FLUENT® for different PDE’s lengths. The asterisks are used to represent a chocked condition. The flow at the rear of the detonation wave is supersonic as the asterisks indicate, so the open end is chocked once the detonation wave arrives. This condition occurs in a small period of time and then it is followed by a subsonic condition and a supersonic condition again during the arrival of the outgoing rarefaction wave (rarefaction wave shown in Figure 4-3).

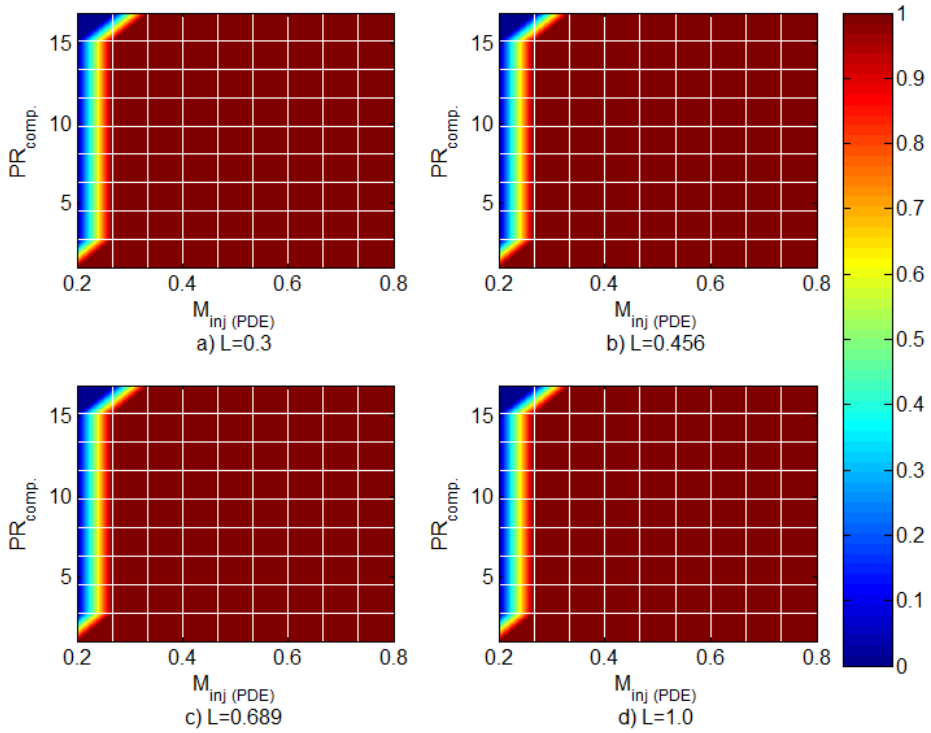

Figure 4-14 Throttling condition at the open end of the PDE as consequence of the turbine compressor ratio, the PDE injection Mach number and the PDE length (red – throttled flow, blue – un-throttled flow)

Table 16 Values implemented by the CFD models to inject dilution air into the Manifold

Dilution air (Total Properties)		
T_0	576.3	K
p_0	5.1	atm
p	4.97	atm
Dilution air (mass fraction)		
Y_{O_2}	0.23	n/a
Y_{N_2}	0.77	n/a

Table 17 Values implemented by the CFD model to set the injection of reactants into the PDE

Reactants injection (Total Properties)		
T_0	576.3	K
p_0	5.1	atm
p	4.97	atm
Seal air (mass fraction)		
Y_{O_2}	0.23	n/a
Y_{N_2}	0.77	n/a
Reactants (mass fraction)		
Y_{O_2}	0.218	n/a
Y_{N_2}	0.718	n/a
Y_f	0.064	n/a

Y_{O_2}

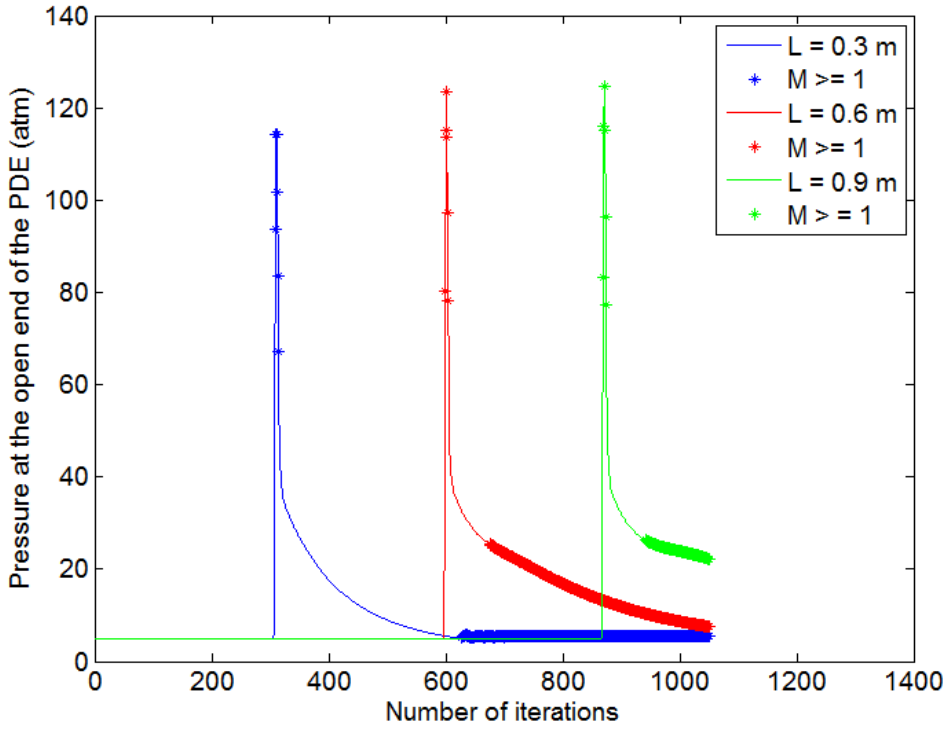

Figure 4-15 Pressure profile at the PDE's open end for different PDE lengths (asterisk indicates chocked conditions)

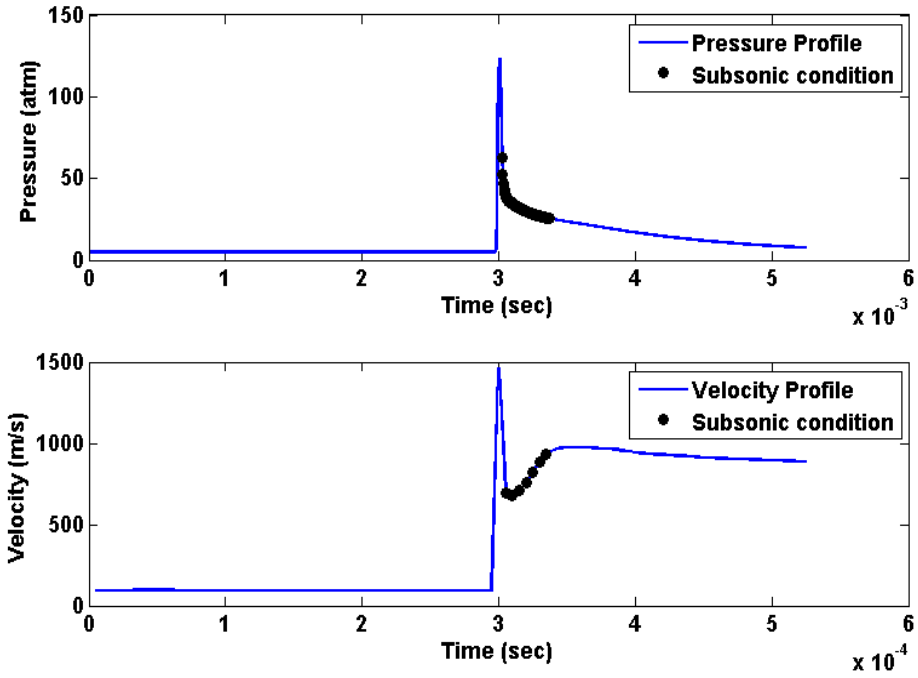

Figure 4-16 Pressure (top) and velocity (bottom) profile at the PDE's open end (black dots indicate a subsonic condition after the detonation)

Figure 4-16 presents the velocity profile predicted by ANSYS FLUENT® and the dots are used to denote a subsonic condition after the detonation arrival at the open end. The observed increase of the flow velocity during the subsonic condition and the smooth change of the pressure profile between the subsonic and supersonic flow are important aspects to be highlighted, since this behaviour contrasts with the model proposed by Wintenberger.

A comparison between Figure 4-17 and Figure 4-3 is useful to understand the discrepancies observed. Firstly, an increase of the flow velocity must produce a reduction of the slope displayed by the contact wave in an x-t diagram. Secondly, a C- characteristic able to increase the flow Mach number to one must be vertical and therefore it is unable to reach the open end of the PDE if it is reflected by the contact surface.

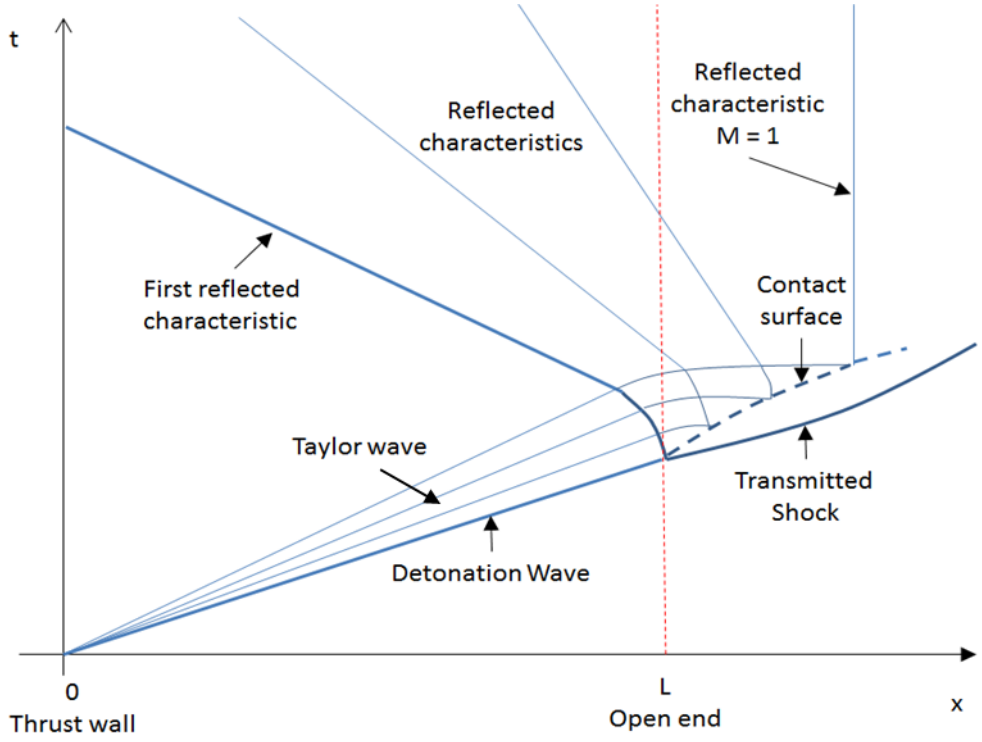

Figure 4-17 Characteristics of the transient process observed in a 2D model of the PDE when the injection Mach number is equal to 0.2

Based on the above, the behaviour predicted by ANSYS FLUENT® must be produced by a different source than that described by Wintenberger. The discrepancy could be a consequence of the simple combustion model implemented in ANSYS FLUENT®, since it predicts a supersonic flow attached to the detonation wave at low injection Mach numbers in contrast to the subsonic flow anticipated by the NASA CEA code. The supersonic condition isolates the fluid contained inside the PDE from the contact wave and therefore the reflection of the rarefaction wave is unfeasible.

Due to the absence of additional information able to explain the phenomenon, the in-house code is modified to allow only the reflection of the first and second C+ characteristics contained inside the rarefaction wave (0.7 % the width of the rarefaction wave in average) when the injection Mach number is equal to 0.2 (see Figure 4-18). This approaches allows a smoother increase of the velocity than the profile produced by the sudden throttling and it prevents a reduction of

the flow velocity at the open end; a balance between the model of Wintenberger and the 2D CFD prediction.

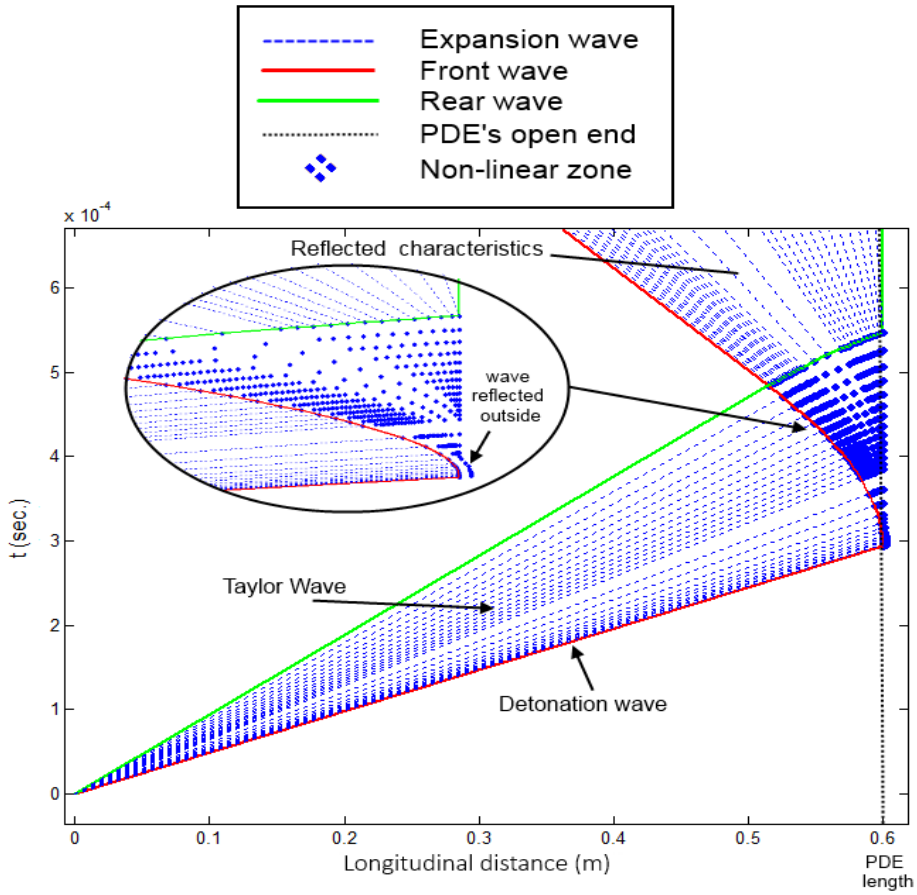

Figure 4-18 Characteristics of the transient process observed in a 2D model of the PDE when the injection Mach number is equal to 0.2

4.6 Performance evaluation of a PDEs array connected into a gas turbine

The performance of PDEs as a component of gas turbines is evaluated by using the same baseline turbine implemented in chapter 3 (turbofan engine for business jets), see Table 1. The control variables are the injection Mach number, the PDEs length and the compressor pressure ratio.

The exhaust temperature of the PDE is not a control variable in this case, since the reactive mixture must be at the stoichiometric conditions inside the chamber (Mawid et al. 2000; M. A. Mawid et al. 2003; Wintenberger et al. 2002; F. R.

Schauer et al. 2005). Therefore, the detonation inside the PDE produces burned gases whose elevated temperature must be reduced to prevent damages in the turbine.

Based on the above, a temperature control can be set by mixing burned gases with cold air in a manifold located downstream of the device. This technique is equivalent to the injection of dilution air into conventional combustion chambers but in this case the dilution air requires an additional compression before it is injected inside the manifold. Figure 4-19 show a t-s diagram that represents the new cycle.

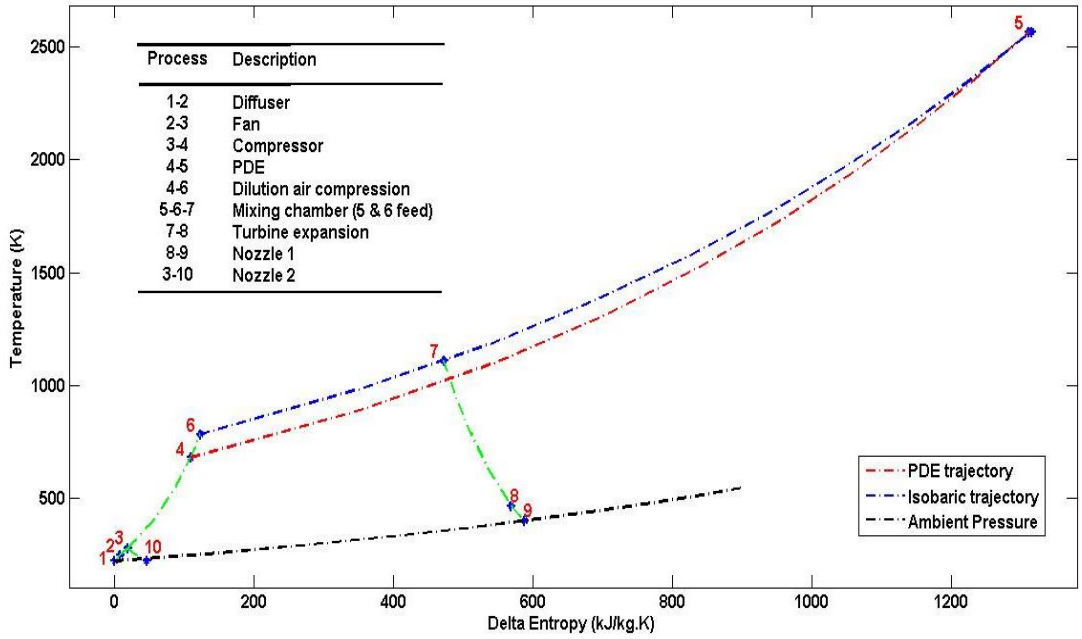

Figure 4-19 T-s diagram of a gas turbine with a PDEs array as combustion chamber

Through the performance evaluation, the injection Mach number changes in a range between 0.2 and 0.8, the PDEs' length changes in a range between 0.3 m and 1.0 m, and the compressor pressure ratio changes in a range between 1 and 16.91.

Although the thermal evaluation of the cycle considers the gas turbine specific thrust, the specific fuel consumption and the efficiency of energy conversion,

other variables such as the number of PDEs required by the turbine, the compressor pressure ratio for the dilution air and the PDEs frequency are also discussed.

4.7 Thermal evaluation

This section presents an analysis about the specific thrust, specific fuel consumption and efficiency of energy conversion obtained during the performance evaluation of PDEs as the combustion chamber of future gas turbines. The evaluation of the thermal cycle is performed assuming cold standard air to keep the same baseline cycle as that implemented during the WR evaluated in chapter 3.

Figure 4-20 shows the specific thrust obtained from the simulation, this variable is strongly influenced by the pressure ratio and it achieves its maximum when the compressor pressure ratio is between three and six.

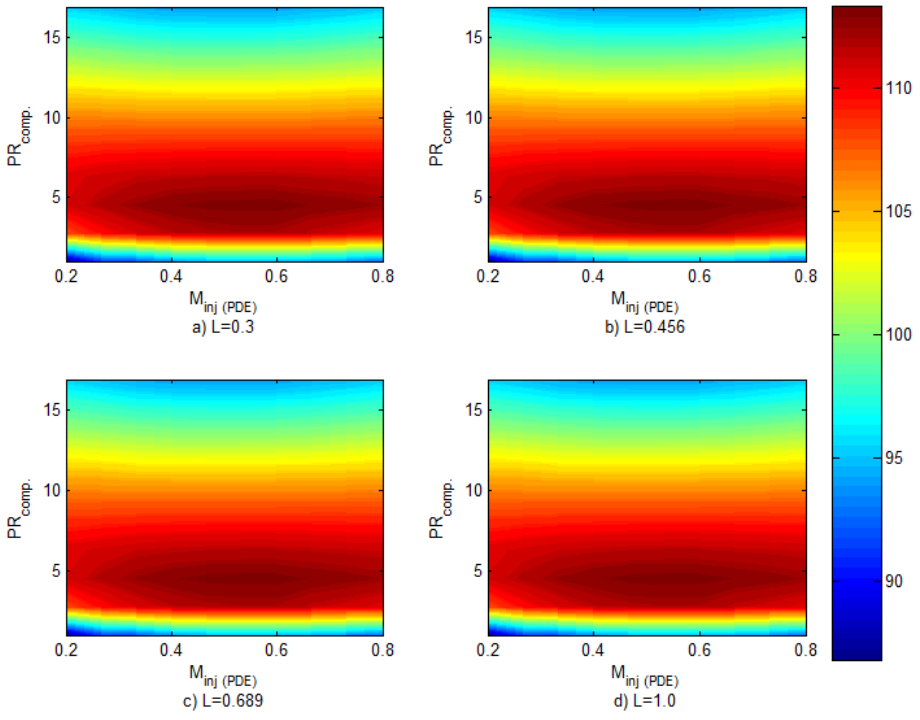

Figure 4-20 Specific thrust F_s in $(N \cdot s/kg)$– Performance evaluation of PDEs

The specific thrust is less influenced by the injection Mach number. However, the better performance is obtained when the injection Mach number is between

0.4 and 0.6. The length of the PDEs does not have a significant influence in the studied variable.

The maximum specific thrust is 113 N.s/kg obtained when the injection Mach number is 0.533, the compressor pressure ratio is 4.54 and the PDEs' length is 0.3.

Figure 4-21 shows values of specific fuel consumption "SFC" obtained from the simulation. The SFC is inversely influenced by the compressor pressure ratio; its minimum values are found when the compressor pressure ratio is over 10.

The injection Mach number has a smaller influence in the SFC than the compressor pressure ratio. However, the SFC achieves its lowest values when injection Mach number is in a range between 0.3 and 0.7.

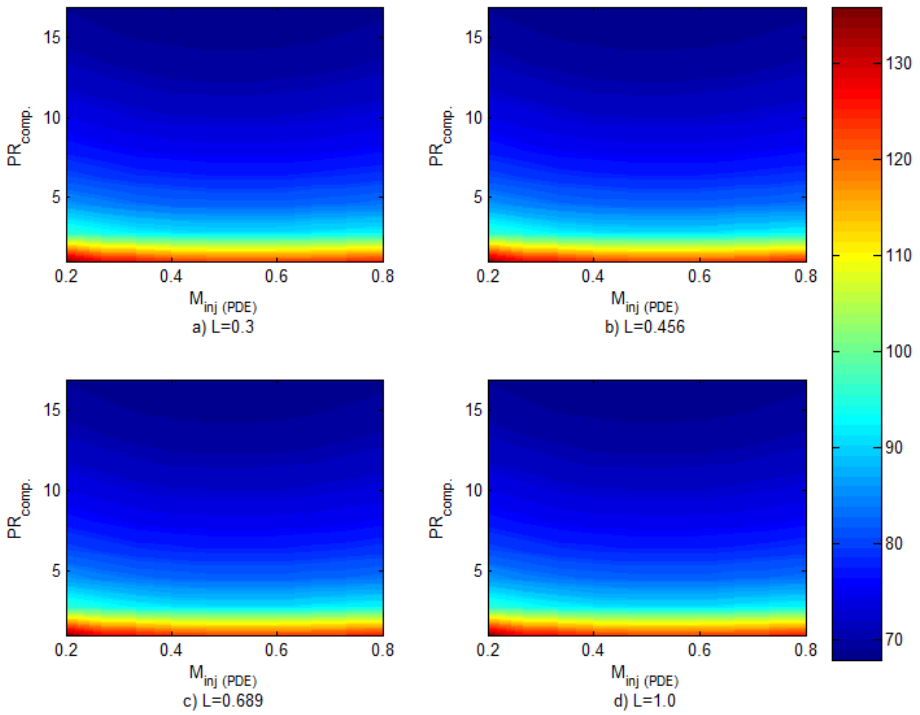

Figure 4-21 Specific fuel consumption (SFC) in $(kg/kN.h)$– performance evaluation of PDEs

The length of PDEs does not have significant influence on the studied variable as it happens with the specific thrust. The minimum SFC is 66.7 $kg/kN.h$

obtained for a compressor pressure ratio of 16.91, an injection Mach number of 0.533 and a PDEs' length of 0.3 m.

Figure 4-22 shows the efficiency of energy conversion obtained from the simulation. This variable is highly influenced by the compressor pressure ratio such as the previous cases, but its maximum values are obtained for pressure ratios between 9 and 12.

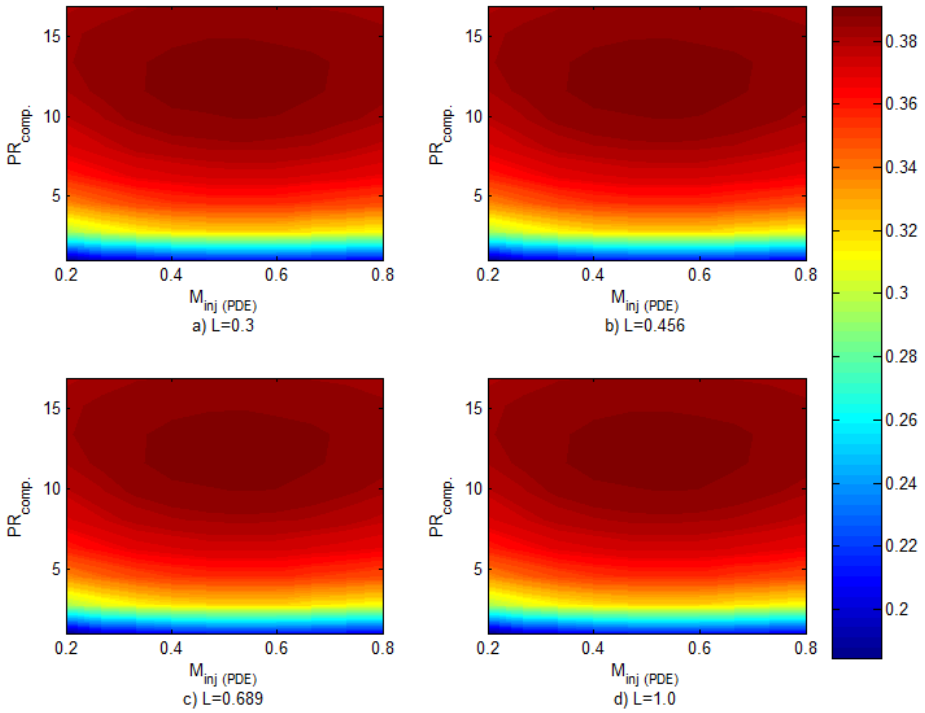

Figure 4-22 Efficiency of energy conversion (η_e) -performance evaluation of PDEs

The injection Mach number has a smaller influence in the efficiency of energy conversion than the compressor pressure ratio. However, the best performance is obtained if the Mach number is between 0.3 and 0.7.

The length of the PDEs does not have an appreciable effect on this variable, such as happened with the SFC and the specific thrust. The maximum efficiency of energy conversion is 0.402 obtained when the compressor pressure ratio is 9.84, the injection Mach number is 0.333 and the PDEs' length is 0.841 m.

4.8 Analysis of additional variables

4.8.1 Relationship between the number of PDEs and their diameter

Figure 4-23 shows the contour given by Eq. (4-11) which gives an idea about the number of PDEs required to drive the mass flow of the gas turbine when their diameter is fixed.

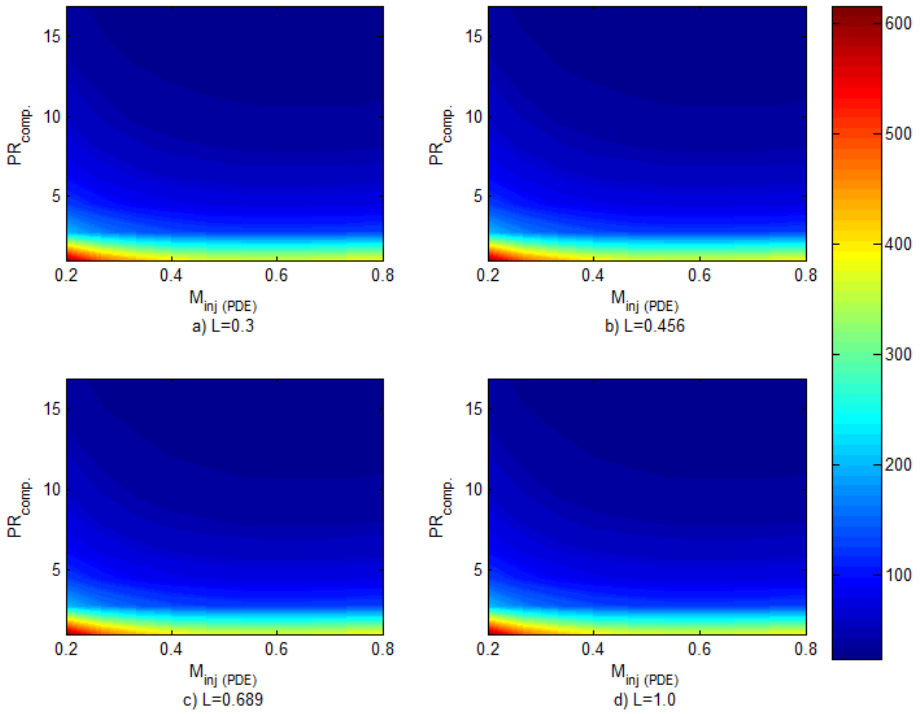

Figure 4-23 Contour of Eq. (4-11) (m^2)– performance evaluation of PDE

$$\#_{PDE}.\emptyset_{PDE}^2 = \mathrm{f}\left(L, M_{inj}, PR_{comp}\right) = \frac{\dot{m}_{core}.\Delta t_{cycle}.4}{\pi.\rho.L} \qquad \textbf{(4-11)}$$

The number of PDEs $(\#_{PDE})$ increases when the compressor pressure ratio and/or the injection Mach number are/is reduced. This effect is a consequence of the density reduction experienced by a fluid when the pressure decreases and/or the reduction of the PDEs operational frequency due to an increase of the filling time.

Moreover, the increase of the PDEs' length has negligible effects on the diameter, since the operational frequency behaves inversely proportional to the

PDEs' length, so the diameter is unchanged to manage the same mass flow required by the turbine. The maximum and minimum values obtained from this variable are 0.986 and 0.0384.

4.8.2 PDEs operational frequency

Figure 4-24 shows the cycle frequency obtained during the PDEs evaluation, the highest value is 772 Hz per PDE obtained at elevated compressor pressure ratios, elevated injection Mach numbers and shorter PDEs.

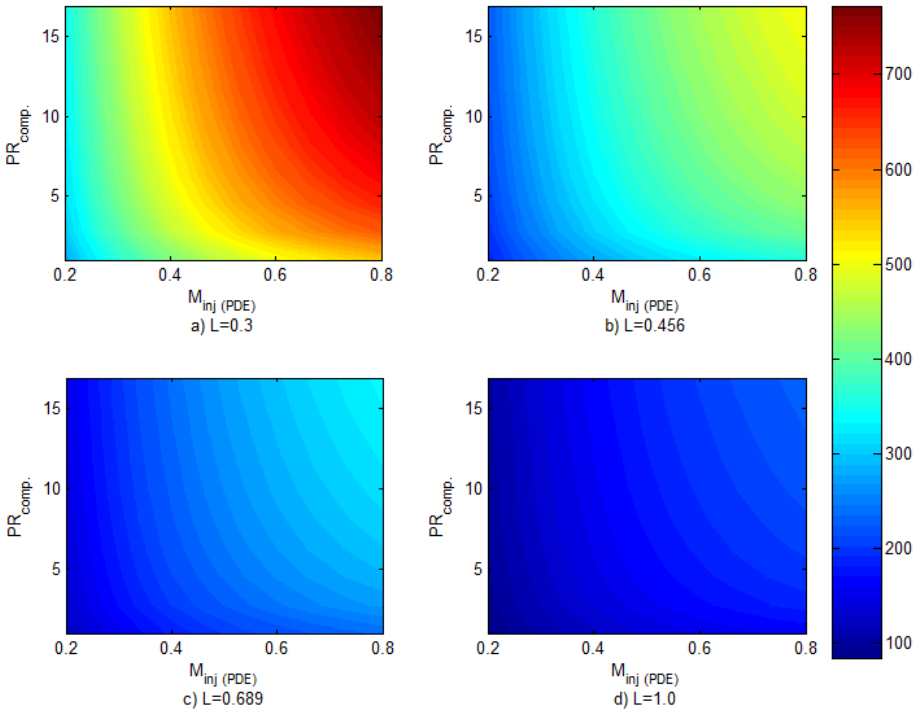

Figure 4-24 PDE frequency (Hz) -performance evaluation of PDEs

Moreover, a larger PDE requires longer intervals of time per cycle to drive the mass flow and therefore its frequency can decrease to a minimum of 84.8 Hz.

4.8.3 Compressor pressure ration of dilution air

Figure 4-25 shows the additional compressor pressure ratio required to inject the dilution air into the manifold located downstream of the PDEs array (path 4-6 of Figure 4-19), to reduce the temperature of burned gases before the turbine feeding.

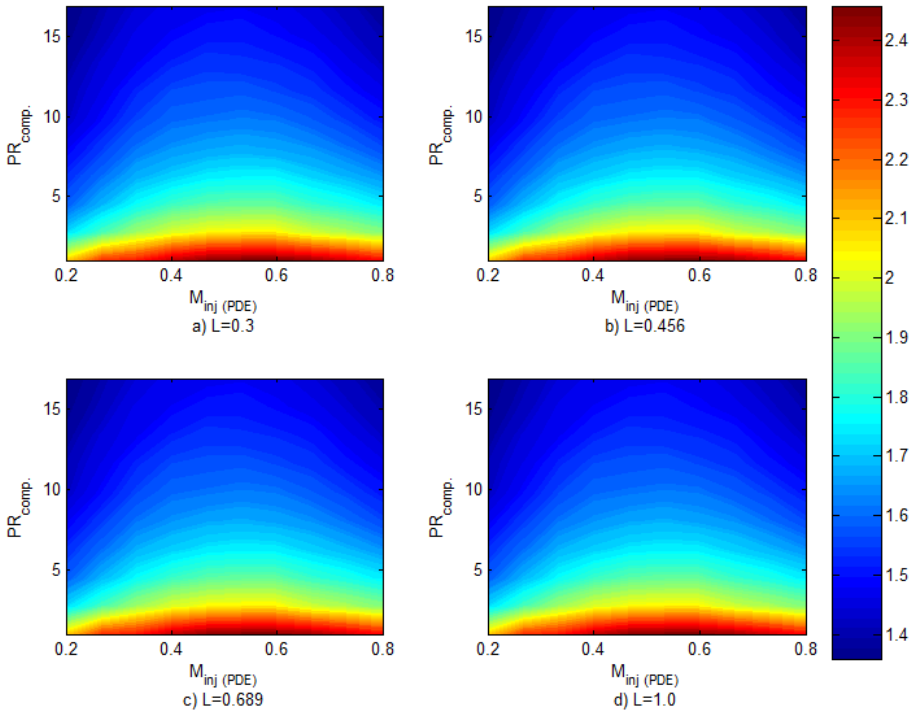

Figure 4-25 Additional compressor pressure ratio for the dilution air (path 4-6 of Figure 4-19) - performance evaluation of PDEs

The simulation indicates that higher compressor pressure ratios for the dilution air are necessary at low compressor pressure ratios of the core flow. The situation deteriorates if the injection Mach number is set between 0.3 and 0.7. The pressure ratio of the additional compressor achieved a maximum of 2.46 and a minimum of 1.36 during the whole experiment. The channel's length has a negligible influence in the studied variable

4.9 Frequency and Amplitude spectra of PDEs

Considering the aim of this work, the best option is a PDEs array with the lowest SFC since it promotes a reduction of gas turbine emissions. However, the analysis performed above does not define a unique PDEs' geometry, since the SFC is little influenced by the length of the PDEs. Therefore a different criterion must be set to obtain the device's geometrical configuration.

In this regard, this section pretends to compare the frequency spectrum between different PDEs' arrays and the expected from a gas turbine

combustion chamber. The selected option must vibrate with similar vibrational modes to the combustion flame to prevent the turbine resonance. The evaluated parameters are the PDEs' length and its diameter, since the first parameter has a strong influence on the device operational frequency while the second parameter is linked to the number of PDEs that drive the core flow of the turbine and therefore it is associated to the amplitude of the attenuated pressure signal in the manifold.

In a typical combustion chamber, the burners' vibrational spectrum changes between 31.5 Hz and 16000 Hz and displays two peaks frequencies. One peak is at the low frequency spectrum (from 200 Hz to 500 Hz) as a consequence of combustion roar and the other peak is at the high frequency spectrum as consequence of fuel jet injection (from 1000 Hz to 8000 Hz.), see Figure 4-26 (Baukal & Schwartz 2001).

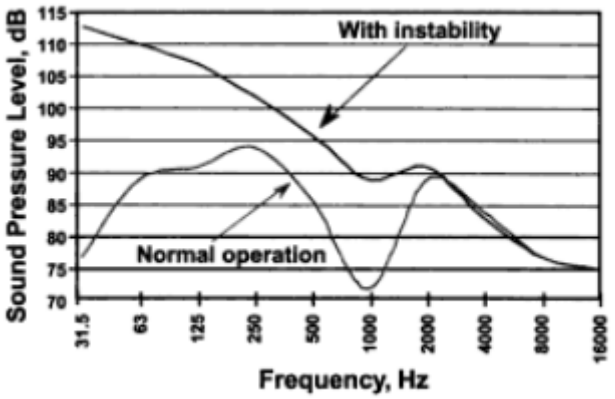

Figure 4-26 Sound pressure levels in burners (Normal operation and instability) (Baukal & Schwartz 2001)

To achieve the goal, a new code able to evaluate the amplitude spectrum generated by the PDEs array is built, the evaluation is performed through the following steps:

- The static pressure profile at the open end of a single PDE predicted by the code developed in section 4.4 is homogeneously replicated through the interval of time of a single PDE cycle a number of times equal to the number of PDEs that comprise the array

- An average pressure profile is computed from the homogeneous distribution mentioned above. This new profile of pressure is called attenuated signal and it is used as the pressure profile generated inside the manifold
- The attenuated signal is decomposed through the fast Fourier transform and the amplitude spectrum obtained is compared with the frequency spectrum expected in a combustion chamber

Figure 4-27 shows the pressure signals at the open end of seven PDEs homogeneously distributed through a single PDE's cycle and the attenuated signal generated in the downstream manifold; all of them processed by the new code. The signals at the open ends are denoted by coloured lines while the attenuated signal is represented by a dotted line.

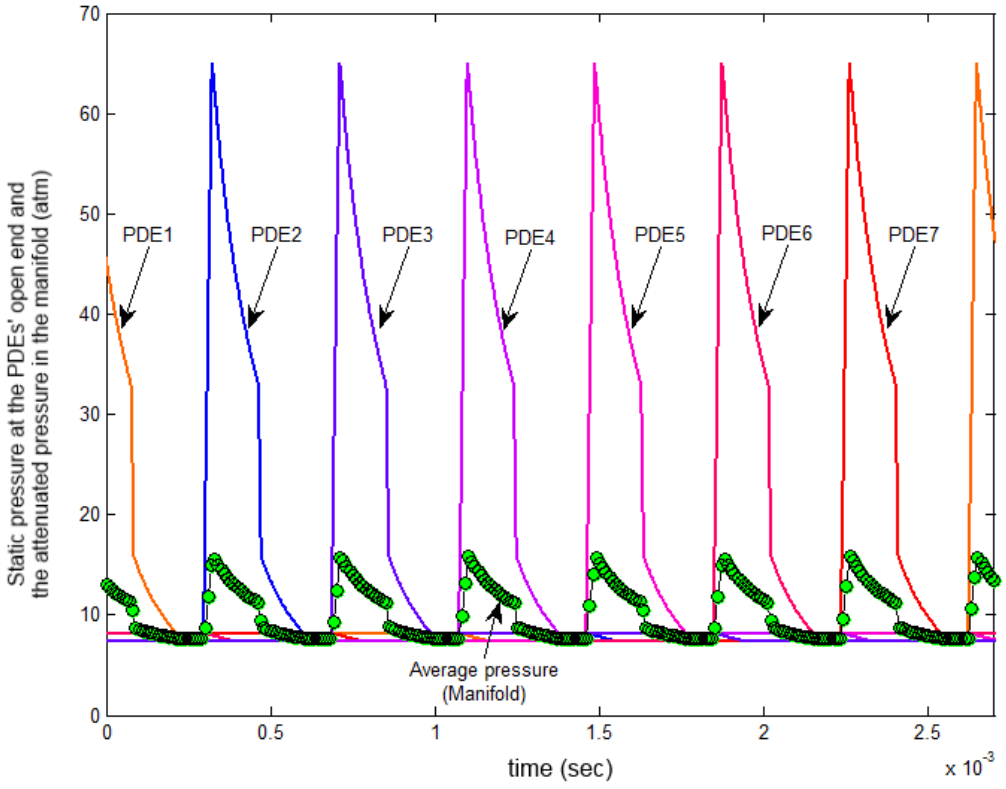

Figure 4-27 Signals of absolute static pressure at the open end of seven PDEs operating in sequence and the attenuated pressure signal (average pressure) in the downstream manifold

The input data is free of experimental noise since it comes from a deterministic technique. Therefore, the Fourier decomposition must split the attenuated signal into sinusoidal functions called harmonics. Among the characteristics of the harmonics, the existence of a fundamental frequency (f_0) that has the highest amplitude and the lowest frequency, as well as the presence of multiple sinusoidal functions whose frequencies are related to the fundamental frequency, is highlighted.

Figure 4-28 shows the decomposition of a square wave through multiple sinusoidal functions that correspond to the Fourier series shown in Eq.(4-12)., where ω_0 represents the angular frequency , t the evaluated time and $f_{(t)}$ the square wave.

The red curves represent the consecutive sum of the displayed sinusoidal functions. The error of the approximation is reduced when more components of the Fourier series are included (see Figure 4-28 (d))

$$f_{(t)} = \frac{4}{\pi} cos(\omega_0 t) - \frac{4}{3\pi} cos(3\omega_0 t) + \frac{4}{5\pi} cos(5\omega_0 t) - \frac{4}{7\pi} cos(7\omega_0 t) + error \quad \textbf{(4-12)}$$

Besides, the sinusoidal wave displayed in Figure 4-28 (a) has the maximum amplitude and minimum frequency in respect to the other sinusoidal functions. Therefore, this wave is driven by the fundamental frequency.

Figure 4-29 presents the amplitude spectrum of the squared wave shown in Figure 4-28. The first jump discontinuity is given by the fundamental frequency so the amplitude must be equal to the amplitude of the sinusoidal wave displayed in Figure 4-28 (a), while the second, third and fourth jump are obtained from the other sinusoidal waves and their frequency is related to the fundamental frequency by a ratio of 3, 5 and 7, as Figure 4-28 indicates.

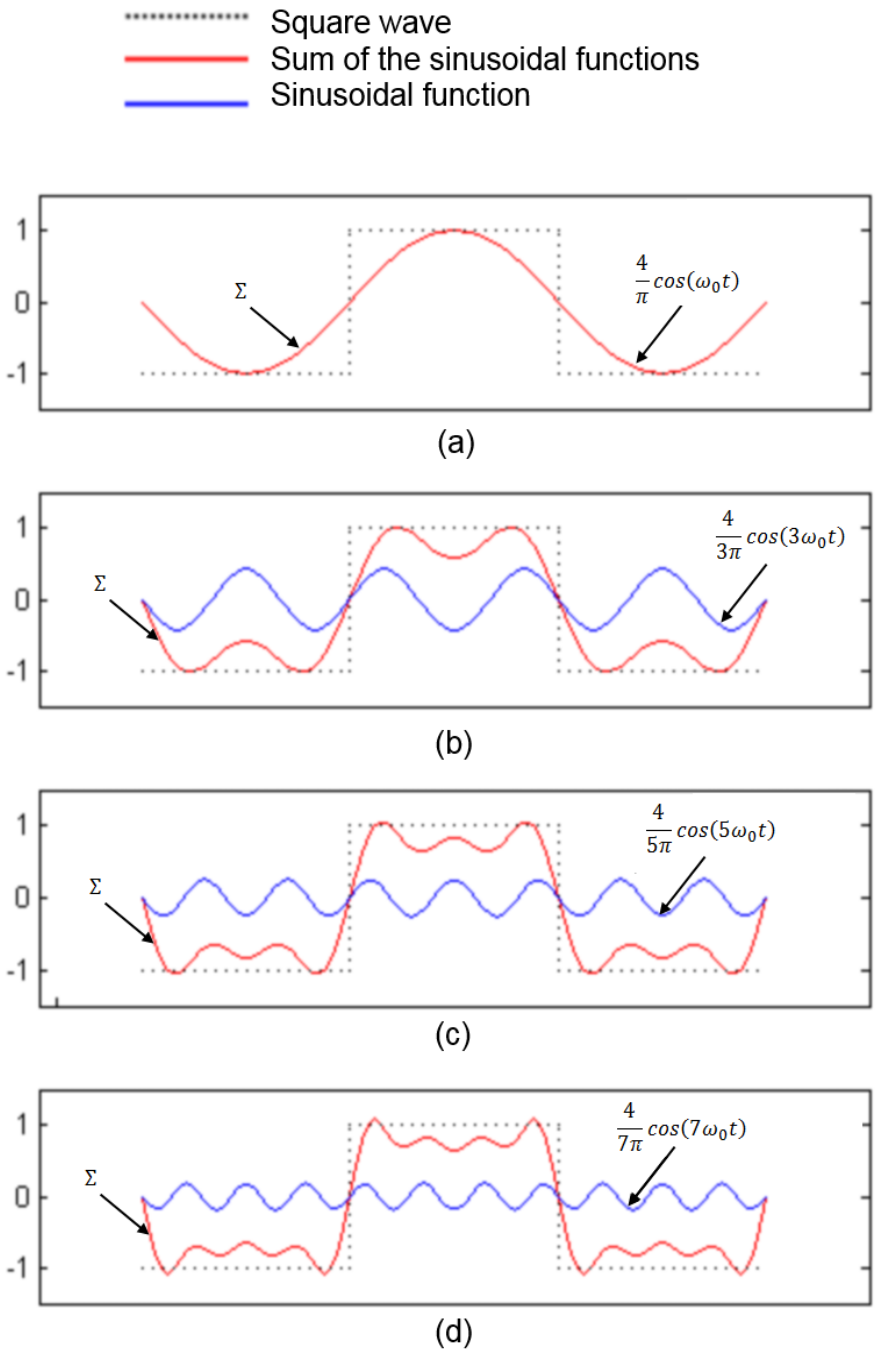

Figure 4-28 Approximation of the Fourier series of an square wave with 2 units of height and a period of $T = 2\pi/\omega_0$ (Chapra & Canale 2005)

The decomposition performed by the new code is achieved by implementing the algorithm of the Fast Fourier Transform "FFT" included in MATLAB (The

MathWorks Inc 2011). The FFT algorithm needs the examples of the attenuated signal (dotted line in Figure 4-27) but uses the signal average value (change of reference) as reference and the number of FFT points (computed as the power of two of the data samples) as input parameters. The change of reference frame is done through Eq.(4-13); where the subscript (*) indicates the attenuated signal of the new reference frame.

$$p_{att}{}^{*}(t) = p_{att}(t) - \bar{p}_{att} \quad \textbf{(4-13)}$$

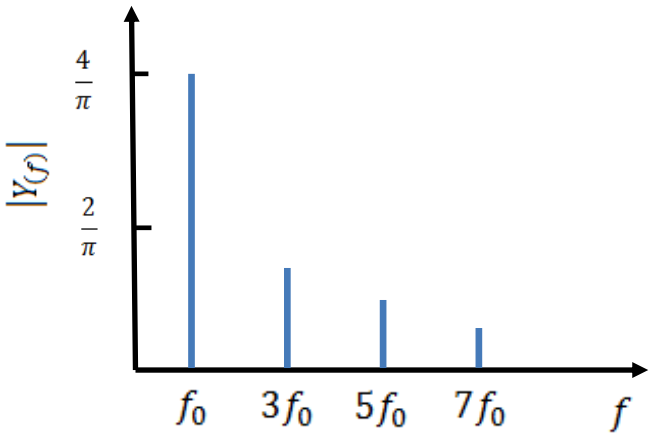

Figure 4-29 Amplitude spectrum of the waves that comprise the Fourier decomposition of the squared wave shown in Figure 4-28 (Chapra & Canale 2005)

The performed evaluation considers PDEs' lengths of 0.3, 0.6 and 0.9 meters and PDEs' diameters of 0.04, 0.06, 0.08 and 0.1 meters. The number of examples is changed between 1551 and 4683, the data frequency is 0.1 MHz and the time length of the signal is changed between 20 milliseconds and 80 milliseconds. The data does not implement zero-padding.

The parameters above ensure a waveform frequency resolution between 22 HZ and 65 HZ and a FFT resolution between 12 Hz and 49 Hz; both resolutions are below of the 2.28 % of all the fundamental frequencies computed during the analysis. Table 18 shows the values obtained in each case of the evaluation while Figure 4-30 and Figure 4-31 show the single-sided amplitude spectrum produced by the evaluated arrays; $|Y(f)|$ represents the amplitude of the

sinusoidal waves ascribed to the harmonics frequency (f) (see Figure 4-29), $|Y(f)|$ is in atmospheres and (f) in Hz.

Table 18 Quality of the signal evaluated by the FFT

	Ø=0.04 m				Ø=0.06 m			
L (m)	Fs (kHz)	f_{FFT} (Hz)	f_w (Hz)	No. of samples	Fs (kHz)	f_{FFT} (Hz)	f_w (Hz)	No. of samples
0.3	101	49	65	1551	101	49	65	1551
0.6	100	25	32	3091	100	25	32	3091
0.9	100	12	22	4631	100	12	22	4631
	Ø=0.08 m				Ø=0.1 m			
L (m)	Fs (kHz)	f_{FFT} (Hz)	f_w (Hz)	No. of samples	Fs (kHz)	f_{FFT} (Hz)	f_w (Hz)	No. of samples
0.3	101	49	65	1551	101	49	65	1551
0.6	100	25	32	3091	100	25	32	3091
0.9	100	12	22	4631	100	12	22	4631

A direct comparison between Figure 4-26, Figure 4-30 and Figure 4-31 indicates that only the studied cases with a length of 0.9 m are able to operate within the frequency spectrum between 31.5 Hz and 16000 Hz. In contrast, PDEs' lengths of 0.6 and 0.3 produce a frequency spectrum up to 22500 Hz and 45000 Hz.

The fundamental frequency (f_F) behaves inversely proportional to the PDEs' length and changes from 954 Hz to 15 kHz, the first case is for a PDEs array with a length of 0.9 and a diameter of 0.1m whilst the second case is for a PDEs arrray with a length of 0.3 and a diameter of 0.04 m. In addition, the frequency ratio between the second harmonic and the fundamental frequency is equal to 2 and the subsequent harmonic ratios are 3,4,5,6, etc. The described behaviour produces a reduction of the width of the frequencies spectrum when the PDEs' diameter is reduced or the PDEs' length is increased.

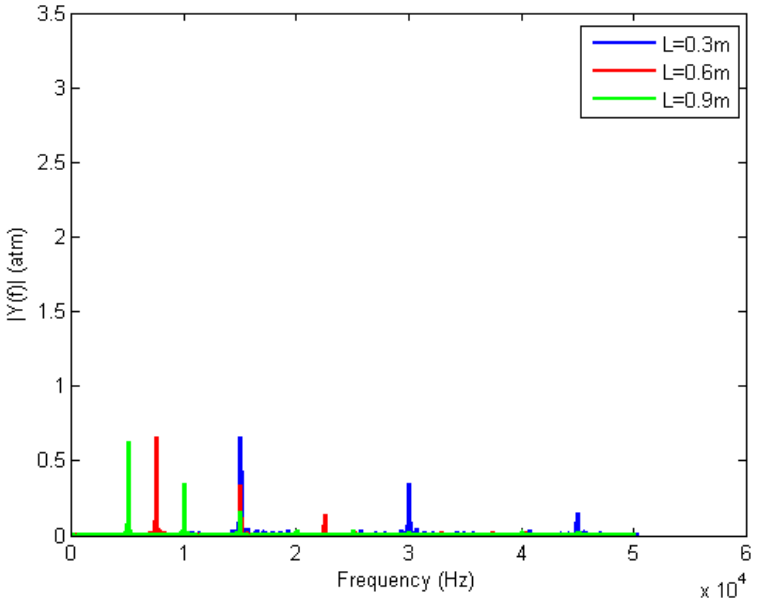

(a)

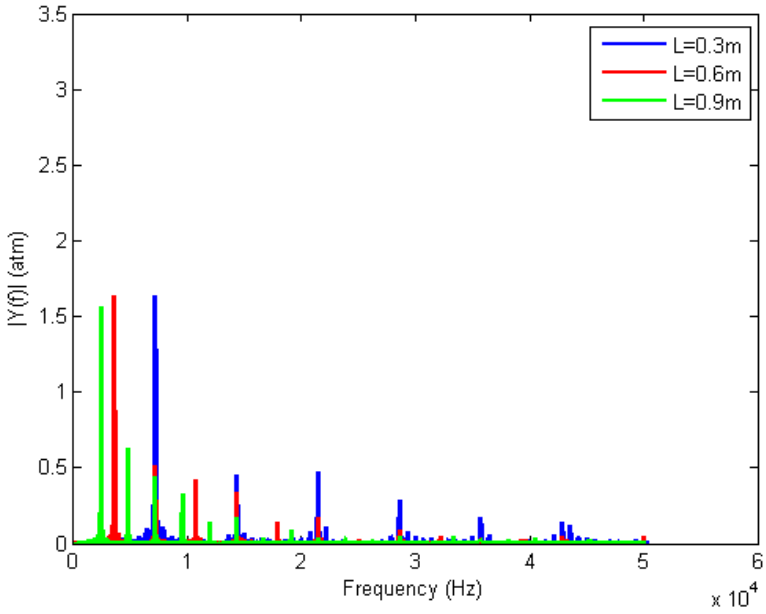

(b)

Figure 4-30 Harmonic produced by different PDEs' lengths and diameters equal to: a) 0.04 m b) 0.06

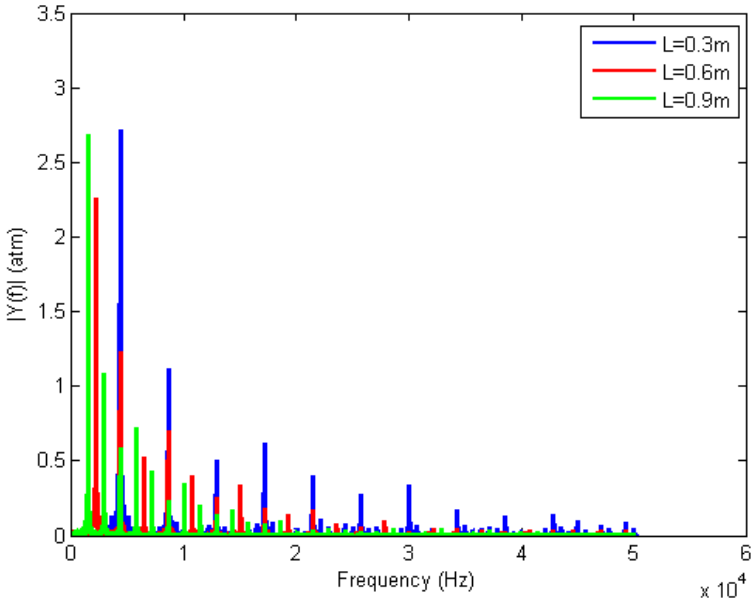

(c)

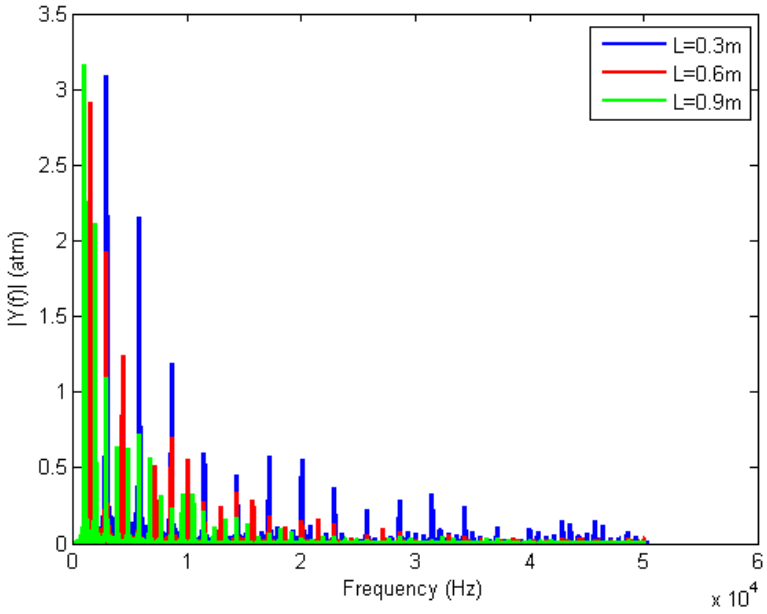

(d)

Figure 4-31 Harmonic produced by different PDEs' length and diameters equal to: c) 0.08 d) 0.1

Meanwhile, an increase of the PDEs' length and their diameter generate higher amplitude of the fundamental frequency, since this configuration requires a low number of PDEs to drive the turbine mass flow. So, a robust manifold is

required to avoid its future failure due to the fatigue. Table 19 shows the amplitude and fundamental frequency of the pressure signal produced by the evaluated configurations and the number of PDEs implemented in each array.

Table 19 Information about the fundamental frequency and the number of PDE required by the PDEs array in each of the studied cases

	Ø=0.04 m			Ø=0.06 m		
L (m)	0.3	0.6	0.9	0.3	0.6	0.9
$\|Y\|_{max}\ (atm)$	0.6282	0.662	0.6642	1.564	1.633	1.633
Ff (Hz)	5005	7497	15000	2386	3577	7131
# PDEs	24	24	24	11	11	11
	Ø=0.08 m			Ø=0.1 m		
L (m)	0.3	0.6	0.9	0.3	0.6	0.9
$\|Y\|_{max}\ (atm)$	2.684	2.262	2.715	3.165	2.911	3.094
Ff (Hz)	1432	2132	2.262	954	1421	2852
# PDEs	6	6	6	4	4	4

4.10 PDE evaluation through a CFD model based on the finite volume method

A CFD simulation is performed with ANSYS FLUENT® to verify the method of characteristics previously implemented and to predict the NOx emission expected during the PDE operation. The 2D model represents a PDE with a diameter of 0.04m and a length of 0.6m, since these values were included in the previous evaluation.

Figure 4-32 describes the problem evaluated with ANSYS FLUENT®. Dilution air is expanded through the nozzle and then it is injected into the manifold, while the nozzle's throat prevents the arrival of any perturbation to the upstream compressor.

A single PDE is placed in the centre of the nozzle with a length of 0.6 meters and its left side is used to inject the reactants into the PDE.

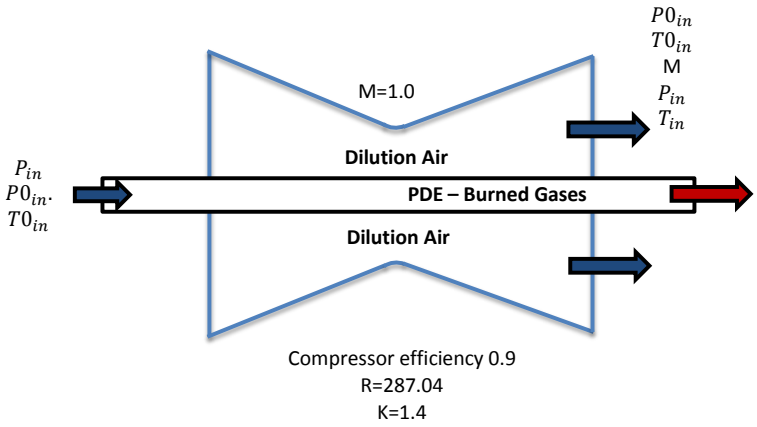

Figure 4-32 Schematic of the problem

Figure 4-33 shows the 2D domain used during the simulation. The boundary condition “inlet 1” allows the injection of seal air and reactants into the PDE by fixing the values of the fluid stagnation properties and its composition. Then, this boundary condition is switched to wall before the detonation to model the close end of the PDE.

The nozzle is not physically included into the model but its effect is incorporated by fixing the stagnation properties of the dilution air at the boundary condition called “inlet 2”. The gases discharge is achieved through the outlet boundary condition by fixing the fluid static pressure and temperature.

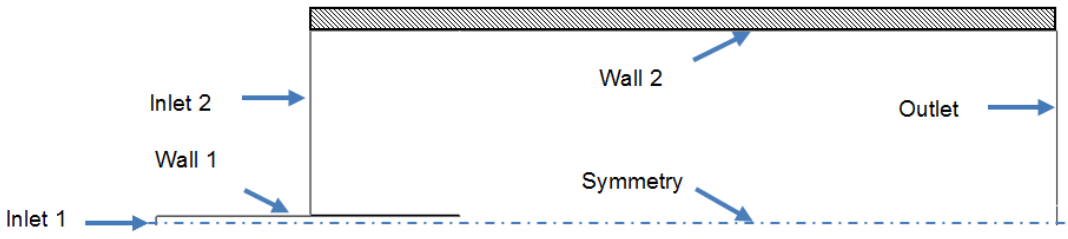

Figure 4-33 Computational domain implemented to simulate the PDE in ANSYS FLUENT®

SIMPLE is the solution algorithm selected to solve the distinct transport equations and QUICK is implemented to correct the false diffusion effect. The fuel implemented during the simulation is kerosene with an equivalence ratio of

one. The detonation starts using a charge of nitrogen located at the left side of the PDE, see Figure 4-34. The pressure and temperature of the charge are 40 atm. and 2500 K.

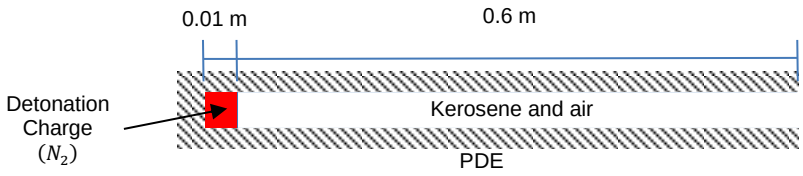

Figure 4-34 Scheme of the PDE - location of the detonation charge

Table 20 displays the properties' value used to inject dilution air into the manifold through the boundary condition inlet 2, whilst Table 21 displays the properties' value required to set the outlet boundary condition (see Figure 4-33).

Table 20 Values implemented by the CFD model to inject dilution air into the manifold through the boundary condition "inlet 2" shown in Figure 4-33

Dilution air (Total Properties)		
T_0	703	K
p_0	9.63	Atm
p	4.86	Atm
Dilution air (mass fraction)		
Y_{O_2}	0.23	n/a
Y_{N_2}	0.77	n/a

Table 21 Values implemented by the CFD model to set the outlet boundary condition shown in Figure 4-33

Outlet conditions		
p	4.86	Atm
T	1200	K
(Gases mass fraction)		
Y_{O_2}	0.23	n/a
Y_{N_2}	0.77	n/a

Table 22 displays the fluid properties and the components' mass concentrations implemented to model the injection of seal air and reactants into the PDE

through the boundary condition “inlet 1” presented in Figure 4-15. The seal air is injected first followed by the reactants, once the seal air penetrates 1.5 cm into the PDE; a penetration that ensures the isolation of reactants from burned gases.

Table 22 Values implemented by the CFD model to set the injection of reactants and seal air into the PDE (boundary condition “inlet 1” shown in Figure 4-15.)

Reactants injection (Total Properties)		
T_0	601	K
p_0	5.9	atm
p	4.86	atm
Seal air (mass fraction)		
Y_{O_2}	0.23	n/a
Y_{N_2}	0.77	n/a
Reactants (mass fraction)		
Y_{O_2}	0.218	n/a
Y_{N_2}	0.718	n/a
Y_f	0.064	n/a

4.10.1 Sensitivity analysis

A sensitivity analysis of a model that represents the PDE and the model that represents the manifold is conducted independently from each other through the following sections to separate the combustion effect of the detonation from the compression effect of the shock wave, whose propagation velocities are different.

The 2D-CFD simulation implements a combustion model with a single reaction step able to overestimate the temperature predicted by the NASA CEA code (3021 K) in more than 200 K (6.62 %); a behaviour also highlighted by (Saddawi 2013) when the combustion of hydrogen is simulated with an equivalent reaction mechanism.

However, the implementation of this type of model is suitable in the preliminary design of PDEs since it does not require an enormous computational effort. Therefore, a relative difference fewer than 6.62% is going to be accepted as

valid during the sensitivity analysis and the 2D simulation is going to be implemented only to verify the 1D-CFD model.

4.10.1.1 PDE sensitivity analysis

The sensitivity analysis of the PDE is conducted with different mesh resolutions from 500 cells per meter to 1000 cells per meter, whilst the cells aspect ratio is kept lower than 2 through the radial axis. Moreover, four time steps are evaluated as follows: a) $2x10^{-6}$seconds b) $1x10^{-6}$seconds c) $0.5x10^{-6}$ seconds d) $0.25x10^{-6}$ seconds.

The NASA-CEA code estimates a detonation velocity near to 2020 m/s in respect to the PDE, so the evaluated ranges included Courant numbers under and over one, such as the sensitivity analysis performed during the WR evaluation.

Figure 4-35 presents the pressure profile at the PDE axis after 0.54 milliseconds (time required by the detonation to reach half of the length of the PDE) for different mesh resolutions and a time step equal to 5e-7 seconds. The position of the detonation is well defined in all the cases and only small changes of the pressure profile are observed behind it.

The same behaviour is obtained when the other time steps are evaluated. So, the mesh density in the PDE is not of significant importance when it is between the values considered during the evaluation.

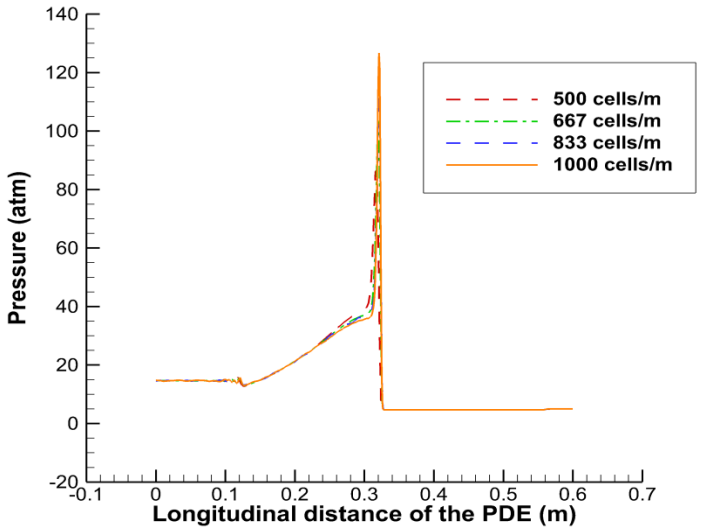

Figure 4-35 Pressure profile on the axis of the PDE after 0.54 milliseconds for a time step equal to $0.5x10^{-6}$ seconds and different mesh resolutions

The velocity of the detonation predicted by the CFD model is highly influenced by the time step implemented during the simulation, but the difference in velocities is minimised when the time step is reduced. Table 23 presents the position of the shock wave predicted by the different time steps after 0.54 milliseconds of detonation (time required by the detonation wave to reach half of the length of the modelled PDE).

Table 23 Position of the detonation through the PDE length estimate by the CFD code for different time steps

case	Time step (sec.)	Position (m)	Difference respect case 4 (%)
1	$2.0x10^{-6}$	0.284	14.4
2	$1.0x10^{-6}$	0.301	9.22
3	$0.5x10^{-6}$	0.324	2.24
4	$0.25x10^{-6}$	0.332	0

Based on the statement presented in section 4.10, a time step of 5e-7 seconds is selected to perform the evaluation of the detonation process since it ensures a relative difference of 2.24 %. Nevertheless, the resolution of the mesh is defined after the Manifold evaluation, firstly because all the evaluated meshes predict an accurate position of the detonation and secondly because it is important to keep a reasonable aspect ratio of the cell near to the interface between the PDE and the manifold.

4.10.1.2 Manifold sensitivity analysis

The sensitivity analysis of the manifold model is performed with three resolutions of the mesh throughout the manifold's length, as follows: 333 cells per meter, 555 cells per meter and 667 cells per meter, while the time integration is executed with a time step of 2e-6 seconds, 1e-6 second and 5e-7 seconds. The aspect ratio of the cells is kept lower than 4.

The new ranges selected in this analysis are less demanding than those implemented during the previous section because the shock wave moves at lower speeds than the detonation wave.

Each case starts from the end of the detonation inside the PDE (obtained from the previous analysis) and covers the interval of time spent by the shock wave to cross half of the manifold (up to 0.83 milliseconds after the detonation initiation). The pressure profile at the "symmetry" boundary condition shown in Figure 4-33 is implemented to compare the obtained results.

Figure 4-40 presents the pressure profiles predicted by the model for different mesh resolutions when a time step of 1e-6 seconds is implemented, whilst Figure 4-37 presents the relative difference of the model in respect to the solution of the denser mesh.

Despite the pressure profiles predicted by the model looking similar, a density of 555 cells per meter ensures relative differences fewer than 5% when the time step is 1e-6 seconds; and these differences are reduced when the time step is reduced. Meanwhile, a density of 333 cells per meter generates relative differences under 9% with the same trend at shorter time steps.

Figure 4-42 presents the pressure profiles predicted by the model for different time steps when the mesh density is 555 cells per meter and the cells aspect ratio is lower 4, whilst Figure 4-39 shows the relative difference between the cases with a long time step and the case with the shortest time step.

The pressure profiles predicted by the model for different time steps look similar. However, a time step of 1e-6 seconds ensures relative differences under 5% while a time step of 2e-6 ensures relative differences under 7.1 %. These differences are slightly reduced when the mesh density increases.

Based on the statement presented in section 4.10, a mesh density of 555 cells per meter and a time step of 1e-6 seconds are selected to perform the simulation of the shock wave displacement through the manifold as well as the filling process of the PDE.

A mesh density of 667 cells per meter is selected to discretise the PDE, since it allows the cell width to be kept constant through the PDE as well as the smoother transition of the mesh between the PDE and the Manifold.

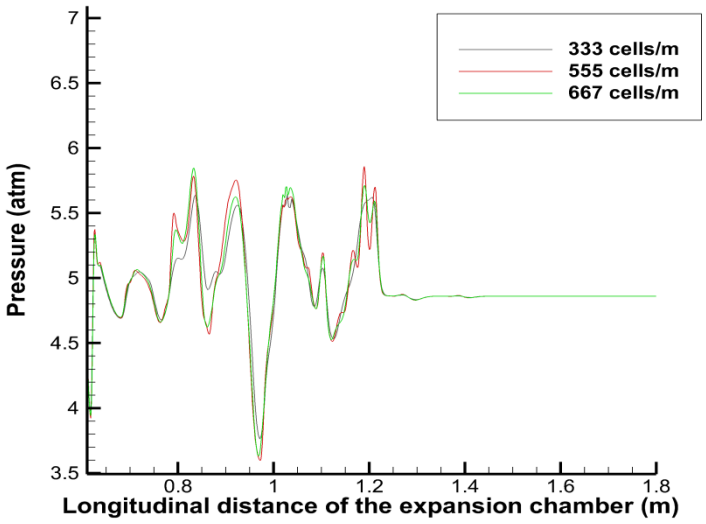

Figure 4-36 Effect of the mesh density in the static pressure predicted through the symmetry condition of the manifold model after 0.83 milliseconds for a time step of 1e-6 seconds

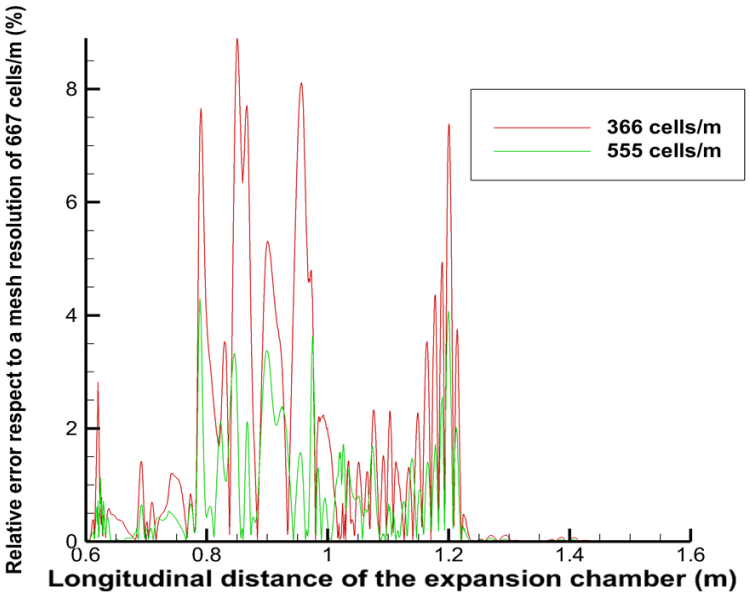

Figure 4-37 Relative difference between the pressure profile observed in Figure 4-36 and the pressure profile predicted by the denser mesh

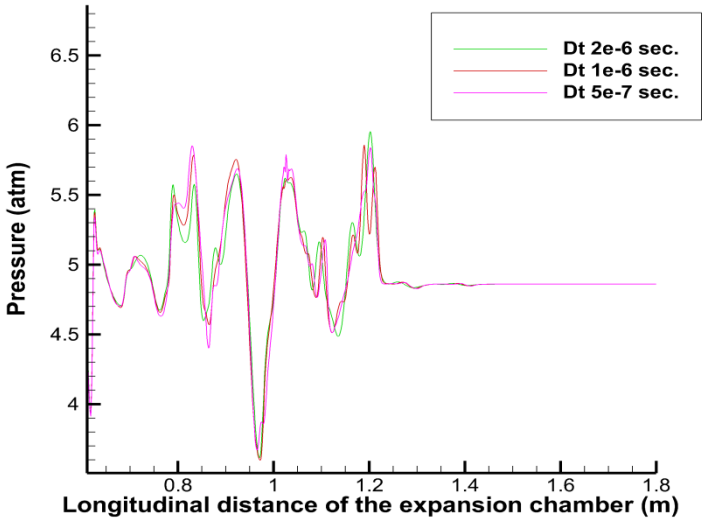

Figure 4-38 Effect of the time step in the static pressure predicted through the symmetry condition of the manifold model after 0.83 milliseconds for a mesh density of 555 cells per meter

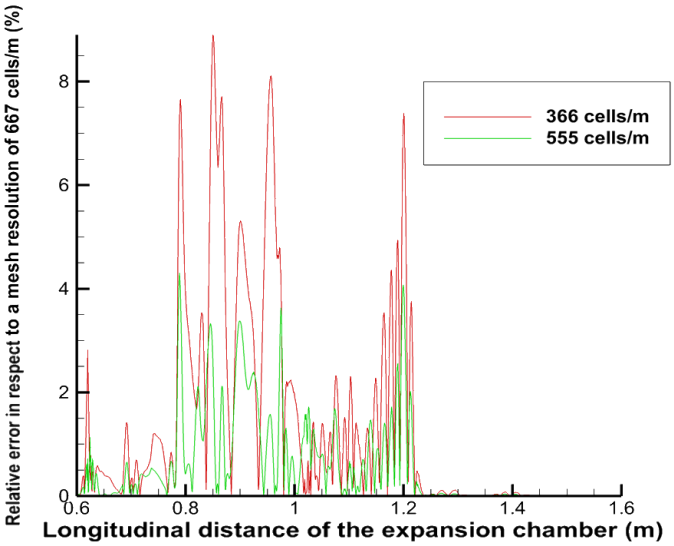

Figure 4-39 Relative difference between the pressure profile observed in Figure 4-38 and the pressure profile predicted by the model with the smallest time step

4.10.2 2D CFD results

Figure 4-40 and Figure 4-41 display the profile of total pressure and temperature at the exhaust of the PDE predicted by the method of characteristics and by ANSYS FLUENT® after three cycles. The main features observed between the profiles are as follows:

The detonation wave reaches the open end with a difference of 0.044 milliseconds while the cycle is performed with a difference of 0.18 msec. All of these values seem reasonable due to the different nature of the CFD models used during the evaluation.

The peaks of pressure have a large discrepancy but this difference is achieved during a tiny period of time compared with the whole cycle, so it could be neglected during the PDE performance analysis.

The withdrawal of gases from the PDE is done with a difference of total temperature close to 100 K, which represents less than 5 % the magnitude of the total temperature predicted by the method of characteristics (2446 K -2239 K); A difference of temperature is accepted as reasonable during the sensitivity analysis performed by this work (see section 4.10.1)

The in–house code based on the method of characteristics requires 1.95 seconds to execute the simulation of a PDE, whilst ANSYS FLUENT® requires 9.81 hr (35316 sec) to run a single cycle in an Intel core i5. This fact helps to understand the advantage of the method of characteristics when different PDEs' configurations are evaluated.

However, the process of splitting the 2D simulation in two regions with different time steps produces an important reduction of the computational effort, since the detonation process only occurs during 10% of the time required by a PDE's cycle to be completed.

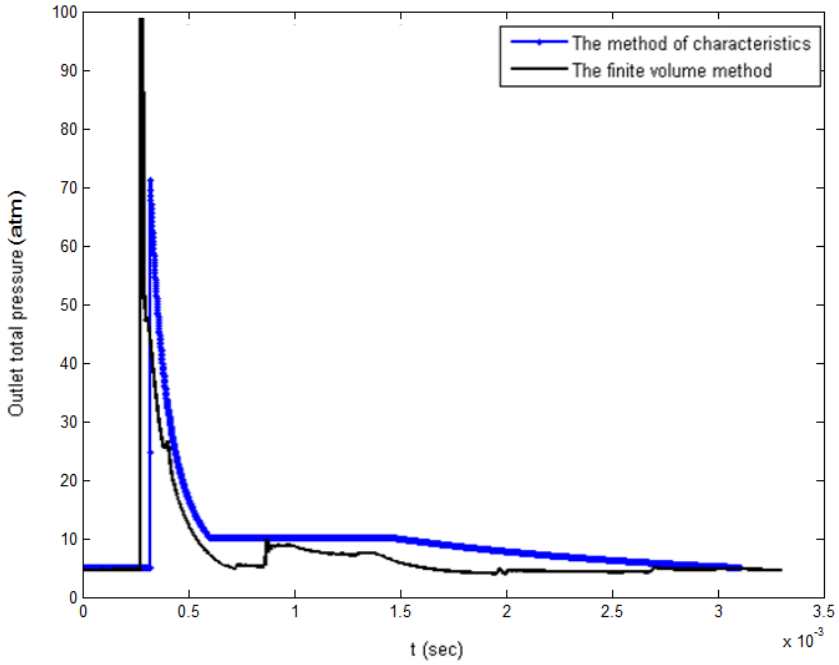

Figure 4-40 Differences between the profile of total pressure predicted by the method of characteristics and the finite volume method at the PDE's open end

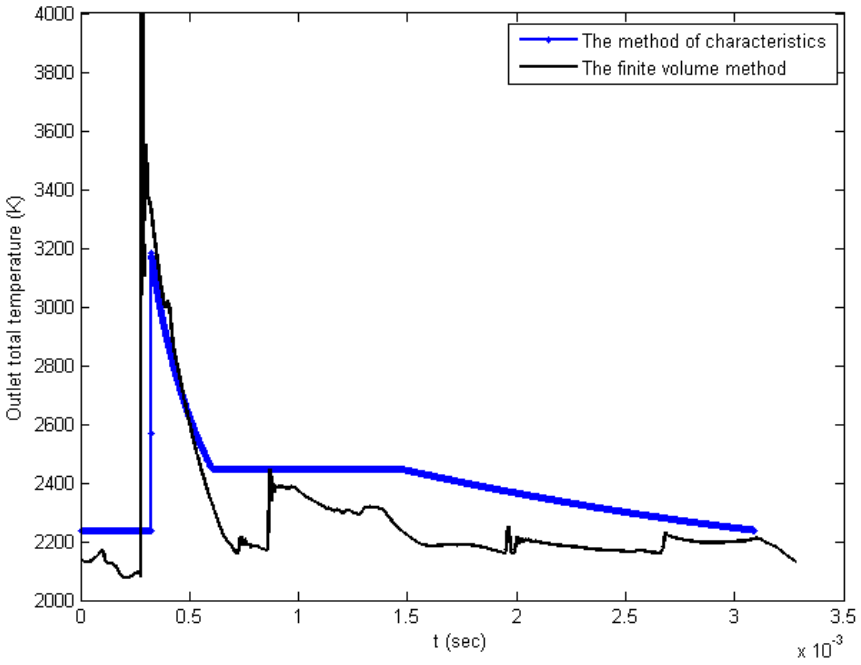

Figure 4-41 Differences between the profile of temperature predicted by the method of characteristics and the finite volume method at the PDE's open end

4.10.3 NOx emission predicted by ANSYS FLUENT® (Thermal NOx)

The PDE evaluation as a component of gas turbines is being limited only to a reactive mixture with an equivalence ratio equal to one to minimise the SFC, as stated in section 4.4. However, a low rate of NOx formation is also expected with this configuration because most of the available atoms of oxygen react with atoms of carbon and hydrogen comprising the fuel before the triple bond of nitrogen molecules is broken.

In this regard, the simulation which was performed only predicts a peak of NOx mass fraction that follows the detonation and reaches the open end of the PDE in 0.284 milliseconds after the cycle initiation. This peak of NOx is a consequence of the temperature change experienced by the reactants during the combustion, which rise steeply above 3000 K.

Figure 4-42 show the profiles of temperature, pressure, oxygen mass fraction, and NOx mass fraction predicted by the numerical model 0.23 milliseconds after initiating the third cycle. Despite the temperature being above 2200 K, the low

level of oxygen concentration that results from the detonation prevents the NOx formation, whose mass flow is equal to 0.0565e-001 g/sec (7.67 ppm mass).

The temperature of gases removed at the PDE's open end is kept over 2000 K during the whole cycle (see Figure 4-43); therefore the rate of NOx could increase if the mixing process in the manifold is unable to achieve a sharp reduction of the gases temperature during a short period of time.

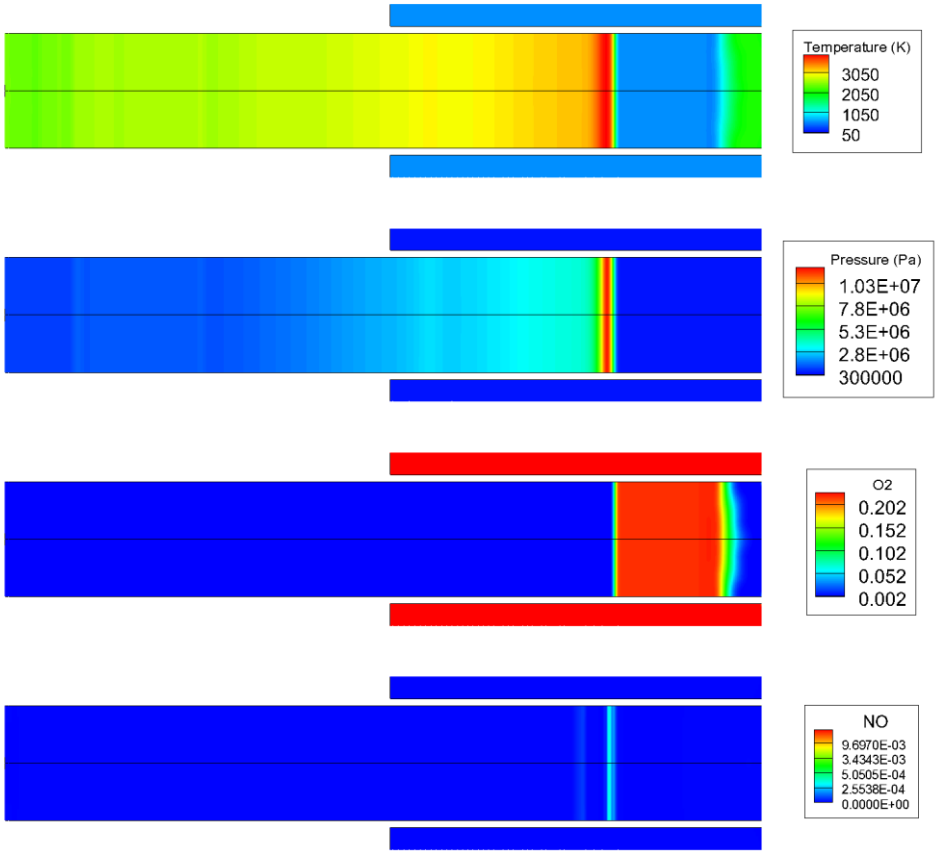

Figure 4-42 Profile of temperature, Pressure, mass fraction of O2, mass fraction of NOx predicted by ANSYS FLUENT® 0.00023 sec. after initiating the third cycle

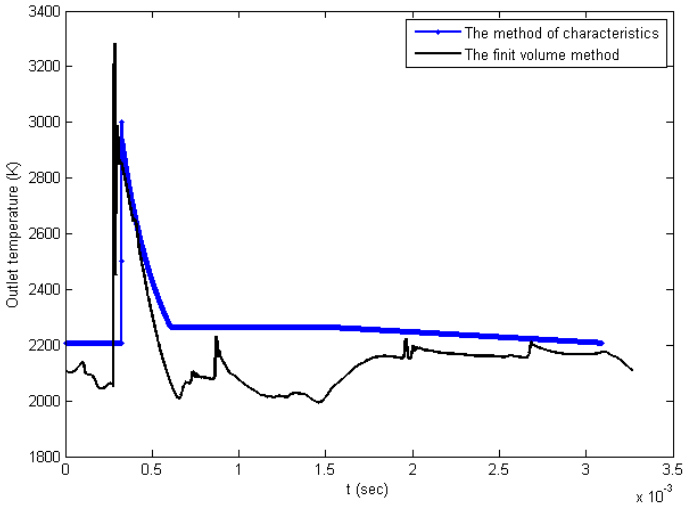

Figure 4-43 Differences between the profile of temperature predicted by the method of characteristics and the finite volume method at the PDE's open end

4.11 Chapter summary

This chapter assesses the performance of pulse detonation engines as components of gas turbines. The performance is computed after executing a routine able to predict the path followed by the fluid inside the gas turbine during its travel along each component.

The transient process inside a single PDE is assessed with the NASA CEA code that gives information about the detonation mechanism and the method of characteristics that is implemented to track the rarefaction waves generated inside the PDE through all the transient process.

The routine is executed in less than 2 seconds and it gives information about the properties profile at the open end of the PDE. So, multiple PDEs configurations can be evaluated within a reasonable interval of time.

As a result, the lowest SFC is 66.7 $kg/kN.hr$, whilst the highest specific thrust and efficiency of energy conversion are 113 N.s/kg and 40.2 % respectively. The PDEs' length does not have a significant influence in the SFC. However, the best length should be over 0.9 m to generate harmonics with the same frequencies as obtained from a common combustion chamber.

A PDE with a diameter of 0.04 m is suggested to reduce the amplitude of the frequency spectrum into the manifold. This is because this effect reduces the fluctuating stress that the new gas turbine has to overcome.

The NOx generated inside a single PDE is in the order of 8 ppm because the reactive mixture has an equivalence ratio equal to one. The mixing of burned gases with dilution air must be effective to keep the NOx generation as low as possible, since the temperature of gases at the open end is above 2000 K.

5 PERFORMANCE EVALUATION OF ICWR (SHOCK-IGNITED DETONATION MODE)

5.1 ICWR operating as component of future gas turbines

In common gas turbines, the combustion chamber operates with excess air to reduce the temperature of burned gases before they enter into the turbine (expansion process). An ICWR with the same fuel air ratio can operate only if the fuel is injected by package (fuel stratification) or if the turbine core flow is split into primary air and dilution air; the primary air is implemented to feed the wave rotor with an equivalence ratio close to one whilst dilution air is implemented to reduce the temperature of burned gases in a separate mixing chamber.

The possible implementation of the second option in a gas turbine is a complex issue, since the detonation process releases a significant amount of energy at high pressure and temperature throughout the channels. So, the mixing of these gases with dilution air requires the incorporation of a compressor able to deliver elevated compressor pressure ratios that not only increases the reverse work but also the cycle losses. Therefore, this option is discarded.

Figure 5-1 presents an ICWR with fuel stratification. The main characteristic of this configuration is the complete management of the gas turbine core flow. The fuel stratification enables the detonation to be performed in a narrow section of each channel with an appropriate fuel/air ratio and part of the released energy is distributed through each channel by shock waves.

The grey band observed in Figure 5-1 represents the fuel stratification, which is separated from product gases through a seal made with fresh air to prevent the fuel auto ignition.

The detonation is initiated by a shock wave that comes from the air stagnated at the right end of the channel due to its sudden closure. The closure is set once the product gases are removed from the channel to prevent the loss of fresh air, such as in wave rotors (see sub-section 3.1).

The detonation process concludes once the fuel is consumed but it generates two shock waves, a strong shock wave that travels to the left end of the channel compressing the downstream air and its arrival to the injection port indicates the closure timing of the channels' left end, and a second shock wave that travels to the right plate to compress the sealed air.

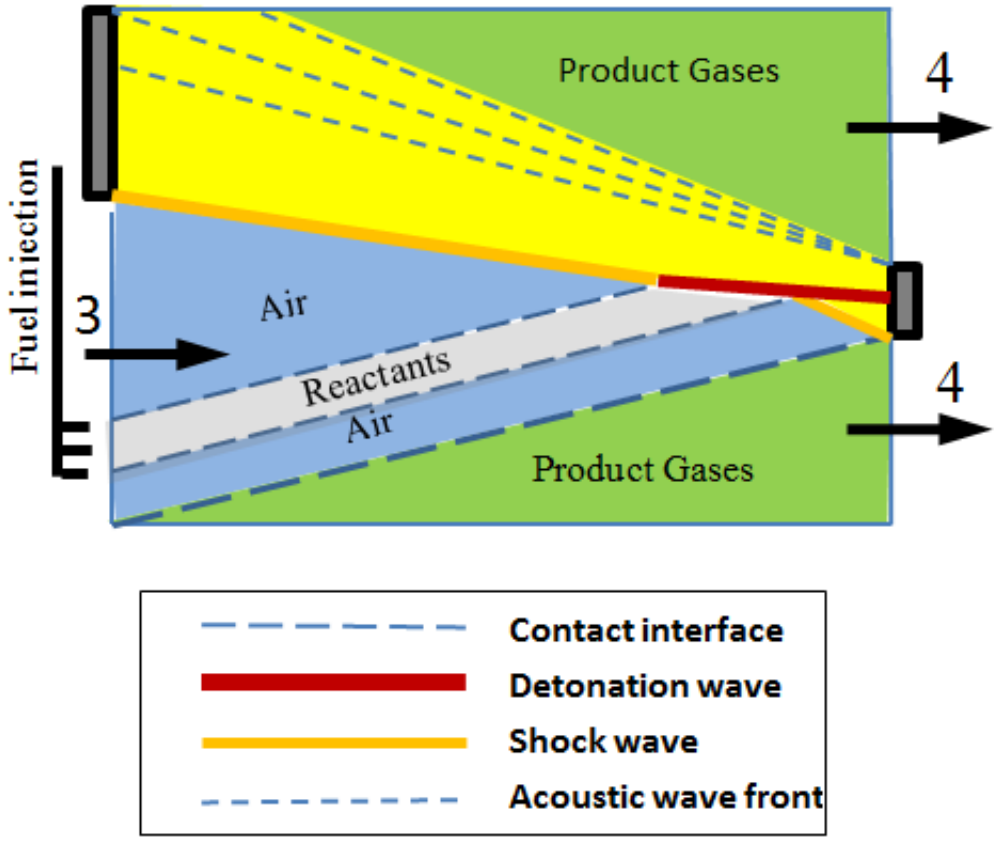

Figure 5-1 Schematic representation of an ICWR

The opening of the right end of the channel produces an expansion wave that travels through the channel and is reflected by the left plate of the ICWR. The left end of the channel opens again to start injecting new reactants once the pressure at the left plate is equal to the injection pressure to start the cycle again.

Figure 5-2 presents a schematic representation of an ICWR connected into a gas turbine.

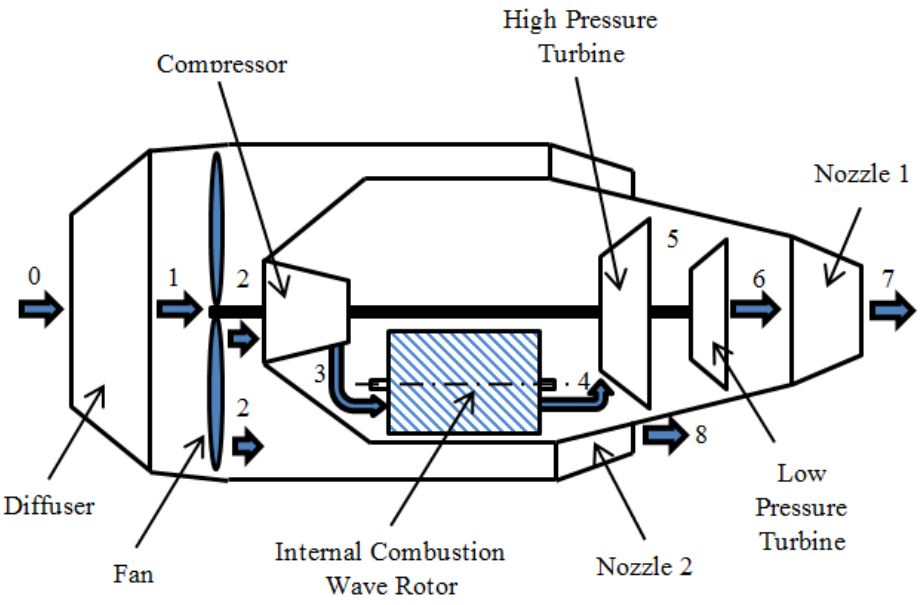

Figure 5-2 Schematic representation of an ICWR connected to a gas turbine

5.2 Modification of the in-house CFD code to simulate detonation

Chapter 3 presented an in-house CFD code able to predict the wave rotors' dimensioning. Now in this chapter, the same code is implemented to obtain the dimensioning and performance evaluation of internal combustion wave rotors by incorporating a combustion mode able to reproduce the detonation process inside the device.

The following sub-sections are focused on describing the procedure conducted to accomplish the goals.

5.2.1 Energy equation

By definition, the differential shape of the non-conservative Euler equation of energy is given by Eq. (5-1). The first right term represents the transient term, the second right term represents the flux of energy (convection) and the right term represents the source term to include any source of energy or its dissipation; such as radiation models.

$$\frac{\partial}{\partial t}(\rho H) + \nabla.(\rho \vec{v} H) = S_h \quad \textbf{(5-1)}$$

In the previous equation, H is the enthalpy computed through Eq. (5-2), in which j represents a component that participates and N the number of chemical species.

$$H = \sum_{j=1}^{N} Y_j H_j \quad \textbf{(5-2)}$$

Since detonation is a combustion process, the total enthalpy of each species j is computed through Eq. (5-3), which includes the specie enthalpy of formation ($\Delta h^o_{f,i}$).

$$H_j = \int_{T_{ref,j}}^{T} C_{p,j}\, dT + \Delta h^o_{f,i} = \left(h_j(T) - h_j\left(T_{ref,j}\right)\right) + \Delta h^o_{f,i} \quad \textbf{(5-3)}$$

The numerical solution of Eq. (5-3) is accounted by using the JANAF Thermochemical Tables (Chase et al. 1985), in which polynomial coefficients are implemented to estimate the specific heat (C_p), the specific enthalpy and the specific entropy of the participant specie as a function of temperature through equations from Eq. (5-4) to Eq. (5-6).

$$C_p/R_u = a_1 + a_2 T + a_3 T^2 + a_4 T^3 + a_5 T^4 \quad \textbf{(5-4)}$$

$$H/R_u T = a_1 + a_2 T/2 + a_3 T^2/3 + a_4 T^3/4 + a_5 T^4/5 + a_6/T \quad \textbf{(5-5)}$$

$$S/R_u = a_1 ln(T) + a_2 T + a_3 T^2/3 + a_4 T^3/3 + a_5 T^4/4 + a_7 \quad \textbf{(5-6)}$$

Appendix C presents the polynomial of the chemical species considered by the developed code.

5.2.2 Transport equations

The transport equation of each of the species that participate in the reaction process has the same shape as the transport equation of the normalized variable implemented in the in-house code developed in chapter 3, but in this case a source term to model the species production or destruction is necessary, see Eq. (5-7).

$$\frac{\partial \rho Y_i}{\partial t} + \frac{\partial \rho u Y_i}{\partial x} = \dot{\omega}_i \tag{5-7}$$

The source term for a simple non-reversible reaction mechanism without the participation of a third body, such as that observed in Eq. (5-8), can be computed through Eq. (5-9), where k_f represents the forward rate constant of the reaction, η'_a and η'_b the rate exponents of reactant's species a and b, C_A and C_b the molar concentration of species a and b in the reaction $(kmol/m^3)$, and M_m the apparent molar mass of the mixture.

$$a + b \rightarrow c + d \tag{5-8}$$

$$\dot{\omega}_i = \frac{\mathrm{RR}}{\mathrm{Mm}} = k_f \cdot [C_a]^{\eta'_a} \cdot [C_b]^{\eta'_b} / Mm \tag{5-9}$$

In a detonation process the forward rate constant (k_f) can be estimated through the Arrhenius equation (see Eq. (5-10)) (ANSYS 2013), where A is the pre-exponential factor in $(m^3/kmol)^{(\eta'_a+\eta'_b)-1}/\left(K^{-\beta}s\right)$, β is the temperature exponent, and E is the activation energy in $(J/kmol)$. A full explanation of the Arrhenius law can be found in (Kuo 2005; Poinsot & Veynante 2005; Versteeg & Malalasekera 2007).

$$k_f = \mathrm{A} * T^{\beta} * \exp\left(\frac{-E}{R_u T}\right) \tag{5-10}$$

The system of equations solved during the combustion simulation includes N-1 transport equations plus the global mass conservation equation (see Eq. (5-11)) if N molecules are involved in the reaction mechanism.

The global mass conservation equation usually computes the mass fraction of the molecule that has the highest participation in the mixture to prevent the presence of instabilities during the iterative process; such as a negative value of the computed mass concentrations.

$$\sum_{i=1}^{N} Y_i = 1 \qquad \textbf{(5-11)}$$

5.2.3 Reaction Mechanism (Kerosene – $C_{12}H_{23}$)

A model of Jet-A is implemented to perform the numerical evaluation of a detonation process inside an ICWR. Since, Jet-A is a fuel commonly used in civil aircraft.

The combustion model is obtained from the material library of ANSYS FLUENT® (ANSYS 2013) and considers the complete burning of fuel through a non-reversible single-reaction step, see Eq. (5-12).

$$C_{12}H_{23} + 17.75\ O_2 \rightarrow 12CO_2 + 11.5H_2O \qquad \textbf{(5-12)}$$

Table 24 and Table 25 present the various constants that define the combustion model.

Table 24 Rate exponents implemented in the Kerosene's reaction model

MOLECULE	RATE EXPONENT $(\eta'_{j,r})$
$C_{12}H_{23}$	0.25
O_2	1.5
CO_2	0
H_2O	0

The incorporation of the Jet-A model into the in-house code is simple and allows the construction of a CFD code able to run quick simulations, since only four transport equations are included. However, due to its simplicity the model is

unable to capture the induction effect and it is susceptible to overestimation of the temperature field, such as other one-reaction step models (Saddawi 2013).

Table 25 Constants of the Arrhenius equation implemented in the Kerosene's reaction model

VARIABLE	VALUE	UNITS
Pre-Exponential factor (A)	2.587e+09	$\left(\frac{\mathrm{m}^3}{\mathrm{kmol}}\right)^{0.75}$
Activation Energy (E)	1.256e+08	$\left(\frac{\mathrm{J}}{\mathrm{kmol}}\right)$
Temperature Exponent (β)	0	N/A

5.2.4 Source term integration

ODE45 is a medium order method included in MATLAB's toolbox able to solve non-stiff differential equations efficiently (The MathWorks Inc 2011), so it is implemented during the integration of the source term on each of the chemical species.

The integration of source terms requires knowing in advance the path followed by the temperature through the integration interval. To sort out the problem, the in-house code assumes a linear change of temperature whose derivative is computed in each interaction using the temperature obtained in the previous time (T^o) and the temperature computed during the iterative loop (T^*) through Eq. (5-13).

$$\frac{dT}{dt} = \frac{T^* - T^o}{Dt} \qquad \textbf{(5-13)}$$

5.2.5 Boundary conditions

Besides the detonation process, shock waves and rarefaction waves participate during the transient process of ICWR, such as the WR (see sub-section 2.5.2.1). Therefore, the boundary conditions implemented by the new 1D-CFD for the mass, momentum and energy conservation equations are the same as those defined in subsections 3.6.1.1, 3.6.1.2 and 3.6.1.3.

Table 26 shows the boundary conditions implemented to solve the N-1 species transport equations.

Table 26 Numerical approximation of distinct boundary conditions implemented in the simulation of ICWR

Type of boundary condition	Numerical approximation
Wall	Neumann boundary condition (derivative of the chemical component concentration is equal to zero)
Stagnation pressure and temperature at the inlet	Dirichlet boundary condition (the concentration of the mixture components is set)
Static pressure at the outlet	Dirichlet boundary condition (the concentration of the mixture components is equal to the concentration at the upstream node)

5.3 NO_x emissions

This work assumed that NO_x generation does not have a significant influence either in the energy equation or in the concentration of other chemical species to model the NO_x emissions. Therefore, the NO_x concentration is predicted by using an additional module that post-processes the results given by the in-house CFD code (uncoupled solution). The proposed module is based on the theoretical information offered by section 20.1 of FLUENT User's guide "NO_x formation" (ANSYS 2013).

Equation (5-14) is the Euler transport equation of nitric oxide (NO) solved by the developed module to predict the NOx formation. The first term at the left hand is implemented to model the transient behaviour, the second term represents the flux of NO_x due to convection and the right-hand term represents the source or destruction of NO_x during the reaction process.

$$\frac{\partial \rho Y_{NO}}{\partial t} + \frac{\partial \rho u Y_{NO}}{\partial x} = \dot{\omega}_{NO} \qquad \textbf{(5-14)}$$

In any combustion process, the formation of NO_x could be a consequence of four different chemical kinetic processes as follows (ANSYS 2013):

- Thermal NO_x results from the oxidation of nitrogen contained in the combustion air

- Prompt NO_x is a consequence of fast reactions, such as in cases with low reaction temperatures, fuel-rich conditions and where residence times are short
- Fuel NO_x results from oxidation of nitrogen contained in the fuel
- NO_x through $[N^2O]$ is also possible through the oxidation of nitrogen at elevated pressures in oxygen-rich conditions

Thermal NO_x is responsible for the main source of NO_X during a detonation process since the temperature of the working fluid reaches values far above 1800 K during the reaction (Giuliani et al. 2010). The other NO_x sources are assumed less important at the operational condition of ICWR, since prompt NO_x is negligible compared with thermal NO_x at extremely high temperatures. Jet-A does not contain nitrogen in its composition and the fuel is injected in packages with equivalence ratios near to one (concentration of oxygen near to the stoichiometric). So, they are omitted in the module developed.

5.3.1 Thermal NOx

Equation (5-15) presents the extended Zeldovich mechanism implemented to predict thermal NO_x (Hill & Smoot 2000), whilst Table 27 shows the reaction rate constants developed by R. K. Hanson and S. Salimian (1984) to model this mechanism (as cited by (ANSYS 2013)).

The whole reaction mechanism is driven by the first reaction step whose activation energy is elevated. Therefore, high temperatures are necessary to produce a significant amount of NO (Westbrook & Dryer 1984).

The extended Zeldovich mechanism requires in advance the concentration of [O], [OH], [H] and [N] to compute the net rate of formation of NOx (see Eq. (5-15)). However, the reaction mechanism implemented to model the combustion of Jet-A is simple and therefore the required chemical species are not solved during the simulation.

$$O + N_2 \rightleftharpoons N + NO$$
$$N + O_2 \rightleftharpoons O + NO$$
$$N + OH \rightleftharpoons H + NO \quad \textbf{(5-15)}$$

Table 27 Rate constants of Zeldovich mechanism

Reaction #	$\mathbf{k_f}$	$\mathbf{k_r}$
1	$1.8\text{x}10^{8}\text{e}^{-38370/\text{T}}$	$3.8\text{x}10^{7}\text{e}^{-425/\text{T}}$
2	$1.8\text{x}10^{4}\text{Te}^{-4680/\text{T}}$	$3.81\text{x}10^{3}\text{Te}^{-20820/\text{T}}$
3	$7.1\text{x}10^{7}\text{e}^{-450/\text{T}}$	$1.7\text{x}10^{8}\text{e}^{-24560/\text{T}}$

To overcome the problem stated above ANSYS FLUENT® implements correlations that estimate the new chemical species concentration by post-processing the simulation results; each of these options is enumerated as follows:

5.3.2 The quasi-steady assumption of [N]

This model assumes that consumption of free atoms of [N] becomes equal to its formation. Thermal NOx is produced at elevated temperatures to break the strong triple bond of [N2] molecules whilst the oxidation of N atoms is achieved by a mechanism with low activation energy.

After the quasi-steady assumption described above, the net rate of formation of NOx can be computed from Eq. (5-16) (ANSYS 2013), in which the concentration of Nitrogen atoms (N) is not included; the k subscript indicates the reaction direction ("f" when reaction is forward and "r" when reaction is reversed), whilst the number indicates the reaction number in the extended Zeldovich mechanism.

$$\frac{d[NO]}{dt} = 2.k_{f,1}[O][N_2]\frac{\left(1-\frac{k_{r,1}k_{r,2}[NO]^2}{k_{f,1}[N_2]k_{f,2}[O_2]}\right)}{\left(1+\frac{k_{r,1}[NO]}{k_{f,2}[O_2]+k_{f,3}[OH]}\right)}\ (gmol/m^3 s) \quad \textbf{(5-16)}$$

5.3.3 Partial equilibrium approach of O

Combustion at high temperature promotes the equilibrium condition of [O] radicals since thermal NOx formation comes from a slow reaction mechanism compared with the combustion process and the overshoot of [O] radicals is attenuated at higher flame temperatures.

However, the third-body reaction also participates in the [O^2] dissociation and recombination (see Eq. (5-17)). Therefore, a higher concentration of [O] radicals is expected. The resultant correlation is called partial equilibrium approach of O, and it is given by Eq. (5-18)

$$O_2 + M \rightleftharpoons O + O + M \quad \textbf{(5-17)}$$

$$[O] = 36.64.T^{0.5}.[O^2]^{0.5}.exp(27123/T)\ \ (gmol/m^3) \quad \textbf{(5-18)}$$

5.3.4 Partial equilibrium approach of OH

To predict the [OH] concentration without solving the transport equation of [OH] during the combustion simulation, ANSYS FLUENT® implements the correlation shown in Eq. (5-19), which comes from the work developed by D. L. Baulch et al. (1992) and C. Westbrook and F. Dryer (1984), (as cited by (ANSYS 2013)).

$$[OH] = 2.129x10^2.T^{-0.57}.exp(-4595/T)\ [O]^{0.5}\ [H_2O]^{0.5} \quad (gmol/m^3) \quad \textbf{(5-19)}$$

5.4 Code Verification – Combustion of Kerosene

The code's verification was performed by comparing the results between the in-house code and ANSYS FLUENT®. The test case is a shock tube as was presented by (Shapiro 1954), but the driver zone is filled with nitrogen whilst half of the driven zone is filled with pure air and the other half with a mixture of air plus kerosene with an equivalence ratio of 0.7; the package of reactants is located just in the middle of the driver zone. Figure 5-3 gives information about the model initial conditions.

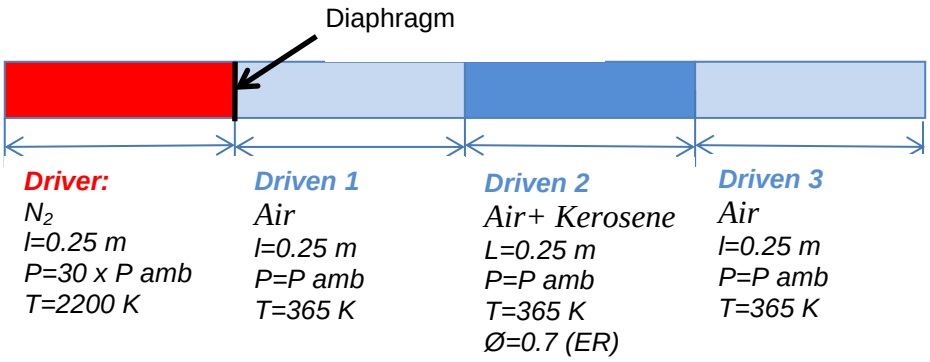

Figure 5-3 Test case implemented to evaluate the temperature's paths during the integration of source term

The simulation in ANSYS FLUENT® is performed by two CFD models, the first model implements a third order MUSCL scheme to compute the advection in each of the transport equations (High order interpolation scheme) and a second order implicit scheme to compute the transient term, whilst the second model implements a first order upwind scheme to compute the advection in each of the transport equations and a first order implicit scheme to compute the transient term (Low order interpolation scheme).

The SIMPLE algorithm is selected to link the momentum equation with continuity. The fluid density is computed through the equation of state (ideal gas) and a least squares cell-based technique is applied to estimate the scalars gradient.

5.4.1 Sensitivity analysis

The validation process performed in section 3.6.3 indicates that the 1D-CFD code is susceptible to generate false diffusion so the shape of the shock wave responsible of the detonation initiation can be seriously affected as well as the fuel stratification. However, the error is dissipated by reducing the time step of the simulation, since the main source of this error is associated to the time integration scheme implemented by the code (see section 3.6.3).

Based on the above, a sensitivity analysis with shorter time steps than implemented in the WR evaluation is performed, as follows: 9e-6 sec, 9e-7 sec. and 5e-7 sec. The first value is equal to the time step implemented during the WR simulation, the second value is one order of magnitude lower than the first and the third value is equal to the time step implemented to perform the modelling of the detonation wave inside the PDE.

In addition, 160 cells per meter, 320 cells per meter and 480 cells per meter are implemented to evaluate the effect of the mesh density. These values allow Courant numbers under and above 1 to be considered, such as the sensitivity analysis performed in the previous sections.

Figure 5-4 presents the pressure profiles predicted by the CFD code after 0.45 milliseconds for a mesh density of 160 cells per meter, 320 cells per meter and 480 cells per meter. Each plot displays the results given by the time steps implemented during the evaluation, except the pressure profile with a mesh density of 480 cells per meter and a time step of 9e-6 seconds, since the code was unable to run due to some instability during the iterative process; the main characteristic of this condition is that it has a Courant number of 6 which is the highest of the whole evaluated range.

The expansion wave behind the shock wave experiences a maximum difference of 0.4941 atm when a model with a time step of 9e-6 seconds is compared with the reference model (model with the shortest time step) and this difference is the highest obtained from the whole evaluation. However, this value represents only 5.45 % of the jump of pressure produced by the shock discontinuity and therefore it satisfies the criterion implemented in section 4.10.1.

Although the statement above is true, the shape of the shock is not as sharp as was obtained with the other time steps, so its reflection at the right end of the tube may result in a weak wave that could be unable to start the detonation process, as stated at the beginning of this section. In this regard a time step of 9e-6 seconds is not recommended in the ICWR evaluation.

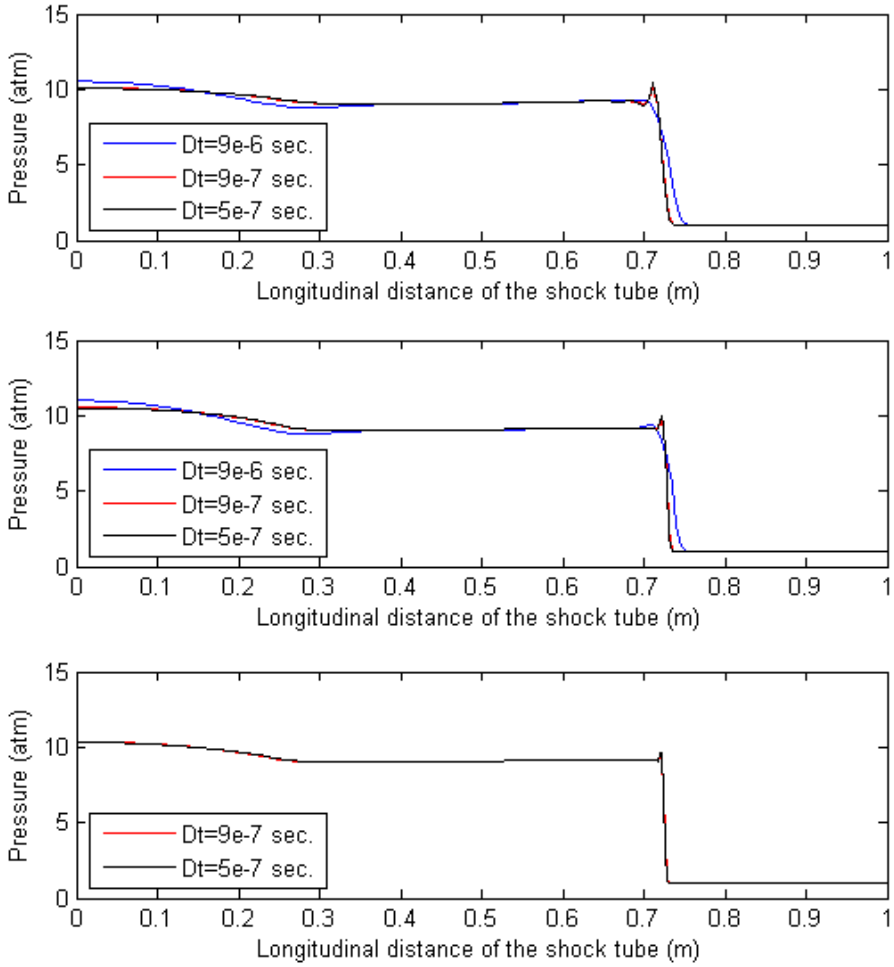

Figure 5-4 Pressure profile through the longitudinal distance of the tube after 0.45 milliseconds of simulation for different time steps and mesh densities 0- a) 160 cells per meter, b) 320 cells per meter and c) 480 cells per meter

The profile of the shock wave predicted by a time step of 9e-7 seconds is sharp and it almost overlaps the shock wave obtained with the shortest time step. Therefore, a time step of 9e-7 seconds is selected to perform the future simulations.

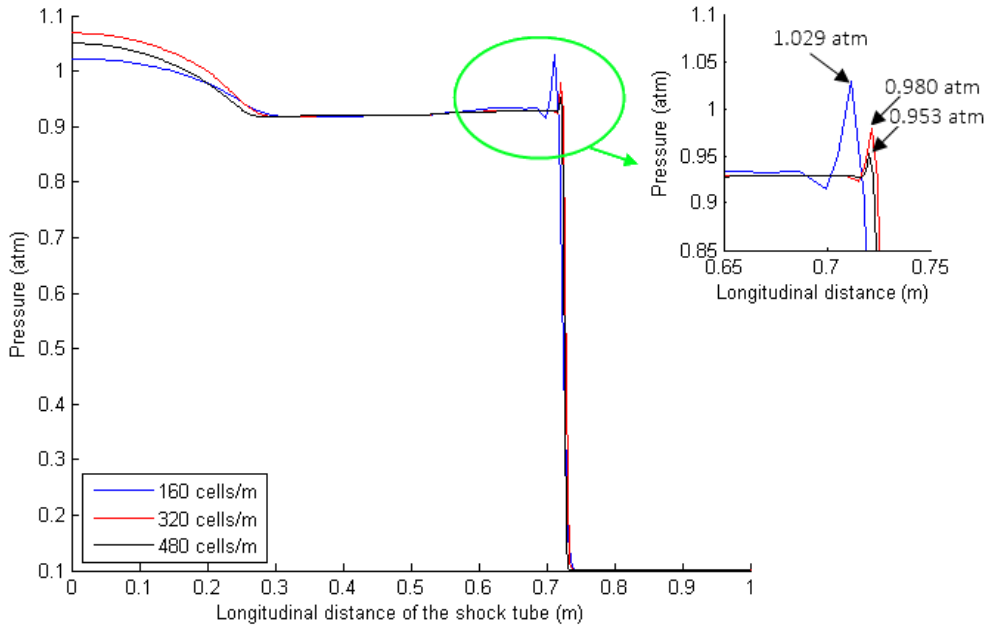

Figure 5-5 Pressure profile through the longitudinal distance of the shock tube after 0.45 milliseconds for different mesh densities and a time step of 9e-7 seconds

Figure 5-5 displays the pressure profile through the longitudinal distance of the tube after 0.45 milliseconds for different mesh densities and a time step of 9e-7 seconds to evaluate the effect of the mesh density on the simulation.

The pressure profile of the expansion wave is the highest for a mesh density of 320 cells per meter and it is the lowest for a mesh density of 160 cells per meter. However, the differences of pressure in respect to the dense mesh are only 1.98% and 3.09% of the pressure jump discontinuity. So, these differences are not enough to discard one of the evaluated options.

These models predict a peak in the pressure profile after the compression of the shock wave. The difference in height between the pick predicted by a mesh density of 160 cells per meter and the dense mesh is 8.38% of the pressure jump produced by the shock wave, while the difference in height between the pick of pressure predicted by a mesh density of 320 cells per meter and the dense mesh is only of 2.97%. Therefore a mesh density of 320 cells per meter is selected to perform future simulations.

5.4.2 Verification of the 1D-CFD code

Figure 5-6, Figure 5-8, Figure 5-8 and Figure 5-9 show the profiles of pressure, absolute velocity, temperature and mass concentration of fuel along the shock tube at five hundred, one thousand, and one thousand five hundred time steps of the simulation.

The pressure profiles shown in Figure 5-6 are similar in all the cases as well as the position and shape of the shock wave during the transient process. However, small distortions are observed near the shock wave when the high order interpolation scheme is implemented in ANSYS FLUENT®.

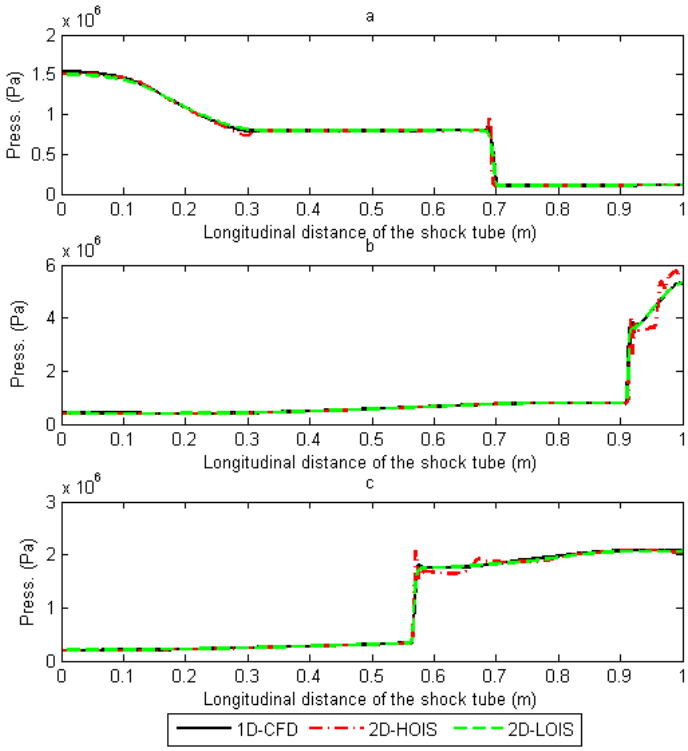

Figure 5-6 Pressure profile throughout the shock tube at: a) 500 time steps b) 1000 times steps c) 1500 time steps (Time step = 9e-7 sec) estimated by the in-house code and by ANSYS FLUENT® when the high order interpolation scheme (HOIS) and the low order interpolation scheme (LOIS) are implemented

The absolute velocity profiles shown in Figure 5-7 are similar but the in-house code predicts a contour slightly smoother near the shock wave as a consequence of the false diffusion effect. At the same time, some oscillations of

the velocity profile are observed near the shock wave when the high order interpolation scheme is implemented in ANSYS FLUENT®, as happens in the pressure profiles.

The temperature profiles shown in Figure 5-8 follow the same trend displayed by the pressure and velocity profiles presented above. However, the in-house code predicts a smoother change near the expansion waves and during the reaction process which causes the in-house code to predict lower temperature peaks than the commercial software. However, the profiles of temperature predicted by FLUENT in each of its own models also present significant discrepancies.

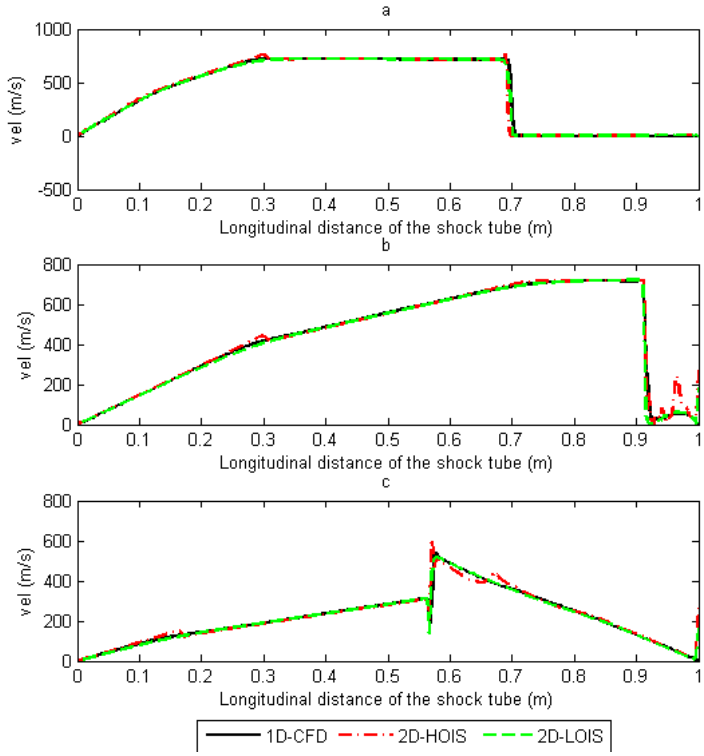

Figure 5-7 Absolute velocity throughout the shock tube at: a) 500 time steps b) 1000 times steps c) 1500 time steps (Time step = 9e-7 sec) estimated by the in-house code and by ANSYS FLUENT® when the high order interpolation scheme (HOIS) and the low order interpolation scheme (LOIS) are implemented

The transport of fuel mass fraction predicted by the in-house code is also susceptible to false diffusion (see Figure 5-9). The smoother surface obtained in

the in-house code is similar to the surface obtained by FLUENT when low dimensional interpolation schemes are implemented.

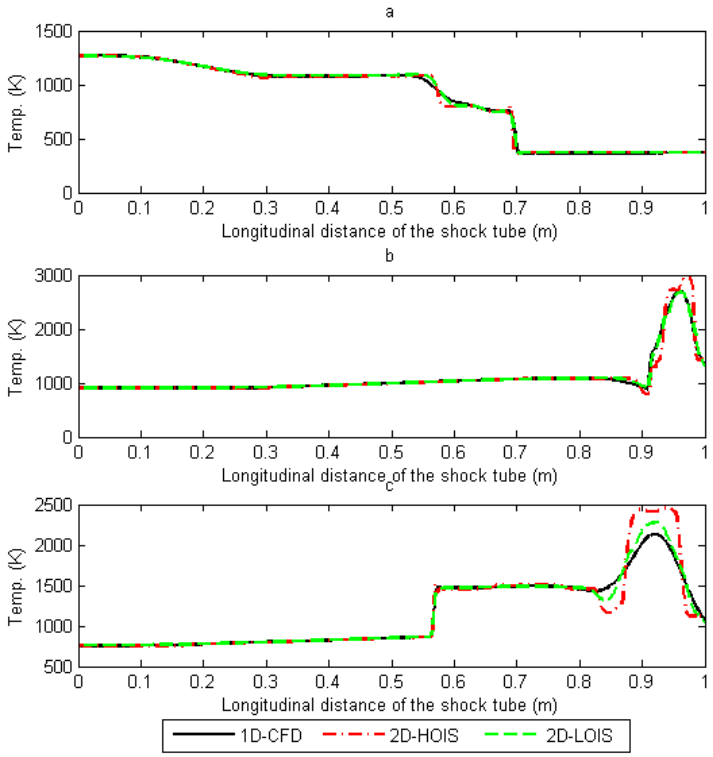

Figure 5-8 Temperature profile throughout the shock tube at: a) 500 time steps b) 1000 times steps c) 1500 time steps (Time step = 9e-7 sec) estimated by the in-house code and by ANSYS FLUENT® when the high order interpolation scheme (HOIS) and the low order interpolation scheme (LOIS) are implemented

Fuel is consumed faster when the in-house code is implemented and the maximum fuel concentration at the end of the reaction is lower than 1e-5, such as the selected convergence criterion.

Figure 5-10 shows the thermal NOx concentration predicted by the distinct model. The in-house code achieves the lowest pick of NOx followed by the low order interpolation scheme and the high order interpolation scheme.

A remarkable difference in the NOx concentration is observed when the high order interpolation schemes is implemented, due to the elevated temperature profile predicted by the model, since the NOx production is expected to double

for every 90 K increase when the gases temperature is near to 2200 K (ANSYS FLUENT®).

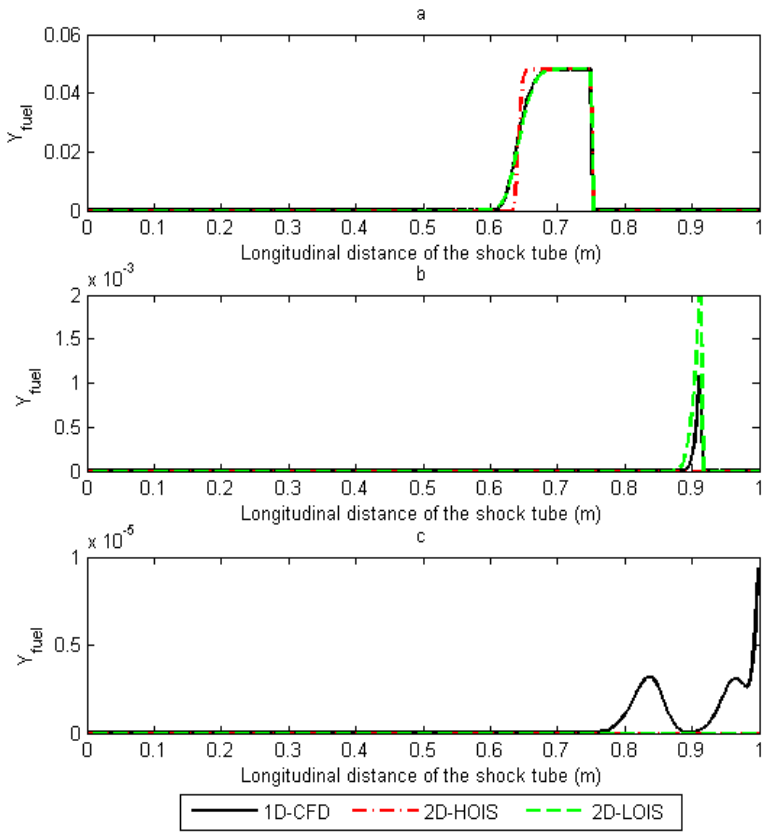

Figure 5-9 Mass fraction of fuel throughout the shock tube at: a) 500 time steps b) 1000 times steps c) 1500 time steps (Time step = 9e-7 sec) estimated by the in-house code and by ANSYS FLUENT® when the high order interpolation scheme (HOIS) and the low order interpolation scheme (LOIS) are implemented

The NOx concentrations predicted by the in-house code and by the low order interpolation scheme are in the same order but with smoother profiles predicted in the first case.

Although these results about the accuracy of the NOx model are not conclusive, they confirm that the proposed alternative is able to predict the trend of the NOx formation.

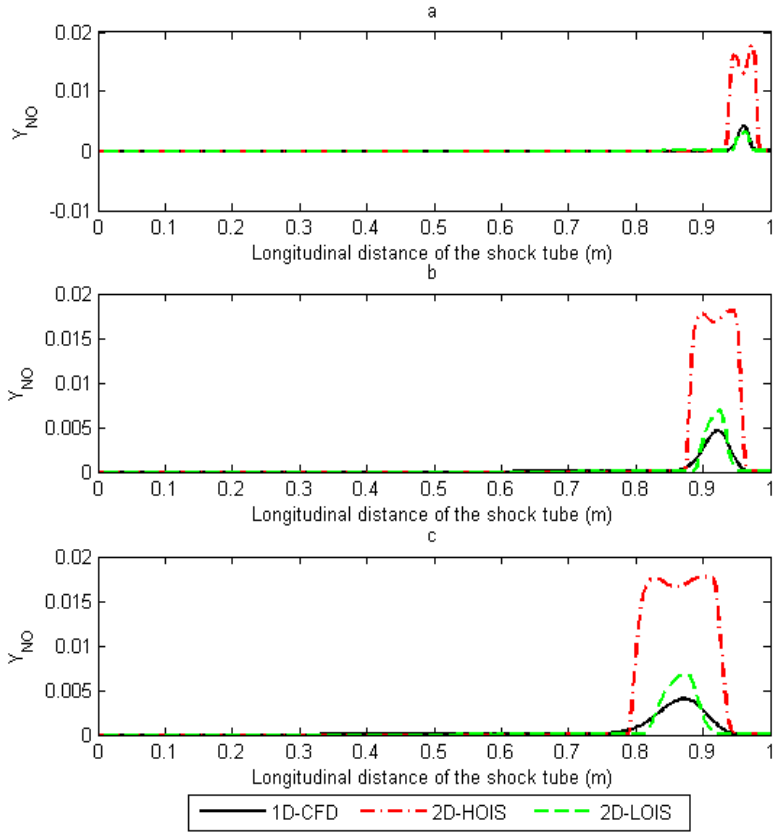

Figure 5-10 Mass fraction of NO throughout the shock tube at: a) 500 time steps b) 1000 times steps c) 1500 time steps (Time step = 9e-7 sec) estimated by the in-house code and by ANSYS FLUENT® when the high order interpolation scheme (HOIS) and the low order interpolation scheme (LOIS) are implemented

5.5 Boundary conditions interaction during the ICWR simulation

A channel located at the bottom of the scheme shown in Figure 5-1 is selected to start the simulation (origin of the cycle). At this position the channel's ends are open; one end in contact with the right port to feed the turbine with burned gases and the other end in contact with the left port to feed the ICWR with fresh air and fuel. The CFD model is set by fixing *"stagnation properties"* at the left side and *"static properties"* at the right side as boundary conditions.

The injection is performed in three stages as follows: The first stage injects pure air to produce the required seal (see sub-section 5.1). The second stage injects

reactants for the fuel stratification, and the third stage injects the remaining air from the core flow managed by the gas turbine.

The stagnation properties implemented to model the injection of air and reactants into the ICWR are the same thus the composition of the fluid is only changed during the distinct stages.

The in-house code solves a transport equation of a normalized scalar to track the contact wave that separates burned gases from fresh air, as it was performed during the wave rotor dimensioning (see sub-section 3.6.2.3).

However, in this case the normalized scalar value is alternated between 0 and 1 at the injection port during each cycle as Figure 5-11 indicates, because the device only has a single injection port. The arrival of the scalar jump discontinuity to the right side indicates the closure of the channel's right end (wall boundary condition).

Based on the process described in section 5.1, the program keeps monitoring the pressure signal at each side of the channel to capture the sudden increase of pressure produced by the shock waves generated after the detonation. The arrival of these jump discontinuities to the channels' ends are implemented by the code to close the left port of the ICWR and to open the right port of the ICWR, see Figure 5-1.

The simulation of the cycle ends when the pressure at the left plate drops enough to start the injection of seal air; the drop in pressure is produced by the arrival of the rarefaction wave generated when the interaction between the channels and the right port of the ICWR is initiated (see section 5.1).

It is important to solve at least four cycles to reduce the noise generated by the initial values. The ports' location, their lengths and the average value of the fluid properties when it crosses them are post-processed once the simulation culminates; the average values of the fluid's properties at the right port are required to continue the heat balance of the gas turbine.

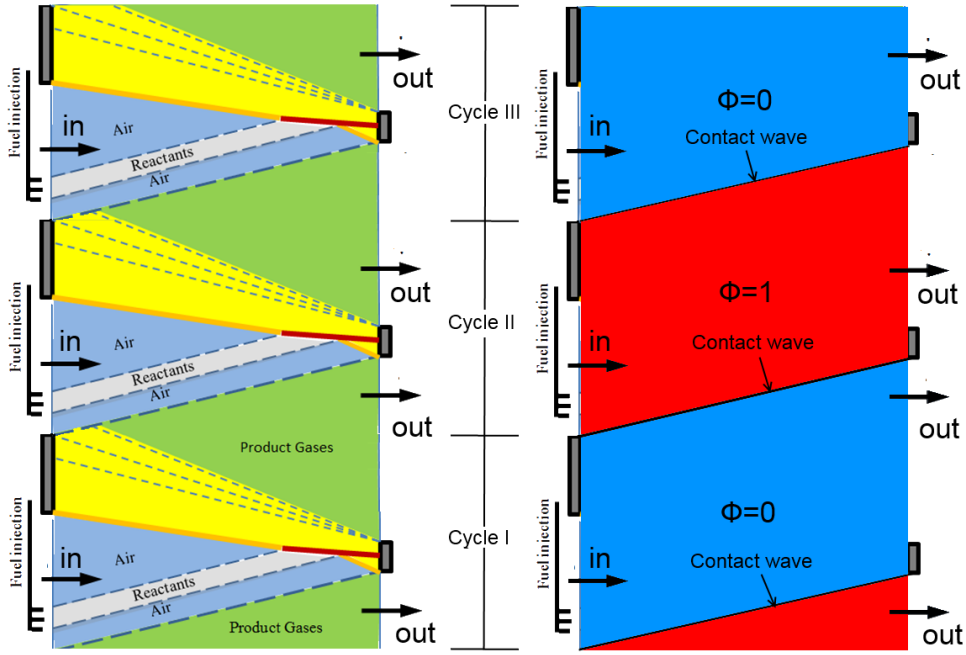

Figure 5-11 Representation of the normalized scalar implemented to track the contact wave between fresh air and burned gases

5.6 Strength of the compression shock wave and the auto-ignition of fuel (one step reaction mechanism)

Sub-section 5.2.3 presented the reaction mechanism implemented by the in-house code developed in this work to simulate the detonation. Now, this sub-section tries to predict the reactants condition to prevent the auto-ignition of fuel during its injection into the ICWR and the strength required by a shock wave to initiate a detonation combustion process using the proposed reaction model.

Figure 5-12 presents the auto-ignition delay time (in msec.) of different fuels multiplied by the reactants pressure (in atm) at different values of temperature. In addition, Figure 5-13 shows the Jet-A curve extracted from Figure 5-12, but with a new scale to make any future calculation easier.

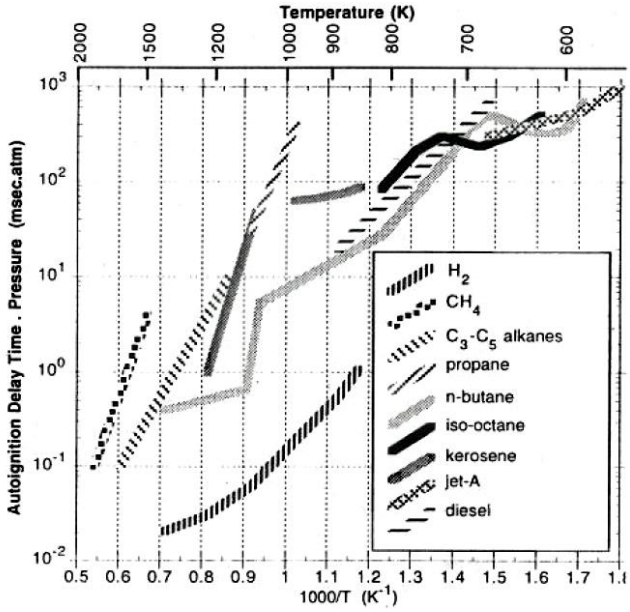

Figure 5-12 Auto-ignition delay for common fuels (M. R. Nalim 1999)

Table 28 shows the auto-ignition delay of Jet-A for different values of pressure and temperature. The minimum time reported is 0.012 sec. and it is obtained when pressure and temperature are the highest among the studied cases. In this table, $f(T)$ represents the auto-ignition time multiplied by the fluid pressure and it is acquired from Figure 5-13; $f(T)$ at 700 K is obtained through extrapolation.

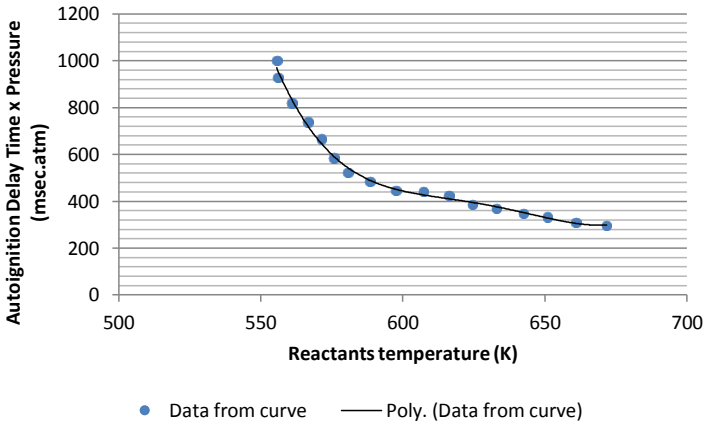

Figure 5-13 Auto-ignition delay for common extracted from Figure 5-12

Table 28 Auto-ignition delay time of Jet-A at different values of pressure and temperature of reactants

p (atm)	T (K)	f(T) Figure 5-13 $(msec \cdot atm)$	Auto-ignition delay time (sec)
1	560	820	0.82
10	560	820	0.082
20	560	820	0.041
1	600	450	0.45
10	600	450	0.045
20	600	450	0.0225
1	650	330	0.33
10	650	330	0.033
20	650	330	0.0165
1	700	240	0.24
10	700	240	0.024
20	700	240	0.012

The evaluation of future ICWR considers the injection of reactants that behaves such as air with a Mach number between 0.2 and 1. Therefore, the injection time should change from 0.009 sec/m to 0.002 sec/m approximately; at least one order of magnitude below the auto-ignition times of reactants injected with a temperature between 560 K and 700 K (as shown in Table 28). So, this range of temperatures looks suitable to avoid any problem related with the auto-ignition of fuel.

Figure 5-14 displays the reaction trajectories given by a mixture of Jet-A (Kerosene) and air at 600 K predicted by the reaction mechanism presented in sub-section 5.2.3. The trajectory is computed from ODE45 (The MathWorks Inc 2011) for distinct values of pressures and equivalence ratios (ø). The time integration is set up to 0.009 sec; which is the maximum filling time per meter of channel expected during the injection of reactants.

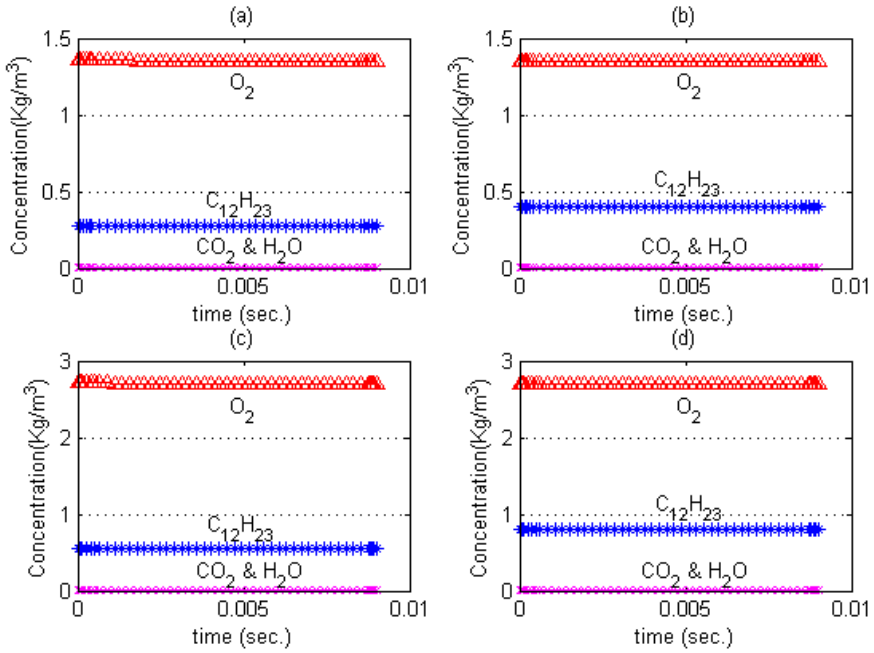

Figure 5-14 Reaction trajectories of Jet-A (Kerosene) and air at 600 K and: a) Ø=0.7 and 10 atm, b) Ø=1.0 and 10 atm, c) Ø=0.7 and 20 atm, d) Ø=1.0 and 20 atm.

A constant value of the molecules concentration is observed through the entire interval of time in all these cases. So, the reaction model of Jet-A does not predict combustion initiation at those conditions. These results agree with Nalim's observations, who stated that auto-ignition of fuel is unfeasible in an ICWR when the temperature of reactants is lower than 600 K (M. R. Nalim 1999). The same prediction is given by the simulation when the reactant temperature is lower than 700 K.

Once the injection temperature of reactants is selected to prevent the fuel auto-ignition, it is important to know the minimum strength required by a shock wave to start the detonation. The initiation of the reaction behind the shock wave is feasible if the fluid temperature after the shock compression is above 900 K, since the chemical induction time is reduced to about 0.01 millisecond (M. R. Nalim 1999).

The strength of the shock wave generated inside the ICWR is strongly associated with the energy of the fluid injected into the channels and therefore it is linked to state 3 shown in Figure 5-2, as well as the diameter of the ICWR

and its angular velocity (ω). The last two parameters enable the computation of the tangential velocity of the channels (see Eq. (5-20)) to change the reference frame from the stator to the rotor of the device, since the flow relative velocity is modified and this change in the velocity also affects the total properties of the fluid, regardless that the static properties are constant between the stator and the rotor (see Figure 5-15).

$$u_t = \omega . D . \pi \qquad \textbf{(5-20)}$$

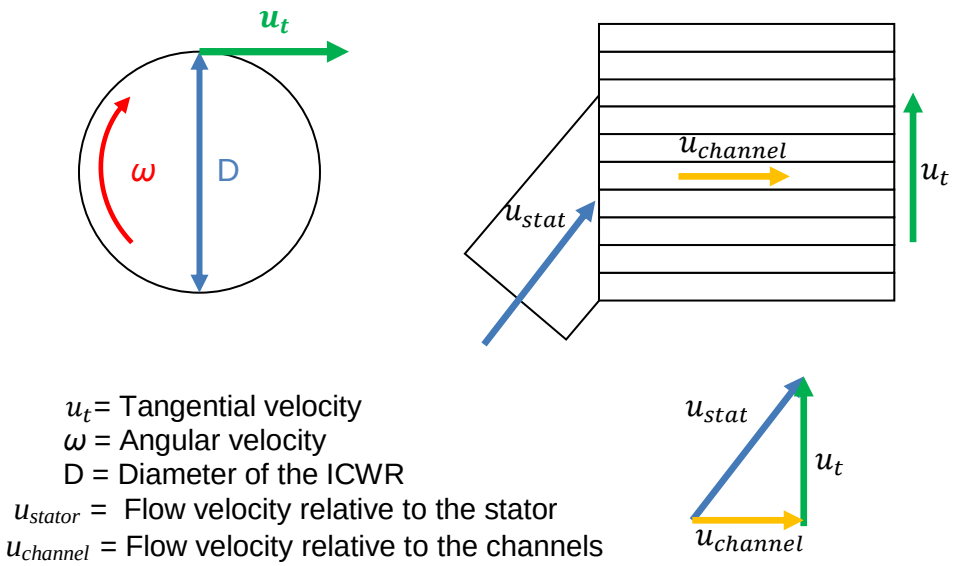

u_t= Tangential velocity
ω = Angular velocity
D = Diameter of the ICWR
u_{stator} = Flow velocity relative to the stator
$u_{channel}$ = Flow velocity relative to the channels

Figure 5-15 Effect of the angular velocity and diameter of the ICWR on the flow relative velocity

The state of the fluid after the compression (state 3 in Figure 5-2) is computed by assuming a gas turbine operating with the same data sheet as the baseline engine implemented during the wave rotor evaluation (see Table 1), but with a compressor pressure ratio that changes from 1 to 40 and a reactants injection Mach number that changes from 0.2 to 1.

Moreover, the diameter of the ICWR and its angular velocity (ω) are set equal to 1 meter and 3600 RPM, analogous to the WR selected in chapter 3, see Table 9. This approximation is made due to the similarities between both devices and

because the actual dimensions of the ICWR are only obtained at the end of the preliminary design.

The reactants are injected through the injection port only in the axial direction of the ICWR to maximise the strength of the shock wave since the flow velocity relative to the channel increases in magnitude over the flow velocity relative to the stator and therefore the stagnation properties also increase their magnitude (see Figure 5-16); a topic addressed in section 3.2. The channels' angle is computed implementing the velocity triangle.

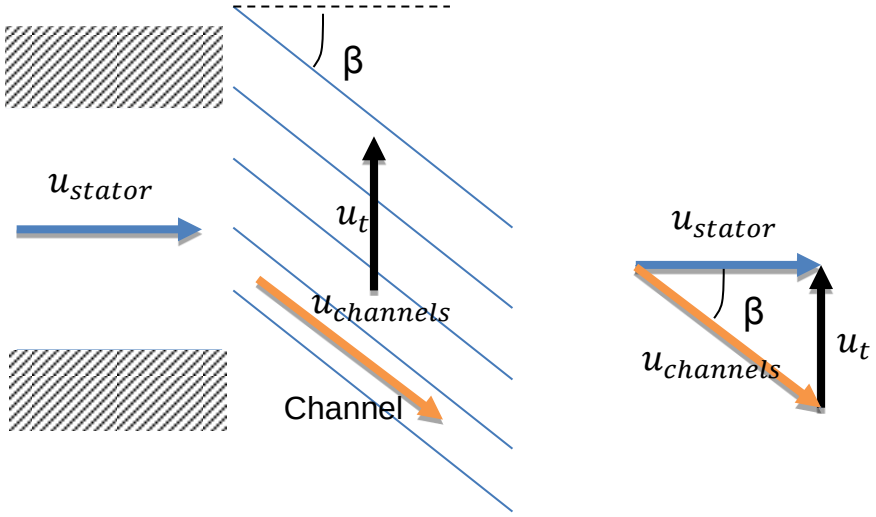

Figure 5-16 Triangle of velocities obtained when reactants are injected in the axial direction of the ICWR,

Figure 5-17 shows the temperature profile obtained after computing the injection state of reactants for different compressor pressure ratios and injection's Mach numbers. The entire range of injection's Mach numbers is able to ensure injection temperatures between 600 K and 700 K (temperatures that prevent self-ignition) whilst the compressor pressure ratio is limited to a range from 12 to 32.5.

The shock wave strength is obtained through equations from Eq. (A- 4) to Eq. (A- 6), such as was done by Weber during the computation of the strength given by the first shock wave in a WR (see section 3.2). In this stage, the state of the fluid during the injection process is implemented as input-data.

As a result, Figure 5-18 displays the temperature reached by the reactants after the shock wave compression for different compressor pressure ratios and injection's Mach numbers.

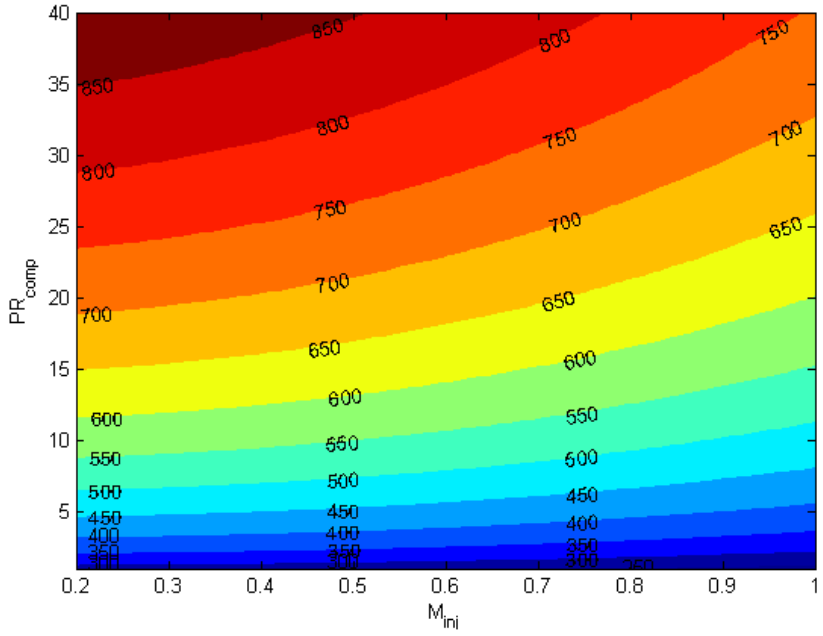

Figure 5-17 Temperature of reactants in Kelvin during their injection into the ICWR for different compressor pressure ratios and injection's Mach numbers

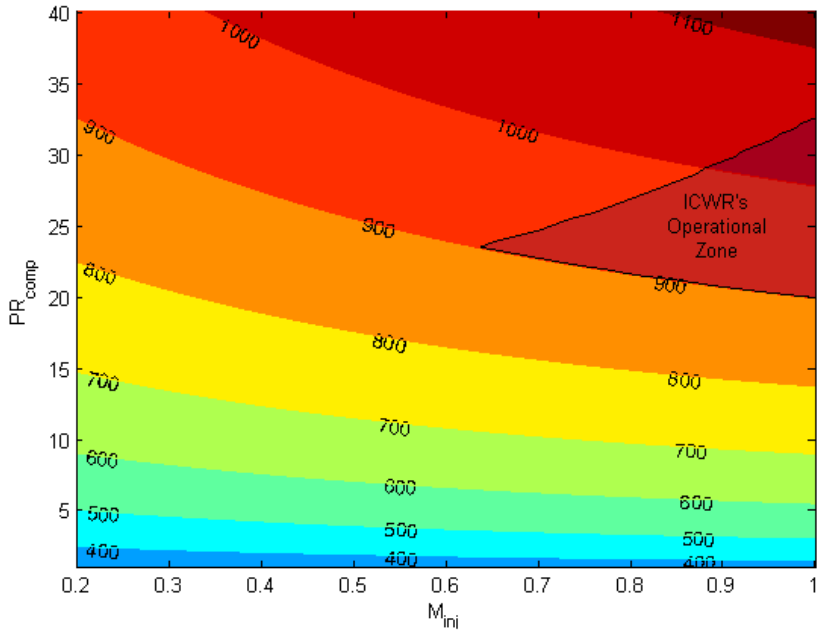

Figure 5-18 Temperature of reactants in Kelvin after the compression of the shock wave for different compressor pressure ratios and injection Mach numbers; the shaded region represents the ICWR's operational zone

The shaded region shown in Figure 5-18 represents states of the ICWR where auto-ignition is prevented during the reactants injection ($T_{inj} \leq 700K$) and where the shock wave is strong enough to promote the fuel detonation ($T \geq 900\ K$ after the shock wave compression). This clearly indicates the necessity of an ICWR with an injection's Mach number higher than 0.6 and an elevated compressor pressure ratio between 20 and 32.5.

To corroborate the capability of the in-house code to simulate the ICWR, the reaction mode is evaluated again but at 900 K and different values of pressure and equivalence ratios ($\emptyset$). Figure 5-19 shows the predicted reaction trajectory of a reactive mixture which comprises Jet-A (kerosene) and air. In all the cases the reaction mechanism is reproducing the expected behaviour since the reaction is initiated before the first 5e-4 seconds.

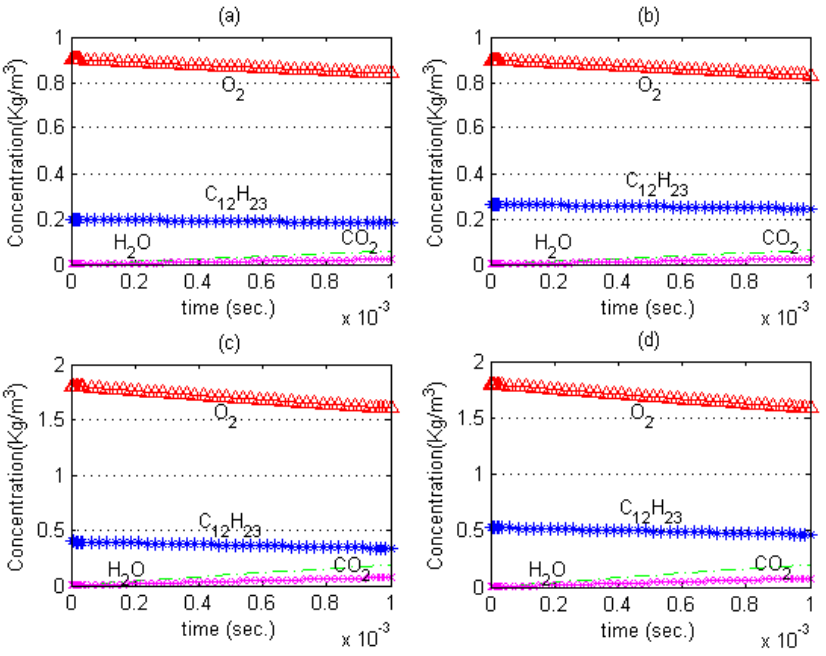

Figure 5-19 Reaction trajectories of Jet-A (Kerosene) and air at 900 K and: a) Ø=0.7 and p=10 atm, b) Ø=1.0 and p=10 atm, c) Ø=0.7 and p=20 atm, d) Ø=1.0 and p=20 atm.

Figure 5-20 shows the acoustic transition time (time required by the compression shock wave to travel one meter of distance), which results from the inverse of the shock wave velocity relative to the fluid. The acoustic transition time in the ICWR's operational zone changes between 1.310^{-3} sec/m and $1.1x10^{-3}$ sec/m. These numbers are one order of magnitude higher that the reaction initiation time obtained above, resulting in an imminent detonation wave (M. R. Nalim 1999).

In summary, the ICWR's operational zone defines the conditions that lets an ICWR to burn Jet-A through a self-generated detonation process. In this region the reaction model has shown its capability of reproducing the detonation since it approves the validation process.

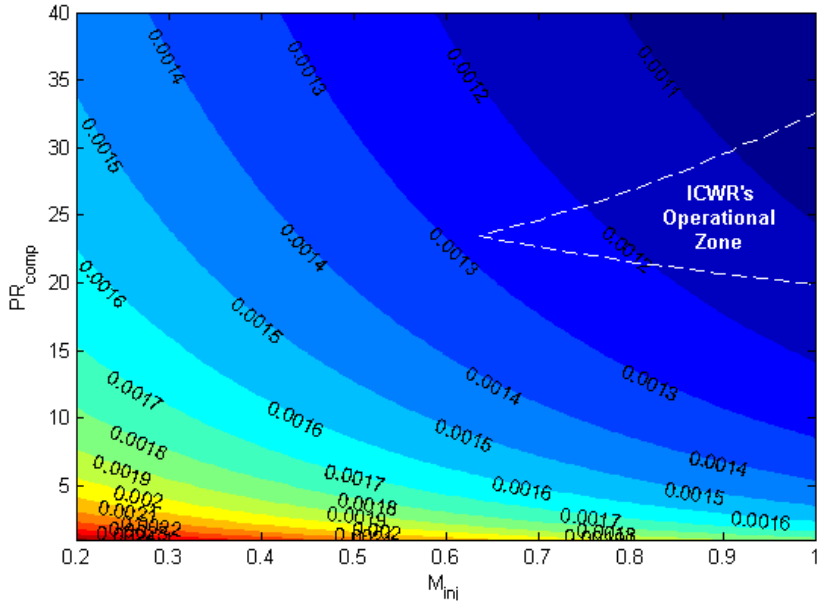

Figure 5-20 Acoustic transition time in (sec/m),

5.7 ICWR design procedure

The procedure followed to obtain the dimensions of an ICWR is composed of three stages.

5.7.1 Stage 1

The state of the fluid that crosses the injection port of an ICWR is estimated for a gas turbine of an airplane flying at a specified altitude with a fixed Mach number. Parameters such as adiabatic efficiency of the diffuser, isentropic efficiency of the compressor, compressor pressure ratio and the injection Mach number are necessary to accomplish this stage.

The injection Mach number and the compressor pressure ratio are taken from the ICWR's operational zone observed in Figure 5-18 and Figure 5-20, whilst the other parameters are taken from Table 1. The computed properties at the injection port are: total pressure, total temperature, static pressure, static temperature, injection velocity and density.

5.7.2 Stage 2

The injection velocity and the channels' angle (β) are computed using the rotor as a new reference frame through a velocity triangle that includes the tangential velocity given by Eq. (5-20), see Figure 5-16.

The new velocity and the static properties at the injection port are then employed to compute the stagnation properties relative to the rotor. This data is required to set the boundary conditions of the 1D-CFD model.

5.7.3 Stage 3

The CFD model is set using the data estimated above. The total pressure and temperature relative to the rotor are used as boundary conditions at the left side of the channels (pressure and temperature at the inlet), whilst the static pressure at the withdrawal port is implemented as a boundary condition at the right side of the channels (pressure at the outlet). By default, the length of the channels is set equal to 0.9.

Once the CFD-1D model converges, the angular velocity is corrected through Eq. (5-21); where $\Delta t_{cycle.}$ *is* the time per cycle predicted by the simulation in seconds and 60 is a conversion factor from seconds to minutes.

$$RPM = \frac{60}{\Delta t_{cycle}} \quad \textbf{(5-21)}$$

The new RPM is only implemented to calculate a corrected diameter through Eq. (5-22), since the values u_t and β are kept constant.

$$D = \frac{u_t}{\pi} \quad \textbf{(5-22)}$$

To conclude the dimensioning process, the mass flow estimated in Eq. (5-23) is compared with the core flow managed by the gas turbine. If they differ from each other than the height of the channels (h) is changed until both values are the same.

The integration is numerically performed with the trapezoidal rule whilst the interval of integration is defined as the time in which the injection port is kept opened.

$$\dot{m}_{inj} = \frac{\int \rho_{inj}.u_{inj}.dt_{inj}.cos(\beta).h}{u_t} \quad \textbf{(5-23)}$$

The stagnation properties at the exit port of the ICWR are computed after changing the reference frame from the rotor to the stator with a procedure similar to that discussed in stage 2. The mean stagnation temperature is obtained through a mass-weighted average and the mean stagnation pressure through an area-weighted average.

5.8 Performance assessment of ICWR

The performance assessment of an ICWR as a component of aircraft gas turbines considers the evaluation of three different states within the ICWR's operational zones, as shown in Figure 5-21. These states are selected because they operate near the lower limit, thus requiring lower compressor pressure ratios than other options. But at the same time the states are slightly above the lower limit to ensure a temperature higher than 900 K able to initiate the detonation process (the ICWR's operational zones is obtained from the simplified analytical solution and therefore it has a level of error).

Operating conditions selected to perform the evaluation of the ICWR over the contour of temperature of reactants in Kelvin exposed in Figure 5-18; the shaded region represents the ICWR's operational zone

Table 29 shows the compressor pressure ratios and injection Mach number of each option as well as the fluid properties required by the 1D-CFD code, whilst Table 30 shows the channels' angle and the tangential velocity of the rotor. The properties are obtained after implementing stages 1 and 2 described in sub-sections 5.7.1 and 5.7.2.

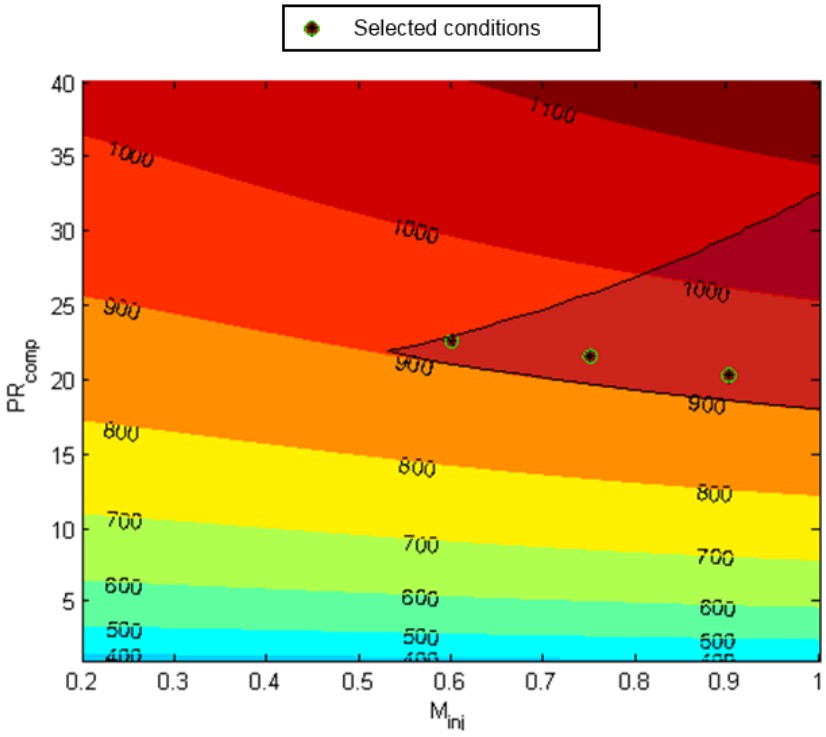

Figure 5-21 Operating conditions selected to perform the evaluation of the ICWR over the contour of temperature of reactants in Kelvin exposed in Figure 5-18; the shaded region represents the ICWR's operational zone

Table 29 Properties calculated in steps 1 and 2 under the experimental conditions selected for the performance evaluation of ICWR

Case	M_{inj}	PR_{com}	T_0(K)	p_0 (Pa)	T (K)	p (Pa)	ρ	u
1	0.6	22.5	7.63E+02	1.28E+06	6.96E+02	9.25E+05	4.63	3.69E+02
2	0.75	21.5	7.53E+02	1.22E+06	6.61E+02	7.76E+05	4.09	4.30E+02
3	0.9	20.25	7.61E+02	1.27E+06	6.39E+02	6.89E+05	3.76	4.94E+02

Table 30 Channels' angle (β) and rotor tangential velocity.

Case	β(^{o})	u_t (m/s)
1	-30.7	188
2	-25.9	188
3	-22.7	188

It is important to remark that even though the evaluation conditions are selected near the lower limit of the ICWR's operational zone, as described above, the compressor pressure ratio is well above the maximum compressor pressure ratio implemented by the baseline gas turbine (see Table 1), therefore this device has a penalty factor included in the performance evaluation conducted in the following chapter. Table 31 shows the compressor pressure ratios required at each of the evaluated conditions shown in Figure 5-21.

Table 31 Total pressure ratio required by the experimental conditions selected for the performance evaluation of ICWR

Case	PR_{total}
1	30.60
2	29.24
3	27054

The evaluation of ICWR is performed considering equivalence ratios of 0.7 and 1 during the fuel injection. In addition, the injection of fresh air and reactants into the ICWR is performed in three stages, as stated in section 5.5. However, there is not a criterion available to define these stages in advance.

To overcome the problem, the injection time of reactants was estimated from an iterative process that evaluates the gases temperature after their mixture at the exit port of the ICWR, whose value is limited to 1110 K (maximum temperature allowed by the turbine baseline).

The process followed is computationally expensive, since four cycles are necessary at least to calculate the outflow conditions whilst the average temperature is quite sensitive to small changes in the injection time.

Table 32 shows the time interval in each stage applied to the various equivalence ratios considered in this analysis.

Table 32 Interval of time implemented during each injection stage to model the ICWR

Stage	Time
Time to inject the seal air	7.38e-004 sec
Time to inject the reactive mixture ($\emptyset = 0.7$)	8.82 e-004sec
Time to inject the reactive mixture ($\emptyset = 1$)	6.17 e-004sec
Time to inject the air in excess	It is defined by the arrival of the shock wave to the left end of the channels

Under these conditions, the average outlet temperature is less than ± 7% of the desired value.

5.8.1 Code results

Figure 5-22 presents the transient profile of fuel mass fraction inside the ICWR predicted by the 1D-CFD code, as well as the distinct stages implemented to simulate the injection port.

The coordinate system employed in this figure is axial length -peripheral length. So the procedure described in sub-section 3.6.2.4 is followed during the coordinate transformation since the 1D-CFD code uses channel's length vs time as a coordinate system.

The fuel concentration is reduced near to zero in the detonation zone due to the reaction mechanism. The smooth interface between air and reactants during the fuel injection is a consequence of the false diffusion effect whilst the change in the injection velocity experienced by the reactants at half of the channels' length is a consequence of the dynamic of the cycle.

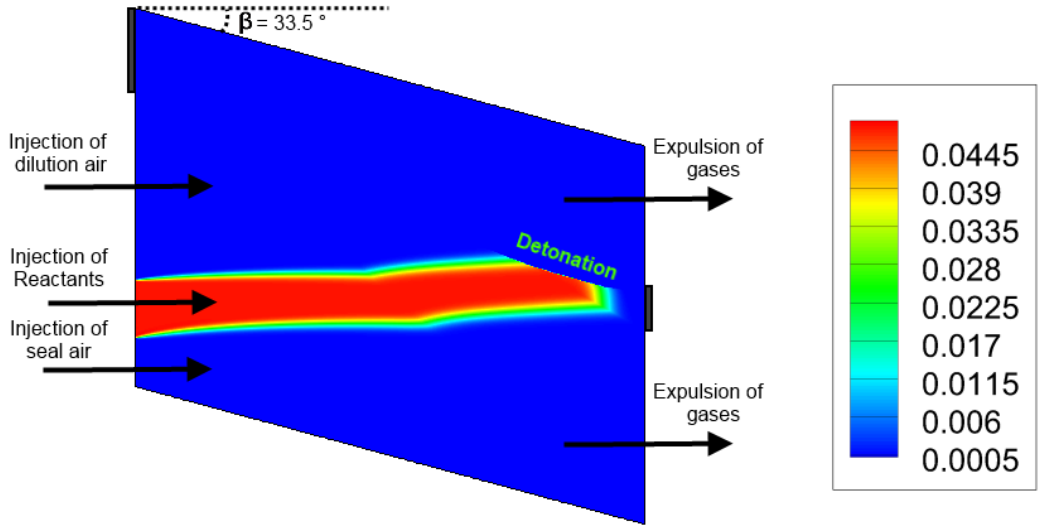

Figure 5-22 Transient profile of the fuel mass fraction inside the ICWR predicted by the 1D-CFD code

Figure 5-23 presents the transient profile of pressure inside the ICWR and enumerates the distinct waves described in section 5.1.

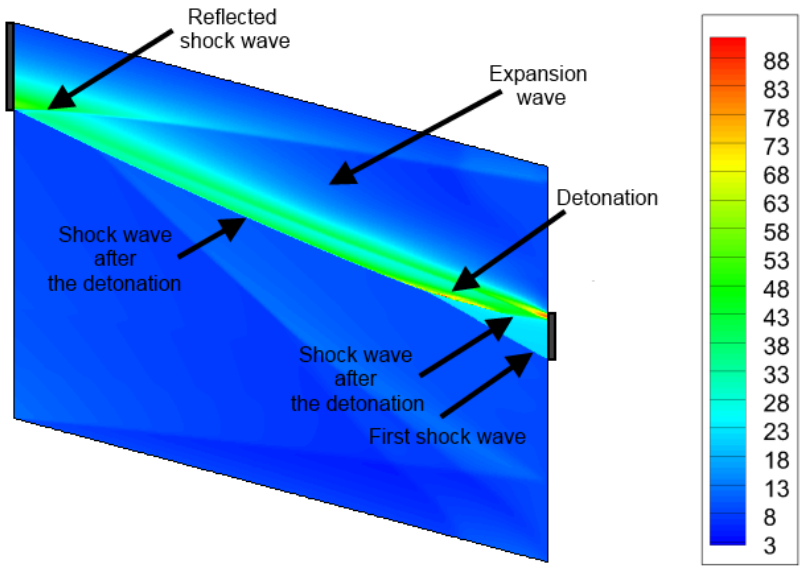

Figure 5-23 Transient profile of pressure inside the ICWR predicted by the 1D-CFD code (atm)

The maximum pressure estimated by the model is achieved during the detonation and it is transferred forward and backward over the channels through the 2nd and the 3rd shock waves.

The 2nd shock wave is reflected at the left plate and later on at the exhaust port. The second reflection is the main one responsible for the distortion in the mass concentration of fuel commented on above.

A weak wave emerges once the interaction between the channels and the injection port initiates, as a consequence of the pressure difference between the channels and the port.

Figure 5-24 shows the transient profile of temperature inside the ICWR. The ICWR injects compressed air and burned gases into the withdrawal port with a remarkable difference of temperature. Therefore, this configuration requires the design of a device able to mix these streams to reduce the gases temperature before the turbine feeding.

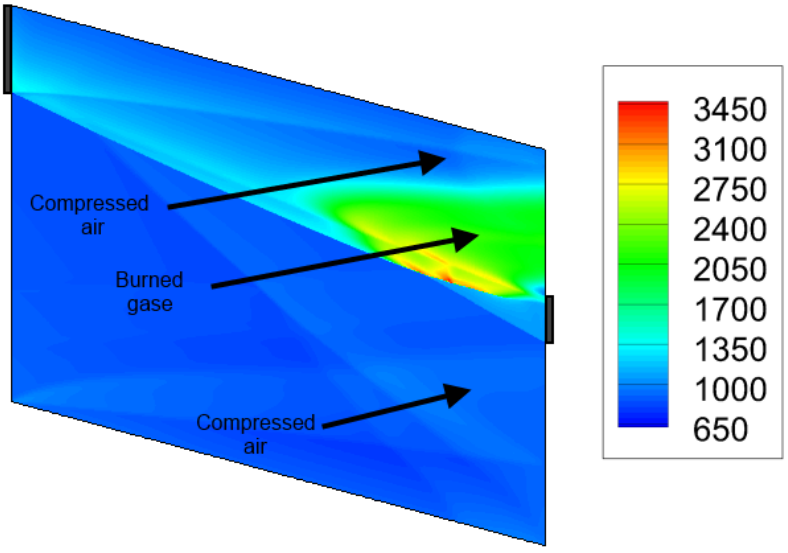

Figure 5-24 Transient profile of temperature inside the ICWR predicted by the 1D-CFD code (K)

Table 33 shows the mass flow that crosses the ends of each channel per cycle computed through Eq. (5-24) and Eq. (5-25) and the date given by the fourth cycle of each simulation.

Although the program does not implement the mass tracking as a technique to set the port closure, the methodology followed is stable and ensures a good level of accuracy of the mass conservation.

Table 33 Mass that crosses the ends of each channel per unit of channels transversal area $m_{CH,LP}/A$ and $m_{CH,RP}/A$

	$\dot{m}_{CH,LP}$	$\dot{m}_{CH,RP}$	error %
Case 1, Φ=0.7	63.4	63.1	-0.244
Case 2, Φ=0.7	63.4	63.3	-0.176
Case 3, Φ=0.7	63.4	63.3	0.179
Case 1, Φ=1	63.4	63.2	0.268
Case 2, Φ=1	63.4	63.1	0.368
Case 3, Φ=1	63.4	63.3	0.118

$$\dot{m}_{in} = u_t \cdot h \cdot \int \rho_{in}.u_{in} \cdot cos(\beta)\ dt \quad \textbf{(5-24)}$$

$$\dot{m}_{out} = u_t \cdot h \cdot \int \rho_{out}.u_{out} \cdot cos(\beta)\ dt \quad \textbf{(5-25)}$$

Figure 5-25 shows the overall mass unbalance produced by the model in a channel during each cycle of the simulation. The mass unbalance is reduced when a larger number of cycles are performed, but the error reduction rate also becomes smaller. Therefore, a more demanding convergence criterion is only possible by including more cycles with smaller time steps. However, this option was discarded due to the expected increase in the computational cost.

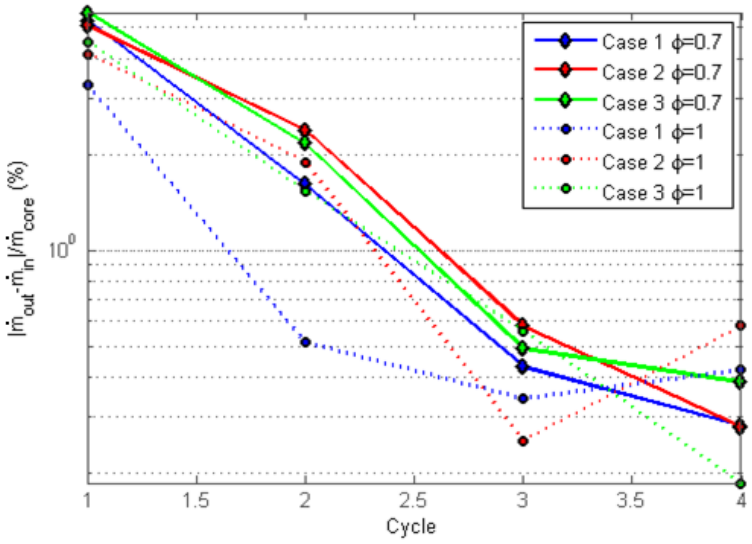

Figure 5-25 Masses flow imbalance relative to the core flow of the gas turbine computed during each cycle of the simulation

Figure 5-26 shows the pressure profile at the right side of the ICWR during a cycle whilst Figure 5-27 shows the Mach number. The pressure picks are achieved when the channel's right end is closed. This condition is represented in the profile as dotted lines.

The first jump of pressure is a consequence of the sudden reduction experienced by the flow velocity. This increase of pressure is implemented to generate the shock wave that produces the detonation of the reactive mixture.

The second pressure jump is the higher and it comes from the arrival and reflection of the third shock wave (see Figure 5-23). The highest peaks of pressure are given when the equivalence ratio is equal to 1.

In most of the cases the fluid is throttled during a small period of time once the right end of the channel is opened (M=1), see Figure 5-27. This behaviour is a consequence of the withdrawal of air trapped at the right side of the channel (seal air), whose temperature is low compared with burned gases.

Then, the withdrawal of the burned gases produces a sharp drop of the Mach number due to its elevated temperature and therefore the pressure field experiences a sharp change to its lowest value.

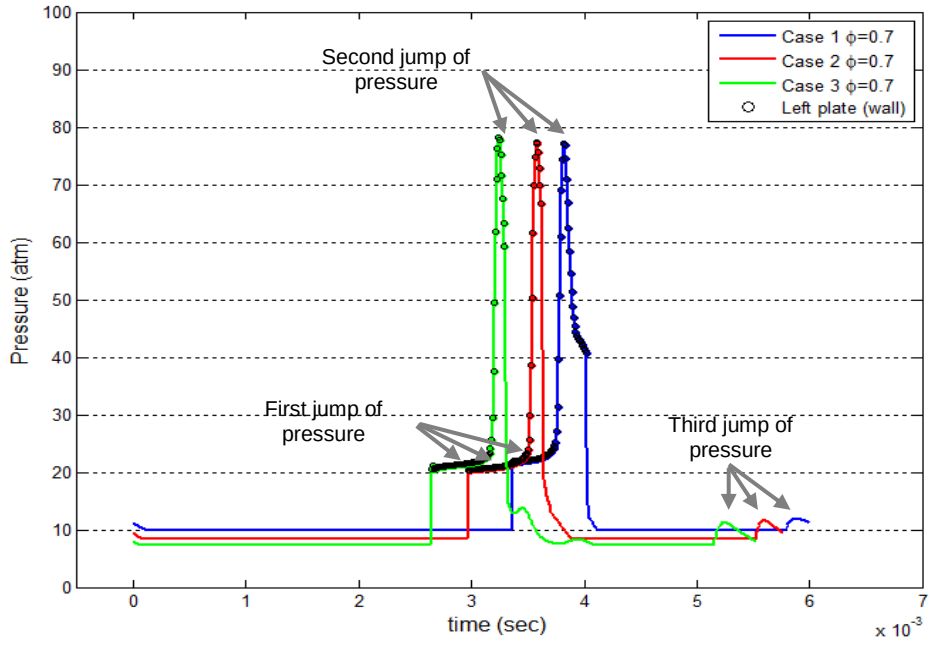

(a)

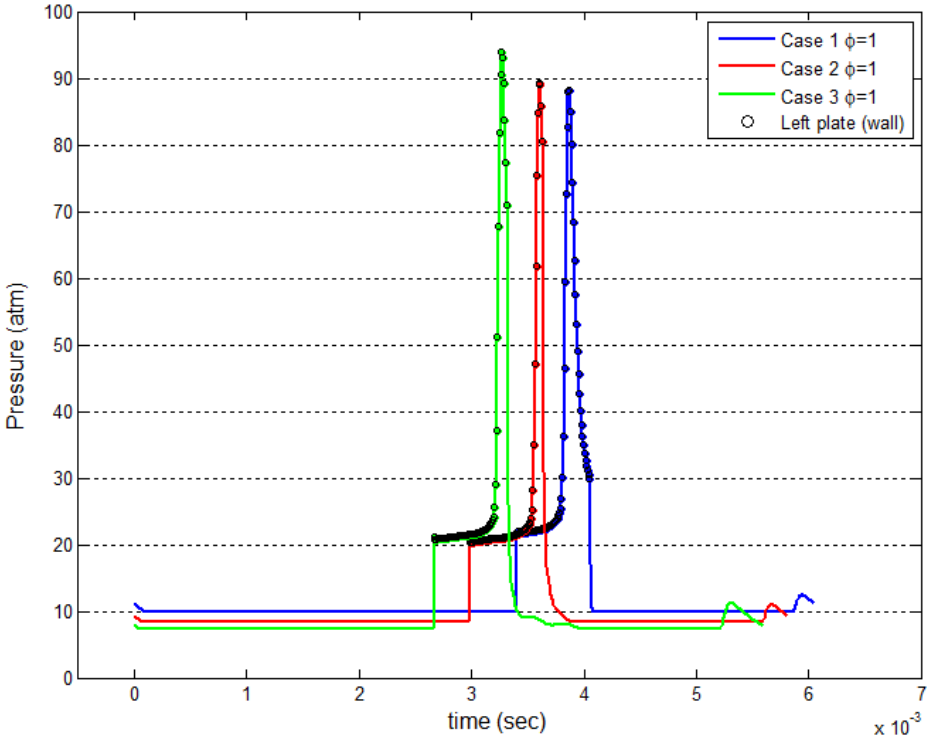

(b)

Figure 5-26 Pressure profile at the right side of the ICWR for a) $\phi = 0.7$ and b) $\phi = 1$

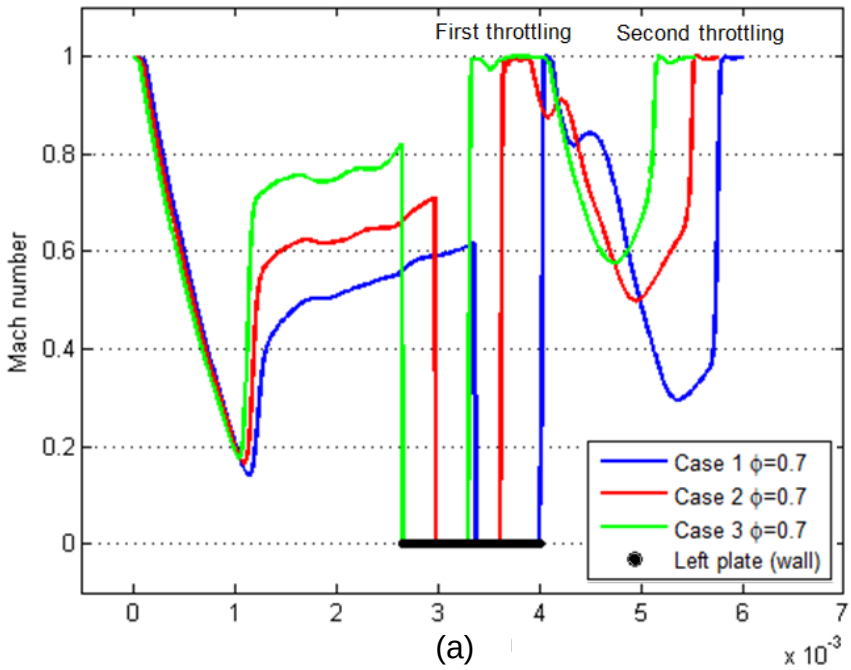

(a)

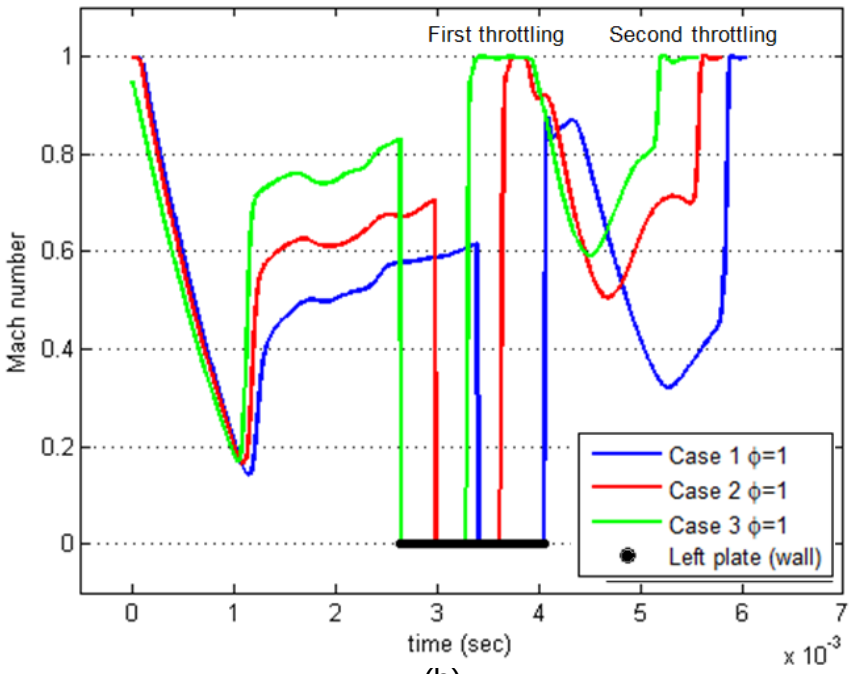

(b)

Figure 5-27 Mach number profile at the right side of the ICWR for a) $\phi = 0.7$ and b) $\phi = 1$

The next jump of pressure is produced once the second shock wave arrives at the right end of the channel, after its reflection. At this stage only compressed

air remains inside the channel at temperatures significantly below the burned gases, this condition makes the fluid become throttled again (M=1). The throttling condition is kept during a short period of time after the initiation of the following cycle.

Figure 5-28 shows the temperature profile at the right side of the ICWR. The temperature increases up to 900 K when the channel's right end is closed (dotted zones in the curves). Therefore, the sudden reduction of velocity does not expose the plate to elevated temperatures.

However, the arrival of the third shock wave is intense enough to generate a peak of temperature up to 1267 K when Φ is equal to 0.7 and 1323 K when Φ is equal to 1. If natural conduction of the material is not enough to keep the plate safely operating then an additional cooling system would be necessary.

The maximum temperature of burned gases at the withdrawal port oscillates between 1958 K and 2218 K whilst the temperature of the compressed air oscillates between 725 K and 765 K. This result corroborates the necessity of mixing both streams before the turbine feeding.

In cases one and three (Ø of 0.7), the burned gases exhibit a temperature difference of 200 K over other cases, as indicated in Figure 5-28. This effect is a consequence of a delay in combustion initiation after the reactants are compressed by the shock wave.

Figure 5-29 shows the normalised contour of temperature and the normalised contour of fuel mass fraction, which are overlapped through Eq. (5-26), to corroborate the statement above (-1 is used to represent the reactants and 1 is used to represent the flame). T and Y_{fuel} represent the temperature and the fuel mass fraction whilst subscript *i* is implemented to identify the node where the normalized values are computed; the maximum and minimum values of these variables (represented by the subscripts max and min) are obtained after the simulation of the whole cycle.

$$TY = \frac{T_i - T_{min}}{T_{max} - T_{min}} - \left(\frac{Y_{f,i} - Y_{f,min}}{Y_{f,max} - Y_{f,min}} \right) \quad \textbf{(5-26)}$$

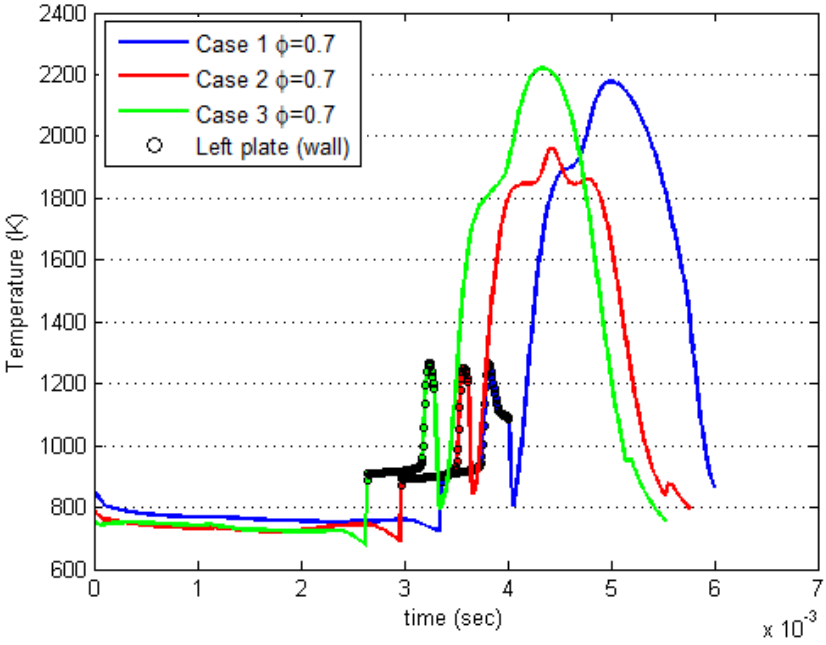

(a)

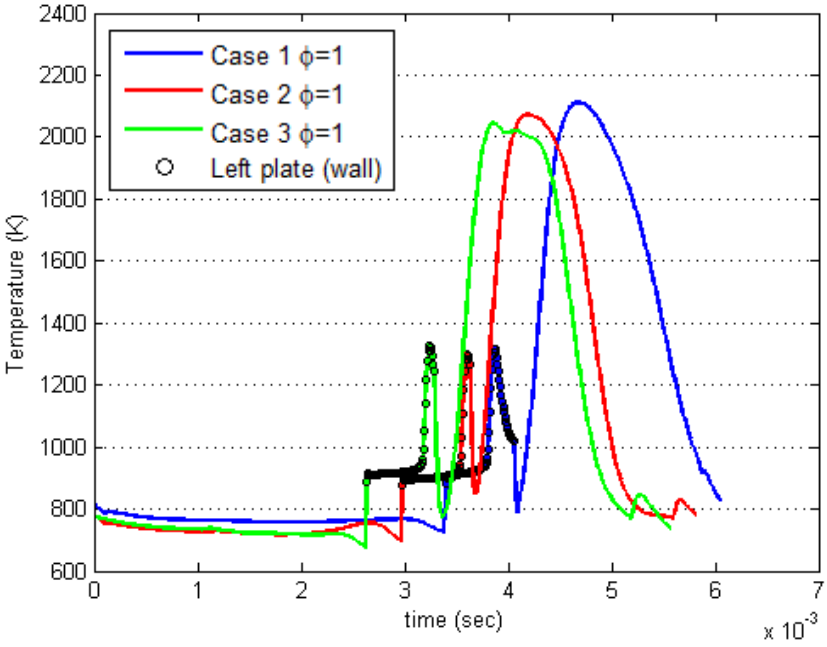

(b)

Figure 5-28 Temperature profile at the right side of the ICWR for a) $\phi = 0.7$ and b) $\phi = 1$

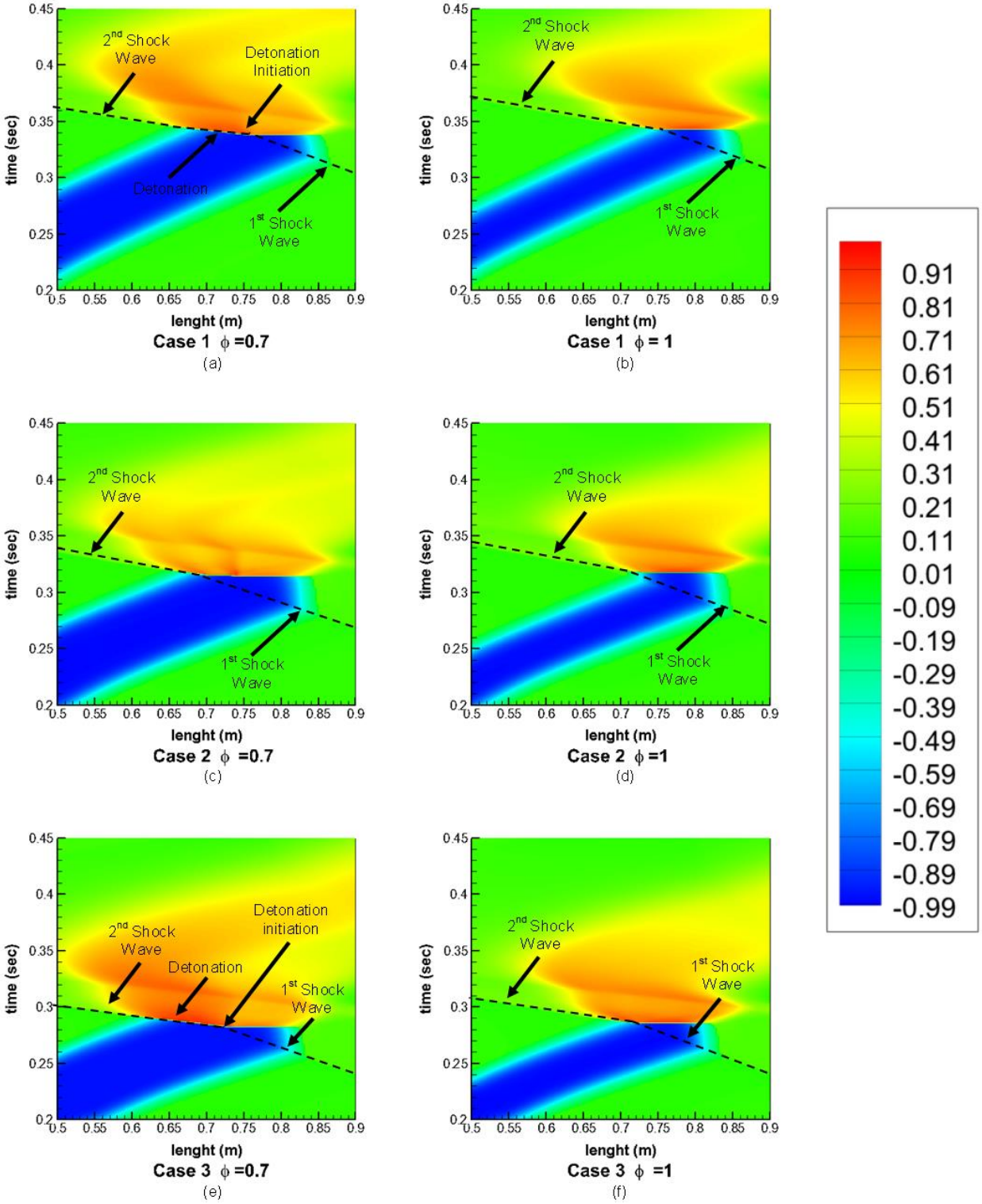

Figure 5-29 Contour of Eq. (5-26) obtained from the cases shown in Table 31 and different equivalence ratios

The shock wave represented by black dashed lines penetrates into the reaction zone to initiate the combustion process in all the cases. However, in Figure 5-29 (a) and Figure 5-29 (e) only the reaction process occurs just after the compression of the shock wave, whilst in the other cases the reaction process occurs a few milliseconds later (such as in deflagration combustion processes).

These results are a consequence of the following two factors:

- Case B produces a shock wave capable of compressing the reactants with a temperature increase between 895 K and 915 K for both equivalence ratios while the expected value is above 900 K, as observed in Figure 5-21. Unfortunately, the actual injection process is affected by some waves that remain inside the channel from the previous cycle and they produce a reduction of the temperature profile by layers such as the black lines observed in Figure 5-30.
- Reactants with higher stoichiometric ratios must be injected in a shorter period of time to prevent temperatures higher than the maximum admissible in the turbine. This produces a reduction in the width of the fuel stratification such as that observed in Figure 5-29, so the initiation of detonation is difficult to achieve.

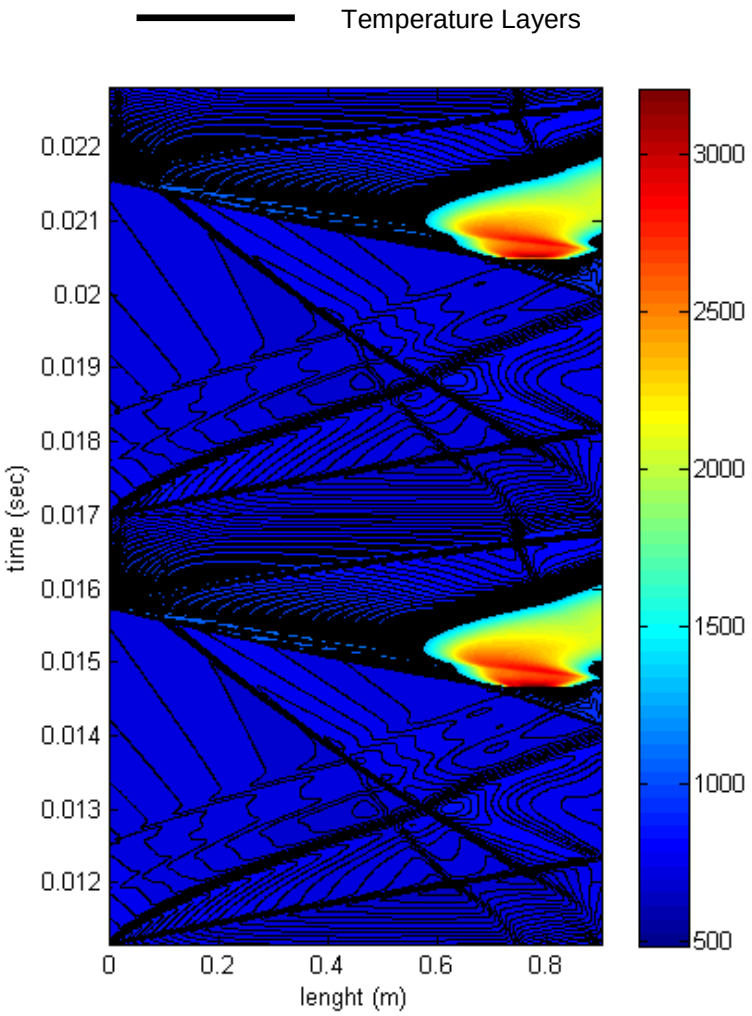

Figure 5-30 Effect of transient waves at the low levels of the temperature profile inside an ICWR – contour of temperature in Kelvin

Figure 5-26, Figure 5-27 and Figure 5-28 also indicate that case 3 requires the shortest period of time to complete the cycle, since fresh air and reactants are able to fill the channels quickly whilst the withdrawal of burned gases is done in a shorter period of time.

As a consequence, the circumferential perimeter and the diameter of the ICWR are the smallest as indicated in Table 34.

Table 34 Rotor perimeter and diameter required in each of the studied cases

	time/cycle (sec)	Rotor perimeter (m)	Rotor diameter (m)
Case 1, Φ=0.7	0.0060	1.129	0.359
Case 2, Φ=0.7	0.0058	1.085	0.345
Case 3, Φ=0.7	0.0055	1.039	0.331
Case 1, Φ=1	0.0060	1.137	0.362
Case 2, Φ=1	0.0058	1.091	0.347
Case 3, Φ=1	0.0056	1.051	0.335

5.9 Thermal Performance of ICWR

The thermal evaluation is conducted in each of the cases studied in section 5.8. The working fluid is cold standard-air as it is assumed during the thermal evaluation of gas turbines operating with WRs and PDEs. Table 1 gives information about the performance of the gas turbine components. The properties at the exhaust of the ICWR are obtained by post-processing the simulation results.

Table 35 shows the specific thrust, specific fuel consumption and efficiency of energy conversion obtained from the evaluation. These parameters are computed through Eq. (3-3), Eq. (3-4) and Eq. (3-5).

Figure 5-31 and Figure 5-32 display the trajectories followed by each cycle through a T-s diagram. The specific thrust, specific fuel consumption and efficiency of energy conversion are obtained from Eq. (3-3), Eq. (3-4) and Eq. (3-5).

The heat of combustion ($Q_{net,p}$) implemented to compute the efficiency of energy conversion is equal in magnitude to the enthalpy of combustion of Kerosene, since the correction factor for isochoric trajectories is less than 0.2%, as demonstrated in Appendix B.

Table 35 Specific thrust, specific fuel consumption and efficiency of energy conversion calculated for each of the cases considered during the performance assessment of ICWR

Φ=0.7	*Case 1*	*Case 2*	*Case 3*
$F_s\ (N \cdot sec/kg)$	99.1	95.1	112
SFC $(kg/kN \cdot h)$	53.9	56.6	52.7
η_e	0.495	0.293	0.548
Φ=1.0	*Case 1*	*Case 2*	*Case 3*
$F_s\ (N \cdot sec/kg)$	51.6	45.8	69.4
SFC $(kg/kN \cdot h)$	73.0	78.4	72.4
η_e	0.321	0.293	0.336

Case 3 offers the best performance from all of the cases studied as indicated in Table 35, since it gives the lowest SFC while the specific thrust and efficiency of energy conversion are the highest. This behaviour is followed by Case 1 and then by Case 2, which offers the worst conditions.

However, the thermal evaluation is highly influenced by the temperature at the exhaust of the ICWR (maximum temperature of the cycle) and it is difficult to reach a unique value of temperature at the discharge of the ICWR after the simulation, as shown in Figure 5-31 and Figure 5-32.

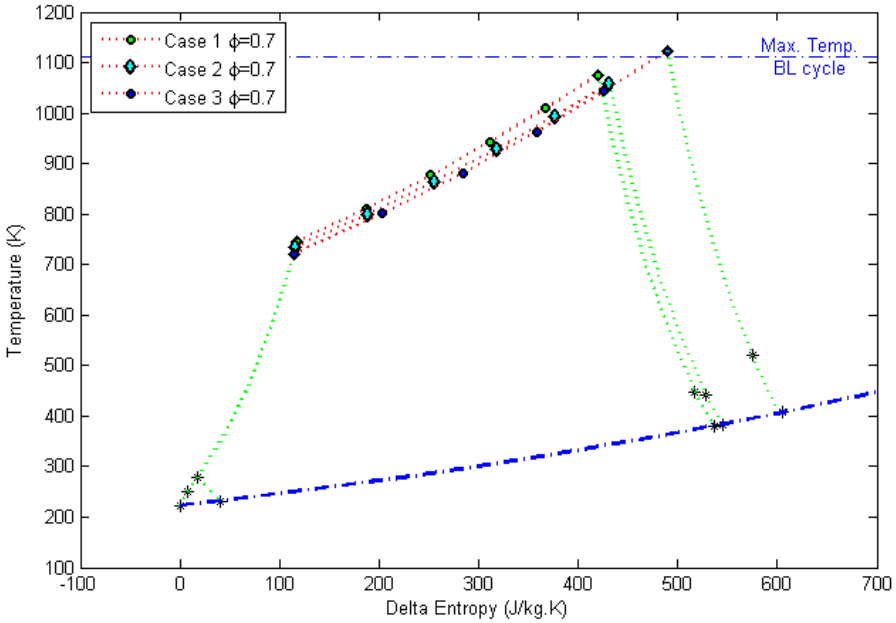

Figure 5-31 T-s diagram of the gas turbine operating with cycles 1, 2 and 3, with an equivalent ratio of 0.7

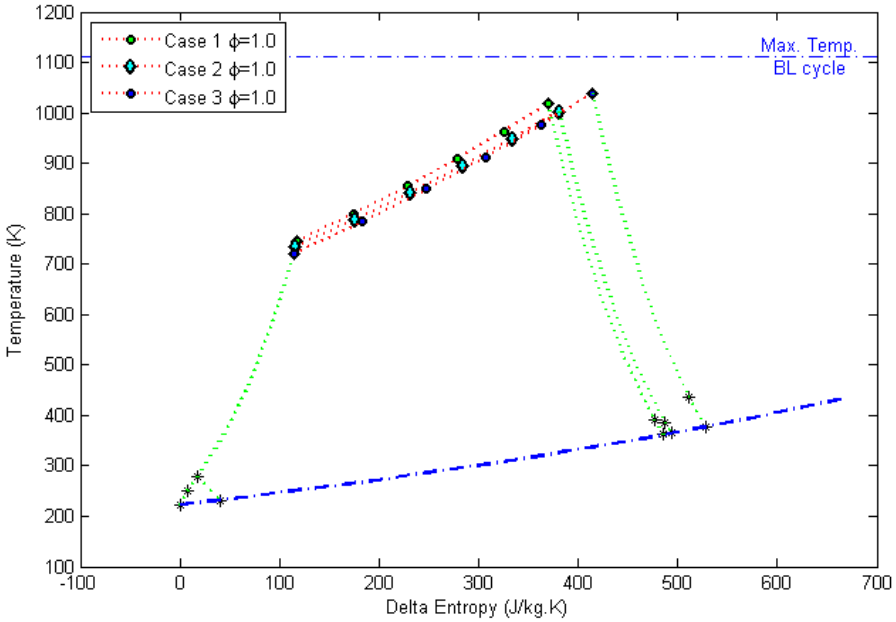

Figure 5-32 T-s diagram of the gas turbine operating with cycles 1, 2 and 3, with an equivalent ratio of 1.0

Therefore, Eq. (5-27) is implemented to measure the performance of the detonation inside the ICWR. This equation compares the trajectory predicted by

the numerical model with the isochoric and isobaric trajectory. Ψ is equal to 0 if the trajectory followed by the numerical model is isochoric and 1 if the trajectory is isobaric.

$$\Psi = \frac{\Delta S_{ICWR} - \Delta S_v}{\Delta S_p - \Delta S_v} \quad \textbf{(5-27)}$$

In the above equation, ΔS_{ICWR} is the change of entropy predicted by the model, ΔS_v is the change of entropy of an ideal gas at constant volume computed from Eq. (5-28) and ΔS_p is the change of entropy of an ideal gas at constant pressure computed from Eq. (5-29)

$$\Delta S_v = c_v \cdot ln\left(\frac{T_{out}}{T_{in}}\right) \quad \textbf{(5-28)}$$

$$\Delta S_p = c_p \cdot ln\left(\frac{T_{out}}{T_{in}}\right) \quad \textbf{(5-29)}$$

Table 36 shows the values of Ψ obtained from each of the studied cases. This result indicates that Case 1 is closer to an isochoric trajectory than the other cases during the combustion process and therefore it offers a better behaviour of the detonation. At the same time, an equivalence ratio equal to 1 performs better than 0.7 since it contributes in the reduction of Ψ.

Table 36 values of Ψ computed from each of the studied cases

	Ø=0.7	Ø=1
Case 1	0.374	0.326
Case 2	0.510	0.475
Case 3	0.447	0.359

The results presented above differ from those observed in Table 25, so the cycle performance must be estimated again, but in this opportunity the maximum temperature is fixed to 1110 K and the states are obtained from

interpolations or extrapolations. The suggested method starts by computing the change of entropy experienced by the fluid inside the ICWR through Eq. (5 26), which comes from manipulating Eq. (5 23).

$$\Delta S_{ICWR} = \Psi \cdot \left(\Delta S_p - \Delta S_v\right) + \Delta S_v \quad \textbf{(5-30)}$$

In the above equation, Ψ is obtained from Table 36 whilst ΔS_p and $\Delta S_p$are computed again from Eq. (5-28) and Eq. (5-29) but for an outlet temperature of 1110 K. Table 37 displays the new results, while Figure 5-33 shows the corrected T-s diagrams of each case.

The new scenario indicates that case 2 with an equivalence ratio of one gives the lowest SFC as well as the maximum efficiency of energy conversion, whilst the specific thrust gets higher when the injection Mach number increases. These results are not conclusive but they point out that a more efficient machine could be obtained.

Table 37 Specific thrust, specific fuel consumption and efficiency of energy conversion recomputed for a cycle maximum temperature of 1110 K.

Φ=0.7	*Case 1*	*Case 2*	*Case 3*
$F_s\ (N \cdot sec/kg)$	83.19	83.73	88.01
SFC $(kg/kN \cdot h)$	64.17	64.27	67.11
η_e	0.38	0.38	0.38
Φ=1.0	*Case 1*	*Case 2*	*Case 3*
$F_s\ (N \cdot sec/kg)$	83.92	84.3	89.4
SFC $(kg/kN \cdot h)$	55.04	54.05	56.2
η_e	0.44	0.46	0.45

5.9.1 NOX generated during the ICWR operation

In a detonation process the reactive mixture experiences a sudden change of temperature that leads product gases to reach temperatures far above 2200 K.

At those conditions the triple bond of nitrogen atoms is broken and thermal NOx generation is initiated.

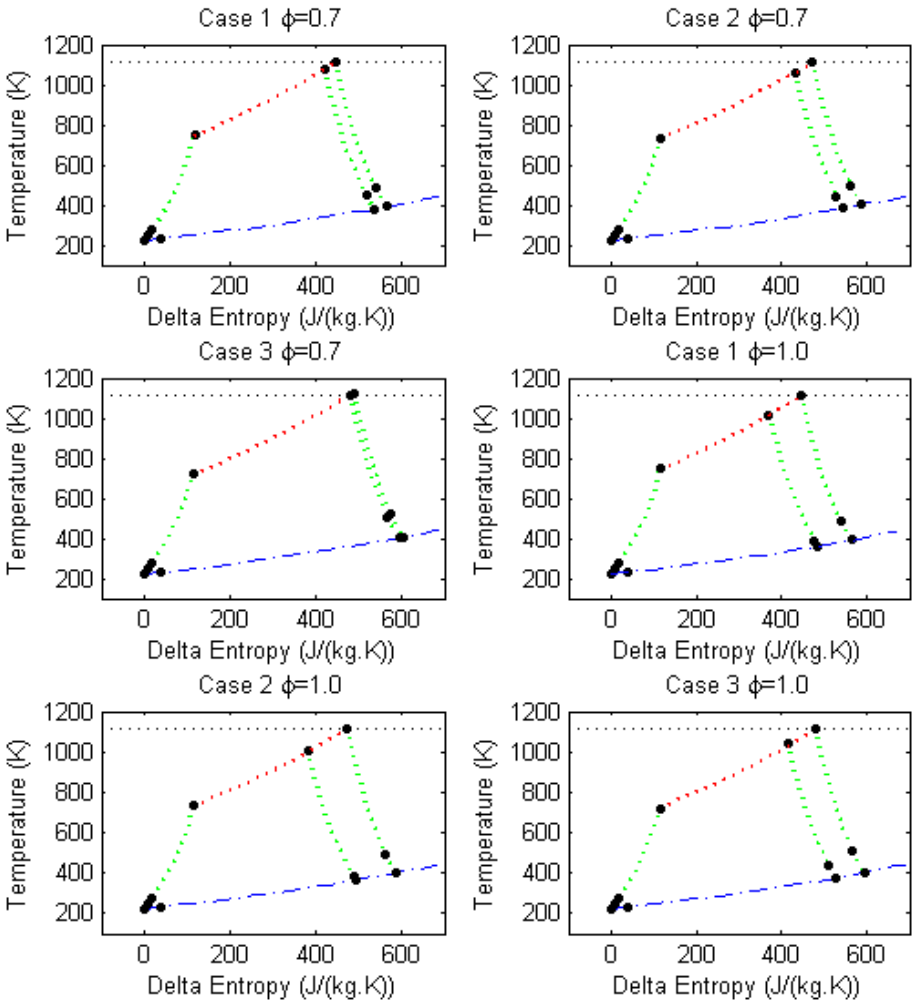

Figure 5-33 T-s diagram of each studied case corrected for an maximum cycle temperature of 1110 K

This section intends to evaluate the NOx emissions produced by the detonation process inside the ICWR when it operates as a component of the gas turbine with the conditions described in section 5.8.

Figure 5-34 presents the mass fraction of NOx in the product gases during their discharge. The maximum peaks are always achieved in case 3, since it also reaches the higher temperatures. The NOx generation obtained from each of

the studied case changes in a range between 569 and 1750 ppm, as indicated in Table 38.

The NOx generation is doubled when the equivalence ratio is reduced from 1 to 0.7. This effect is a consequence of the fuel-lean mixture in which more atoms of oxygen are available to react with atoms of nitrogen. (Saravanamuttoo 2008).

Table 38 Emissions of NOx predicted by the 1D-CFD model

	$\dot{m}_{NOx}$ (kg/sec)	$\dot{m}_{core}$ (kg/sec)	Y_{NOx}	ppm
Case 1, Φ=0.7	9.64E-02	63.3	1.52E-03	1530
Case 2, Φ=0.7	7.37E-02	63.3	1.17E-03	1170
Case 3, Φ=0.7	1.10E-01	63.3	1.75E-03	1750
Case 1, Φ=1	4.51E-002	63.3	7.14E-04	714
Case 2, Φ=1	3.59E-002	63.3	5.69E-004	569
Case 3, Φ=1	5.29E-002	63.3	8.36E-004	836

Moreover, the fuel stratification still generating elevated values of NOx regardless the equivalence ratio implemented in the design, since the interface between air and reactants helps to provide the atoms of oxygen required by the reaction. Therefore, a future control of NOx emission inside the device looks difficult to achieve.

5.10 Chapter summary

This chapter assesses the performance of the ICWR as components of the gas turbine. The performance is computed after executing a routine able to predict the path followed by the fluid inside the gas turbine during its travel along each component.

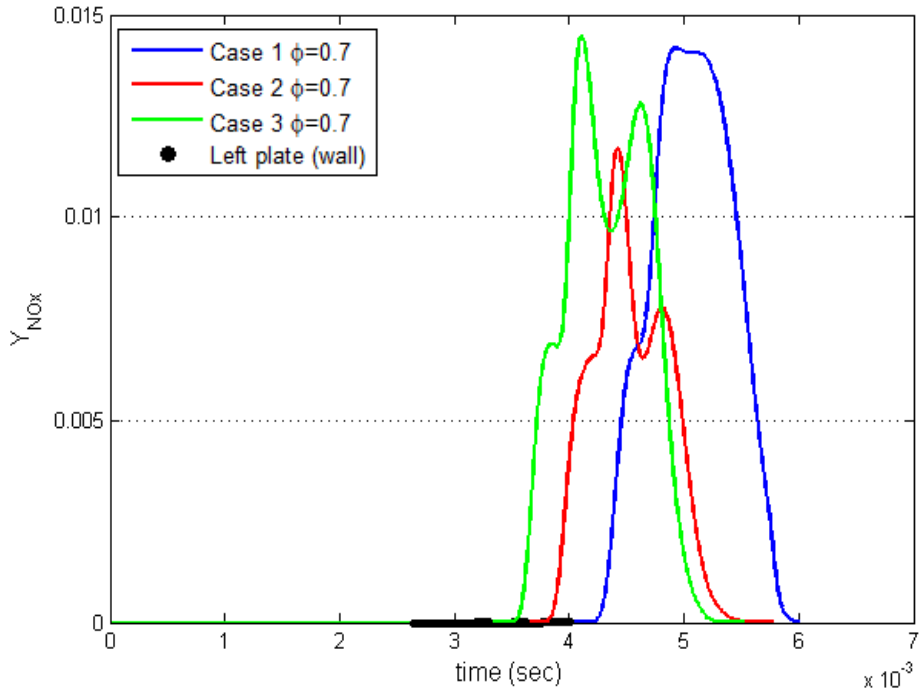

(a)

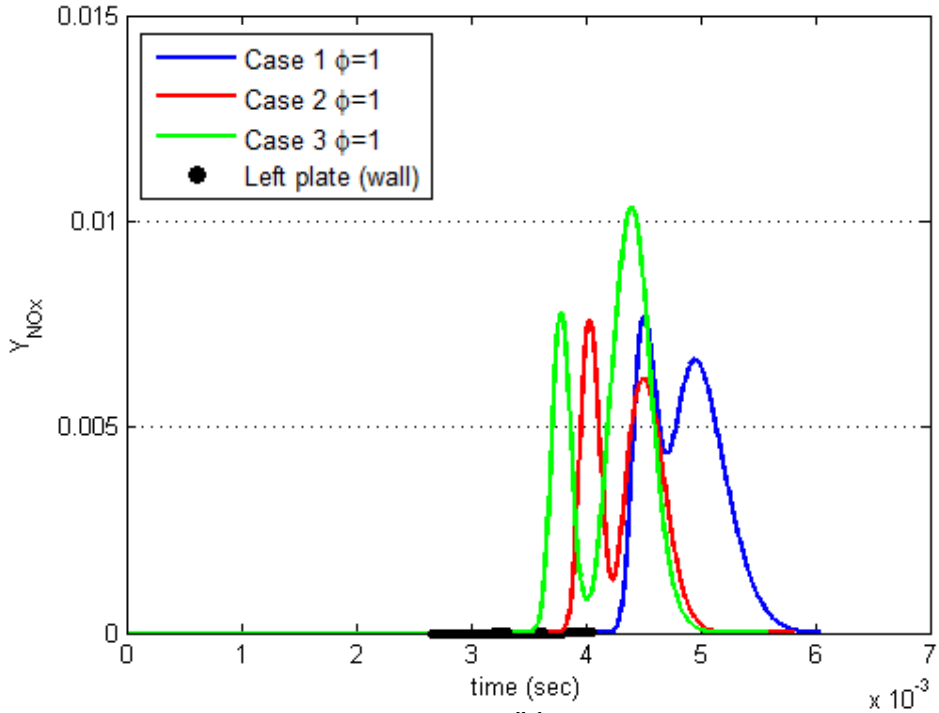

(b)

Figure 5-34 Mass fraction of NOx at the exhaust of the ICWR

The evaluation of the ICWR is performed with an upgraded version of the 1D-CFD code used during the WR assessment. The new version includes the

transport equations of the distinct species that participate inside the process, and the numerical integration of the reaction's source terms.

As result, the ICWR must operate with compressor pressure ratios higher than the baseline engine, to initiate the self-ignition of fuel through a detonation process. The best performance from the studied cases is obtained with an equivalence ratio of 0.7. The minimum SFC reported by the simulation is 52.7$kg/kN \cdot hr$, whilst the maximum specific thrust and efficiency of energy conversion are 112 $N.sec/kg$ and 54.8 % respectively.

The evaluation of the turbine performance is unfair because the cycles' maximum temperature obtained in each case is not constant. So, a process able to predict the properties at the exhaust port for a fixed value of temperature is proposed. The results obtained from this process suggest the possibility of achieving a better performance when the equivalence ratio gets closer to one.

The temperature of burned gases is above 2000 K and the compressed air inside the ICWR is kept under 900 K, so, these fluids must be mixed before their injection into the turbine to prevent any damage.

The gases' temperature causes the formation of NOx regardless of the equivalence ratio, since air near to fuel stratification helps to supply oxygen to the reaction. However, the generation of this pollutant gets reduced when the equivalence ratio is close to one.

The mixing chamber must ensure an efficient and quick mixture of burned gases with dilution air to prevent an increase of the NOx concentration due to the elevated temperature of burned gases when they reach the exhaust port of the ICWR.

6 DISCRIMINATION PROCESS – THE NOVEL GAS TURBINE CONCEPT

Chapters 3, 4 and 5 conducted the performance evaluation of WRs, PDEs and ICWRs as component of aircraft gas turbines to measure the improvement in specific fuel consumption, specific thrust and efficiency of energy conversion expected from each option when compared with a baseline gas turbine.

This chapter intends to discern between the advantages of the distinct options to select the best alternative as a component of future aircraft gas turbines, and therefore a decision making matrix is implemented as a tool during the discrimination.

The decision making matrix is composed of six comparison criteria to perform the evaluation, one criterion with a question scale (yes or no) and five criteria with a rank scale (a scale from 1 to 4 between the worst and the best option). The comparison criteria are as follows:

6.1 Specific fuel consumption

SFC is a direct measure of the CO_2 reduction. A minimization of the mass flow rate of fuel promotes a reduction of CO2 in burned gases for a fixed value of thrust. Therefore, SFC is considered an important factor.

The evaluation of the SFC is performed with a ranking scale where a value of one is set for a zero reduction of SFC in respect to the baseline engine, two is for a reduction of SFC higher than 0 but under 5%, three is for a SFC higher than or equal to 5% but under 10%, and four is for a reduction of SFC equal to or higher than 10%.

The maximum reduction of SFC is computed from the data obtained during the simulation of the distinct devices that is performed in the previous chapters.

6.2 Specific Thrust (F_s)

The analysis conducted during the previous chapters assumes a novel cycle with the same thrust delivered by the baseline gas turbine. So, an increase of

the specific thrust results in a reduction of the mass flow rate of air and therefore a reduction of the engine size.

The engine size increases the drag that aircraft has to overcome and therefore smaller machines also require a reduction of the turbine's thrust to keep the new aircraft flying at the same cruiser conditions set by the baseline cycle. This effect is directly associated with a reduction of the fuel consumption and therefore F_s is included as a factor in the decision making matrix.

However, the specific thrust is considered of less importance than SFC during the performance analysis since they commonly behave inversely proportional to each other. So, this work assumes that a novel cycle for civil aircraft improves the specific thrust if its F_s is higher than that delivered by the baseline engine, once the SFC reaches its minimum.

The evaluation of this criterion is performed with a ranking scale of four intervals that quantify the increase of F_s from 0% to 7.54 %; the last percentage corresponds to the highest F_s obtained from the studied cases. An scale number of one is set for an increase of F_s from 0% to 1.89% in respect to the baseline engine, two for an increase of F_s equal or higher than 1.89% but lower than 3.77%, three for an increase of F_s equal or higher than 3.77% but lower than 5.66% and four for an increase of F_s equal or higher than 5.66 up to 7.54%

6.3 External source of energy for the detonation

Among the options considered in this study only the PDE is a device that requires a continuous supply of energy to promote the detonation during the cycle, the injected energy is high enough to include it as a factor in the decision making matrix.

The evaluation of this factor is performed with a question scale where one indicates the necessity of an external source of energy to obtain the detonation whilst two indicates the capacity of the device to promote the auto-ignition.

6.4 Simple design and operation

The installation of the different devices as components of the gas turbine is simple when the resultant configuration looks similar to a conventional combustion chamber. Thus, features such as the presence of a single port to inject burned gases into the turbine, the homogeneity of the temperature profile at the exhaust port and the simple operation of the device at off-design conditions are included in this evaluation.

The evaluation of the devices' simplicity is performed with a ranking scale, where one indicates the lack of all the features, two indicates that only one feature is possible, three indicates that two features are possible and four indicates that all the features are possible.

6.5 Device length and diameter

A factor that a new gas turbine must take into account is the extra weight they give to the aircraft, since a heavier aircraft has a lower capacity to transport people. In other words, any reduction of the fuel consumption achieved by the new cycle could be non-effective if the fuel consumption per passenger is increased.

The length and diameter of the various components is a measure of the increase or reduction in weight of the new gas turbine so they are included in the decision making matrix. However these variables are studied separately since the diameter also has an influence in the aircraft drag when it is greater than the baseline turbine.

The evaluation of these factors is performed with a ranking scale that discriminates the devices from 0.35 m to 0.9 m; the first value corresponds to the length of the baseline combustion chamber (approximately) whilst the second value corresponds to the maximum length obtained from the designed devices.

The distribution of the ranking scales is performed as follows: one is for a device's length higher or equal to 0.76 meters up to 0.9 meters, two is for a

device's length higher or equal to 0.63 meters but under 0.76 meters, three is for a device's length higher or equal to 0.49 meters but under 0.63 meters, and four is for a device's length higher or equal to 0.35 but under to 0.49 meters.

Moreover, in the case of the devices' external diameter, a value of one indicates a diameter higher than or equal to 0.95 m (diameter of the whole turbofan), two indicates a diameter higher than or equal to 0.80 m but lower than 0.95 m, three indicates a diameter higher than 0.70 m but lower than 0.80 m and four indicates a diameter lower than 0.70 m (external diameter of the baseline combustion chamber).

6.6 Weighting Factors

The score selected for each criterion is normalized through Eq. (6-1), where ∅ represents the assigned score of each criterion whilst $\emptyset_{low}$ and $\emptyset_{high}$ represent the limit scores of the rank. Then, each of the normalized scores is weighted according to their level of importance. Table 39 displays the weighting factor assumed by this work.

The selected weighting factors are not conclusive so they can change according to the point of view of experts in the area. However, the main idea of this section is to set a procedure able to discriminate among the studied devices to select the prominent option.

$$\emptyset_n = \frac{\emptyset - \emptyset_{low}}{\emptyset_{high} - \emptyset_{low}} \quad \textbf{(6-1)}$$

6.7 Options Evaluation

Table 40 shows the minimum SFC achieved by each of the novel devices. The lowest SFC is obtained by the ICWR with a reduction of more than 7% the SFC obtained by the baseline engine. Moreover, the WR behaves worst, with a SFC reduction close to 3%.

Table 41 shows the F_s produced by the novel devices when they operate with their minimum SFC. The PDEs array gives the highest F_s with an increase of

7.54 % above the baseline engine, while the ICWR is the worst, with an increase of 6.71 %.

Table 39 Weighting factor implemented to discriminate the studied cases

Criteria	Weighting factor	Description
Specific fuel consumption	0.3	This is the highest weighting factor among the implemented during the evaluation and it is allocated due to the direct relationship that SFC has with the aim of this work
Specific Thrust Simple design and operation Device's external diameter	0.15	This weighting factor is second in magnitude allocated due to the following reasons: The F_s has an indirect effect on emissions of the turbine as indicated above. A simple design ensures a reduction of the design cost and operational cost. The external diameter influences the aircraft's weight and drag
Device's length Detonation energy	0.125	This weighting factor is third in magnitude and was set to highlight the importance of turbine weight on the performance of the turbine, as well as the self-operation capability that some devices have when compared with the gamma of options evaluated.

Table 40 Evaluation of the SFC as criterion of the decision making matrix

	SFC ($kg/kN \cdot h$)	Reduction (%)	Score	Normalisation
Baseline engine	71.65	N/A	N/A	N/A
Wave Rotor	69.4	3.14	2	0.5
PDEs array	66.7	6.91	3	0.75
ICWR	64.7	9.70	4	1

Table 42 is implemented to keep in mind that a PDEs array only operates when a significant amount of energy is injected to initiate the detonation.

Table 43 quantifies the complexity of the distinct options; where F1 is used to indicate the presence of a single port to withdraw burned gases, F2 is used to indicate the homogeneity of gases' temperature at the exhaust of the ICWR, and F3 is used to indicate the feasibility of operating the device at off-design conditions.

Table 41 Evaluation of the F_s as criterion of the decision making matrix

	$F_s(N/s \cdot kg)$	Increase (%)	Score	Normalisation
Baseline engine	85.46	N/A	N/A	N/A
Wave Rotor	91.7	7.30 %	4	1
PDEs array	91.9	7.54%	4	1
ICWR	91.2	6.71 %	4	1

Table 42 External source of energy for the detonation as criterion of the decision making matrix

	Answer	Score	Normalisation
Baseline engine	no	N/A	N/A
Wave Rotor	no	2	1
PDEs array	yes	1	0
ICWR	no	`2	1

The wave rotor rejects F1 since the design proposed by this work has two ports that operate at different pressures to feed the turbine. The PDEs array and the ICWR reject F2 because burned gases are discharged at elevated temperatures, so a mixing chamber is needed to reduce the gases' temperature with dilution air. The wave rotor and the ICWR reject F3 since any change of the shock intensity or the detonation due to a reduction of fuel or a reduction of the compressor pressure ratio affects the gas dynamic inside the device, and

therefore the port location starts being inefficient or the detonation becomes unsustainable.

Table 43 Simple design and operation as criterion of the decision making matrix

	F1	F2	F3	Score	Normalisation
Wave Rotor	no	yes	no	2	0.5
PDEs array	yes	no	yes	3	0.75
ICWR	yes	no	no	2	0.75

Table 44 shows the length of the novel devices, all the options are larger than the combustion chamber of the baseline turbine, so the score reached by this criterion is low.

Table 44 Device's length as criterion of the decision making matrix

	Length (m)	$(L_{BL}/L) \cdot 100$	Score	Normalisation
Baseline engine	0.36	N/A	N/A	N/A
Wave Rotor	0.84	233 %	1	0.25
PDEs array	0.9	280 %	1	0.25
ICWR	0.809	224.72 %	1	0.25

Table 45 shows the external diameter of the novel devices, the PDEs array requires the smallest diameter; smaller than the combustion chamber and therefore it receives the highest score. The wave rotor is the worst option since its diameter is longer than the whole gas turbine, so the drag must increase.

Table 45 Device's diameter as criterion of the decision making matrix

	Diameter (m)	$(D_{BL}/D) \cdot 100$	Score	Normalisation
Baseline engine	0.95	N/A	N/A	N/A
Wave Rotor	1.104	116.21	1	0
PDEs array	0.346	36.42	4	1
ICWR	0.832	0.875	2	0.5

6.7.1 Decision making matrix

Table 46 shows the decision making matrix obtained after multiplying the normalized score of each criterion by the weighting factor displayed in Table 39. The best option is the ICWR whose evaluation accumulates a value of 0.794; this device is followed by the PDEs array that accumulates 0.7. The worst option is the Wave Rotor.

This result indicates that devices with detonation perform better than the pressure exchanger, since they give an additional compression of the working fluid due to the presence of shock waves plus a reduction of the heat injected into the cycle due to the isochoric trajectory ($C_v < C_p$). All of this results in a greater reduction of the fuel consumption.

Table 46 Decision making matrix –normalised criteria

	C1	C2	C3	C4	C5	C6	Total
Wave Rotor	0.15	0.15	0.13	0.08	0.031	0	0.541
PDEs array	0.23	0.15	0	0.11	0.063	0.15	0.703
ICWR	0.3	0.15	0.13	0.11	0.031	0.075	0.796

6.8 Why the NOx generation is not considered as criterion

The international civil aviation organization (ICAO) is implementing regulations to control NOx emission in civil aircraft engines that exceed 26.7 kN of thrust (ICAO 2013). These regulations are set to control the emissions of aircraft during their landing and take-off (airplanes with an altitude between the ground

level and 914 m (3000 ft)) to reduce the air pollutants in urban areas near to airports.

Otherwise, NOx generated during the cruiser condition is considered an important precursor gas in the formation of tropospheric ozone and therefore it contributes to protect the earth from the UV radiation (GREENAIR 2014).

In this scenario, NOx generation would be included into the decision making matrix. However, the lack of information about the turbine conditions during the aircraft landing and take-off does not allow the inclusion of this variable as a criterion.

The NOx evaluation performed during the previous sections is presented to understand how detonation can influence the generation of NOx. It enables experience to be gained about the configuration that offers low values of emissions as well as awareness about the necessity of designing new devices able to reduce the NOx emission.

6.9 Chapter summary

This chapter presents the procedure followed by this work to compare the distinct options as future components of gas turbines. The selection is based on these six criteria: the specific fuel consumption, the specific thrust, simple design and operation, the device's external diameter, the device's length and detonation energy (external energy to produce detonation).

Each criterion is weighted to give a level of priority over the others. The SFC receives the maximum weight due to its direct impact on the CO_2 generation, followed by the specific thrust, simple design and operation and device's external diameter, all of them equally weighted, to conclude with the device's length and the detonation energy, which have the lowest weight.

After performing the evaluation, the ICWR achieved a score of 0.796, followed by the PDEs array with 0.703. The WR receives the worst qualification since it has a poor improvement of the SFC and promotes an increase in the drag due to its diameter that is greater than that required by the baseline turbine.

7 Conclusions and future works recommendation

7.1 Conclusions

The next sections present separate conclusions of the devices studied in this work. In addition, a general conclusion is presented at the end of the chapter.

7.1.1 WR

- The Weber algorithm was successfully implemented to perform the thermal analysis of a cross flow WR attached to a gas turbine.
- The velocity and temperature of the injected air influence the compression and expansion efficiency inside the WR, better performance is obtained when the injection Mach number is between 0.46 and 0.53.
- A 1-D CFD code based on the finite volume method was developed to predict the dimensioning of WR, the 1D-CFD code was validated with a shock tube experiment and the maximum error was found over the shock wave, since the code models the sharp jump of the shock wave with a smooth curve due to the false diffusion effect. Nevertheless, the code is able to track most of the wave inside the shock tube (except the weak waves) and it predicts the fluid state after its compression or expansion with a reasonable level of accuracy.
- The 1D-CFD model was able to predict the dimensioning of a WR using the fluid properties predicted by Weber's algorithm at each port of the device, the dimensioning was performed by tracking the different waves that participate in the device's transient process.
- Some inconsistences were found between the CFD model and the analytical solution as a consequence of the simplifications assumed by the analytical model. The prompt closure of the LPG1 port used to withdraw the gases that feed the high pressure gas turbine is the main effect observed from the comparison, and therefore the mass distribution driven by the withdrawals ports is different between both models, so the estimated performance of the gas turbine could be affected.

- A delay in the position of the contact wave is predicted by the 2D-CFD simulation when it is compared with the results of the 1D-CFD code. So, a certain amount of hot gas gets trapped at the left end of the channel when the second expansion port is closed. Although a depth analysis of the phenomenon was not performed, a reduction of the injection velocity could be ascribed to the inability of the 1D model to reproduce the gradual opening effect (Okamoto 2000).
- From all the evaluated cases it was observed that only the cycles with the same overall pressure ratio as the baseline engine perform better. The turbine is able to deliver the work required by the compressor, fan and wave rotor through all the gamma of injection Mach number, whilst an increase of the specific thrust and a reduction of the SFC in respect to the baseline engine are achieved.
- The performance analysis of this device did not consider the generation of NOx because the temperature of the gases is less than 1800 K over the whole cycle and therefore there is not enough energy to break the triple-bonds of the nitrogen molecules.

7.1.2 PDE

- A 1D CFD code was developed to evaluate the gas dynamics inside a PDE. This proposal obtains information about the detonation process through the NASA-CEA code and then it implements the method of characteristic to track the different rarefaction waves that follow the detonation wave.
- The result of the in-house code was verified with a 2D-CFD model of a PDE with an expansion chamber that represents the downstream manifold. Despite the developed code overestimating the profile of pressure and temperature predicted by the 2D-CFD model, the trend of the studied variables followed the same path. Moreover, the observed differences are not conclusive about the accuracy of the developed code

since both models implement simplifications that introduce inaccuracies into the final solution.

- The developed code only requires 1.95 seconds to be executed. This represents a small fraction of the time required by the 2D-CFD model to accomplish one cycle of the PDE (0.0055%). Therefore, the in-house code looks to be an appropriate tool in the preliminary design of future PDEs.

- The evaluation of PDEs as a combustion chamber of future gas turbines was achieved using the compressor pressure ratio, the length of the PDEs and the reactants injection Mach number as independent variables. The results obtained indicated that only the injection Mach number and the compressor pressure ratio have an effect on the specific thrust, the specific fuel consumption and the efficiency of energy conversion. Moreover, the length of the PDEs has an impact on the operational frequency of the device.

- After studying the vibrational mode generated by different arrays of PDEs, it was observed that on the one hand, PDEs with a short length and a small diameter are able to generate a wider frequency spectrum than can be obtained in conventional combustion chambers so this configuration can propitiate resonance. On the other hand, an increment in the number of PDEs produces a reduction of the amplitude reached by the fundamental frequency and therefore the manifold is going to be exposed to less fatigue.

- The 2D simulation of a PDE predicts 7 ppm of NOx generated inside the device when it operates with an equivalence ratio of one (low-NOx device). However, the gases at the exhaust of the PDE are above 2000 K, so their mixture with the dilution air could generate additional NOx.

7.1.3 ICWR

- Algebraic equations, implemented in the study of compressible flow, allowed a range of injection Mach numbers and compressor pressure

ratios to be defined that ensure the auto-detonation of reactants within the ICWR. As result, the injection Mach number must be over 0.6 and the compressor pressure ratio must be between 20 and 32.5 to generate a shock wave with enough energy to generate the reactants detonation.

- 1-D CFD code based on the finite volume method was built to predict the dimensioning of ICWR, in order to follow the same idea implemented during the design of WR. The 1D-CFD code was verified with a 2D model executed in ANSYS FLUENT® and a good agreement was observed between most of the obtained results; some discrepancies are observed in the NOx generation, but the trend predicted by both codes is similar.

- The program was executed to design an ICWR whose length and angular velocity are similar to those obtained by the best configuration of WR designed in chapter 3. The ports' position in the new device, as well as the fluid dynamics inside the device, was successfully predicted. However, the performance evaluation was difficult to assess since the maximum temperature of the gas-turbine cycle is non-linearly related to the studied variables; small changes in the injection Mach number can generate huge changes to the cycle maximum temperature.

- An extrapolation technique based on the fluid entropy suggests the possible presence of conditions with better performance that that obtained during the numerical evaluation. Therefore, these new options must be explored.

- The CFD model of the ICWR indicates that the plate which closes the right end of the channels and causes the 1st shockwave to form is exposed to elevated temperatures during the cycle operation (over 1200K). Therefore, if the conduction mechanism of the material is not enough to keep the plate operating safely then a cooling system must be designed.

- NOx generation is elevated and increases when the equivalence ratio is below one, since the high temperature produced by the detonation is

followed by a mixture of gases rich in oxygen and nitrogen. Moreover, the interface between pure air and reactants (due to the stratification) makes the generation of additional NOx possible since pure air is an additional source of oxygen for the reaction.

7.1.4 New contributions of this work

- The 1D-CFD code designed in this work predicts the closure of the WR's ports by implementing a novel tracking technique based on the mass flow. The technique ensures the mass balance of the device once the dynamic equilibrium is obtained.
- The 1D-CFD code was built by employing a technique based on the solution of the system of equation through the SIMPLE algorithm. This pressure based solver was demonstrated to be stable during the design of WR and ICWR.

- A new code that integrates the NASA_CEA code with the Method of Characteristic is implemented to evaluate the performance of the PDE. The developed code is able to consider the throttling and non-throttling conditions experienced by the fluid when it is ejected through the PDE's open end. Although, the code's calibration was performed with another numerical solution it is able to reproduce the pressure and temperature profile at the open end of the device anticipated by a most sophisticated CFD model based on the finite volume method.

7.1.5 General

- The ICWR is considered, in principle, to be the best option for emissions reduction, followed by the PDEs array.

7.2 Future work recommendations

- The 1D-CFD code has the potential of incorporating more realistic options such as the change of specific heat with temperature, the losses of heat and also a zero-equations-turbulence model to improve the thermal evaluation of the WR + GT cycle.

- The dimensioning of the WR and ICWR offers enough information to start working with 2D and 3D models in order to study the effect on the device's performance of more complex patterns that are not captured by the 1D model; such as the port progressive opening and the Coriolis acceleration.
- CFD is a tool able to give approximations of physical phenomena that involve fluid flow, heat transfer, and combustion, among others. However, it is important to conduct some experiments to validate the CFD results in order to be more confident about the predicted solutions.
- The incorporation of libraries with a larger number of reaction steps into the 1D-CFD code will improve the combustion model and therefore a better estimation of the detonation process and the emission concentrations can be achieved.
- The incorporation of a hybrid boundary condition (wall + total pressure) can be implemented into the 1D-CFD code to model the progressive opening and closure of the ports. This improvement will help in reducing the velocity difference of the contact waves observed between the 1D and 2D CFD models, so a more accurate prediction of the ports' position can be achieved.
- The evaluation of a WR with a single expansion port is recommended, since its integration into the gas turbine cycle reduces the number of modifications of the baseline turbine and simplifies the operation of the cycle; all the gases driven by the device can be injected directly to the high pressure turbine.

THE AUTHOR'S PUBLICATIONS

Materano, G., and Savill, M. (2013), "Preliminary Design of a Double Expansion Through Flow Wave Rotor: Thermal and Gas Dynamic Analysis", In: *Proceedings of ASME Turbo Expo*, Paper No.GT2013-94987, 3-7 June 2013, San Antonio, USA, ASME.

Materano, G., and Savill, M. (2014), "Preliminary Design of a Double Expansion Through Flow Wave Rotor: Wave Rotor Dimensioning", In: *CIMENICS 2014*, CIM-182, 24-26 March 2013, Margarita, Venezuela, p. 8.

REFERENCES

Akbari, P. et al., (2013), "Boosting Gas-Turbine Efficiency with Constant-Volume Combustion'', *IUPUI*, Available at: http://www.iupui.edu/~nalim/cprl/images/projects/Poster07.pdf.

Akbari, P. and Muller, N., (2003), "Performance Investigation of Small Gas Turbine Engines Topped with Wave Rotors". In: 39th *AIAA/ASME/SAE/ASEE Joint Propulsion Conference and Exhibit, Paper No* AIAA *2003-4414, 20-23* July 2003, Huntsville, Alabama:, p. 11.

Akbari, P. and Müller, N., (2003), "Preliminary Design Procedure for Gas Turbine Topping Reverse-Flow Wave Rotor". In: *GTSJ, ed. Proceedings of the International Gas Turbine Congress*, Paper No fr-301, 02-07 November 2003, Tokyo 2003. p. 001.

Akbari, P. and Nalim, R., (2006), "Analysis of Flow Processes in Detonative Wave Rotors and Pulse Detonation Engines". In: *AIAA, ed. 44th AIAA Aerospace Sciences Meeting and Exhibit. Aerospace Sciences Meetings*. Paper No AIAA 2006- 1236, 09-12 January 2006, Reno, Nevada: American Institute of Aeronautics and Astronautics, p. 13.

Akbari, P., Nalim, R. and Li, H., (2006), “Analytic Aerothermodynamic Cycle Model of the Combustion Wave Rotor in a Gas Turbine Engine”. In: *AIAA, ed. 4th International Energy Conversion Engineering Conference and Exhibit (06CEC)*. Paper No AIAA 2006-4176, 26-29 June 2006, San Diego, p. 14.

Akbari, P., Nalim, R. and Mueller, N., (2006), “A Review of Wave Rotor Technology and Its Applications”. *Journal of Engineering for Gas Turbines and Power-transactions of The ASME*, Vol.128, No. 4, p.717-735.

Akbari, P., Nalim, R. and Muller, N., (2006), “Performance Enhancement of Microturbine Engines Topped With Wave Rotors”. *Journal of Engineering for Gas Turbines and Power-transactions of The ASME*, Vol.128, No. 1, p. 190-202.

Akbari, P., Nalim, R. and Snyder, P., (2006), “Numerical Simulation and Design of a Combustion Wave Rotor for Deflagrative and Detonative Propagation”. In: *AIAA, ed. 42nd AIAA/ASME/SAE/ASEE Joint Propulsion Conference & Exhibit*. Paper No AIAA 2006-5134, 09-12 July 2006, Sacramento, California, p. 20.

Al-Falahi, A., Yusoff, M.Z. and Yusaf, T., (2010), “Numerical Simulation of Inviscid Transient Flows in Shock Tube and its Validations”. *International Journal of Mathematical, Physical, & Engineering*, Vol. 4, No 1, p.320-330.

Anderson, J.D., (2003), “*Modern compressible flow with historical perspective” (3rd ed)*, McGraw-Hill, Boston.

Anon, (2004), *The NASA Computer program CEA- Chemical Equilibrium with Applications*, version 2, NASA Glenn’s.

ANSYS, (2013), *ANSYS FLUENT® 14 Documentation*, version 14, Canonsburg, ANSYS INC.

Baronia, D., Nalim, M. and Akbari, P., (2007), “Numerical Study of Wave Rotor Ignition and Flame Propagation in a Single-Channel Rig”. In: *43rd AIAA/ASME/SAE/ASEE Joint Propulsion Conference & Exhibit. Joint Propulsion Conferences*. Paper No AIAA 2007-5054, 08-11 July 2007, Cincinnati, OH: AIAA, p. 18.

Baukal, C.E. and Schwartz, R.E., (2001), *The John Zink combustion handbook C. Press*, Tulsa, USA.

Canteins, G. et al., (2006), “Experimental and numerical investigations on PDE performance augmentation by means of an ejector”. In: *Shock Waves.* Vol. 15, No 2, pp.103–112.

Cengel, Y.A. and Boles, M.A., (2007), “*Thermodynamics : an engineering approach”* (6th ed), McGraw-Hill, New York.

Chapra, S. and Canale, R. (2005), “*Numerical methods for engineers” (5th* ed), McGraw-Hill, New York.

Chase, M.W.J. et al., (1985), “*JANAF Thermochemical Tables”* (3rd ed), Journal of Physical and Chemical, Michigan, USA.

CleanSky Project, (2011), CleanSky Web Site. Available at: http://www.cleansky.eu/, (accessed 12 February 2011).

Daniau, E. et al., (2001), “Effects of Nozzles of Different Length and Shape on the Propulsion Performance of Pulse Detonation Engines”. In: *G. ; Roy et al., (editors), High-Speed Deflagration and Detonation - Fundamentals and Control*. Publishers ELEX-KM, Moscow, p. 251–262.

Davis, W.C., (1997), “Introduction to Explosives”. In: J. A. Zukas and W. Walters, (editors), *Explosive Effects and Applications (Shock Wave and High Pressure Phenomena)*. Publisher Springer, New York, p. 1–435.

Demirdžić, I. and Lilek, Ž., (1993), “A collocated finite volume method for predicting flows at all speeds”. *International Journal for Numerical Methods in Fluids*, Vol.16, p.1029–1050.

Ebrahimi, H.B. and Merkle, C.L., (2002), “Numerical Simulation of a Pulse Detonation Engine with Hydrogen Fuels”. *Journal of Propulsion and Power*, Vol.18, No 5, p.1042–1048.

Endo, T. et al., (2004), “Pressure History at the Thrust Wall of a Simplified Pulse Detonation Engine”. *AIAA Journal*, Vol. 42 No 9, p.1921–1930.

Endo, T. and Fujiwara, T., (2002), “A Simplified Analysis on a Pulse Detonation Engine Model”. *Transactions of the Japan Society for Aeronautical and Space Sciences*, Vol. 44, No 146, p.217–222.

Ferziger, J.H. and Perić, M., (1997), “*Computational Methods for Fluid Dynamics” (3rd ed)*, Springer, Berlin.

Frackowiak, M. et al., (2004), “Numerical Simulation of Unsteady-Flow Processes in Wave Rotors”. In*: ASME, ed. 2004 ASME International Mechanical Engineering Congress - IMECE04*. Paper No IMEC 2004-609, 13-19 November 2004, California, p. 16.

Scientist and Friends (2007), “History of Jet Engines”. Available at: http://www.scientistsandfriends.com/jets1.html, (accessed 20 July 2011).

GE Global Research, (2013), “Advanced Propulsion”. General Electric. Available at: http://ge.geglobalresearch.com/technologies/advanced-technologies/advanced-propulsion/, (accessed 19 September 2011).

Giuliani, F. et al., (2010), “Pulse detonation as an option for future innovative gas turbine combustion technologies: a concept assessment”. In: *27th International Congress of the Aeronautical Sciences*. Paper No ICAS 2010- 4.3.2, 19-24 September 2010, Nice France, p. 10.

Glassman, I. and Yetter, R.A., (2008), *Combustion (4th ed),* Elsevier, Boston.

GREENAIR, (2014), “US EPA aligns with ICAO on new NOx standards for aircraft engines as FAA pledges action on GA leaded fuel”. Available at: http://www.greenaironline.com/news.php?viewStory=1566, (Accessed 6 April 2014).

Hagen, H., (1975), “Constant Volume Combustion Gas Turbine with Intermittent Flows”, US Patent: 3,877,219.

Heiser, W.H. and Pratt, D.T., (2002), “Thermodynamic Cycle Analysis of Pulse Detonation Engines”. *Journal of Propulsion and Power*, Vol. 18, No 1, p.68–76.

Helfrich, T.M., (2006), “*Cycle Performance of a Pulse Detonation Engine with Supercritical Fuel Injection”.* MSc. Thesis. Air Force Institute of Technology, Ohio.

Hill, S.C. and Smoot, L.D., (2000), “Modeling of nitrogen oxides formation and destruction in combustion systems A”. *Progress in energy and combustion science*, Vol. 26, p.417- 458. (Accessed 20 September 2013).

Hirceaga, M., Iancu, F. and Muller, N., (2005), “Wave Rotors Technology and Applications”. In: the 11th International Conference on Vibration Engineering. 27-30 September 2005, Timisoara, Romania. p.7

Huber, P.W., Fitton, C.E.J. and Delpino, F., (1949), “*Experimental investigation of moving pressure disturbances and shock waves and correlation with one-dimensional unsteady-flow theory”,* report number ADA 380464, NASA, Washington DC.

Hutchins, T.E. and Metghalchi, M., (2003), “Energy and Exergy Analyses of the Pulse Detonation Engine”. *Journal of Engineering for Gas Turbines and Power*, Vol. 125, No 4, pp.1075–1080

Iancu, F. and Müller, N., (2005), “Efficiency of shock wave compression in a microchannel”. *Microfluidics and Nanofluidics*, Vol. 2, No 1, p.50–63.

Iancu, F., Piechna, J. and Muller, N., (2008), “Basic design scheme for wave rotors”. *Shock Waves*, Vol, 18, No 5, p.365–378.

Iancu, F., Piechna, J. And Müller, N., (2005), “Numerical Solutions for Ultra-Micro Wave Rotors (UmWR)”. In: *35th AIAA Fluid Dynamics Conference and Exhibit. Fluid Dynamics and Co-located Conferences*. Paper No AIAA 2005-5034, 06-09 June 2005, Toronto, Ontario Canada, p. 18.

ICAO, (2013),”Exhaust Emissions Standards for New Aircraft Gas Turbine Engines and Identification Plate for Aircraft Engines”, Federal Register, Vol. 78, No 205, Federal Aviation Administration, Department of Transportation USA.

Johnson, J.E., Dunbar, L.W. and Butler, L., (2002). “Combined cycle pulse detonation turbine engine”, US Patent 6442930.

Kailasanath, K., 2003. “Recent Developments in the Research on Pulse Detonation Engines”. *AIAA Journal*, Vol. 41, No 2, p.145–159.

Karki, K.C. and Patankar, S. V, (1989), “Pressure based calculation procedure for viscous flows at all speeds in arbitrary configurations”. *AIAA Journal*, Vol. 27, No 9, p.1167–1174.

Kelly, J., (2003), “After Combustion: Detonation”, POPSCI, September 2003, p.51–56

Khalid, S. et al., (2006), “Two-Dimensional Numerical Modelling of Mixture Inflow in a Combustion Wave Rotor”. In: *4th International Energy Conversion Engineering Conference and Exhibit (IECEC).* Paper No AIAA 2006-4125 , 26-29 June 2006, San Diego, California, p. 13.

Kistiakowsky, G.B. and Mangelsdorf, P.C., (1956), “Gaseous Detonation, VIII. Two-Stage Detonations in Acetylene-Oxygen Mixtures”. *The Journal of Chemical Physics*, Vol. 25, No 3, p. 516–519.

Kuo, K.K., (2005), “Principles of combustion”, (2nd ed), J. Wiley, New Jersey.

Kuznetsov, M., Alekseev, V. and Matsukov, I., (2002), “Detonation Transmission from one Mixture to Another of Lower Sensitivity”, In: *G. Roy et al. (editors). Advances in Confined Detonations*, Torus Press, Moscow, p. 60–64.

Lam, M. et al., (2004), “*Pulse Detonation Engine Technology: An Overview”*, Report number APSC 201, University of British Columbia, Canada.

M. R. Nalim, (1999), “Assessment of Combustion Modes for Internal Combustion Wave Rotors”. *J. Eng. Gas Turbines Power*, Vol. 121, No 2, p.265–271.

Ma, F., Choi, J.-Y. and Yang, V., (2005), “Thrust Chamber Dynamics and Propulsive Performance of Single-Tube Pulse Detonation Engines”. *Journal of Propulsion and Power*, Vol. 21, No 3, p. 512–526.

Martin, W.A., (1958), “A Review of Shock Tube and Shock Tunnels”, Report number ZR-658-050, CONVAIR, San Diego.

The MathWorks Inc.,(2011), MATLAB (R2011a), version 7.12.0.635, computer software, The MathWorks Inc., Natick, Massachusetts.

Mawid, M., Park, T. and Sekar, B., (2000), “Performance analysis of a pulse detonation device as an afterburner”. In: *35th Intersociety Energy Conversion Engineering Conference and Exhibit. Joint Propulsion Conferences*. Paper No AIAA 00-3474, 16-19 July 2000, Huntsville, Alabama, p. 21.

Mawid, M.A. et al., (2003), “Application of Pulse Detonation Combustion to Turbofan Engines”. *J. Eng. Gas Turbines Power*, Vol. 125, No 1, p.270–283.

Müller, N., (2003), “Performance Improvement of Small Gas Turbines through use of Wave Rotor Topping Cycles”. In: *Entropy*., Atlanta, Georgia, Paper No GT 2003-38772, 16-19 Jun 2003, Huntsville, Alabama, p. 11.

Nalim, M., (1997), “Numerical study of stratified charge combustion in wave rotors”. In: *33rd Joint Propulsion Conference and Exhibit.* Paper No AIAA-97-3141, 06-09 July 1997, Seattle, Washington, p. 15.

Nalim, M. and Izzy, Z., (2001), “Rotary ejector enhanced pulsed detonation system”. In: *37th Joint Propulsion Conference and Exhibit.* Paper No AIAA- 2001 3613, 08-10 July 2001, Salt Lake City, p. 09.

Nalim, M.R., (2000), “Longitudinally Stratified Combustion in Wave Rotors”. *Journal of Propulsion and Power*, Vol. 16, No 6, p.1060–1068.

Nalim, M.R., (1995), “Preliminary assessment of combustion modes for internal combustion wave rotors”. *31 st AIAA/ASME/SAE/ASEE Joint Propulsion Conference and Exhibit.* Paper No AIAA-95-2801, 10-12 July 1995, San Diego CA, p. 17.

Nalim, M.R., Izzy, Z.A. and Akbari, P., (2012), “Rotary wave-ejector enhanced pulse detonation engine”. *Shock Waves*, Vol. 22, No 1, p.23–38.

Nalim, M.R. and Paxson, D.E., (1997), “A Numerical Investigation of Premixed Combustion in Wave Rotors”. *Journal of Engineering for Gas Turbines and Power*, Vol. 119, No 3, p.668–675.

Nikitin, V.F. et al., (2009), “Pulse detonation engines: Technical approaches”. *Acta Astronautica,* Vol. 64, No 2–3, p. 281–287.

Okamoto, K., (2000), “Wave Rotor Gas Dynamics for an Aeropropulsion system”, In: *22nd Congress of International Council of the Aeronautical Sciences*, Paper No ICAS 2000-7.3.4, 28 August/01 September 2000, Harrogate, UK, p. 09.

Okamoto, K., Nagashima, T. and Yamaguchi, K., (2003), “Introductory Investigation of Micro Wave Rotor”, In: *Proceedings of the International Gas Turbine Congress*, Paper No FR-302, 02-07 November 2003, Tokyo, p. 07.

Online, E.B., (2013), Turbojet. Available at: http://www.britannica.com/EBchecked/topic/609597/turbojet. (Accessed 25 Jun 2012).

Papalexandris, M. V et al., (2007), “Structural characteristics of detonation expansion from a small channel to a larger one”. *Proceedings of the Combustion Institute*, Vol. 31, No 2, p.2407–2414.

Paxson, D., Wilson, J. and Welch, G., (2007), “Comparison between simulated and experimentally measured performance of a four port wave rotor”, In: *43rd AIAA/ASME/SAE/ASEE Joint Propulsion Conference & Exhibit.* Paper No AIAA-2007-5049, 08-11 July 2007, Cincinnati, OH, p. 17.

Paxson, D.E., (1995), “Comparison between numerically modelled and experimentally measured wave-rotor loss mechanisms”. *Journal of Propulsion and Power*, Vol. 11, No 5, p.908–914.

Pegg, R., Couch, B. and Hunter, L., (1996), “Pulse detonation engine air induction system analysis”, In: *32nd Joint Propulsion Conference and Exhibit*. Paper No AIAA-96-2918, 01-03 July 1996, Lake Buena Vista, FL., p. 17

Pezhman, A. et al., (2005), “Numerical Analysis of Hydrogen-Fuelled Wave Rotors for Gas Turbine Applications”, In *Proceedings International Hydrogen Energy Congress and Exhibition IHEC 2005*. 13-15 July 2005, Istanbul, p. 11.

Piechna, J. et al., (2010), “Numerical Analysis of the Wave Topping Unit for Small Turbojet”, In: *ASME, ed. ASME Turbo Expo 2010: Power for Land, Sea, and Air*. Paper No GT 2010- 23064, 14-18 June 2010, Glasgow, p. 9.

Piechna, J. et al., (2004), “Radial-Flow Wave Rotor concepts, unconventional designs and Applications” 13-19 November 2004, California, p.11.

Pintgen, F. et al., (2003), “Direct observations of reaction zone structure in propagating detonations”. *Combustion and Flame*, Vol. 133, No 3, p.211–229.

Poinsot, T. and Veynante, D., (2005), "Theoretical and numerical combustion” (2nd ed), Edwards, Philadelphia.

Price, D.J., (2012), “Smoothed particle hydrodynamics and magnetohydrodynamics”. *Journal of Computational Physics*, Vol. 231, No 3, p.759–794.

Roy, G.D. et al., (2004), “Pulse detonation propulsion: challenges, current status, and future perspective”. *Progress in Energy and Combustion Science*, Vol. 30, No 6, p.545–672.

Rolls Royce (2011), AE-3007 Gas Turbine. Available at: http://www.rolls-royce.com/civil/products/smallaircraft/ae_3007/

S. Browne, J.Z. and Shepherd, J.E., (2008), “Numerical Solution Methods for Shock and Detonation Jump Conditions”, Report number FM2006.006, GALCIT, Pasadena, CA.

Saddawi, S.D., (2013), “*Multi-Objective Computational Engineering Design Optimisation for Micro-Combustor Devices”* (PhD Thesis, Cranfield University, Cranfield).

Saravanamuttoo, H., (2008), “Gas turbine theory” (6th ed), Pearson Prentice Hall, Upper Saddle River, N.J.

Schauer, F.R. et al., (2005), “Detonation Initiation of Hydrocarbon-Air Mixtures in a Pulsed Detonation Engine”, In: *43rd AIAA Aerospace Sciences Meeting.* Paper No 2005-1343, 10-13 January 2005, p. 10.

Selppel, C., (1946), “*Pressure Exchanger”*, US Patent 2,399,394.

Shapiro, A.H., (1954), “The Dynamics and thermodynamics of compressible fluid flow”, Vol.1, Ronald Press, New York.

Sharpe, G.J., (2001), “Transverse waves in numerical simulations of cellular detonations”. *Journal of Fluid Mechanics*, Vol.447, p.31–51.

Snyder, P., Alparslan, B. and Nalim, R., (2002), “Gas Dynamic Analysis of the CVC, A Novel Detonation Cycle”, In: *38th AIAA/ASME/SAE/ASEE Joint Propulsion Conference & Exhibit*. Paper No AIAA 2002-4069, 07-10 July 2002, p. 11.

Vasil’ev, A.A., (2002), “Optimization of DDT Accelerators”, In: G. Roy et al., (editors). Advances in Confined Detonations. Torus Press, Moscow, p. 31–35.

Versteeg, H.K. and Malalasekera, W., (2007), “An introduction to computational fluid dynamics: the finite volume method (2^{nd} ed), Prentice Hall, Glasgow.

Wark, K., (1995), “Advanced thermodynamics for engineers”, McGraw-Hill, New York.

Weber, H., (1995), “Shock wave engine design”, John Wiley, New York.

Weber, H.E., (1992), “Wave Engine Aerothermodynamic Design”. *Journal of Engineering for Gas Turbines and Power-transactions of The Asme*, Vol. 114, No 4, p.790-796.

Welch, G.E., Scott, J.M. and Paxson, D.E., (1995), “Wave rotor-enhanced gas turbine engines”, *31 st AIAA/ASME/SAE/ASEE Joint Propulsion Conference and Exhibit.* Paper No AIAA-95-2801, 10-12 July 1995, San Diego CA, p. 14.

Westbrook, C.K. and Dryer, F.L., (1984). “Chemical kinetic modelling of hydrocarbon combustion”. *Progress in Energy and Combustion Science*, Vol. 10, No 1, p.1–57.

Wildon, F. and William C., D., (2000), “Detonation Theory and Experiments”, Dover ,New York.

William, H.H. and David, T.P., (2002), “Thermodynamic Cycle Analysis of Pulse Detonation Engines”. *Thermodynamic Cycle Analysis of Pulse Detonation Engines*, Vol. 18, No 1, p.68–76.

Wilson, J., (1997), “Design of the NASA Lewis 4-Port Wave Rotor Experiment”, In: *33rd Joint Propulsion Conference and Exhibit*. Paper No AIAA 97-3139, 06-09 July 1997, p. 10.

Wilson, J. and Paxson, D.E., (1993), “*Jet engine performance enhancement through use of a wave-rotor topping cycle”,* Report number NASA- TM-4486, NASA, Cleveland, Ohio.

Wintenberger, E. et al. (2003), “Analytical Model for the Impulse of Single-Cycle Pulse Detonation Tube*”. Journal of Propulsion and Power*, Vol. 19, No 1, p.22–38.

Wintenberger, E., (2004), “*Application of Steady and Unsteady Detonation Waves to Propulsion”*, (PhD Thesis, California Institute of Technology, California).

Wintenberger, E. et al., (2002), “Impulse of a Single-Pulse Detonation Tube”, Report number FM 00-8, California Institute of Technology, Pasadena, C.A.

Wintenberger, E. and Shepherd, J.E., (2004), “Thermodynamic Analysis of Combustion Processes for Propulsion Systems”, In: *AIAA, ed. 42nd AIAA Aerospace Sciences Meeting and Exhibit*. Paper No 2004-1033, 05-08 January 2004, Reno, NV, p. 18.

Yuhui, W., Fuhua, M. and Vigor, Y., (2003), “System Performance and Thermodynamic Cycle Analysis of Airbreathing Pulse Detonation Engines”. *Journal of Propulsion and Power*, Vol. 19, No 4, p.556–567.

Yungster, S., Radhakrishnan, K. and Breisacher, K., (2006), “Computational study of NOx formation in hydrogen-fuelled pulse detonation engines”. *Combustion Theory and Modelling*, Vol. 10, No 6, p.981-1002.

Zdvorak, E.H., (1999), “*Constant Volume Combustion Turbine with Plurality Flow Turbine Wheels”*, US Patent 5,960,625.

APPENDICES

Appendix A Commonly Used Gas Dynamic Equations

The first group of algebraic equations provides the relationship between the stagnation properties and the static one, as well as the area ratio.

$$\frac{\mathrm{T}_0}{T} = 1 + \frac{k-1}{2}M^2 \quad \textbf{(A- 1)}$$

$$\frac{\mathrm{p}_0}{p} = \left(\frac{T_0}{T}\right)^{\frac{k}{k-1}} \quad \textbf{(A- 2)}$$

$$\frac{\mathrm{A}}{A^*} = \frac{1}{M}\left(\frac{2}{(k+1)}\left(1 + \frac{k-1}{2}M^2\right)\right)^{\frac{k+1}{2(k-1)}} \quad \textbf{(A- 3)}$$

By means of Eq. (A- 1) to Eq. (A- 2) we are allowed to link the pressure, temperature and density of gas that have the same stagnation properties.

The second group of equations considers the compression effect given by shock waves, once the initial condition of the gases is set.

$$\left(\frac{a_2}{a_1}\right)^2 = \frac{T_2}{T_1} = 1 + \frac{2(k-1)}{(k+1)^2}\left[kM_x^2 - \frac{1}{M_x^2} + 1 - k\right] \quad \textbf{(A- 4)}$$

$$\left(\frac{u_2 - u_1}{a_1}\right) = \pm\frac{2}{(k+1)}\left[M_x - \frac{1}{M_x}\right] \quad \textbf{(A- 5)}$$

$$\left(\frac{p_2}{p_1}\right) = 1 + \frac{2k}{(k+1)}[M_x^2 - 1] \quad \textbf{(A- 6)}$$

The sub-index x indicates that the Mach number is obtained by fixing the reference on the shock wave, instead of the wave rotor channel.

Finally, the third group of algebraic equations evaluates the properties of gases after the intersection with a rarefaction wave, when their initial condition is known.

$$\frac{a_2}{a_1} = 1 \pm \frac{k-1}{2}\left(\frac{u_2 - u_1}{a_1}\right) \quad \textbf{(A- 7)}$$

$$\frac{T_2}{T_1} = \left(\frac{a_2}{a_1}\right)^2 \quad \textbf{(A- 8)}$$

$$\frac{p_2}{p_1} = \left(\frac{a_2}{a_1}\right)^{\frac{2k}{k-1}} \quad \textbf{(A- 9)}$$

The sign (+) or (-) in Eq. (A- 5) and Eq. (A- 7) depend upon the direction of the shock or rarefaction wave. So if they are moving in positive axis, the sign (+) is used and if they are moving in negative axis the sign (-) is used. At the same time, for all equations, 1 and 2 indicate the fluid properties before and after the crossing of the wave.

Appendix B

Equation B- 1 is the stoichiometric balance of Jet-A and the coefficients that precede each specie represent the number of kilo-moles (N_i) of the component (i) in the reaction.

$$C_{12}H_{23} + 17.75O_2 + 66.74\,N_2 \rightarrow 12CO_2 + 11.5H_2O + 66.74N_2 \quad \textbf{B- 1}$$

Equation **B- 2** is the first law of thermodynamic implemented in a closed system without the interaction of any type of work.

$$Q_{in} + \sum_{i=1}^{N} (N_i \bar{u}_i)_{in} = \sum_{i=1}^{N} (N_i \bar{u}_i)_{out} \quad \textbf{B- 2}$$

Moreover, Eq. B- 3 is the enthalpy definition, Eq. B 4 is the equation of state of ideal gases, and Eq. B- 5 computes the enthalpy of a component of the mixture using its enthalpy of formation.

$$\bar{h}_i = \bar{u}_i + p\bar{v} \quad \textbf{B- 3}$$

$$p\bar{v} = R_u T \quad \textbf{B 4}$$

$$\bar{h}_i = \bar{h}^o_{f,i} + \left(\bar{h}_{i,T} - \bar{h}_{i,297K}\right) \quad \textbf{B- 5}$$

The substitution of Eq. D- 3, Eq. D- 4 and Eq. D- 5 into Eq. B- 2, followed by its manipulation given as result Eq. B- 6.

$$\bar{Q}_{in} = \sum_{i=1}^{N} \left(N_i\left(\bar{h}^o_{f,i}\right)\right)_{out} - \sum_{i=1}^{N} \left(N_i\left(\bar{h}^o_{f,i}\right)\right)_{in} + R_u \sum_{i=1}^{N} (N_i T)_{in} - R_u \sum_{i=1}^{N} (N_i T)_{out} \quad \textbf{B- 6}$$

The first two terms at the right of this equation represent the heat value of fuel whilst the last two terms represent the correction factor since the process is at constant volume, see Eq. B- 7.

$$\bar{q}_{in} = -Q_{net,p} + R_u T \left(\sum_{i=1}^{N} (N_i)_{in} - \sum_{i=1}^{N} (N_i)_{out} \right) \quad \textbf{B- 7}$$

The heat value of fuel is calculated using 298 K as the reference temperature and therefore the same value of temperature must be implemented into the correction factor.

The correction factor for Jet-A is then calculated as:

$$8.314\frac{kJ}{kmol\cdot K}\cdot 298\ \mathrm{K}\cdot(85.49\ kmol-90.24kmol)=-11768.467\ kJ \qquad \textbf{B- 8}$$

Since the heat released is computed for one kmole of fuel ($N_{fuel}=1\ kmol$ in Eq. (B- 1)), then the computed value is also represented by:

$$-11768.467\ kJ/kmol_{fuel} \qquad \textbf{B- 9}$$

Moreover, the heat value of fuel implemented in Jet-A is:

$$Q_{net,p}=43100\ \frac{kJ}{kg_f}\ \rightarrow 7197700\ \frac{kJ}{kmol_f} \qquad \textbf{B- 10}$$

The correction factor is less than 0.2 % of the heat value of fuel at constant pressure, so it can be neglected.

Appendix C

The following tables present the polynomial coefficients implemented to compute the Cp of each of the components involved in the reaction mechanism of kerosene.

Piecewise-polynomials are implemented to estimate the enthalpy of each component. The first group estimates the enthalpy in a temperature range from 300 K to 1000 K (see Table C-1), the other group estimates the enthalpy in a temperature range from 1000 K to 3000 K (see Table C-2).

Table C-1 Polynomial coefficients implemented in a temperature range from 300 K to 1000 K

	a_1	a_2	a_3	a_4	a_5	a_6	a_7
$C_{12}H_{22}$	2.0869E+00	1.3315E-01	-8.1157E-05	2.9409E-08	-6.5195E-12	-3.5913E+04	2.7355E+01
O_2	3.7825E+00	-2.9967E-03	9.8473E-06	-9.6813E-09	3.2437E-12	-1.0639E+03	3.6577E+00
N_2	3.2987E+00	1.4082E-03	-3.9632E-06	5.6415E-09	-2.4449E-12	-1.0209E+03	3.9504E+00
CO_2	2.3568E+00	8.9846E-03	-7.1236E-06	2.4592E-09	-1.4370E-13	-4.8372E+04	9.9011E+00
H_2O	4.1986E+00	-2.0364E-03	6.5204E-06	-5.4880E-09	1.7720E-12	-3.0294E+04	-8.4903E-01

Table C-2 Polynomial coefficients implemented in a temperature range from 1000 K to 3000 K

	a_1	a_2	a_3	a_4	a_5	a_6	a_7
$C_{12}H_{22}$	2.4880E+01	7.8250E-02	-3.1551E-05	5.7879E-09	-3.9828E-13	-4.3111E+04	-9.3655E+01
O_2	3.2825E+00	1.4831E-03	-7.5797E-07	2.0947E-10	-2.1672E-14	-1.0885E+03	5.4532E+00
N_2	2.9266E+00	1.4880E-03	-5.6848E-07	1.0097E-10	-6.7534E-15	-9.2280E+02	5.9805E+00
CO_2	3.8575E+00	4.4144E-03	-2.2148E-06	5.2349E-10	-4.7208E-14	-4.8759E+04	2.2716E+00
H_2O	3.0340E+00	2.1769E-03	-1.6407E-07	-9.7042E-11	1.6820E-14	-3.0004E+04	4.9668E+00